ornl

OAK RIDGE NATIONAL LABORATORY

LOCKHEED MARTIN

MANAGED AND OPERATED BY
LOCKHEED MARTIN ENERGY RESEARCH CORPORATION
FOR THE UNITED STATES
DEPARTMENT OF ENERGY

ORNL-27 (3-96)

ORNL/TM-13395

Heavy Vehicle Propulsion System Materials Program Semiannual Progress Report for April 1996 Through September 1996

Prepared for
U.S. Department of Energy
Assistant Secretary for
Energy Efficiency and Renewable Energy
Office of Transportation Technologies

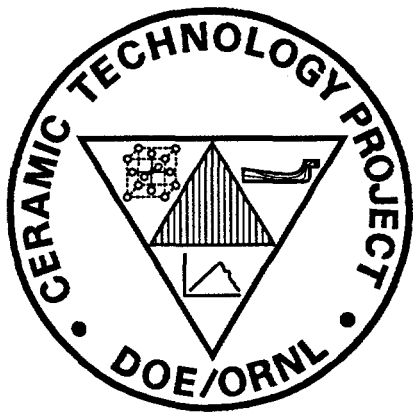

ORNL/TM-13395

Metals and Ceramics Division

HEAVY VEHICLE PROPULSION SYSTEM MATERIALS PROGRAM SEMIANNUAL PROGRESS REPORT FOR APRIL 1996 THROUGH SEPTEMBER 1996

D. R. Johnson
Program Manager

Date Published: April 1997

Prepared for
U.S. Department of Energy
Assistant Secretary for Energy Efficiency and Renewable Energy
Office of Transportation Technologies
EE 07 01 00 0

Prepared by the
OAK RIDGE NATIONAL LABORATORY
Oak Ridge, Tennessee 37831-6285
managed by
LOCKHEED MARTIN ENERGY RESEARCH CORP.
for the
U.S. DEPARTMENT OF ENERGY
under Contract DE-AC05-96OR22464

REPORTS PREVIOUSLY ISSUED

ORNL/TM-9325	Period March 1983-September 1983
ORNL/TM-9466	Period October 1983-March 1984
ORNL/TM-9497	Period April 1984-September 1984
ORNL/TM-9673	Period October 1984-March 1985
ORNL/IM-9947	Period April 1985-September 1985
ORNL/TM-10079	Period October 1985-March 1986
ORNL/TM-10308	Period April 1986-September 1986
ORNL/TM-10469	Period October 1986-March 1987
ORNL/TM-10705	Period April 1987-September 1987
ORNL/TM-10838	Period October 1987-March 1988
ORNL/TM-11116	Period April 1988-September 1988
ORNL/TM-11239	Period October 1988-March 1989
ORNL/TM-11489	Period April 1989-September 1989
ORNL/TM-11586	Period October 1989-March 1990
ORNL/TM-11719	Period April 1990-September 1990
ORNL/TM-11859	Period October 1990-March 1991
ORNL/TM-11984	Period April 1991-September 1991
ORNL/TM-12133	Period October 1991-March 1992
ORNL/TM-12363	Period April 1992-September 1992
ORNL/TM-12428	Period October 1992-March 1993
ORNL/TM-12674	Period April 1993-September 1993
ORNL/TM-12778	Period October 1993-March 1994
ORNL/TM-12924	Period April 1994-September 1994
ORNL/TM-13046	Period October 1994-March 1995
ORNL/TM-13219	Period April 1995-September 1995
ORNL/TM-13262	Period October 1995-March 1996

Research sponsored by the U.S. Department of Energy, Assistant Secretary for Energy Efficiency and Renewable Energy, Office of Transportation Technologies, as part of the Heavy Vehicle Propulsion System Materials Program, under contract DE-AC05-96OR22464 with Lockheed Martin Energy Research Corporation.

CONTENTS

HEAVY VEHICLE PROPULSION SYSTEM MATERIALS PROGRAM
SEMIANNUAL PROGRESS REPORT
FOR APRIL 1996 THROUGH SEPTEMBER 1996

SUMMARY AND INTRODUCTION

The purpose of the Heavy Vehicle Propulsion System Materials Program is the development of materials: ceramics, intermetallics, metal alloys, and metal and ceramic coatings, to support the dieselization of class 1-3 trucks to realize a 35% fuel-economy improvement over current gasoline-fueled trucks and to support commercialization of fuel-flexible LE-55 low-emissions, high-efficiency diesel engines for class 7-8 trucks.

The Office of Transportation Technologies, Office of Heavy Vehicle Technologies (OTT OHVT) has an active program to develop the technology for advanced LE-55 diesel engines with 55% efficiency and low emissions levels of 2.0 g/bhp-h NOx and 0.05 g/bhp-h particulates. The goal is also for the LE-55 engine to run on natural gas with efficiency approaching that of diesel fuel. The LE-55 program is being completed in FY 1997 and, after approximately 10 years of effort, has largely met the program goals of 55% efficiency and low emissions. However, the commercialization of the LE-55 technology requires more durable materials than those that have been used to demonstrate the goals. Heavy Vehicle Propulsion System Materials will, in concert with the heavy duty diesel engine companies, develop the durable materials required to commercialize the LE-55 technologies.

OTT OHVT also recognizes a significant opportunity for reduction in petroleum consumption by dieselization of pickup trucks, vans, and sport utility vehicles. Application of the diesel engine to class 1, 2, and 3 trucks is expected to yield a 35% increase in fuel economy per vehicle. The foremost barrier to diesel use in this market is emission control. Once an engine is made certifiable, subsequent challenges will be in cost; noise, vibration, and harshness (NVH); and performance.

The design of advanced components for high-efficiency diesel engines has, in some cases, pushed the performance envelope for materials of construction past the point of reliable operation. Higher mechanical and tribological stresses and higher temperatures of advanced designs limit the engine designer; advanced materials allow the design of components that may operate reliably at higher stresses and temperatures, thus enabling more efficient engine designs. Advanced materials also offer the opportunity to improve the emissions, NVH, and performance of diesel engines for pickup trucks, vans, and sport utility vehicles.

The principal areas of research are:

Cost Effective High Performance Materials and Processing
Advanced Manufacturing Technology
Testing and Characterization
Materials and Testing Standards

COST EFFECTIVE HIGH PERFORMANCE MATERIALS AND PROCESSING

COST-EFFECTIVE SINTERED REACTION-BONDED SILICON NITRIDE AND MICROWAVE ANNEALING OF SILICON NITRIDE

J. O. Kiggans, jr., T. N. Tiegs, H. T. Lin, F. C. Montgomery, D. L. Barker,
J. M. Snodgrass, D. W. Coffey, J. L. Schroeder and C. C. Davisson
Oak Ridge National Laboratory
Oak Ridge, TN 37831

Objective / Scope

There are three major objectives of this research element: the first objective is the development and characterization of new sintered reaction-bonded silicon nitride materials (SRBSN) as cost-effective materials for use in high temperature applications such as diesel engines; the second objective is the development of techniques for the scale-up of the nitridation of silicon materials for industrial purposes using microwave heating; the third objective is the treatment of dense silicon nitride materials (Si_3N_4) using microwave heating (for improved high temperature creep properties) followed by an analysis of the changes in the mechanical properties, the microstructures, and chemical phases of those materials.

Technical Highlights

Previous Semi-annual Results

During the first semi-annual reporting period, a number results were obtained in the task of developing new and improved SRBSN materials. The type of silicon powder (Si), sintering additives, and α-Si_3N_4 seed type were found to influence the processing and final mechanical properties of sintered reaction bonded silicon nitride.

High purity silicon powders produced low α-Si_3N_4 content during nitridation. The Si powder type had no apparent effect on densification. More complete nitridation and higher room temperature mechanical properties were observed for the Si powders with higher Fe contents. However, the higher Fe contents resulted in greater high temperature strength degradation and so there was better high temperature strength retention with the higher purity Si.

High α-Si_3N_4 contents were found after nitridation with α-Si_3N_4 seeded materials and with MgO-Y_2O_3 as the sintering additive. Densification was inhibited by refractory additives, such as Y_2O_3-SiO_2. The highest room temperature strength and fracture toughness values correlated to high nitrided α-Si_3N_4 contents. The high temperature strength behavior was similar for all additive types. In a second group of samples it was found that the most promising sintering aid combinations were Si_3N_4-9% Y_2O_3-3% Al_2O_3 (9Y3A), Si_3N_4-9% Y_2O_3-3% Al_2O_3-0.4% Cr_2O_3 (9Y3A-Cr_2O_3), and Si_3N_4-8% Y_2O_3-4% Al_2O_3 (8Y4A).

It was also found that of the SRBSN materials produced by the addition of one of 6 different α-Si_3N_4 seeds, the materials containing E10, S1, or M11 α-Si_3N_4 seeds exhibited the highest strength and toughness; the material containing the added β-Si_3N_4 seed also gave favorable results.

SRBSN Composition Work- Present Report

In the previous reporting period, a number of SRBSN materials were fabricated using the standard densification condition of sintering in a graphite furnace for 2 h at 1800 °C. Some of the density results obtained for samples were lower than expected. It was thought that

longer sintering times might be necessary to achieve acceptable densification of some compositions. To address this possibility, additional samples were fabricated and sintered for 10 h at 1800 °C. Standard conditions, as have been discussed in previous reports were used for the sample preparation and processing. The densities of sintered materials were measured by alcohol immersion, and the materials were sent to Chand Kare Inc. for MOR bar preparation.

Table 1 lists the densities, tensile strengths, and toughness values for the different SRBSN compositions. These data show that the increased sintering time results increased densities for all samples processed. The SRB-23 sample did not densify as much as hoped, so composition changes will be made to improve the densification. Table 1 shows that some compositions showed increased strength for the 10 h sintering period (versus the 2 h time), several compositions exhibited the same strength, and the SRB-25 composition (containing the Globe silicon) had a reduced strength. Some increase in strength values for the 10h samples was expected with increased the densification. The reason for the drop in strength by the SRB-25 was unexpected. Data in Table 1 shows that the toughness increased substantially for all samples sintered for the 10 h time. Broken bars from each sample type are being polished for SEM analysis, to help relate the toghness increases to sintering time and to compare differences in sample compositions

Sample bars from SRB-11 and SRB-21 sintered for 2 and 10 were given to H. T. Lin for determination of the creep properties (SRB-11 sample composition is Si_3N_4-9% Y_2O_3-3% Al_2O_3 and the SRB-21 composition is Si_3N_4-8% Y_2O_3-4% Al_2O_3). The flexural creep tests were conducted at 1200 °C at selected applied stress levels in air. The specimens were loaded in a four-point bending fixture of sintered α-SiC with inner and outer spans of 19 and 38 mm, respectively. The stress was directly applied through a sintered α-SiC pushrod using a dead weight loading system. The midspan deflection of the tensile surface of bend bars, with respect to the points on the tensile surface aligned with the inner loading points, was continuously monitored by a high-temperature three-probe extensometer. The applied stress and resultant creep strain were calculated from the load and displacement data using the procedures described by Hollenberg. Figure 1 is a graph showing the creep properties of two compositions. There was a dramatic improvement in the creep properties observed for the samples sintered for 10h. The creep properties of a gas-pressure sintered silicon nitride (GPSSN) containing 5% Y_2O_3-2% is presented for reference..

The third activity of this report was the preparation of new SRBSN compositions and some favorable die-pressed compositions analyzed in previous reports, using "gelcast techniques". Of particular interest in these new samples was the addition of the low-cost Dow silicon nitride powder for α–seed materials for the SRBSN materials. Previous studies have shown that low-cost Starck S1 silicon nitride powders performed nearly as well as the expensive Ube E-10 powder. Starck no longer synthesizes the S1 powder or a cheap powder of equivalent particle size, so the Dow powder may provide a good alternative.

Table 2 lists several new SRBSN precursor powders (SRB 27-31) with the component chemicals. Two kg of each powder batch was turbomilled in isopropyl alcohol (IPA) according to procedures given in previous bi-monthly reports. The powders were dried, and a portion of each batch was attritor milled with gelcast reagents, and cast into 10 by 10 by 1.2 cm plates (SRB-30 could not be gelled, so die-pressed samples were made). In addition, gelcast plates were made of other silicon powder batches of interest (SRB-1 and TM-154). All the plates were isopressed, fired in air to remove the binders, and furnace treated for nitridation and sintering. The final sintering conditions were 2 or 10 h at 1800°C. Following sintering the densities of each plates was measured (Table 2). The sintering data followed the previous trend of higher sintered densities achieved for the

longer 10 h sintering treatment. The plates were then sent to Chand Kare Inc. for the preparation of MOR bars. Strength and toughness measurements and SEM analysis will be made on these bars, and the data will be presented in future reports.

Supplemental Silicon Analysis for SRBSN Studies

In order to have more information on three of the most promising batches of silicon powders, the particle sizes were determined using a Horiba LA-700 Laser Scattering Size Distribution Analyzer. For this procedure, a 1 wt % solution of each silicon powder was dispersed with an ultrasonic probe in IPA containing 0.5 wt % PVP-K15 and 0.5 wt % Darvan 821A.

Table 3 lists the three different silicon powders under study: Elkem metallurgical grade, lot # JS-19; Elkem metallurgical grade, lot # 49485; and Globe metallurgical grade, lot # 77-877. Also listed are the particle sizes provided by the manufacture, and the particle sizes obtained by the Horiba laser scattering technique at ORNL. Figures 2, 3, and 4 are graphs showing the particle sizes of the three powder batches. These data show that the two Elkem metallurgical grades had almost identical mean particle sizes and particle size distributions, and the Globe silicon batch exhibited a much higher mean particle size and a broader particle size distribution than both Elkem powder batches. In previous work, it was noted the silicon preforms made with the Globe powder pressed to much higher green densities affor equivalent isopresspressures than did samples made with the Elkem powders. The higher green densities of the Globe samples were probably due to the higher particle packing possible with the broader particle size distribution. Overall, this study pointed out the deficiency in particle size data from manufactures and the need to obtain a good analyses in order to understand the effects of particle sizes on the samples properties.

Scale-Up of Microwave Nitridation of Silicon Preforms

Eaton Corp. and Southern Illinois (SIU) University Studies

A collaborative study has begun with the SIU and Eaton Corp. involving the scale-up of SRBSN fabrication using microwave heating for the nitridation (ORNL) and sintering via the continuous belt furnace at SIU. Eaton Co. is the supplier of some materials (silicon preforms) for this study. Several types of silicon preforms of a proprietary composition were shipped to Oak Ridge for microwave nitridation.

Several batches of the silicon preforms have been nitrided using microwave heating. Two batches of 49 silicon rods each, two batches of 45 discs each, and one batch of 250 bars were nitrided by microwave heating. Each batch of 49 rods was processed as a single layer of samples placed on a boron nitride (BN) setter plate; each batch of 45 discs was processed with 9 discs per layer on five stacked setter plates; and the group of 250 bars was processed as 5 layers of 50 bars on BN sheets. Figures 5 and 6 show photographs of individual layers of discs and bars on BN setters, and Figure 7 shows a photograph of a layer of bars inside the insulation box used for microwave heating. The heating arrangements used were similar to the process developed at ORNL for processing of silicon preforms produced by Golden Technologies, Inc. Nitridation was performed in nitrogen with 4 vol % hydrogen. The maximum temperature in the nitridation was 1300°C as measured by a type "C" thermocouple. The weights of samples were measured before and after processing.

Figure 8 is a graph which shows the microwave power versus the temperature during the nitridation of the silicon rods (similar power curves were obtained for the other processing runs). The large drop in the microwave power at approximately 1150 °C signals the onset

of nitridation of the silicon parts. The visual appearance of nitride samples was uniform with the exception of appearance of some whisker growth on samples near the edge of the package walls and the tops of samples on the top layer of preforms within the multilayered packages. The average weight gain for the rods was 64.3 %, with a standard deviation of 0.022 %. Similar results were obtained for other sample groups.

The first sintering treatment of microwave nitrided pre-SRBSN preforms (prepared in the June-July work period at ORNL) in the continuous belt furnace at Southern Illinois University was not as successful as hoped. Warping of bars and dimpling of some disc samples was noted. The BN setter plates used for nitridation may have had a material interaction with the samples, or more likely, the BN plates, with their high thermal conductivity, caused too high heat transfer from one side of the small parts, thus causing an uneven nitridation. New crucible fixtures consisting of refractory silicon nitride setter plates (with a lower thermal conductivity than BN) are now being used for nitridation tests. Approximately 300 microwave are being nitrided for shipment to Dr. Wittmer.

Microwave Annealing of Dense Silicon Nitride

Preparation of materials for annealing studies

Activity 1 was the preparation of gelcast plates of E-10 Si_3N_4 with 6 wt % Y_2O_3 and 2 wt % Al_2O_3 (AY6 Composition). Activity 2 involved the preparation of silicon gelcast preforms containing 9 wt % Y_2O_3 , 3 wt % Al_2O_3, and 1.7 wt % SiO_2 (SRB-1 Composition). Table 4 gives particulars concerning the powders used for preparation of the AY6 and SRB-1 plates.

Approximately 6 kg of AY6 powder and 6 kg of SRB-1 powder were milled using a turbomill and distilled water and IPA as solvents, respectively. Each material was gelcast into twenty, 10 by 10 by 1.2 cm plates using methods discussed in previous bimonthly reports.
Conditions for the binder burnout of the gelcast parts have been discussed in previous reports. Silicon based parts (TM-145) were debindered at a peak temperature of 550°C. Si_3N_4-based parts (AY6) were debindered at a peak temperature of 600 °C. The TM-145 parts were nitrided in a graphite furnace to a final temperature of 1450 °C. The TM-145 nitrided parts were then packed in powder (Si_3N_4-4% Y_2O_3-0.5% SiO_2-10% BN) in a graphite crucible and sintered in N_2 to a final condition of 1800°C for 5 h. The debindered AY6 gelcast parts were packed in Si_3N_4-4% Y_2O_3-0.5% SiO_2-10% BN powder and sintered in the graphite element overpressure furnace according to the following schedule: Heat at 10 °C / min to 1000 °C in vacuum; raise the pressure of N_2 to 0.1 MPa and heat at 10 °C to 1800 °C; heat at 10 °C / min to 1900 °C and simultaneously pressurize the furnace with N_2 to 1 MPa; hold the temperature at 1900 °C for 2 h; heat at 10 °C / min to 1950 °C and then pressurize to 1.3 MPa; hold at 1950 °C for 3 h. Following sintering, densities of all parts were measured using the immersion density technique.

The average densities of the TM-145 SRBSN and the AY6 sintered materials are given in Table 5. These densities were judged to be excellent for annealing studies, however further examination of several of the sintered AY6 parts exhibited a number of small (pin head size) bubble-like defects at the surface. A decision was made to forgo using the gelcast AY6 parts for initial microwave annealing experiments until tests bars could be made to determine if there is an overall large problem (how many defects per piece) with these sintered materials. Several of the sintered gelcast AY6 parts have been sent off for machining into MOR specimens.

To enable the study of microwave annealing of AY6 materials to proceed, the decision was made to make die-pressed preforms from spray dried powders. This method was chosen since earlier results have shown that good properties can be obtained from die pressed preforms made from spray dried powders. A 6 kg batch of spray dried AY6 powder was prepared using a Niro Portable Atomizer. The composition of the powder was identical to the gelcast AY6 batch of powder, except that 1.25 % Elvanol (Grade 75-15) and 1.2% Carbowax 20M were added to insure good granulation during the spray dry process (and the gelcast reagents were deleted). Several trial attempts at spray drying the E-10 based material indicated that a slurry consisting of 26 vol % powders was the upper volumes limit which could be continuously sprayed). The AY6 spray dried powder collected from the bottom port of the spray dryer (by vibration) was screened through a 40 mesh screen to remove a small amount agglomerates (0.5 wt % of the total powder). A second container of spray dried powder, the fine powder collected from the cyclone collector of the spray dryer, was stored for future use. The -40 mesh powder was dried at 80 °C to remove any residual water. The final powder was very flowable and dust free, and could be die pressed effectively without lubricants (normally stearic acid is required for die press operations). Seventeen, 7.6 cm diameter by 1.9 cm thick pellets were pressed and were then isopressed to 275 MPa. The average green density of the parts (after binder burnout) was 1.66 g/cm^3 . Binder burnout was performed according to established procedures, and the discs sintered using the same conditions as the gelcast AY6 preforms. An average density for several of the sintered parts is given in Table 5. The average density was almost identical to that obtained for the sintered gelcast AY6 material.

Annealing runs of the TM-145 SRBSN bars and the sintered AY6 discs in both the conventional and microwave furnaces are underway. A description of the experimental set-up and conditions will be presented in the reports of next fiscal year.

Status of Milestones

Partial Completion of the milestones was achieved. Completion delayed due to the problem discussed below.

Problems Encountered

There was a delay in work by 1 month due to temporary loss of technician during the recent ORNL reduction in force. The support technician was forced to suspend work and start preparation for termination, re-training, etc. The technician has since been notified that he will remain a member of the Ceramic Processing Group and continue to work on the present project.

Publications

J. O. Kiggans, Jr., T. N. Tiegs, C. C. Davisson, M. S. Morrow, and G. J. Garvey, "Scale-up of the Nitridation and Sintering of Silicon Preforms Using Microwave Heating," to published in the Materials Research Society Symposium Proceedings, for the Spring MRS Meeting, April 8-12, 1996, San Francisco, CA..

Communications/Visits/Travel

Presentation of paper entitled, "Effect of Composition On The Processing and Properties of Sintered Reaction-Bonded Silicon Nitride," by J. O. Kiggans at the Materials Research Society Symposium Spring MRS Meeting, April 8-12, 1996, San Francisco, CA..

Table 1. Density values and mechanical properties of SRBSN materials prepared from die-pressed, isopressed silicon preforms which were sintered for 2 and 10 hours.

	S 2h	S 10h	S 2h	S 10h	S 2h	S 10h
Sample ID (Description)	Density (g/cm^3)	Density (g/cm^3)	Strength (MPa)	Strength (MPa)	Toughness ($MPa\sqrt{m}$)	Toughness ($MPa\sqrt{m}$)
Elkem SRB 11 (9Y3A E10)	94.8	99.0	628	625	6.4	8.1
Elkem SRB 14 (9Y3A LC10)	96.2	99.0	526	582	6.0	8.4
Elkem SRB 15 (9Y3A LC10, 20%)	95.4	100.4	475	594	6.5	8.4
Elkem SRB 21 (8Y4A LC10)	97.1	99.8	647	766	5.6	8.2
Elkem SRB 23 (6Y5MgO 0.2CaO LC10)	84.1	91.5	ND	497	ND	8.5
Elkem SRB 24 (5.5Y5.5Spinel LC10)	95.7	98.0	293	596	5.7	7.8
Globe SRB 25 (9Y3A LC10)	94.5	98.1	639	374	5.8	6.6
Elkem SRB 154 (9Y3A Cr_2O_3 LC10)	97.8	99.5	676	665	5.8	7.8

Table 2. SRBSN gelcast and die pressed, isopressed preforms from turbomilled (TM) and attritor milled (AM) powders

Sample ID	Final Composition[a]	Si_3N_4 Seed Type	Sintering Time	Density g/cm³
TM154[b] TM	Si_3N_4-9% Y_2O_3[c]-3% Al_2O_3 - 0.4% Cr_2O_3[d]	LC-10N[e]	2 h	3.25
TM154[b] TM	Si_3N_4-9% Y_2O_3[c]-3% Al_2O_3 - 0.4% Cr_2O_3[d]	LC-10N[e]	10 h	3.28
SRB-27[f] TM	Si_3N_4-9% Y_2O_3[g]-3% Al_2O_3	S1[h]	2 h	3.21
SRB-27[f] TM	Si_3N_4-9% Y_2O_3[g]-3% Al_2O_3	S1[h]	10 h	3.25
SRB-29[i] TM	Si_3N_4-9% Y_2O_3[g]-3% Al_2O_3	Dow # XU3556, 1994[l]	2 h	3.25
SRB-29[i] TM	Si_3N_4-9% Y_2O_3[g]-3% Al_2O_3	Dow # XU3556, 1994[l]	10 h	3.28
SRB-30[i] TM	Si_3N_4-8% Y_2O_3[g]-4% Al_2O_3	Dow # XU3556 lot 102P5[m]	2 h	3.24
SRB-30[i] TM	Si_3N_4-8% Y_2O_3[g]-4% Al_2O_3	Dow # XU3556 lot 102P5[m]	10 h	3.27
SRB-31[i] TM	Si_3N_4-6% Y_2O_3[g]-6% Spinel[n]	Dow # XU3556 lot 102P5[m]	2 h	3.22
SRB-31[i] TM	Si_3N_4-6% Y_2O_3[g]-6% Spinel[n]	Dow # XU3556 lot 102P5[m]	10 h	3.23
SRB-1[b] AM	Si_3N_4-9% Y_2O_3[c]-3% Al_2O_3	LC 10N	10 h	3.28
SRB-1 TM[b], July 95	Si_3N_4-9% Y_2O_3[c]-3% Al_2O_3	LC 10N	10 h	3.28
SRB-1[b] TM, Feb 96	Si_3N_4-9% Y_2O_3[g]-3% Al_2O_3	LC 10	2 h	3.29
SRB-1[b] TM, Mar 96	Si_3N_4-9% Y_2O_3[c,g]-3% Al_2O_3	LC 10 + LC 10N	10 h	3.27

[a]Unless indicated, all compositions contained approximately 1.5 wt. % SiO_2, U. S. Silica, Berkeley Springs, WV, 5 μm particle size; and indicated amounts of Al_2O_3 - Reynolds, Malakoff, TX; Grade RC-HP DBM, and 10 wt % α- Si_3N_4 seed

[b]Silicon, Elkem Metals Co., Buffalo, NY; Metallurgical Grade, (JS-19), < 10 μm particle size

[c]Y_2O_3 - Molycorp, White Plains, NY; Grade 5600, >99.99%

[d]Cr_2O_3 as chrome nitrate (CrN_3O_9), Aldrich, Milwaukee, WI; 99% pure.

[e]Si_3N_4, Starck Gmbh & Co., Berlin, Germany; Grade LC 10-N, 0.5 mean particle size

[f]Silicon, Globe Metallurgical Inc., Beverly, OH; Metallurgical Grade, < 325 mesh

[g]Y_2O_3, Starck, Berlin, Germany; Grade Fine, >99.99%

[h]Si_3N_4, Starck Gmbh & Co., Berlin, Germany; Grade S1, 0.7 mean particle size.

[i]Silicon, Elkem Metals Co., Buffalo, NY; Metallurgical Grade, (lot 49485), < 10 μm particle size.

jMgO, J. T. Baker, Phillipsburg, NJ

[k]CaO added as $CaCO_3$, Mallinckrodt, St. Louis, MO; Analytical Grade

[l]Dow Chemical Co., Midland, MI; Phase I experimental powder

[m]Dow Chemical Co., Midland, MI; Phase II experimental powder

[n]Spinel, lot #34978, Ceralox, Tucson, Arizona

Table 3. Particle sizes of silicon powders

Powder Designation	Manufactures Size Description	Measured Mean Particle Size
Elkem JS-19	D50, 3.4 μm	mean 3.77 μm, median 3.27μm
Elkem 49485	Min. 2 μm, Max 4 μm	mean 3.52 μm, median 3.22 μm
Globe 77-877	325 mesh and down	mean 14.54 μm, median 12.35 μm

Table 4. AY6 and SRB-1 compositions

Sample ID	Final Composition
AY6	Si_3N_4 [a] -6% Y_2O_3 [b]-2% Al_2O_3 [c]
SRB-1 [d]	Si_3N_4 [e] -9% Y_2O_3 [f]-3% Al_2O_3 [c] - 1.7% SiO_2 [g]

[a]Si_3N_4, UBE Industries, LTD, Japan; Grade E-10, 0.2 μm mean particle size.
[b]Y_2O_3 - Starck, Berlin, Germany; Grade Fine, >99.99%
[c]Reynolds, Malakoff, TX; Grade RC-HP DBM.
[d]Silicon, Elkem Metals Co., Buffalo, NY; Metallurgical Grade, (lot JS-19), 3.4 μm particle size.
[e]Si_3N_4, Starck Gmbh & Co., Berlin, Germany; Grade LC 10-N, 0.5 mean particle size
[f]Y_2O_3 - Molycorp, White Plains, NY; Grade 5600, >99.99%
[g]U. S. Silica, Berkeley Springs, WV, 5 μm particle size

Table 5. Samples prepared for microwave annealing study.

Sample	Forming Method	Composition	Average Density (g/cm^3)	% T D (T D)
TM-145-GC	Gelcast	Si_3N_4-9% Y_2O_3-3% Al_2O_3	3.27	99.1 (3.30)
AY6-GC	Gelcast	Si_3N_4-6% Y_2O_3-2% Al_2O_3	3.25	99.6 (3.26)
AY6-DP-IP-SD	Die-Press and Isopress	Si_3N_4-6% Y_2O_3-2% Al_2O_3	3.24	99.4 (3.26)

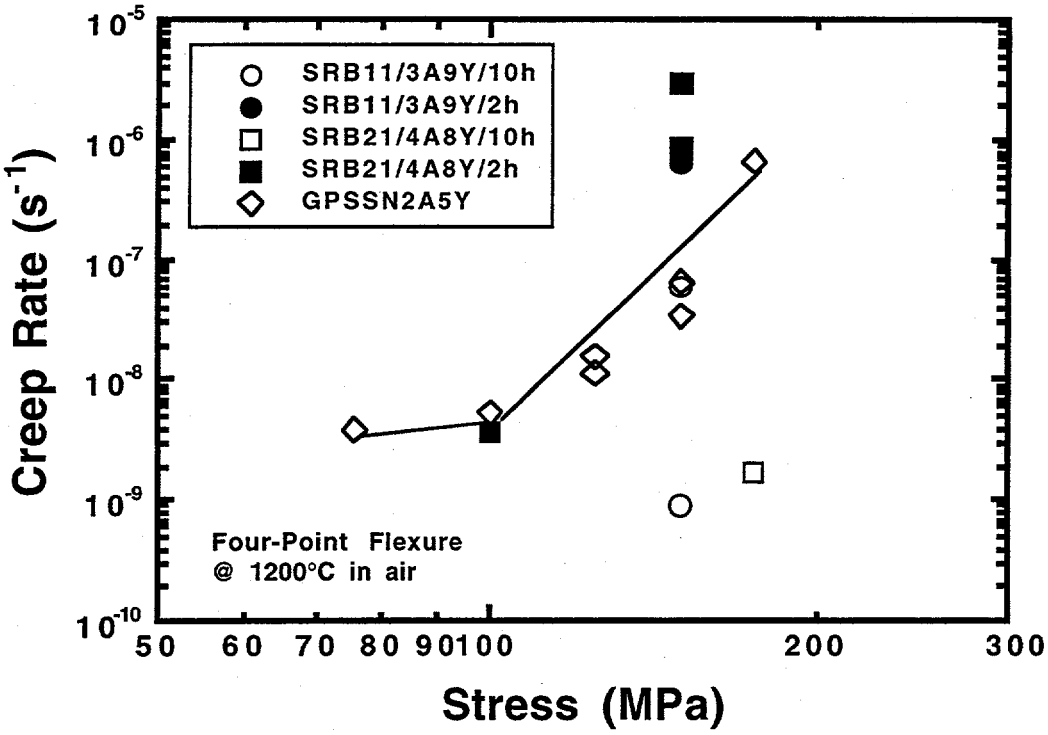

Figure1. Creep properties of two SRBSN compositions that were sintered for 2 h and 10h, respectively. Included is reference data for GPSSN2A5Y.

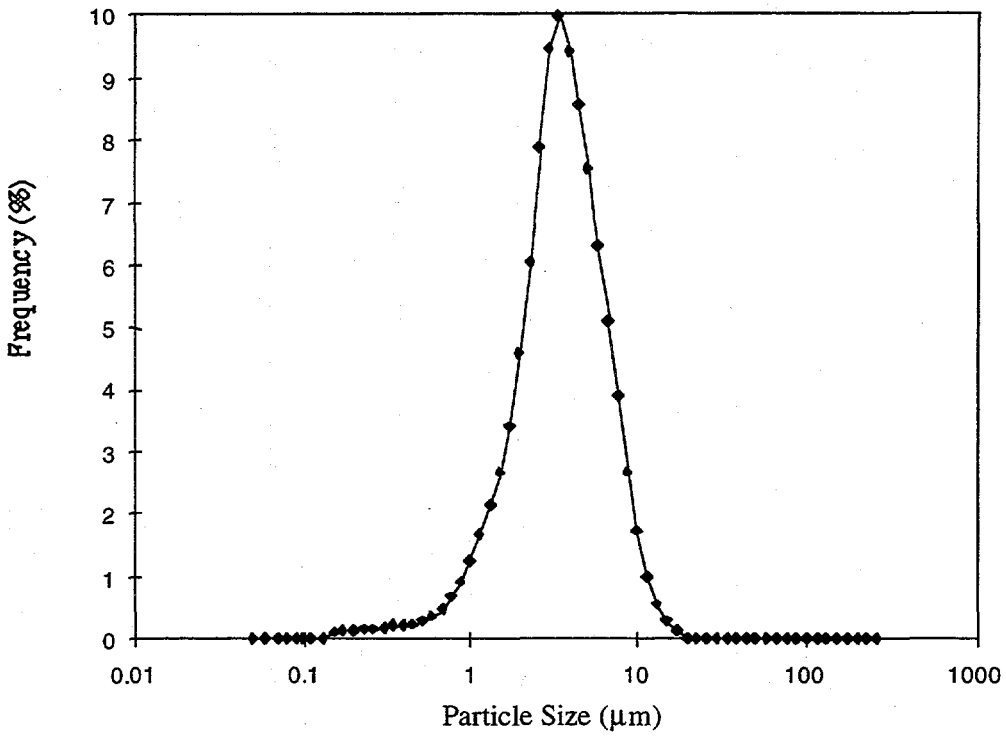

Figure 2. Particle size of JS-19 silicon powder.

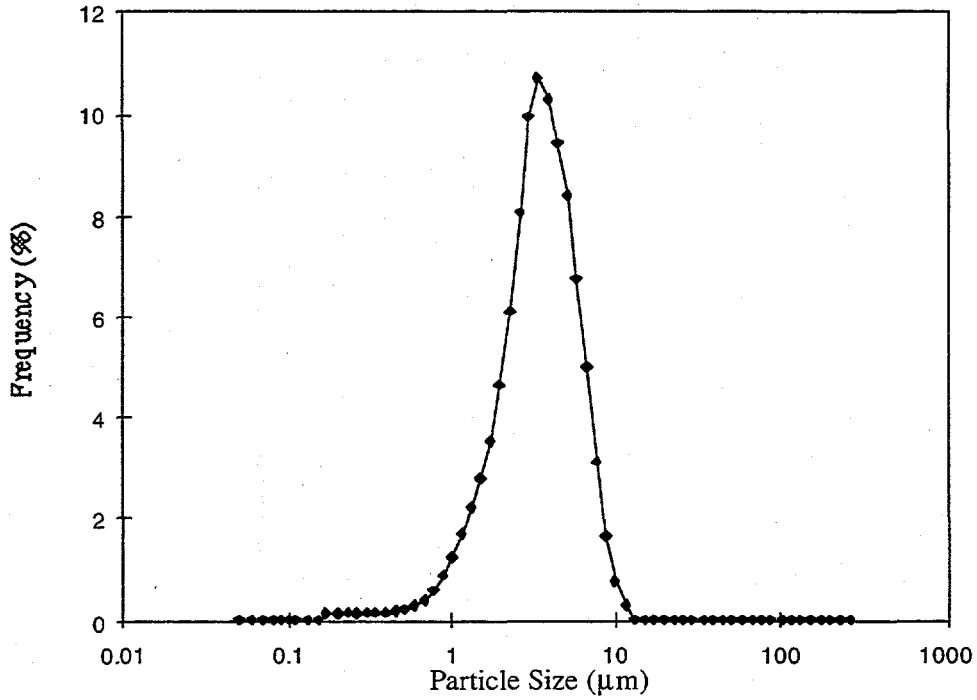

Figure 3. Particle size of 49485 silicon

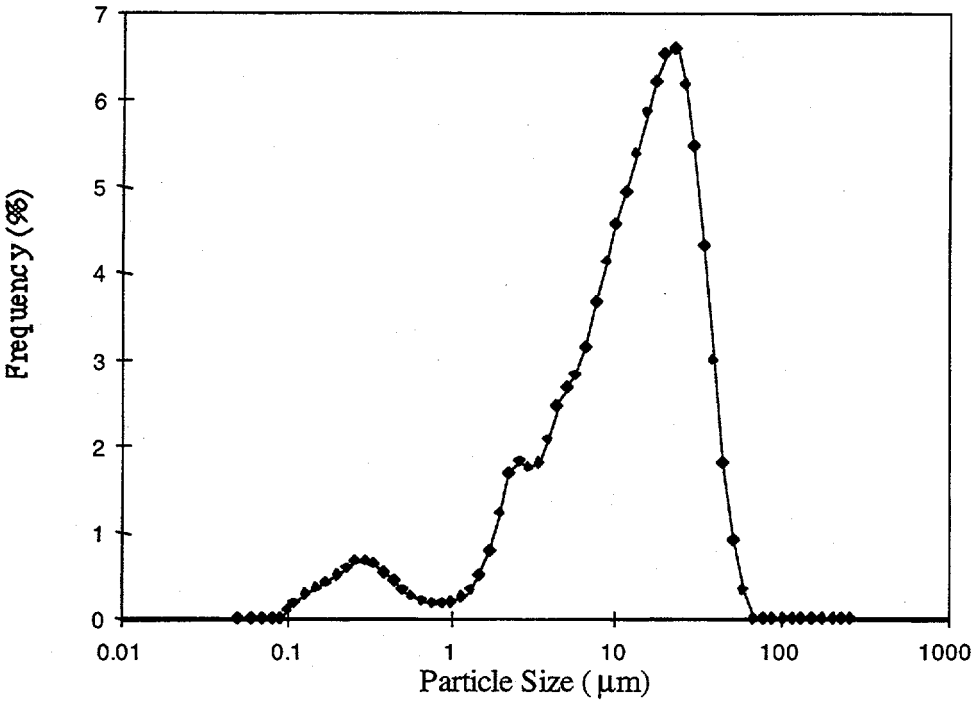

Figure 4. Particle size of Globe silicon powder

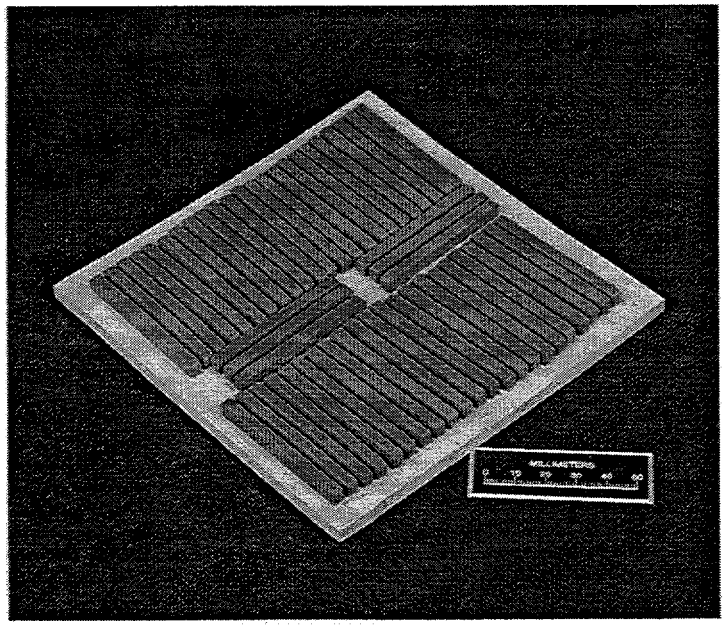

Figure 5. Photgraph of silicon bars as positioned on a BN plate prior to microwave nitridation

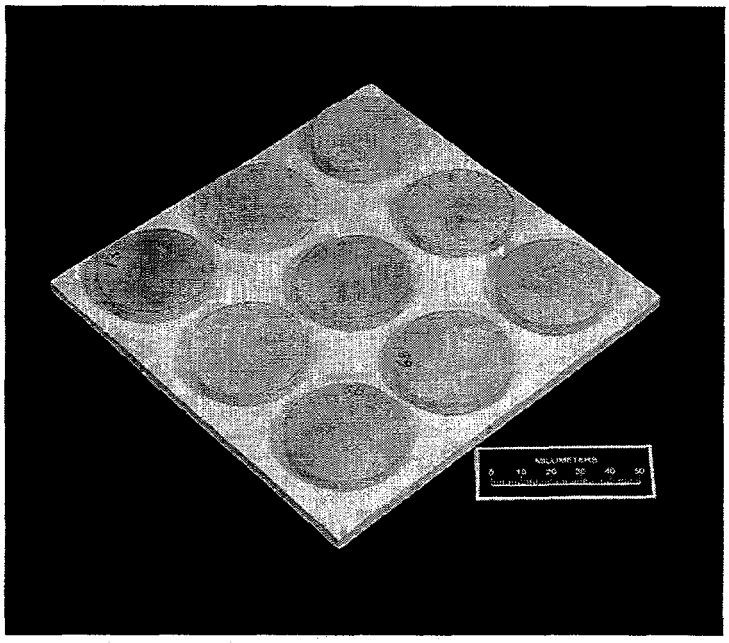

Figure 6. Photograph of silicon discs on a BN plate after microwave nitridation.

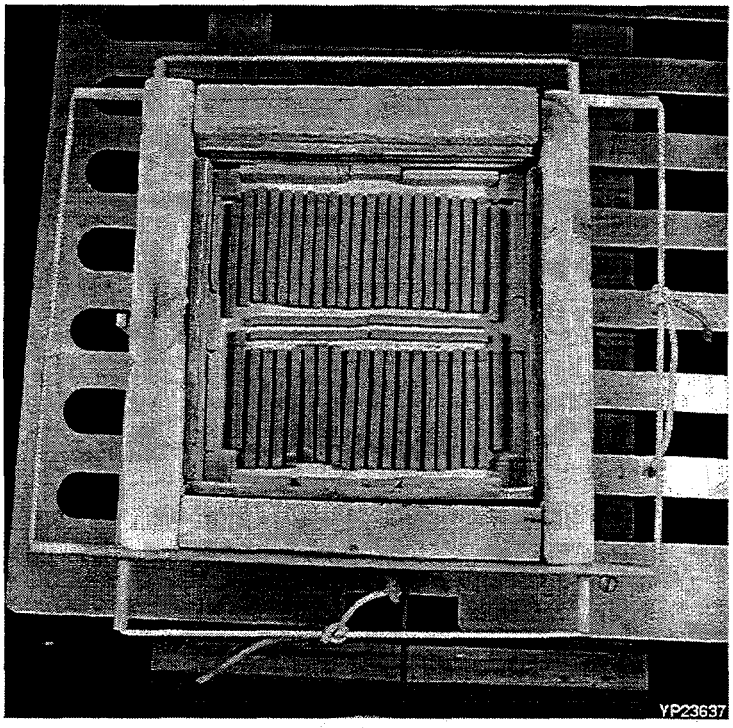

Figure 7. Photograph (overhead view) of a layer of silicon bars inside the insulation package after microwave nitridation.

COST-EFFECTIVE HIGH TOUGHNESS SILICON NITRIDE

T. N. Tiegs, F. C. Montgomery, P. A. Menchhofer, D. L. Barker and J. Schroeder
Oak Ridge National Laboratory
Oak Ridge, TN 37831

Objective/Scope

Significant improvement in the reliability of structural ceramics for advanced engine applications could be attained if the critical fracture toughness (K_{Ic}) were increased without strength degradation. Early results from ORNL research showed that significant increases in fracture toughness could be achieved by manipulating the microstructure to promote toughening mechanisms such as crack bridging. Excellent properties were obtained in this manner for the alumina and mullite matrix systems reinforced with SiC whiskers. In silicon nitride, acicular or elongated grains can be generated by in-situ growth and these can provide significant toughening on the same order as the whisker reinforced materials. Microstructural development to promote this type of growth in silicon nitride is the current emphasis of the project.

Technical Highlights

In-Situ Toughening of Silicon Nitride by Microstructure Development

ß-Si_3N_4 Nucleation and Initial Stage Microstructure Development - As reported previously, a study was initiated to determine the inter-relationships between the raw silicon nitride powders, the sintering additives as the liquid phase forms, ß-phase nucleation and the kinetics of the α-to-ß transformation. This is an area where there is a large body of fragmented data and observations, however, there is no systematic examination of the system. The work plans to examine the effects of the silicon nitride powders, the type of sintering additive and the effect of ß-Si_3N_4 seeds on the initial microstructure development. A summary of the specimen compositions is given in Table 1.

The materials were milled and pressed into pellets. These were then heated to numerous intermediate temperatures for short to long periods of time and analyzed. The short heat-treatments result in partial densification and α-to-ß transformation. Measurement of the densification kinetics allows determination of the activation energies involved in particle rearrangement and during solution-reprecipitation accompanying the α-to-ß transformation.

The samples were then analyzed by x-ray diffraction and the morphology examined by SEM. Results obtained to date on the ß-phase transformation rate as a function of the heating temperature and time are shown in Tables 2 through 4. Currently, the transformation rates are being correlated with Si_3N_4 powder type, sintering additive type, sintering additive amount, Si_3N_4 powder surface area, ß-Si_3N_4 seed type and ß-Si_3N_4 seed amount.

The rate of α-to-ß Si_3N_4 transformation between the different types of Si_3N_4 powders is summarized in Figs. 1 and 2 for two different sintering additive types. As shown, the kinetics are linear with time and the different powders exhibit quite different transformation behavior. For both of the sintering additive types shown, the Starck M11 Si_3N_4 powder generally exhibited the highest transformation rate, while the Dow EXP Si_3N_4 powder had the slowest. The differences in the transformation rates are dependent on the powder surface area and initial ß-Si_3N_4 content. In addition, other factors could possibly be involved, such as the lattice oxygen content, which could affect the Si_3N_4 dissolution rate.

The effect of different sintering additive types on the transformation rate is shown in Figs. 3 through 6 for Ube E-10, Starck M11, Starck GP and Dow EXP Si_3N_4 powders, respectively. Linear rate kinetics are again observed for the various additives. The Y_2O_3-Al_2O_3 (YA) and Y_2O_3-MgO (YM) based materials had the highest transformation rates. These additives also typically would have the lowest liquid phase viscosities during sintering which would tend to enhance the transformation rate. The Y_2O_3-SiO_2 (YS) additive system would have the highest liquid phase viscosity and indeed, the slowest transformation rate is observed with these materials. The Y_2O_3-La_2O_3-SrO (YbLaSr) system was intermediate in transformation kinetics compared to the other systems.

The effect of silicon nitride powder surface area on the transformation rate is given in Figs 7 and 8. Not surprisingly, the silicon nitride powder with the highest surface area exhibits the highest transformation rate. All these powders used for the surface area comparison were fabricated by the diimide process. Consequently, they should have similar initial ß-Si_3N_4 contents and lattice oxygen values, so the only difference in the transformation rate is attributable to the surface area variation.

Results on the transformation rate with different sintering additive amounts are summarized in Figs. 9 and 10. Generally, the larger amount of sintering additive resulted in a slower transformation rate. If the additional sintering additive increases the liquid volume, a slower transformation rate would tend to indicate a diffusion controlled process for the α-to-ß transformation. Additional analysis is required to confirm such a conclusion.

The effect of ß-Si_3N_4 seed additions on the transformation rate is shown in Figs. 11 and 12. As indicated, the ß-seed additions actually increase the α-to-ß transformation rate. While higher transformation rates with ß-seeding have been observed previously, no explanation for this behavior has been reported.

The effect of powder surface area on the transformation rate showed that the silicon nitride powder with the highest surface area exhibited the highest transformation rate. An Arrhenius plot of α-to-ß Si_3N_4 transformation rate as a function of inverse temperature (1/T) for two silicon nitride powders (Ube E-10 and Ube E-03) is shown in Fig. 13. The sintering additive was 6% Y_2O_3-2% Al_2O_3. The activation energies for the two powders are nearly identical with values on the order of 539-556 kJ/mol. These values are similar to previous studies on silicon nitride transformation rate kinetics.[1-3] Since both of the powders were fabricated by the diimide process they should have similar initial ß-Si_3N_4 contents and lattice oxygen values. So the only difference in the transformation rate is attributable to the surface area variation. A plot of the transformation rate as a function of silicon nitride powder surface area for the diimide powders is shown in Fig. 14. As indicated, there appears to be a linear relationship between the rate and the surface area for the data at 1500°C. Additional data will be generated at 1600°C and 1700°C to confirm these results.

Previous work had shown that ß-seed additions into the silicon nitride actually increase the α-to-ß transformation rate. A plot of the transformation rate as a function of ß-seeding is shown in Fig. 15. A linear relationship appears to exist between the transformation rate and the amount of initial ß-seeding. This indicates that transformation rate is a function of the ß-seed nuclei density and surface area which has been speculated in earlier work.[4] Additional tests will be performed to determine the relationships more precisely.

Further analysis of the rate kinetics is currently in progress and the morphology of the grain structures is being examined by SEM.

Status of Milestones

Milestone 123117 - Ambient pressure sintering of silicon nitride to obtain high fracture toughness was completed during the reporting period. The results on microstructural development during ambient pressure heating have been reported in previous bimonthly reports.

Communications/Visits/Travel

Travel by T. N. Tiegs to the American Ceramic Society Annual Meeting in Indianapolis, IN April 14-17, 1996.

Problems Encountered

None.

Publications

None.

References

1. L. J. Bowen, R. J. Weston, T. G. Carruthers and R. J. Brook, "Hot-Pressing and the α-ß transformation in Silicon Nitride," J. Mater. Sci., 13[2]341-350(1978).

2. L. J. Bowen T. G. Carruthers and R. J. Brook, "Hot-Pressing of Si_3N_4 With Y_2O_3 and Li_2O as Additives," J. Am. Ceram Soc., 61[7-8]335-339(1978).

3. F. K. van Dijen, A. Kerber, U. Vogt, W. Pfeiffer, and M. Schulze, "A Comparative Study of Three Silicon Nitride Powders Obtained by Three Different Syntheses," pp. 19-28 in Silicon Nitride 93, Key Engineering Mater., Vol. 89-91, Trans Tech Pub., Aedermannsdorf, Switzerland (1994).

4. W. Dressler, H-J. Kleebe, M. J. Hoffmann, M. Rühle and G. Petzow, "Model Experiments Concerning Abnormal Grain Growth in Silicon Nitride," J. Europ. Ceram. Soc., 16, 3-14(1996).

Table 1 - Experimental plan to determine ß-nucleation process during initial stage growth.

Sample No.	Si_3N_4 Powder Type	Additive Type	ß-Seed Addition
BN-1	Ube E-10	6 w/o Y_2O_3-2 w/o Al_2O_3	0
BN-2	Ube E-03	6 w/o Y_2O_3-2 w/o Al_2O_3	0
BN-3	Starck M11	6 w/o Y_2O_3-2 w/o Al_2O_3	0
BN-4	Starck GP	6 w/o Y_2O_3-2 w/o Al_2O_3	0
BN-5	Dow EXP	6 w/o Y_2O_3-2 w/o Al_2O_3	0
BN-6	Ube E-10	6 w/o Y_2O_3-1 w/o MgO	0
BN-7	Ube E-03	6 w/o Y_2O_3-1 w/o MgO	0
BN-8	Starck M11	6 w/o Y_2O_3-1 w/o MgO	0
BN-9	Starck GP	6 w/o Y_2O_3-1 w/o MgO	0
BN-10	Dow EXP	6 w/o Y_2O_3-1 w/o MgO	0
BN-11	Ube E-10	$Sr_2La_4Yb_4(SiO_4)_6O_2$ (8 eq.% oxygen)	0
BN-12	Ube E-03	$Sr_2La_4Yb_4(SiO_4)_6O_2$ (8 eq.% oxygen)	0
BN-13	Starck M11	$Sr_2La_4Yb_4(SiO_4)_6O_2$ (8 eq.% oxygen)	0
BN-14	Starck GP	$Sr_2La_4Yb_4(SiO_4)_6O_2$ (8 eq.% oxygen)	0
BN-15	Dow EXP	$Sr_2La_4Yb_4(SiO_4)_6O_2$ (8 eq.% oxygen)	0
BN-16	Ube E-10	9 w/o Y_2O_3-3 w/o Al_2O_3	0
BN-17	Starck M11	9 w/o Y_2O_3-3 w/o Al_2O_3	0
BN-18	Ube E-10	$Y_2Si_2O_7$ (5 eq.% oxygen)	0
BN-19	Starck M11	$Y_2Si_2O_7$ (5 eq.% oxygen)	0
BN-20	Ube E-05	6 w/o Y_2O_3-2 w/o Al_2O_3	0
BN-21	Ube E-05	$Sr_2La_4Yb_4(SiO_4)_6O_2$ (8 eq.% oxygen)	0
BN-22	Ube E-10	6 w/o Y_2O_3-2 w/o Al_2O_3	5 % E10/Pwd
BN-23	Ube E-10	6 w/o Y_2O_3-2 w/o Al_2O_3	5 % E3/Pwd
BN-24	Ube E-10	6 w/o Y_2O_3-2 w/o Al_2O_3	5 % S1/Pwd
BN-25	Ube E-10	6 w/o Y_2O_3-2 w/o Al_2O_3	25 % E10/Pwd
BN-26	Ube E-10	6 w/o Y_2O_3-2 w/o Al_2O_3	25 % E3/Pwd
BN-27	Ube E-10	6 w/o Y_2O_3-2 w/o Al_2O_3	25 % S1/Pwd
BN-28	Starck M11	6 w/o Y_2O_3-2 w/o Al_2O_3	5 % E10/Pwd
BN-29	Starck M11	6 w/o Y_2O_3-2 w/o Al_2O_3	5 % E3/Pwd
BN-30	Starck M11	6 w/o Y_2O_3-2 w/o Al_2O_3	5 % S1/Pwd
BN-31	Ube E-10	$Sr_2La_4Yb_4(SiO_4)_6O_2$ (8 eq.% oxygen)	5 % E10/Pwd
BN-32	Ube E-10	$Sr_2La_4Yb_4(SiO_4)_6O_2$ (8 eq.% oxygen)	5 % E3/Pwd
BN-33	Ube E-10	$Sr_2La_4Yb_4(SiO_4)_6O_2$ (8 eq.% oxygen)	5 % S1/Pwd

Table 2 - Summary of results on ß-Si_3N_4 contents after heating to intermediate temperatures (1500°C and 1600°C) and times. These samples contained no initial ß-phase content.

	1500°C			1600°C		
Sample ID	BN-x-5	BN-x-9	BN-x-10	BN-x-1	BN-x-11	BN-x-4
Time (min)	60	180	360	15	30	60
BN-1	9.8%	23.4%	46.6%	25.7%	43.6%	59.5%
BN-2	0.0%	0.6%	1.8%	1.4%	2.1%	3.5%
BN-3	21.5%	37.0%	58.2%	36.9%	52.4%	64.6%
BN-4	14.5%	31.9%	53.7%	31.3%	53.1%	67.9%
BN-5	2.9%	4.4%	7.9%	4.8%	2.3%	13.9%
BN-6	12.0%	17.6%	26.7%	25.9%	44.3%	54.8%
BN-7	3.3%	3.6%	6.7%	3.5%	6.8%	9.7%
BN-8	31.0%	53.6%	74.2%	45.8%	73.8%	85.2%
BN-9	16.8%	34.8%	59.0%	35.1%	65.4%	75.8%
BN-10	4.3%	6.2%	8.4%	7.7%	19.1%	16.4%
BN-11	11.9%	7.6%	11.8%	20.4%	21.8%	30.9%
BN-12	0.0%	0.0%	2.8%	1.1%	0.9%	1.5%
BN-13	17.4%	27.5%	37.7%	41.9%	49.0%	63.4%
BN-14	11.8%	13.6%	20.0%	25.8%	31.6%	42.4%
BN-15	3.9%	2.2%	2.5%	3.7%	4.1%	4.5%
BN-16	8.9%	20.4%	35.1%	26.7%	34.2%	48.4%
BN-17	20.7%	34.8%	49.9%	36.9%	54.5%	67.6%
BN-18	3.3%	3.1%	3.6%	1.5%	9.3%	13.9%
BN-19	9.8%	8.7%	11.0%	25.5%	24.6%	30.8%
BN-20		9.2%	15.8%			
BN-21		2.2%	2.7%			

Table 3 - Summary of results on ß-Si_3N_4 contents after heating to intermediate temperatures (1700°C and 1800°C) and times. These samples contained no initial ß-phase content.

		1700°C		1800°C
Sample ID Time (min)	BN-x-2 15	BN-x-6 60	BN-x-7 15	BN-x-8 60
BN-1	88.5%	100.0%	100.0%	100.0%
BN-2	7.5%	15.9%	26.6%	75.2%
BN-3	93.4%	100.0%	100.0%	100.0%
BN-4	98.8%	100.0%	100.0%	100.0%
BN-5	31.0%	49.4%	64.3%	96.1%
BN-6	86.6%	100.0%	100.0%	99.3%
BN-7	15.5%	36.6%	47.8%	98.9%
BN-8	100.0%	100.0%	100.0%	100.0%
BN-9	100.0%	100.0%	100.0%	100.0%
BN-10	32.5%	56.5%	69.7%	100.0%
BN-11	56.9%	79.0%	95.9%	100.0%
BN-12	5.8%	8.9%	15.2%	38.9%
BN-13	91.2%	100.0%	100.0%	100.0%
BN-14	73.0%	97.5%	100.0%	100.0%
BN-15	17.0%	25.6%	37.2%	78.3%
BN-16	81.9%	97.8%	100.0%	100.0%
BN-17	92.9%	100.0%	100.0%	100.0%
BN-18	40.5%	77.2%	97.4%	99.6%
BN-19	61.6%	78.5%	98.4%	100.0%

Table 4 - Summary of results on amount of α-to-ß Si_3N_4 conversion that occurred after heating to an intermediate temperature (1500°C) and times. These samples contained an initial ß-phase content which were not included in the conversion calculations. The values shown are for the fraction of initial α-phase transformed to ß-phase.

	1500°C		
Sample ID Time (min)	BN-x-9 180	BN-x-10 360	Initial ß-Phase Content
BN-22	38.2%	65.8%	5 % E10/Pwd
BN-23	31.5%	56.6%	5 % E3/Pwd
BN-24	40.1%	67.8%	5 % S1/Pwd
BN-25	71.2%	94.4%	25 % E10/Pwd
BN-26	32.8%	66.4%	25 % E3/Pwd
BN-27	74.4%	95.7%	25 % S1/Pwd
BN-28	39.4%	56.2%	5 % E10/Pwd
BN-29	34.0%	52.0%	5 % E3/Pwd
BN-30	39.2%	55.6%	5 % S1/Pwd
BN-31	16.0%	22.8%	5 % E10/Pwd
BN-32	8.6%	16.3%	5 % E3/Pwd
BN-33	16.1%	24.4%	5 % S1/Pwd

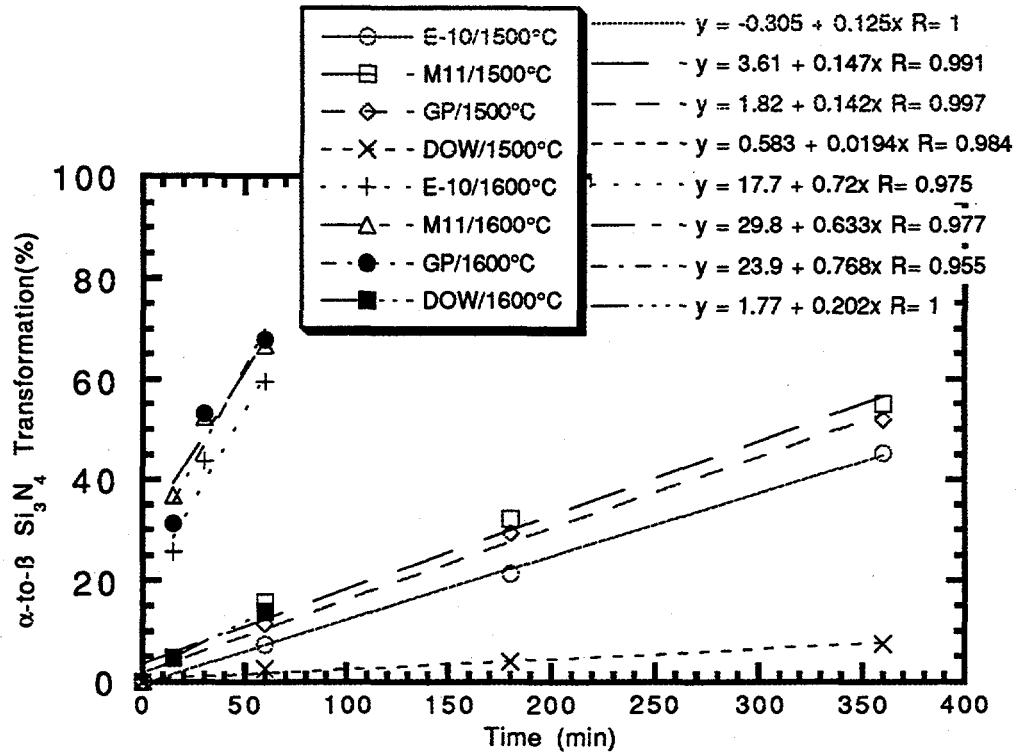

Fig. 1. α-to-ß Si_3N_4 transformation as a function of time for the various silicon nitride powders at 1500°C and 1600°C. The sintering additive was 6% Y_2O_3-2% Al_2O_3.

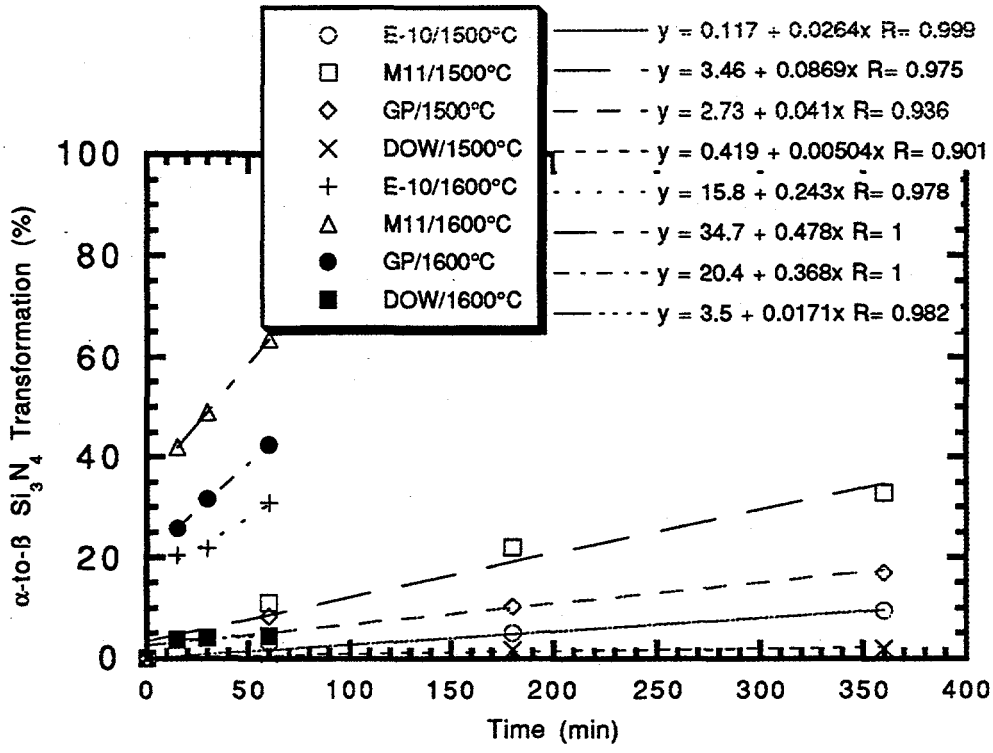

Fig. 2. α-to-ß Si_3N_4 transformation as a function of time for the various silicon nitride powders at 1500°C and 1600°C. The sintering additive was Yb_2O_3-La_2O_3-SrO.

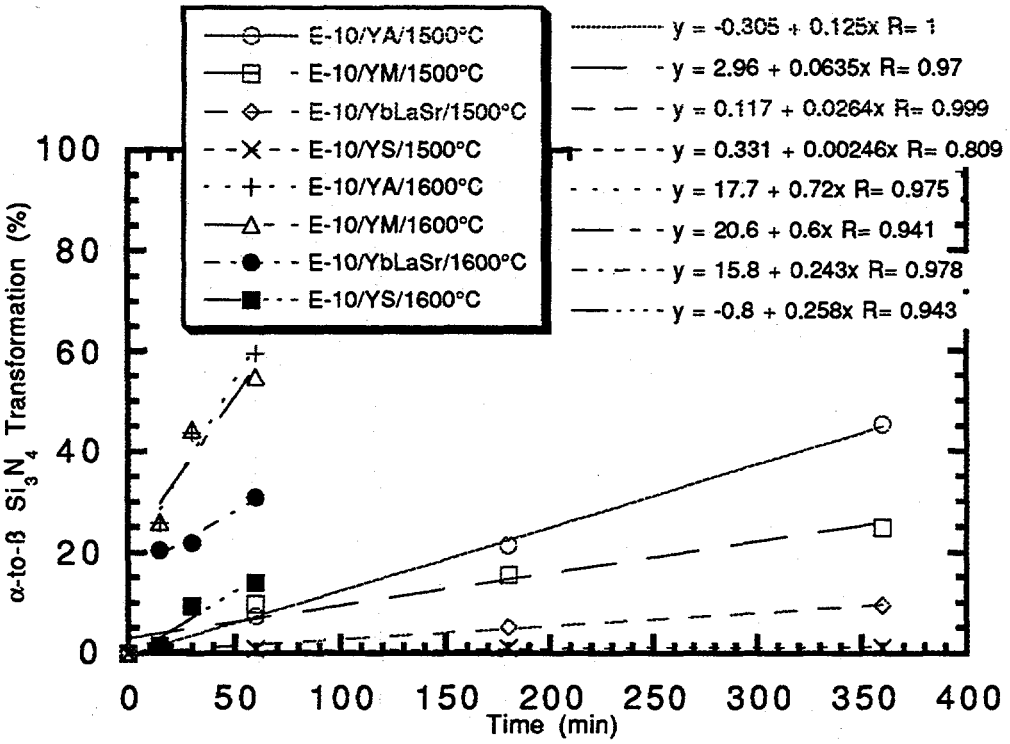

Fig. 3. α-to-ß Si_3N_4 transformation as a function of time for the various types of sintering additives at 1500°C and 1600°C. The silicon nitride powder was Ube E-10.

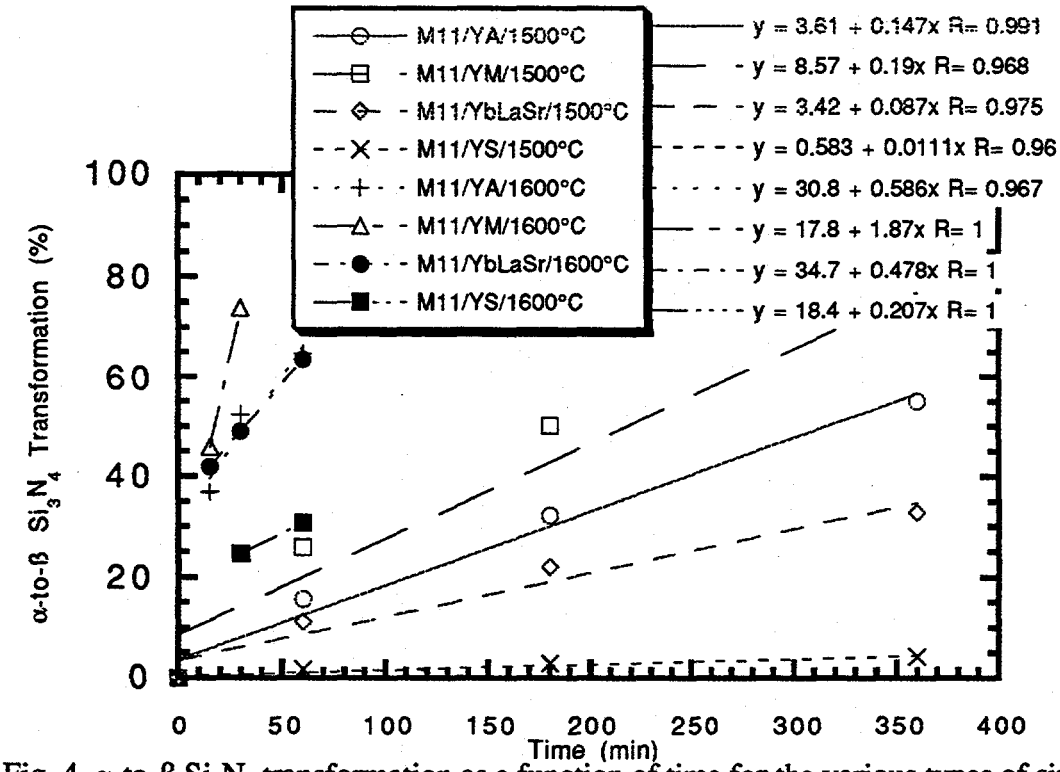

Fig. 4. α-to-ß Si_3N_4 transformation as a function of time for the various types of sintering additives at 1500°C and 1600°C. The silicon nitride powder was Starck M11.

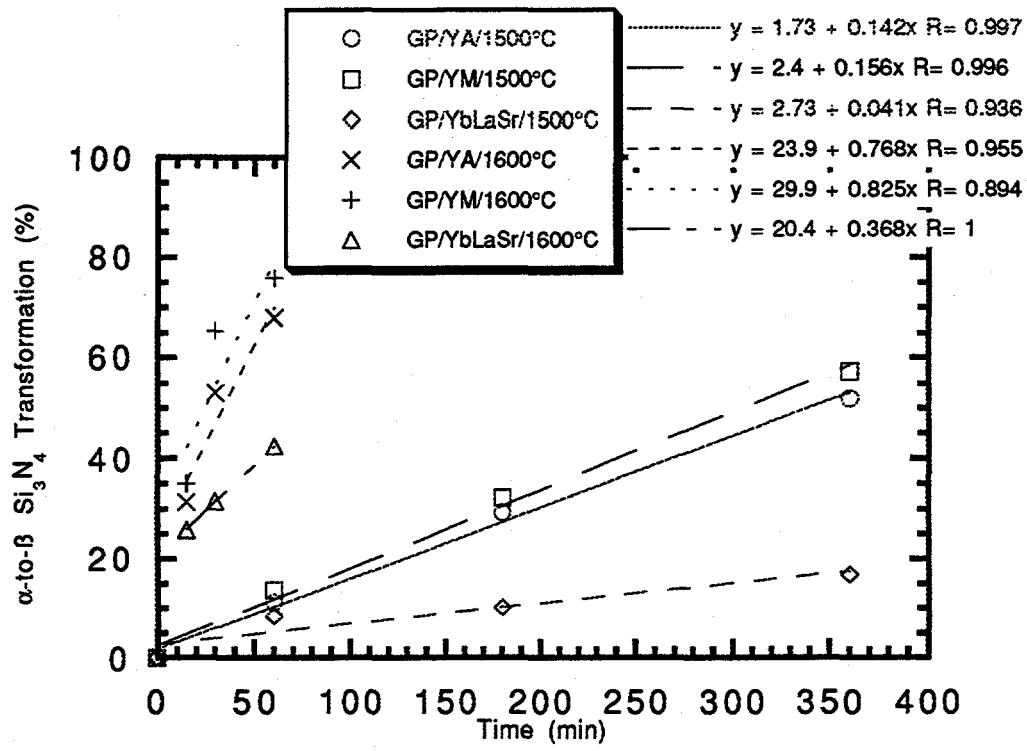

Fig. 5. α-to-ß Si_3N_4 transformation as a function of time for the various types of sintering additives at 1500°C and 1600°C. The silicon nitride powder was Starck GP.

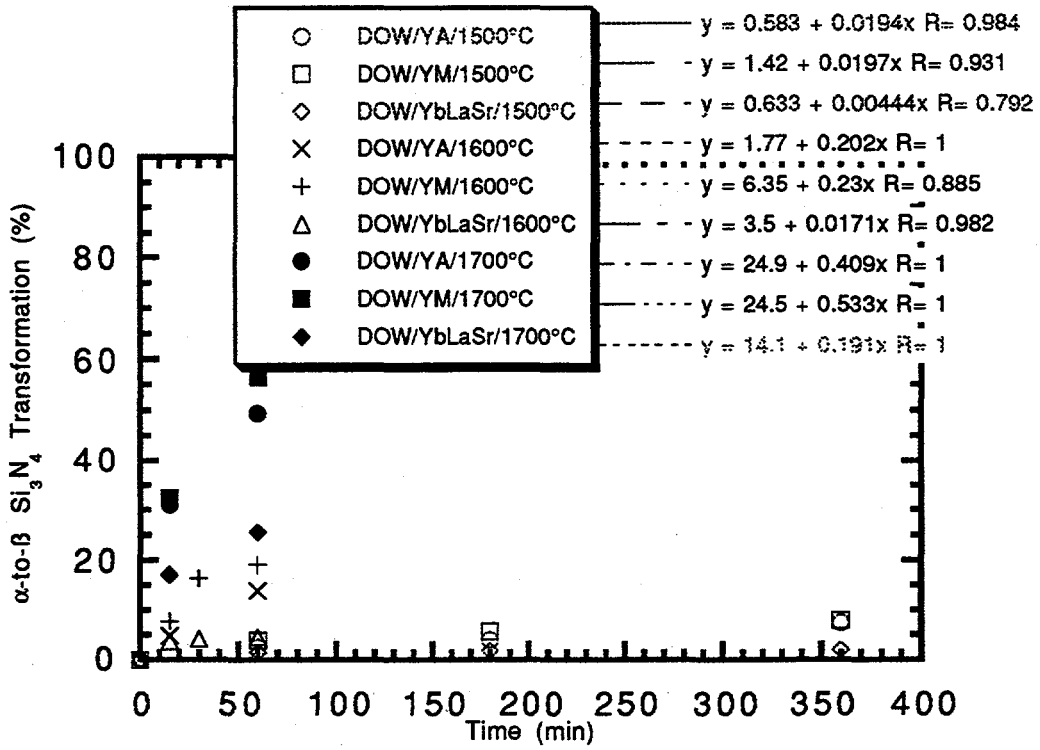

Fig. 6. α-to-ß Si_3N_4 transformation as a function of time for the various types of sintering additives at 1500°C and 1600°C. The silicon nitride powder was Dow EXP.

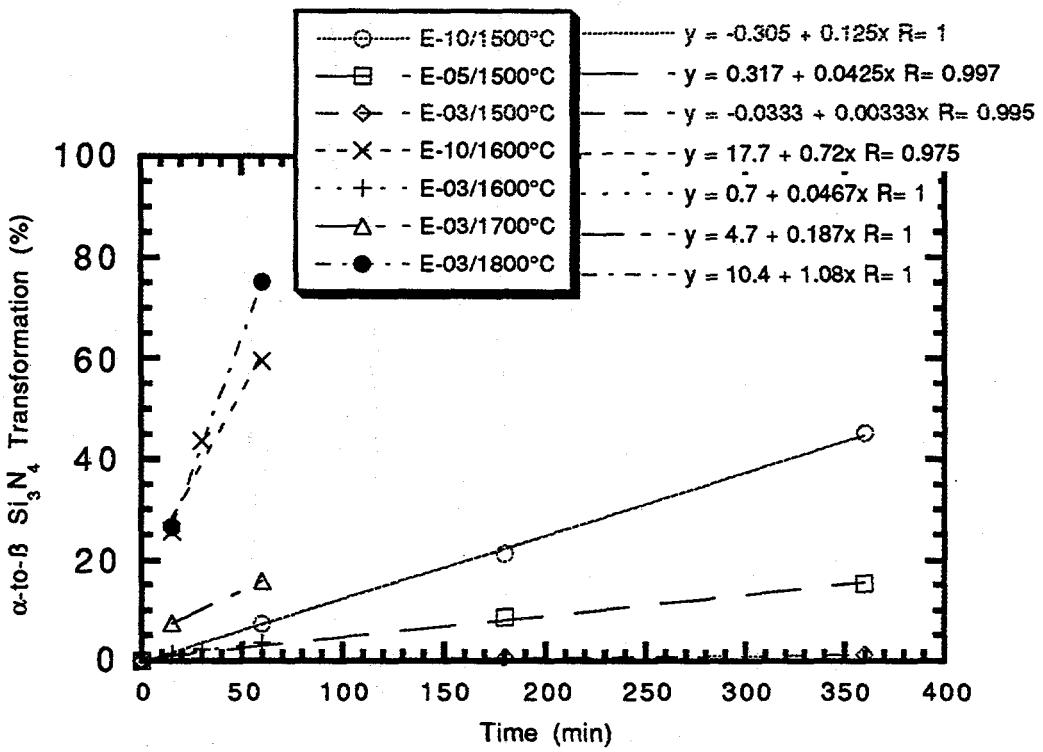

Fig. 7. α-to-ß Si_3N_4 transformation as a function of time for the similar silicon nitride powders with different surface areas at 1500°C and 1600°C. The sintering additive was 6% Y_2O_3-2% Al_2O_3.

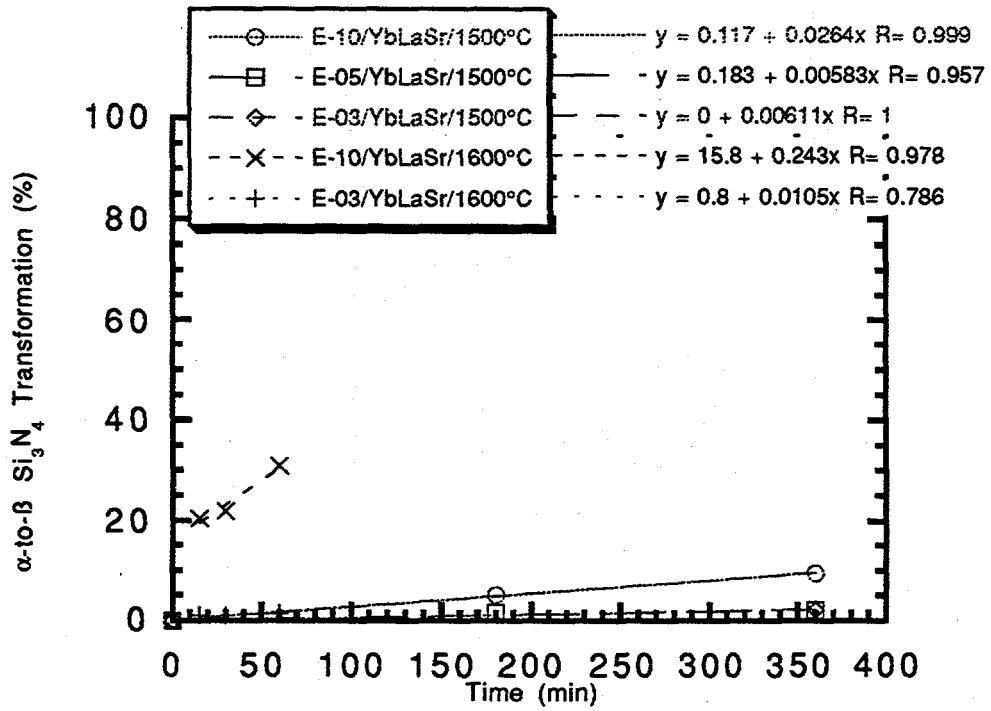

Fig. 8. α-to-ß Si_3N_4 transformation as a function of time for the similar silicon nitride powders with different surface areas at 1500°C and 1600°C. The sintering additive was Yb_2O_3-La_2O_3-SrO.

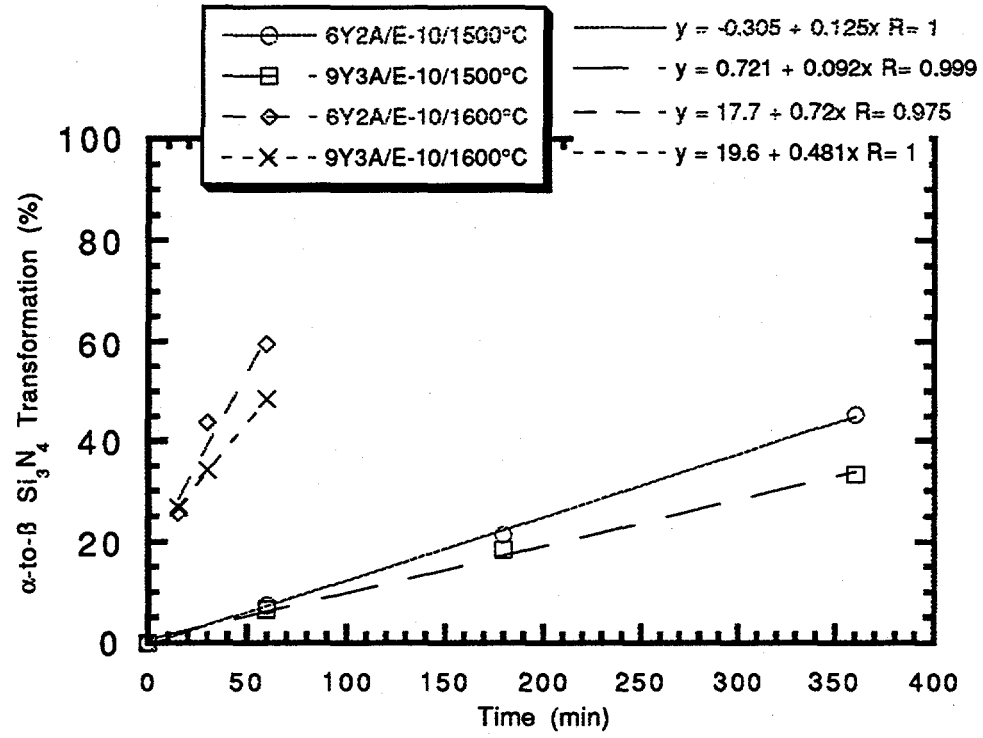

Fig. 9. α-to-ß Si_3N_4 transformation as a function of time for different amounts of sintering additive at 1500°C and 1600°C. The sintering additive was either 6% Y_2O_3-2% Al_2O_3 or 9% Y_2O_3-3% Al_2O_3. The silicon nitride powder was Ube E-10.

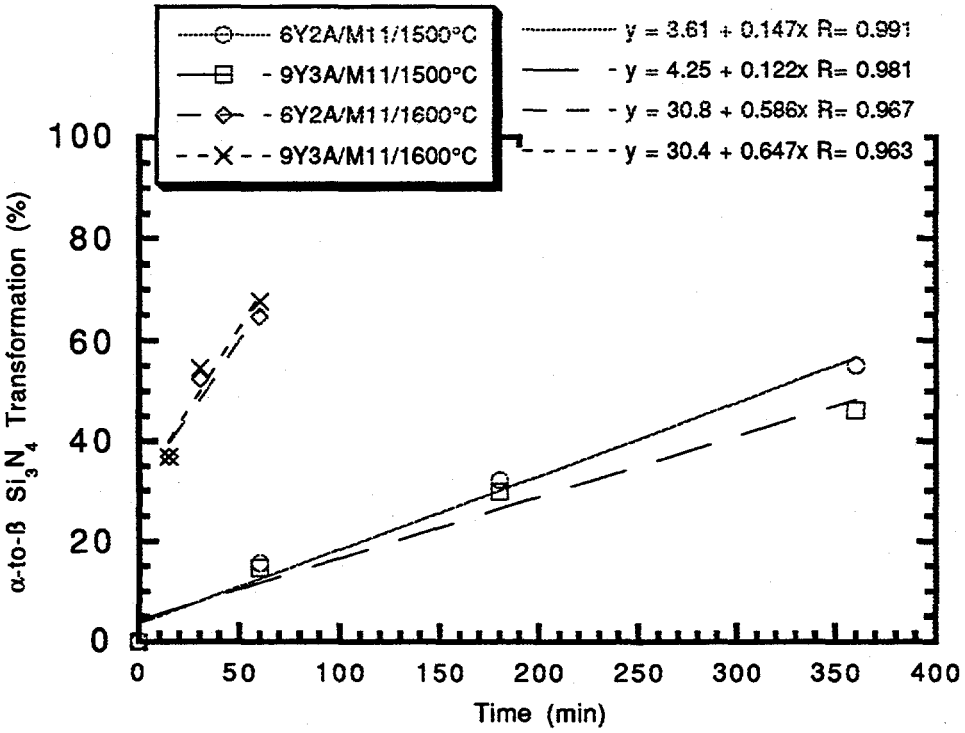

Fig. 10. α-to-ß Si_3N_4 transformation as a function of time for different amounts of sintering additive at 1500°C and 1600°C. The sintering additive was either 6% Y_2O_3-2% Al_2O_3 or 9% Y_2O_3-3% Al_2O_3. The silicon nitride powder was Starck M11.

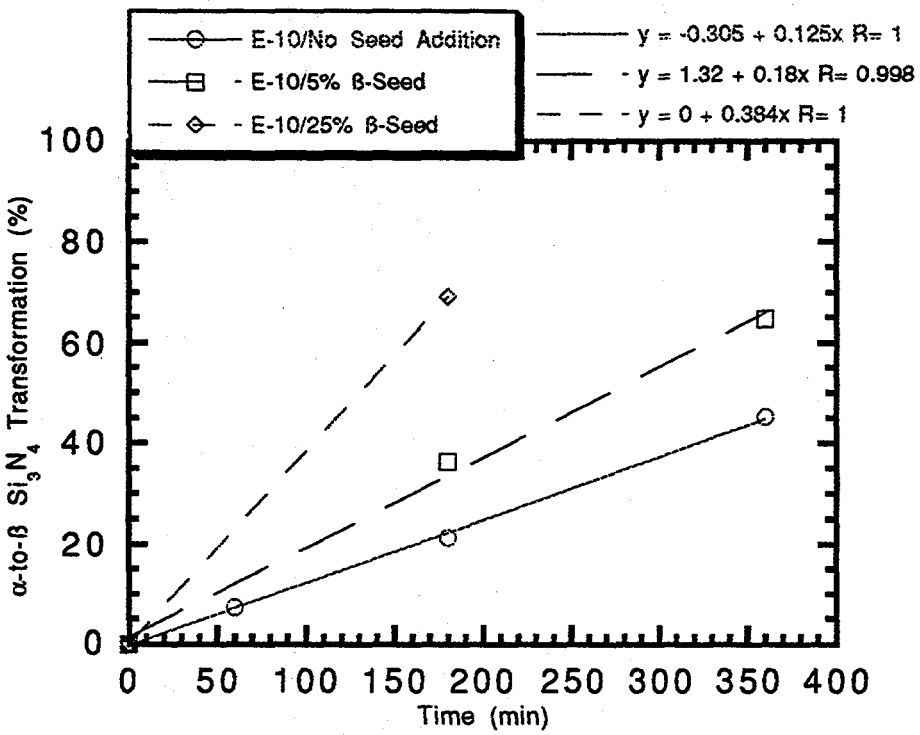

Fig. 11. α-to-ß Si_3N_4 transformation as a function of time for different amounts of ß-Si_3N_4 seed at 1500°C and 1600°C. The sintering additive was 6% Y_2O_3-2% Al_2O_3. The silicon nitride powder was Ube E-10 and the ß-seed was fabricated from Ube E-10 powder.

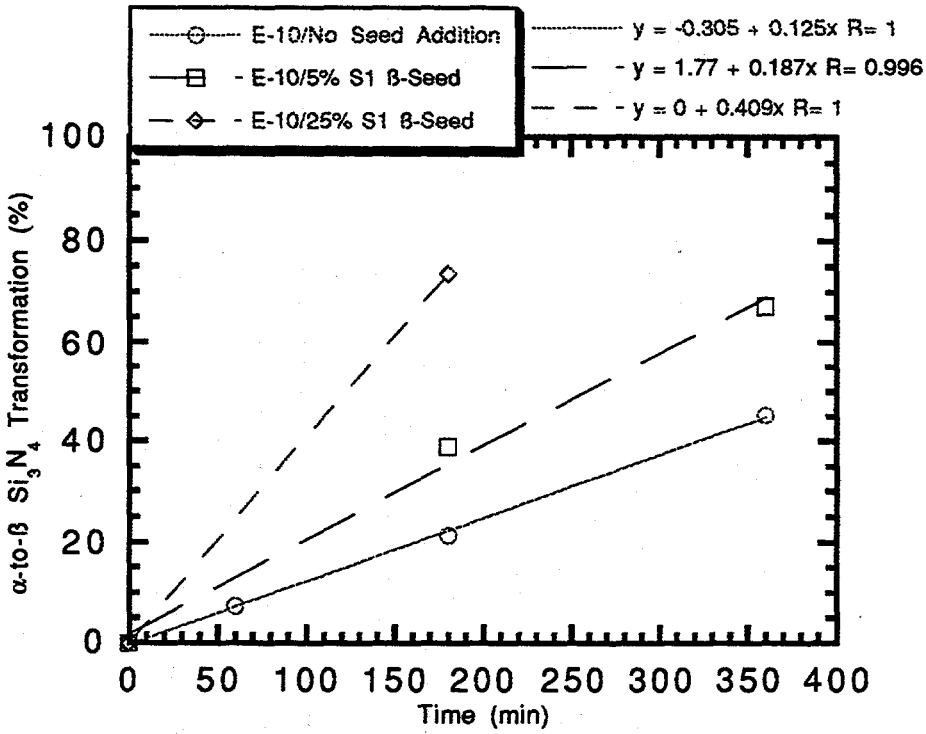

Fig. 12. α-to-ß Si_3N_4 transformation as a function of time for different amounts of ß-Si_3N_4 seed at 1500°C and 1600°C. The sintering additive was 6% Y_2O_3-2% Al_2O_3. The silicon nitride powder was Ube E-10 and the ß-seed was fabricated from Starck S1 powder.

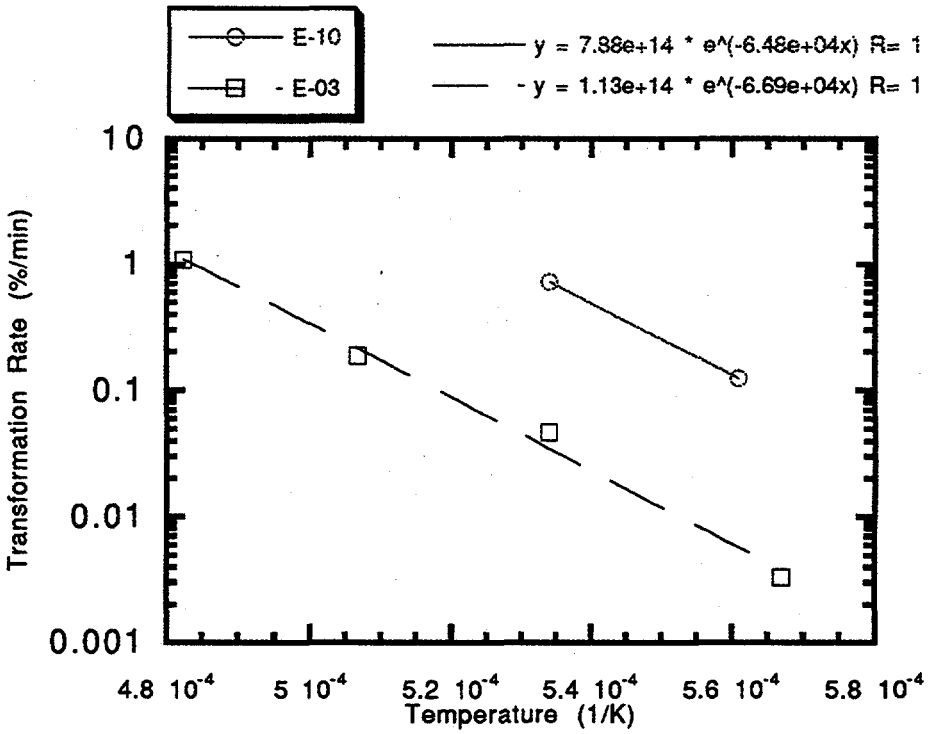

Fig. 13. Arrhenius plot of α-to-ß Si_3N_4 transformation rate as a function of inverse temperature (1/T) for two silicon nitride powders (Ube E-10 and Ube E-03). The sintering additive was 6% Y_2O_3-2% Al_2O_3.

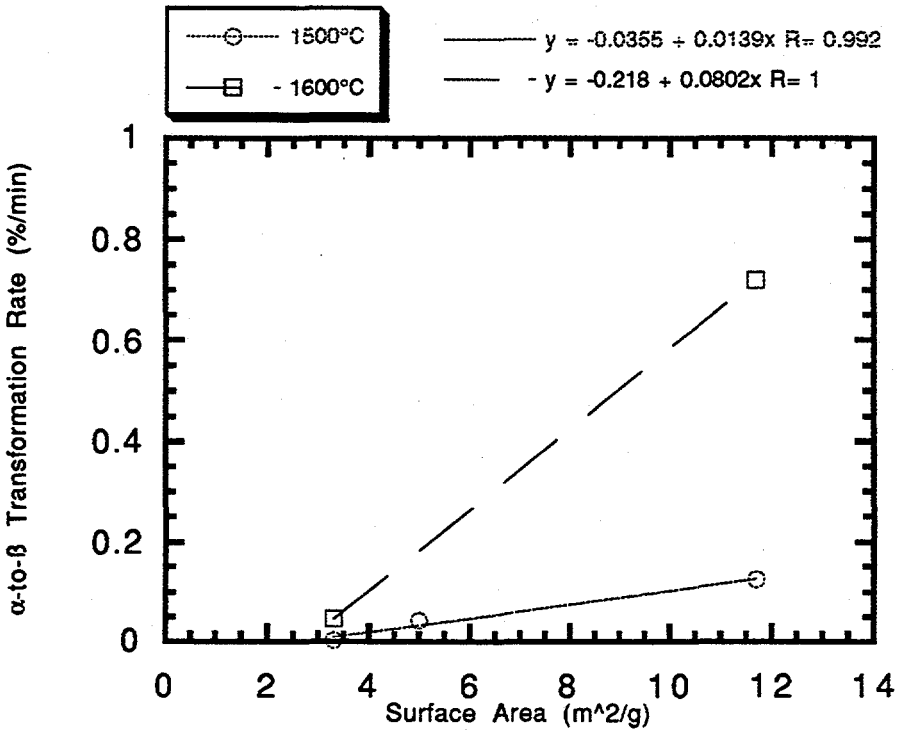

Fig. 14. α-to-ß Si_3N_4 transformation rate as a function of starting silicon nitride surface area for the various silicon nitride powders made by the diimide process (Ube E-10, E-05 and E-03) at 1500°C and 1600°C. The sintering additive was 6% Y_2O_3-2% Al_2O_3.

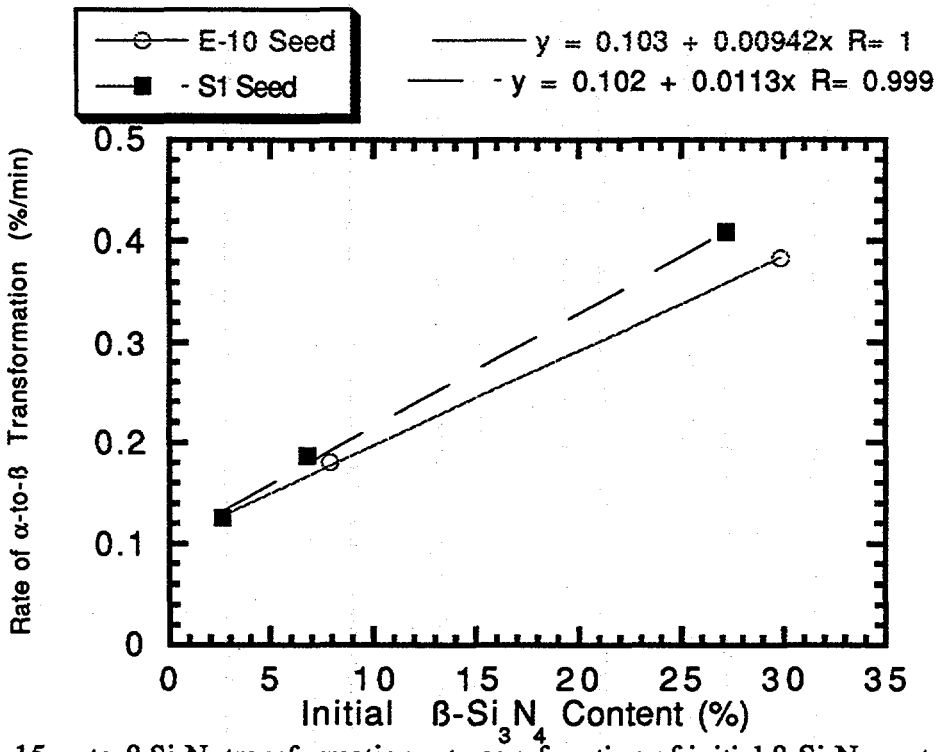

Fig. 15. α-to-ß Si_3N_4 transformation rate as a function of initial ß-Si_3N_4 content for two types of seed. The silicon nitride powder was Ube E-10, the sintering additive was 6% Y_2O_3-2% Al_2O_3 and the tests were at 1500°C.

Cost Effective Sintering of Silicon Nitride Ceramics (SIU-C)-

D. E. Wittmer, Southern Illinois University, Carbondale, IL 62901

Objective/Scope

The purpose of this work is to investigate the potential of cost effective sintering of Si_3N_4 through the development of continuous sintering techniques and the use of lower cost Si_3N_4 powders and sintering aids.

Technical Highlights

Task 1. Refine Economic Model and Design for Chosen Furnace Configuration

This task was completed as reported in a previous semiannual report.

Task 2. Continue evaluation of sintering parameters on properties of selected Si_3N_4 compositions

Processing/Property Evaluations

Industrial Collaboration/Affiliation

Eaton Corporation

During this reporting period, the physical properties for the as-sintered and machined test bars that were sintered over a range of 12 sintering times and temperatures were completed. The density, four-point flexural strength and fracture toughness results for all of the as-sintered test bars are given in Table I, while the results for the machined test bars are given in Tables II and III.

As can be seen from Tables I and II, the highest density was achieved for sintering conditions of 1775°C for 240 min., while the highest 4-Pt. flexural strength was achieved at 1775°C for 90 min.. In general, it appears that the as-sintered strength is controlled by Fe-Si surface defects/inclusions. These defects were readily observed by optical microscopy and further identified by SEM with EDAX to be very prominent, with many of them on the order of several hundred microns in diameter. This would explain the low, fairly uniform strength observed. More detailed microscopy will be conducted to more fully characterize the defects.

For the machined test bars (Tables ii and III), the 4-Pt. flexural strength and the fracture toughness both appear to increase with increased sintering time at each sintering

temperature. It is interesting to note that the strength results for the 1750°C series are higher than for the 1775°C series, while the reverse is true for the fracture toughness.

In one continuous sintering run (1775°C for 240 min.) with the Eaton SRBSN, two different packing densities were run using the same size BN boats. The most dense packed boat contained 387 bars, while the less dense packed boat contained 192 RBSN test bars. The average bulk densities achieved for these conditions were 3.34 g/cc for the most dense packed and 3.35 g/cc for the less dense packed. The corresponding average weight losses were 1.9 and 2.2 %, respectively. For the densest packed boat there did not appear to be any significant differences in bar density as a function of position within each vertical stack, while for the less dense packed boat it appears that the density was somewhat higher in the bottom layers compared with the upper layers. For both packing conditions, weight loss was somewhat higher in the bottom layers, compared with the upper layers. A more detailed analysis of the data is currently being made to confirm these preliminary observations. Test bars have been sent out for machining to determine the flexural strength and fracture toughness as a function of sintering pack density.

In order to determine the thermal profile in the continuous furnace, several continuous sintering runs containing Eaton SRBSN (nitride at Eaton) were made at temperatures from 1725 °C to 1775 °C for from 1 to 4 hours at peak temperature. During these runs a long thermocouple (placed in a BN boat used to shield the TC from the heating element radiation) was used to measure the temperature profile in the belt furnace with and without a load. The densities of all of the test bars from these runs are currently being determined. Once completed a statistical distribution of bars will be machined into ASTM type-B test bars for strength and fracture toughness measurements.

Also, one continuous sintering run was made at 1775°C for 240 min. that contained Eaton SRBSN that was nitrided by Eaton and Eaton SRBSN microwave nitrided by ORNL. Test bars made from the same lot of Eaton SRBSN powder were nitrided by both Eaton and ORNL. In addition, cylinders and disks of Eaton SRBSN from a different lot were also microwave nitrided. The same packing density was used in the BN boats for test bars prepared by both nitriding methods. The sintered densities for these test bars have been completed and selected bars for strength and fracture toughness measurements have been selected. The densities for the microwave nitrided SRBSN appear to be only slightly lower than the same SRBSN nitrided by Eaton (3.33 g/cc and 3.35 g/cc respectively). Also for some of the microwave test bars, warpage appears to have been caused by nonuniform nitridation. These test bars appear to be the ones that were in direct contact with the setter material which may have blocked nitridation of the bottom face. The density data for the cylinders and disks of the microwave nitrided SRBSN are currently being completed. Additional microwave nitridation of SRBSN is planned for the next reporting period.

Norton Advanced Ceramics

During this reporting period, several billets and over 100 full-sized valves were received from NAC as part of the Norton Advanced Ceramics ACMT contract. These materials were continuously sintered under conditions optimized in previous work and then returned to NAC for evaluation. The results are reported by NAC as part of the ACMT contract.

Allied Signal, Inc.

During this reporting period, 12 continuous sintering runs were made containing 8 large blocks and several small cylinders of GS-44 provided by Allied Signal, Inc. Sintering conditions were identified that produced greater than 99% of the target density. These materials were returned to Allied Signal for evaluation and they reported that they were very encouraged by the results.

Richard Schultze and Mike Gibbons from Allied Signal Automotive (Fostoria, OH) visited SIU-C to discuss continuous sintering and the potential for future cooperative work. While at visited SIU-C they visited the continuous sintering laboratory and the high-temperature materials processing laboratory.

Caterpillar Tractor Company

Discussions were initiated with Caterpillar Tractor Company (Peoria, IL) and Greg Wesling and Dave Penning visited SIU-C to tour the continuous sintering laboratory and the high-temperature materials processing laboratory. They are presently considering ways in which CAT and SIU-C can collaborate.

Task 3. Continue Evaluation of Low Cost Si_3N_4 Powder

Starck, Shin-Etsu and Latvian Powders

Work on the Starck M-11 and Shin-Etsu powders was initiated during this reporting period. These powders are being evaluated, along with the use of alumina, zirconia, and silicon nitride milling media. The effects of turbomilling time and milling media time on the sinterability, powder surface area and average particle size are being determined in the A2Y8 formulation. During this reporting period, 4 batches of the M-11 formulation were processed and pressure cast. The disks are presently being sintered in the continuous furnace.

Previously a small sample of Latvian silicon nitride (obtained from Ceramic Quality Products) was sintered to full density. This powder is manufactured with the sintering aids added as part of the powder process. Because of the encouraging results, a 10 kg. lot

of this powder was ordered for extensive evaluation. Although the per kg price of this powder is somewhat high (about $110/kg for small lots), it contains the sintering aids and needs only to be shaped and therefore the cost of the finished parts may be quite competitive with those prepared using the more costly powders.

Dow Powder

Formulations prepared from the Dow Chemical Co. powder continue to be analyzed to try to determine a plausible explanation for reduced sinterability of this powder with increased sintering time and temperature. Previously, two batches of the Dow powder were heat treated in flowing N_2 at 1775°C for 2 h and 1825°C for 2 h in an attempt to nucleate some β-phase in the original powder. This was done in order to try to control growth of the β-phase during sintering of the various formulations being investigated. XRD confirmed that there did not appear to be any change in the phases after heat treatment at 1775 °C; however, heat treatment at 1825 °C did produce some β-phase and significant decomposition of the powder. During processing of the A4Y6 composition from this latter powder, the free Si in the heat treated powder caused problems during casting.

Additional heat treatment of the Dow powder at 1775°C for 4 h was conducted to hopefully eliminate the decomposition and formation of free Si. XRD confirmed the presence of about 2% β-phase in this thermally treated powder, while no free Si was detected. This powder will be processed in the A4Y6 and A2Y8 formulations during the next reporting period.

Meanwhile, XRD has been performed on A2Y6, A4Y6 and A2Y8 formulations that were previously continuously sintered over a range of times and temperatures. The preliminary results show that there is a considerable amount of α-phase remaining in these compositions for all sintering conditions. Based on conversations with the program monitor, Terry Tiegs, it was confirmed that similar observations have been made in the phase stability of the Dow powder in investigations at ORNL. Our XRD results should be completed during the next reporting period and will be discussed at length with Terry Tiegs.

Previously, some preformed β seed (Ube Industries) was added to the as-received Dow powder to attempt to provide a source of β at the onset of sintering. As reported previously, seeding with this type of β seed did not appear to have any measurable effect on the sintering behavior. It was believed that the seed was too fine and was dissolved in the liquid phase, during the initial stage of sintering, and therefore was not an effective nucleating agent. Larger β seed was formed in our laboratory through the addition of 2 wt.% Y_2O_3 to Ube E-5 powder, followed by sintering in the continuous furnace at 1775°C for 4 h. Much larger elongated β grains were formed, compared with the Ube β-phase.

During this reporting period, 4 batches of the A4Y6 formulation processed with Dow powder were continuous sintered for several sintering times and temperatures. These 4 batches include: as-received Dow powder, as-received Dow powder with a 5

wt.% addition of β seed (prepared from Ube E-5 powder), pre-sintered Dow powder (heat treated in flowing N_2 at 1775°C for 4 h), and pre-sintered Dow powder with a 5 wt.% addition of β seed. The densities are presently being determined and when completed some test bars will be prepared to measure strength and fracture toughness where warranted. XRD analyses of all of the Dow formulations are presently being completed to determine the transformation kinetics.

Task 4. Design and Construct Prototype Belt Furnace

This task has been completed. Additional funding has been requested to continue evaluation of the belt furnace through sintering evaluations, using materials provided by industrial partners/collaborators. This work is now being performed in Task 2, but will be the basis for Task 5 if additional funding is approved.

Status of Prototype Belt Furnace

The Model 44-BF belt furnace (with the tungsten hot zone installed) has been in operation for over 1000 hours of high-temperature operation (106 sintering runs) without any major problems with the furnace.

Status of Milestones

1.	Refine Economic Model and Design for Chosen Furnace Configuration	Completed
2.	Continue Evaluation of Sintering Parameters on Properties of Selected Si_3N_4 Compositions	On Schedule Continuing
3.	Continue Evaluation of Low Cost Si_3N_4 Powders	On Schedule Continuing
4.	Design and construct prototype belt furnace	Completed

Communications/Visits/Travel

D. E. Wittmer and J. Guileen, Allied Signal, Morristown, NJ discussed continuous sintering of Allied Signal silicon nitride.

D. E. Wittmer and T. N. Tiegs discussed phase development in Dow silicon nitride.

D. E. Wittmer and J. Guileen and John Pollinger, Allied Signal, Morristown, NJ discussed continuous sintering of Allied Signal silicon nitride.

D. E. Wittmer and S. Etherton visited ORNL to discuss microwave nitriding of SRBSN with Terry Tiegs and Jim Edler (Eaton Corp.)

Richard Schultze and Mike Gibbons from Allied Signal Automotive (Fostoria, OH) visited SIU-C 9/10-9/11 to discuss continuous sintering and the potential for future cooperative work.

Greg Wesling and Dave Penning from Caterpillar Tractor Company (Peoria, IL) visited SIU-C 9/18-9/19 to tour the continuous sintering laboratory and the high-temperature materials processing laboratory.

Problems Encountered

XRD unit at SIU-C was down for a period which delayed completion of XRD analyses of Dow formulations.

Publications

None

Presentations

None

Table I. Physical Properties for Continuously Sintered Eaton SRBSN: As-Sintered Bars

Time (min)	Sintering Temperature											
	1725°C			1750°C			1775°C			1800°C		
	Bulk ρ (g/cc)	Wt. Loss (%)	4-Pt. Flex.* (MPa)	Bulk ρ (g/cc)	Wt. Loss (%)	4-Pt. Flex.* (MPa)	Bulk ρ (g/cc)	Wt. Loss (%)	4-Pt. Flex.* (MPa)	Bulk ρ (g/cc)	Wt. Loss (%)	4-Pt. Flex.* (MPa)
60	---	---	---	3.11	2.16	424 +/- 47	3.19	3.36	420 +/- 53	3.26	5.25	380 +/- 44
90	3.03	1.77	392 +/- 54	3.22	2.5	456 +/- 34	3.29	3.84	485 +/- 40	---	---	---
120	3.18	2.35	380 +/-29	3.25	2.67	450 +/- 28	3.30	4.01	435 +/- 56	---	---	---
240	3.29	2.97	440 +/- 24	3.34	3.83	432 +/- 19	3.35	4.54	390 +/- 49	---	---	---

* 4-point flexural strengths are on the as-sintered bars (10 for each condition).

Density and weight loss values are based on all 84 bars for each sintering condition.

Table II. Physical Properties for Continuously Sintered Eaton Corporation SRBSN: Machined Test Bars

Sintering Time (min)	Sintering Temperature					
	1725°C			1750°C		
	Bulk ρ (g/cc)	K_{IC} (MPa-$m^{1/2}$)	4-Pt. Flex. (MPa)	Bulk ρ (g/cc)	K_{IC} (MPa-$m^{1/2}$)	4-Pt. Flex. (MPa)
60	---	---	---	3.12	4.1	418 +/- 32
90	3.12	4.1	437 +/- 48	3.21	4.6	513 +/- 52
120	3.19	4.3	472 +/-62	3.26	4.5	562 +/- 31
240	3.28	4.6	503 +/- 85	3.34	4.9	584 +/- 14

Bulk density was determined on all 84 test bars for each sintering condition.

Fracture toughness values were determined by the strength method and the value given is based on the average of 3 test bars at each sintering condition.

4-Pt. flexural strength values of machined test bars were determined from the results for 5 test bars at each sintering condition.

Table III. Physical Properties for Continuously Sintered Eaton Corporation SRBSN: Machined Test Bars

Sintering Time (min)	Sintering Temperature					
	1775°C			1800°C		
	Bulk ρ (g/cc)	K_{IC} (MPa-$m^{1/2}$)	4-Pt. Flex. (MPa)	Bulk ρ (g/cc)	K_{IC} (MPa-$m^{1/2}$)	4-Pt. Flex. (MPa)
60	3.20	4.4	416 +/- 21	3.26	5.1	433 +/- 51
90	3.29	4.9	485 +/- 32	---	---	---
120	3.31	5.1	522 +/- 45	---	---	---
240	3.36	5.5	529 +\- 45	---	---	---

* Test bars presently being machined.

Bulk density was determined on all 84 test bars for each sintering condition.

Fracture toughness values were determined by the strength method and the value given is based on the average of 3 test bars at each sintering condition.

4-Pt. flexural strength values of machined test bars were determined from the results for 5 test bars at each sintering condition.

Development of NZP Ceramic Based "Cast-in-Place" Diesel Engine Port Liners

Rama Nageswaran and Santosh Y. Limaye (LoTEC, Inc.).

Objective/Scope

The overall objective of this research is to develop sodium-zirconium-phosphate (NZP) ceramic based "cast-in-place" diesel engine port liners. Specific objectives are: (1) Development and optimization of the overall insulation system, (2) Refinement of compliant layer formation process around the ceramic insulation system, (3) Development and adaptation of cost-effective powder and material fabrication processes, and (4) Creation of database of high temperature properties (stability in diesel exhaust environment, thermal cycling, thermal shock etc.).

Technical Progress

Progress during the last six month reporting period covered the following areas: (i) materials and processes development, (ii) rapid prototyping of complex shapes and dimensional/other evaluation of the same, (iii) metal casting around complex shaped port liners, and (iv) diesel engine exhaust exposure tests of ports lined with BS-25 and CS-50 liners. In the following, these activities have been elaborated and discussed in more detail. Also, Penn State has completed its subcontract with LoTEC.

Materials and Process Development

As part of NZP powder synthesis process development, combustion synthesis was being investigated by Penn State. Bulk samples were made out of NZP powders obtained from combustion synthesis and characterized for XRD and mechnical strengths. At LoTEC, research on new materials targeted the development of high density, high strength NZPs for possible applications in exhaust port liners. A discussion of such materials and processing developments, along with any test results, is provided here below.

Combustion Synthesis of NZP Materials (SCD): BS-25 and CS-50 powders obtained from combustion synthesis process were ball milled for 8 hours followed by drying and screening. Test specimens in the form of bars 5 cm long were pressed in molds (110MPa) and sintered at 1400°C/10 hrs. Table 1 gives the room temperature flexural strength of these specimens. Figure 1 shows the same data together with those obtained on the bars made by the solid state method at LoTEC Inc. (BS-25) or at Oak Ridge National Laboratory (by B. Jackson, BS-25 and CS-50). Strengths of specimens fabricated using combustion powders do not differ

significantly from those made by traditional methods, although the number of data available for CS-50 is very small.

High Density Materials Development at LoTEC: In the area of materials development, high density BS-25 and CS-50 materials were processed successfully using the slip casting route. Flexural strengths of up to 90 and 75 MPa, respectively, were achieved for BS-25 and CS-50 by: (a) altering sintering schedules and (b) by using minor sintering additives. However, there was noticeable slumping or warping of the sintered CS-50 parts and, in some cases where additives were used, phase changes occured after sintering. On the other hand, high density BS-25 parts had little or no warping or slumping.

Rapid Prototyping of Complex Shapes

Based on a modified work plan prior to completion of Phase II, rapid prototyping of complex shaped port liners was embarked upon. The goal of rapid prototyping was to satisfy engine companies' requirements for rapid checks of viability of port liners and port liner manufacturing processes en route to their commercialization. Typically, this time is less than five weeks for each component or process. At LoTEC, procedures and protocols were established for delivering the prototype within the stipulated time. The steps involved in rapid prototyping of a NZP port liner are outlined in the schematic (see Figure 2).

Several complex shaped (Y-shaped, S-shaped, and T-shaped) port liners were fabricated using slip casting as per the rapid prototyping protocols established with engine companies. This activity was done with a two-fold objective: (i) demonstration of complex (green) shapes processing capabilities and (ii) demonstration of dimensional control on sintered complex shaped parts. Major focus of the initial work was on Y-shaped port liners as outlined below.

Slip cast Y-shaped (and other shaped) port liners were sintered and machined using special fixture(s) to dimensions close to those specified in drawings. Some of the machined shapes were sent to engine companies for evaluation. Specifically, Cummins Engine Co. performed measurements of dimensions of the slip cast Y-shaped BS-25 port liner using a Coordinate Measuring Machine (CMM). These measurements were within 0.5mm of the actual dimensions on the overall geometry in almost all places. Further improvement of dimensional accuracy on Y-shapes is a goal for the near future.

Following the rapid prototyping procedures, a few CS-50-based T-shaped manifolds were also successfully slip cast and fired to required density. Two of these manifolds were then sent to the engine company for evaluation. More of these manifolds are being manufactured for dimensional control studies.

Metal Casting Trials Involving Complex Shapes

L-shaped Port Liners: L-shaped ports lined with NZP port liners were successfully cast in metal following the FEA modeling results of and prior experience with straight tubes. Photographic evidence of such a casting is presented in Figure 3. Figures 3(a) and (b) show L-shaped BS-25 and CS-50 port liners, respectively, that have been successfully cast in iron.

Y-shaped Port Liners: Slip cast Y-shaped BS-25 port liners, cut to approximate dimensions, were cast in a shoe box mold with cast iron. It was found that the port liner had cracked at the web of the Y-shape (fork). Although the casting was not entirely successful, it is very likely that by modification of the radius or by increasing the thickness of the compliant layer at the web, the casting could be made to work. Photographs showing a Y-shaped BS-25 port liner before and after casting are shown in Figure 4. More metal casting trials have been planned to evaluate the feasibility of casting gray-iron around such complex shapes.

As is logical, with increasing complexity of the liner geometry the relevance of FEA results of straight tube analysis should be expected to decrease drastically. The first few casting trials with the more complex port liner shape (Y) clearly show the need for (i) new FEA analysis specific to casting and associated stresses in these geometries and (ii) possibly redesigning and altering the dimensions of the port liner itself. The latter course of action will, however, depend on approval from the concerned engine companies.

Diesel Engine Exhaust Exposure Tests

Three straight tubes each of BS-25 and CS-50 were supplied to Cummins for exposure to diesel exhaust environment. All ports were exposed for ~ 1000 hrs. and final results of the tests are being awaited. If the NZP port liners are physically intact, residual property measurements and detailed microstructural examinations will be conducted. One each of L-shaped ports with BS-25 & CS-50 liners were also fixtured for testing in diesel exhaust by Cummins. Exhaust exposure tests of the L-shaped ports have just begun. From shape considerations, the L-shaped tube is more representative of the actual port liner shapes and is more amenable for long term exposure testing.

Future Work

Exhaust exposure tests on L-shaped ports have been initiated to complement the results of testing on straight tubes. Work on Y-shaped, S-shaped, and T-shaped exhaust port liners involving dimensional studies, casting in shoe box molds etc. is underway. FEA of complex shaped port liners in metal casting situation has also been planned. Engine companies are

currently evaluating the various manifolds for dimensions, properties etc. and further work at LoTEC will be based on their feedback. Development work on high density and high strength NZPs which exhibit less warpage and creeping is progressing rapidly.

Status of milestones : Program on schedule.

Communications/Visits/Travel :

1) S. Y. Limaye traveled to : (i) Dearborn, Michigan to attend Annual Automotive Technology Development Contractors Coordination Meeting (AATD/CCM) in October 1996.

Problems Encountered : None.

Publications /Presentations : None.

References : None.

Table 1. Flexural strength of sintered bars made from combustion synthesized CS-50 and BS-25 powders.

Sintering Temp. (°C)	CS-50		BS-25	
	Density (g/cm^3)	Flexural Strength, MPa	Density (g/cm^3)	Flexural Strength, MPa
1400°C/10h	1.933	25.9	1.964	19.2
1400°C/10h	1.977	34.7	1.930	19.0
1400°C/10h	2.639	43.9	1.995	20.3

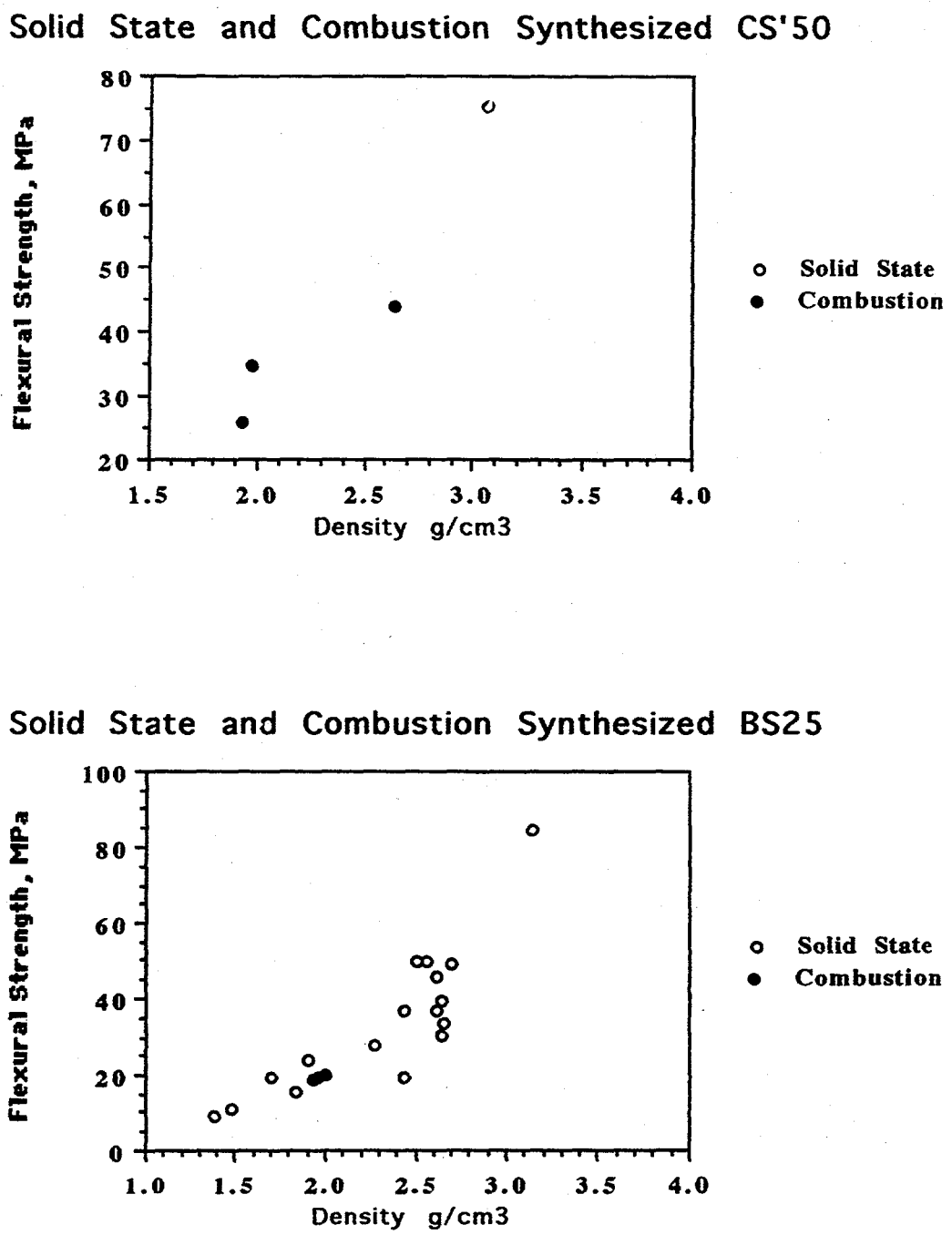

Fig. 1. Comparison of room temperature flexural strength as a function of density of solid state and combustion synthesized CS'50 and BS25.

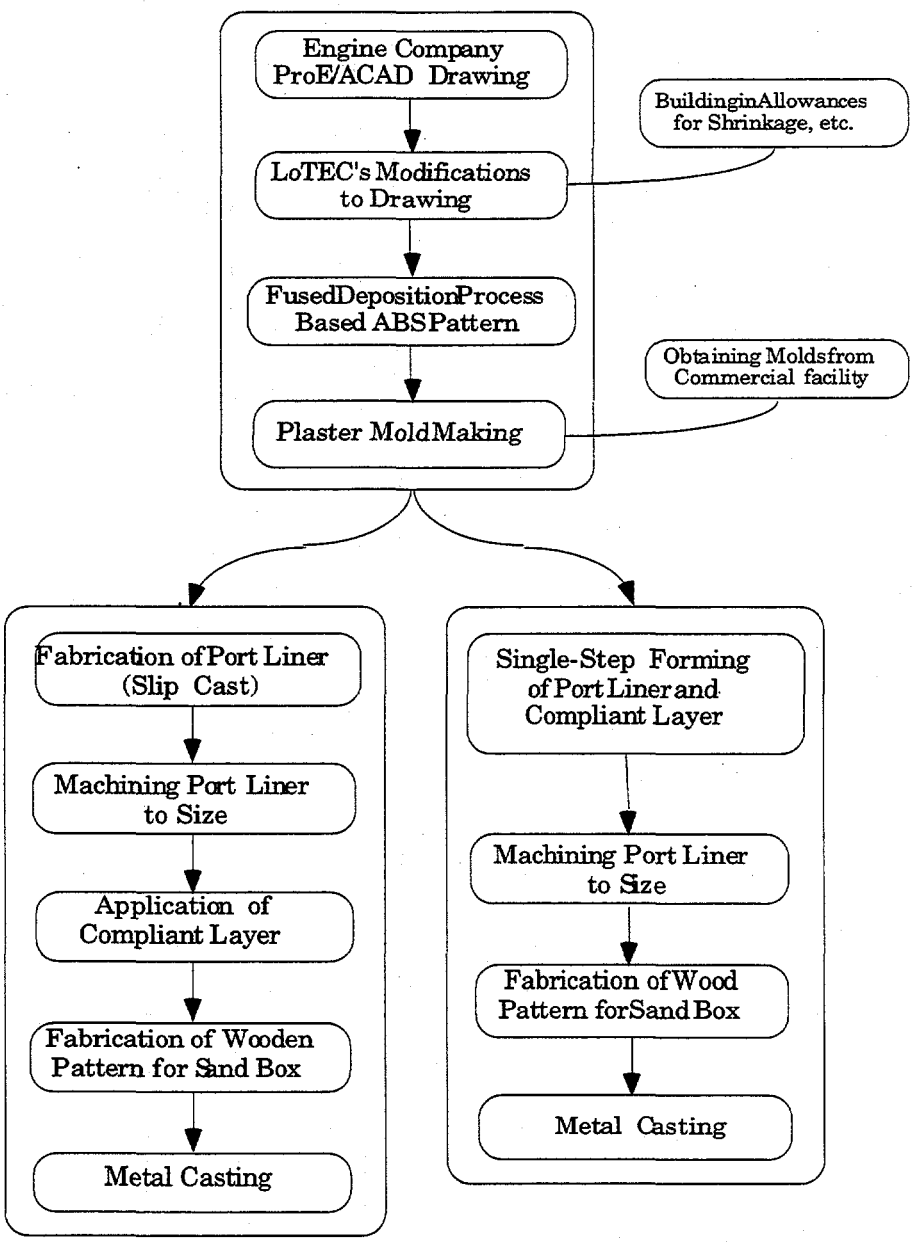

Figure 2. Schematic of Process Steps Involved in Rapid Prototyping of NZP Ceramic based Diesel Engine Exhaust Port Liner and Exhaust Ports.

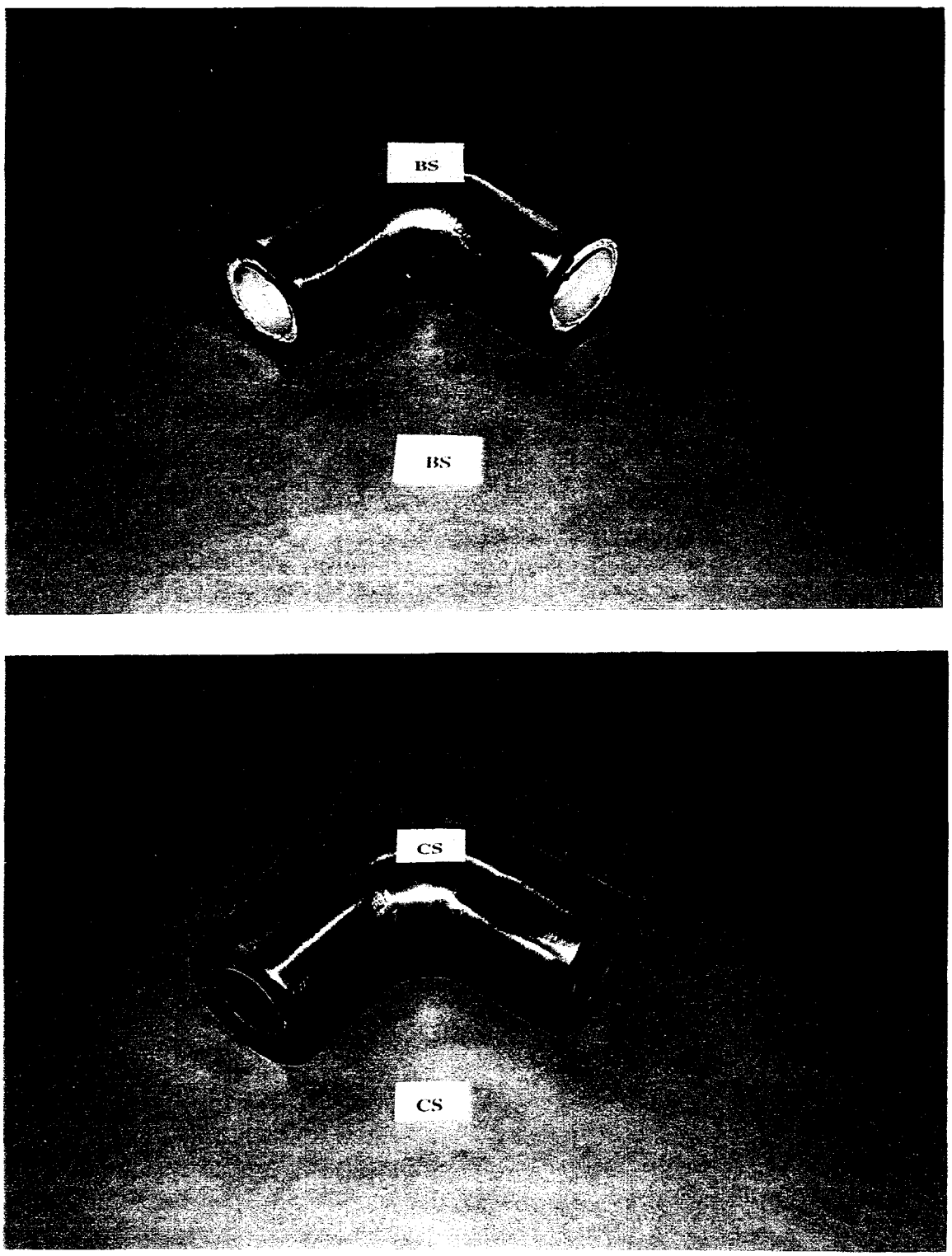

Figure 3. Photographs of successfully cast L-shaped (a) BS-25 and (b) CS-50 based ports cast in gray iron.

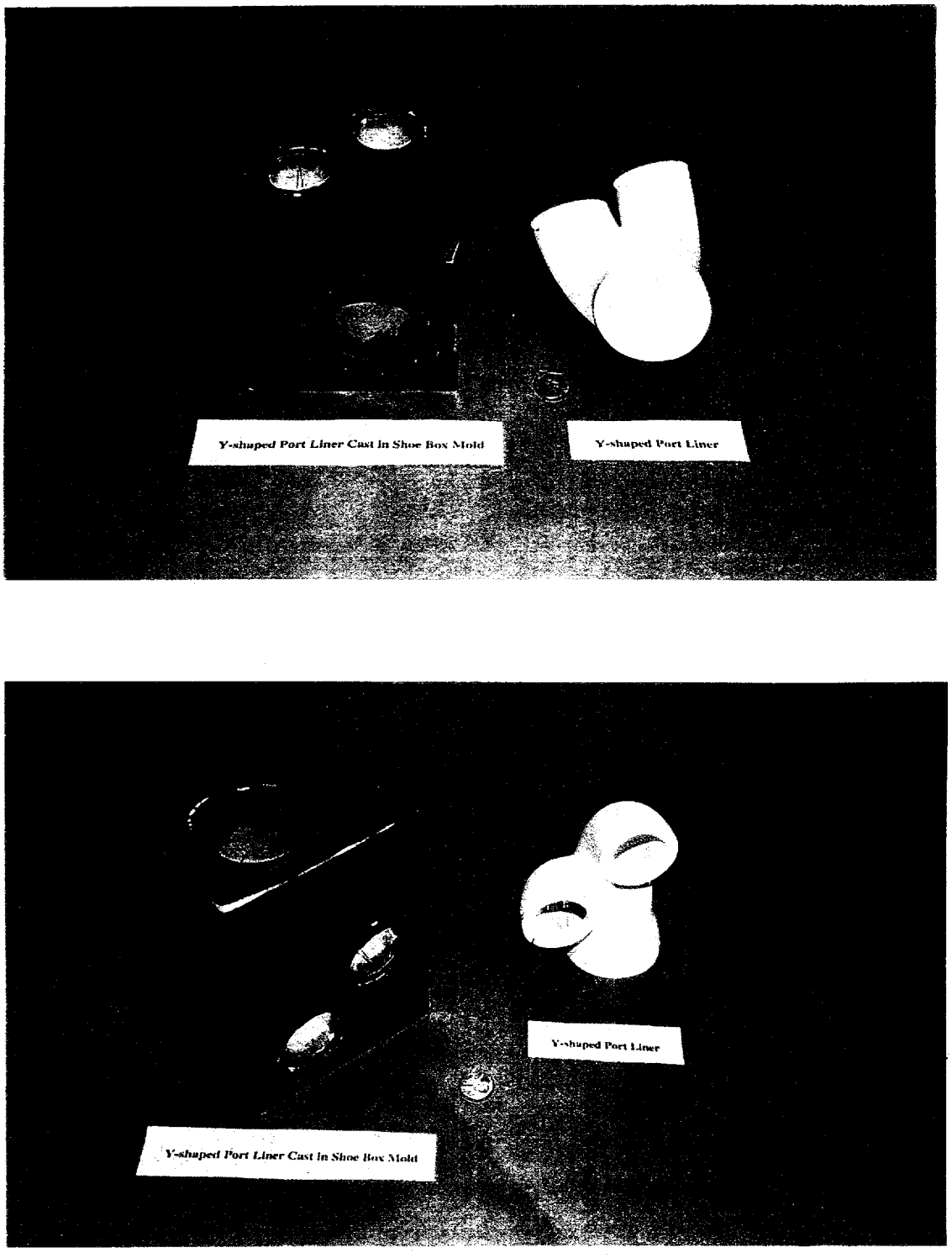

Figure 4. Photographs of a slip cast Y-shaped NZP port liner and a port liner cast in gray iron which, however, has cracks at the "web" between the two "fingers".

Development of Low Cost NZP Powder Synthesis and Processing Technology

Jay Curtis, Rama Nageswaran and Santosh Y. Limaye (LoTEC, Inc.)

Objective/Scope

The overall objective of this research is to develop a suitable technology for low cost synthesis and processing of NZP materials. The two NZP materials of primary interset are BS-25 ($Ba_{1.25}Zr_4Si_{0.5}P_{5.5}O_{24}$) and CS-50 ($Ca_{0.5}Sr_{0.5}Zr_4P_6O_{24}$). Specific objectives to be accomplished are: (1) preliminary assessment of powder techniques of specialist vendors for cost-effective NZP powder synthesis, (2) evaluation of NZP powder samples supplied by vendors (3) selection of up to two finalist powder suppliers based on results of initial evaluation, commercial viability of the process, and scale-up costs; (4) advanced evaluation of powders supplied by two companies based on results of material properties testing such as thermal expansion, strength, elastic modulus, etc.; and (5) metal casting trials involving NZP prototype parts and testing of the prototypes for diesel-engine worthiness. A secondary (and minor) objective will be to set up a hydrothermal (or other) low-cost powder synthesis facility at LoTEC as a parallel effort.

Technical Progress

In addition to accomplishing original objectives (1) through (3), further iterative experimentation and testing (similar to that of objectives (1) and (2)) was done to establish the most optimum powder processing routes based on techno-economic considerations during the last six-month time period. This was done as part of the second stage of the program prior to the next level of scale up. The in-house development of a (acid-base neutralization based) synthesis process for NZP (BS-25 and CS-50) powders was successfully completed. More significantly, the wet chemistry know-how developed at LoTEC as part of the same task was transferred to the two vendors. LoTEC has also acquired a particle density measurement device viz. the Accupyc 1330 pyconometer, for characterization of powder densities. This report summarizes all the above mentioned accomplishments.

Small Scale Processing and Powder Evaluation

The two vendors who were downselected from Phase I of this project (covering objectives 1 and 2 above) were Catalytica and NexTech. Catalytica uses a Microfluidizer™-based direct precipitation route to produce the material, while NexTech employs a hydrothermal synthesis

™ Registered trade mark of Microfluidics Corp., MA.

process. LoTEC provided the two vendors with few pointers related to proprietary experimentation routes developed in-house (discussed in the next section) and meeting the overall objectives of Phase II. Both vendors supplied fairly similar proposals for Phase II of this project (covering objective 4) based on LoTEC's input. An overview of these Phase II activity, including schedules, is given in Table 1.

In addition to the time schedules in the table, LoTEC has planned to spend an additional amount of time (up to 12 weeks) performing advanced evaluation of bulk properties. This evaluation will be performed both at the newly set up Characterization Laboratory of LoTEC and at High Temperature Materials Laboratory (HTML) of Oak Ridge National Laboratories (ORNL) as the second part of an Industrial Fellowship program.

Cerac, which employs a solid state synthesis technique, finally supplied LoTEC with approximately 4 kg of BS-25 on a purchase order basis. Figure 1 is the diffraction pattern obtained from this powder. Peaks which are labeled with a '1' are due to $BaZr(PO_4)_2$ and the peak labeled with a '2' is due to ZrP_2O_7. The presence of significant amount of minor phases is very clear from this pattern. Density measurements were performed on this powder sample using the newly acquired Accupyc pyconometer. Density of this Cerac BS-25 powder was about 3.68 g/cc. which is higher than the theoretical density of BS-25 (~3.5 g/cc). This discrepancy is likely due to the presence of minor or impurity phases.

Research at LoTEC

LoTEC has completed its low-cost NZP powder synthesis experiments at its facility, concurrent with the efforts of the vendors. This research was aimed at identifying possible low-cost precursors, performing small scale bench-top synthesis experiments, and evaluating the results.

Synthesis route for these experiments involved chemical precipitation from acid-base or dissolution reactions. Promising low cost precursors were first chosen and obtained. The reaction procedure consisted of forming an aqueous mix of all precursors, except the acid, and then reacting it with the acid under conditions of steady mixing. X-ray diffraction analyses was performed on the as-reacted powder and powder calcined a 1200°C for 4 hrs. Eleven more experiments were performed with various precursors from various suppliers. X-ray diffraction data showed that as-reacted powders were uniformly amorphous. However, after calcination, several of these reactions resulted in BS-25 phase.

Figures 2 and 3 show diffraction patterns for a successful two stage synthesis of BS-25 using the chemical precipitation route. Included are patterns for the powder before and after calcination. The pattern from the amorphous (as-reacted) powder, Figure 2, shows a distinct peak

at just under 27°, 2θ. This peak may be due to the presence of ZrP_2O_7. However, the higher intensity peaks for ZrP_2O_7 are absent. The pattern from the crystalline powder, Figure 3, shows the material to be primarily BS-25 with small amounts of $BaZr(PO_4)_2$ and ZrP_2O_7, (labelled '1' and '2', respectively) also present.

Most initial experimental runs involving CS-50 had some ZrP_2O_7 present in varying concentrations. Figure 4 shows diffraction patterns for one of the CS-50 samples which had no impurity phase present. This reaction was conducted at a modified pH value of about 10. It is significant because it represents the first sample of either BS-25 or CS-50 powder synthesized at LoTEC using the acid based reaction/precipitation technique where minor phases were absent.

Know how from these benchtop experiments was provided to the vendors by LoTEC, under confidentiality agreement, for incorporation into their processing schemes and further improvement. At the present, both NexTech and Catalytica are working on this economical and environmentally friendly route to produce larger quantities of both BS-25 and CS-50 powders.

Vendor and LoTEC's Cooperative Research

During the last six month period, Catalytica and NexTech, Inc. continued to produce powders which were jointly evaluated by the vendors and by LoTEC. These powders were produced by varying precursors and process conditions in an effort to optimize production and minimize cost. It should be noted that both vendors performed preliminary analysis (XRD) to screen a trial process before supplying LoTEC with a sample. Feedback to vendors was given after each batch of powders was analyzed and this information was used to determine future synthesis procedure, i.e., the process conditions were optimized by iterative synthesis and testing, and by prompt communication between the vendors and LoTEC.

Parameters such as starting reagents, processing temperatures, processing times, reaction pH, calcination temperature etc. were selectively varied in order to determine the best powder synthesis conditions. Knowhow for the benchtop acid based reaction / precipitation technique developed at LoTEC and reported in earlier reports was transferred to the two vendors for improvement and scale up. The precursors and approach used in the "LoTEC" route make this process the most environmentally friendly and economical of all processes examined thus far.

It should be noted that both vendors tried many more synthesis runs than the number of samples that were evaluated at LoTEC would indicate. This is because the vendors attempts to produce the powders were not always successful and because they sent only powders to LoTEC which their preliminary analysis showed to be correct in terms of phase purity. It should also be noted that feedback was provided to vendors after each batch of powders was analyzed and this

information used to determine subsequent synthesis approach. A description of the iterative synthesis and testing procedure that was used to analyze the powders as well as a discussion of results of the various tests is given below.

Powder Analysis Testing Procedures:

In order to evaluate the powders which were supplied by the vendors, the following powder properties were characterized: particle density; surface area; particle size distribution; phase purity; dispersibility; flowability; pressability; and sintered density.

1) Particle density of each sample was analyzed using a Micromeritics AccuPyc 1330 pyconometer. This was done as a preliminary check for the presence of impurity phases or powder irregularities.

2) Surface area was analyzed using a Quantachrome NOVA 2000 Surface Area Analyzer. Surface area is an important factor in pressability and in dispersability. For both processes, a higher surface area should improve the success of the process.

3) Particle size distribution of powder screened to 170 mesh was analyzed using a Horiba LA-910 Laser Scattering Particle Size Analyzer. Particle size is also an important factor in both pressability and dispersability. For dispersability, the smaller the particle sizes, the better the powder will generally disperse. The size distribution should ideally be very narrow or wide in order to facilitate die pressing.

   Distribution width, Sw, is determined from the following equation, which correlates rheological behavior with the particle size distribution of a powder sample[1]:

$$S_w = \frac{2.56}{\log[\frac{d_{90}}{d_{10}}]} \qquad (1)$$

   In eqn.(1), S_W, is the distribution width which should ideally follow the rule : $7 < S_W < 2$ for good pressability of dry powders. d_{10} is the size below which there are 10% of the total particles. d_{90} is the size below which there are 90% of the total particles.

4) Phase purity was analyzed using x-ray diffraction at standard scanning conditions of 10 - 70° 2θ, 0.02° step size, and 0.4 steps/sec. All of the powders were subjected to X-ray analysis. XRD can show impurities that results from insufficient mixing or calcining of precursors, but does not necessarily indicate that the impurity (unreacted) phase will be present upon sintering. Limited XRD of sintered bars demonstrates that any unreacted or intermediate phases usually disappear upon sintering if the stoichiometry of the precursors was correctly calculated.

5) Dispersability (suitability for slip casting) was studied by stirring 2.5 grs of powder, that was screened to 170 mesh, into a mixture of water and 1wt% C286 dispersant. The amount of settling of the powder was qualitatively analyzed after 5 minutes. Results were compared to dispersibility of powders made using the conventional solid state method. In order for a powder to be classified as dispersing well, it had to exhibit dispersing behavior which was equal to or less than powders produced using solid state reactions. Research has shown that only these powders are suitable for slip casting as it is currently performed at LoTEC.

6) Powder flowability was analyzed using an "angle of repose" test. For this test, 12.5 grams of powder (screened to 170 mesh) was dropped through a 60° plastic funnel from a height of 1.5 inches, and the angle the powder formed with the horizontal surface was measured. In general, the more flowable a powder (lower angle) is, the more easily it is supposed to press.

7) Pressability was qualitatively analyzed when the screened powder was uniaxially die pressed into MOR-type bars at 10,000 psi. This test was independent of the results of the flowability tests on the powders.

8) Sintered density was analyzed by die pressing MOR-type specimens at 10,000 psi, isopressing at 25,000 psi, and sintering at 1550°C. Sintered density was, therefore, quite dependent upon pressability. (Sintering studies also enabled qualitative detection of low melting compounds or minor phases etc.)

Results and Discussion:

Particle Density

Tables 2 and 3, and 4 and 5 provide the density data for all BS-25 and CS-50 powders, respectively. As discussed in the previous report, the extent of deviation of particle densities from the theoretical numbers (3.50 gm./cc for BS-25 and 3.32 gm./cc for CS-50) was used as the first indicator of purity of the powders and extent to which crystallization of NZP phase was complete. (It has to be noted that particle density could differ from the theoretical value for other reasons too; such as presence of moisture or hard-shelled hollow particles in the powder.)

In the case of BS-25 powders, particle densities varied either way about the theoretical and the primary impurity phase was a lower order complex oxide $BaZrP_2O_8$. In general, the CS-50 powders from both vendors showed significant negative deviation from the theoretical value. Powders that showed maximum negative deviation had either impurities at undetectable levels or were unknown impurities. Unreacted or excess ZrP_2O_7 was the primary impurity in CS-50 powders. Other impurities or minor phases that were probably present include ZrO_2 (whose peaks overlap with the higher intensity peaks of NZP phase).

Surface Area

Surface areas of NexTech powders (both BS-25s and CS-50s) that were processed using post precipitation hydrothermal treatment were uniformly high. Of these powders, obviously, the amorphous or uncalcined powders had the highest surface area (871-40-2, 871-41-2 etc.). In addition, spray dying seemed to result in a powder with a higher surface area. This is evident from the surface area numbers of Catalytica powders, 871-42-3 and 871-43-3, which are identical except that the latter was spray dried.

Catalytica's powders processed using microfluidizer-based precipitation had lower surface areas compared to NexTech's hydrothermally precipitated powders. When both vendors employed the direct acid-base neutralization process recommended by LoTEC, the surface areas of powders (CZP-10-14 to CZP-10-16) dropped significantly. Although the surface areas dropped to levels comparable to powders produced using solid-state reaction synthesis, the calcination temperatures (temp. required for complete or almost complete crystalline NZP phase formation) for the vendors' powders are significantly lower than that necessary for the solid-state process. With NexTech's hydrothermally derived powders, the calcination temperature necessary was as low as 900°C (compared to 1200°C for the solid-state process). A summary of these results is provided in the schematic below (benchmark for surface areas are LoTEC's powders):

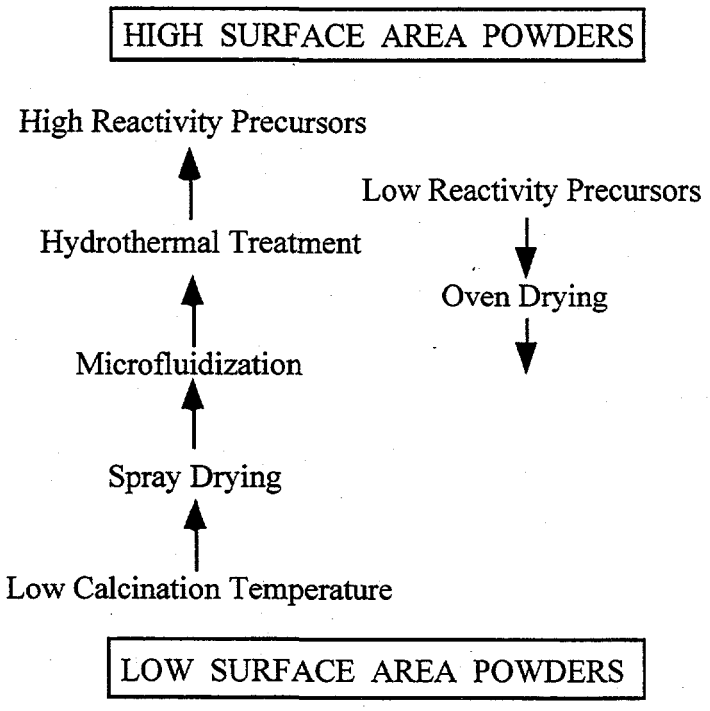

From the above schematic, it can be seen that high reactivity precursors or hydrothermal treatment have a greater effect on producing high surface area powders compared to a lower calcination temperature. Also, the low reactivity of precursors has an effect of overweighing the hydrothermal treatment or microfluidization in producing low surface area powders.

Particle Size and Distribution

Median particle sizes for all the powders are shown in Tables 2 to 5. From the data in Tables 2 to 5, it is deduced that the median sizes of powders does not depend so much on the process as it did on the reactivity of the precursors used. When low reactivity precursors were used or when samples were oven dried prior to calcination, the median particle sizes were fairly high. Post-reaction hydrothermal treatment had the effect of reducing the median particle sizes significantly despite the use of low reactivity precursors or oven drying. This may be due to dehydration and breaking up of agglomerates with hydrated bonds or nucleation of finer precipitate particles. The very large median sizes (~30 to 40 μm) seen in powders synthesized using "LoTEC route" are the result of combined effect of the above two parameters. Oven dried Catalytica powders, 871-85-2 and 871-89-2, had inordinately high particle sizes as compared to the rest of the powders (which were spray dried after wet chemistry). Analysis of the particle sizes as a function of the experimental variables is summarized in the schematic below:

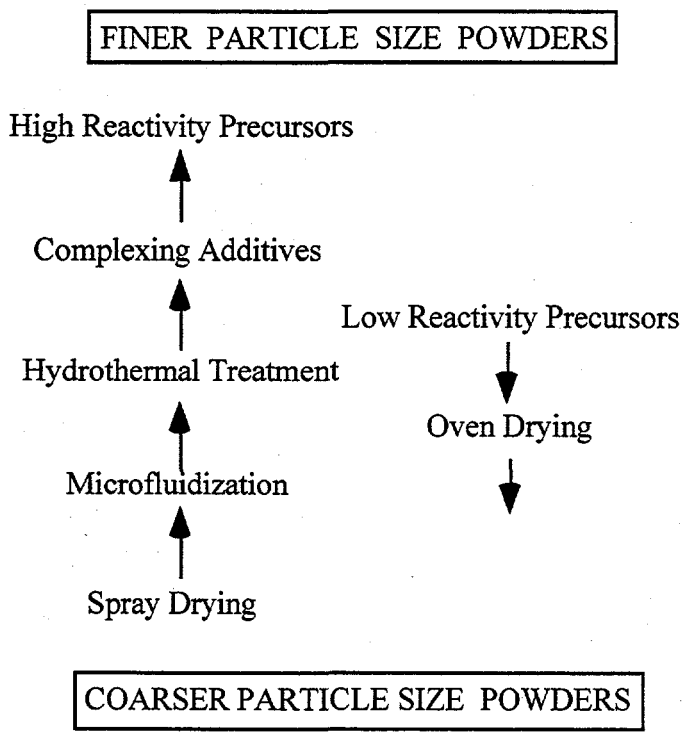

'Sw' values that characterize the distribution widths are also shown in Tables 2 through 5. As mentioned in earlier reports, the desirable range of values of Sw is such that 7< Sw <2 [1]. Distribution widths 'Sw's of NexTech's powders were, in general, in the acceptable range (<2). On the other hand, 'Sw's of the Catalytica powders varied widely between 1 and 5. The most undesirable distribution widths corresponded to the powders processed using the LoTEC route (CZPII-10-13 to CZPII-10-16).

Phase Purity

All Catalytica and NexTech Stage I calcined powders, except CZP #4 (CS-50) which had a small amount of ZrP_2O_7, contained no impurity phases according to high resolution XRD. (As far as the amorphous powders go, they were evaluated for amorphous-to-final-product in a direct sintering process. In general, this approach failed and the bars severely cracked upon sintering, even when the sintering times and temperatures were altered.) During the iterative process and process cost optimization routine of Stage II, experimentation with precursor quality, reaction temperatures, extent of agitation and homogenization (during or prior to reaction), washing of precipitates, pH, calcination temperature, and other processing parameters caused the appearance of trace impurities or minor phases that are routinely observed with LoTEC's solid state reaction synthesis process. (However, it was ensured that these trace or minor phases were within acceptable standards for the powders to be tested further.)

Of the above mentioned parameters; precursor reactivity, reaction temperature, pH, and washing of precipitates prior to drying seemed to influence the presence or absence of impurities the most. For instance, washed (871-43-3a) Catalytica powder had impurity ZrP_2O_7 phase whereas the powder that was not washed (871-43-3) had no impurities. Washing likely led to disappearance of some cations (Ca and (or) Sr) that led to ion imbalance in CS-50. The type of process itself (microfluidization or hydrothermal synthesis) did not seem to have a significant effect on impurities.

Dispersibility, Flowability, and Pressability

Dispersibility tests in water revealed that most Catalytica powders "dispersed well", whereas, most NexTech powders did not disperse as well (see Tables 2 through 5). Rather expectedly, poor dispersibility correlates well with large median particle sizes of powders (> 25.0μm), for eg. all NexTech powders CZPII-10-13 to CZPII-10-16 synthesized using the LoTEC route and oven-dried after precipitation, and analogously processed Catalytica's 871-85-2 and 871-89-2 powders. In a few instances, however, even powders with very large particle sizes dispersed fairly well when the surface areas were relatively high (>5m^2/gm). Specific examples are

Catalytica's original BS-25 and CS-50 powders. The same rationale regarding dispersibility can be extended to most powders with large particle sizes and high surface areas (majority of NexTech's BS-25 and CS-50 powders).

In summary, it can be stated that the difference in range of median particle sizes and, thereof, of the dispersibility behaviors obtained derives mainly from the reactivity of the precursors and the drying step and not from whether the powders were precipitated using microfluidizer or hydrothermal process. The worst dispersibility was observed with powders that were synthesized using low reactivity precursors and oven-drying of the precipitates.

Flowability test was actually the measurement of the "angle of repose" after dropping powder through a funnel. Angles of repose for almost all powders (provided in the Tables) varied between 17° and 55°. However, the powders' angle of repose (flowability) did not seem to play an important role in pressability (how well a powder presses).

Pressability was more directly related to the particle size distribution factor (Sw), as can be seen in the Tables 2 through 5. The powders that pressed the worst (bar samples laminated or cracked or crumbled) had the most undersirable S_w (between 2 and 7) numbers. A few examples are: Catalytica 871-68-3, 871-69-3, 871-44-3a, 871-60-2.5 and 871-62-3, and NexTech CZPII-10-13 to CZPII-10-16 powders.

Sintered Density

Sintered densities of the samples are also shown in Tables 2 to 5. Because samples for sintering were die pressed, these densities are dependent upon pressability, which in turn is dependent upon particle size distribution and particle shapes. However, other factors that could possibly influence sintered density are presence of trace amounts of low melting impurities or minor phases which are not detectable by XRD and particle sizes. Pressability seemed to be influenced to a large extent by the particle size distribution and width (Sw). For example, sintered density of powder 871-61-3 is very high at least partly because it has a favorable (lower than 2.0) particle size distribution factor, Sw. For some of the powders (871-61-3a, 871-63-3a, and 871-66-3a), density could not be determined because the powders did not even press well enough to make bars samples.

Summary

A complete analysis of the results and final selection of the most technologically and commercially attractive processes are scheduled to be done during the course of the next progress period. Up to four processes (two each of each vendor) are planned to be selected for the production of NZP powders at the next scale up level.

Future Work

1) LoTEC and the vendors will decide which processes of each vendor produce the powders with the best combination of properties for scale up to production of kilogram quantities.
2) The vendors will then produce the powders for bulk sample fabrication and testing as described in the fourth objective above.
3) Bulk property testing will be performed, both at LoTEC and at High Temperature Materials Laboratory (HTML) of Oak Ridge National Laboratory (ORNL).

Status of milestones : Program on schedule.

Communications/Visits/Travel :

1) S. Y. Limaye and R. Nageswaran traveled to NexTech Materials, Worthington, OH during April 1996.

Problems Encountered : None

Publications : None.

References :

1) R. M. German, "The Importance of Particle Characteristics in Powder Injection Molding," *Reviews in Particulate Materials*, Vol.1, Metal Powder Industries Federation, Princeton, NJ, 1993, pp 109-160.

Table 1. An overview of the proposed activity for which Phase II contracts were awarded.

Task #	Proposed Accomplishments	Time Allotted
1	Identification and assessment of possible low cost precursors for each process.	2 weeks
2	Production and joint evaluation, with LoTEC, of powders produced by varying process conditions in order to optimize production and minimize cost.	16 weeks
3	Two 5 kg batches of both BS-25 and CS-50 will be supplied to LoTEC by each vendor for powder evaluation and for bulk property assessment as in objective 4 above.	6 weeks

Table 2. Summary of results of testing done on Catalytica microfluidizer-based BS-25 powders.

Powder ID	Process Conditions	Particle Density, g/cc	Sintered Density, g/cc	Surface Area, m^2/g	Median Size, μm	XRD	Dispersibility, Pressability, & Angle of Repose	S w
Phase I BS-25	original	3.48	2.60	11.6	48.6	No detectable impurities	Dispersed fair. Pressed well. Angle not tested	1.96
871-57-2 (uncalcined)	Process 1 Variation A	2.87	2.48	15.4	5.79	Not amorphous Not BS-25 Phase unknown	Dispersed well. Pressed well. Angle = 34°	2.40
871-57-3 (calcined)	Process 1 Variation A	3.42	2.36	6.67	6.94	$BaZrP_2O_8$ impurity	Dispersed fair. Pressed well. Angle not tested	2.46
871-61-3	Process 2 Variation A	3.37	3.12	2.91	12.3	small amount of unknown impurity	Dispersed fair. Pressed well. Angle not tested	1.88
871-61-3A	Process 2 Variation B	3.44	not able to determine	8.38	17.0	very small amount of unknown impurity	Dispersed fair. Pressed poorly. Angle = 18°	3.58
871-63-3A	Process 2 Variation C	3.28	not able to determine	1.25	15.4	No detectable impurities	Dispersed fair. Pressed poorly. Angle = 24°	3.52
871-66-3A	Process 2 Variation D	3.30	not able to determine	0.65	14.3	No detectable impurities	Dispersed fair. Pressed poorly. Angle = 27°	3.52
871-68-3	Process 3 Variation A	3.44	2.30	0.52	30.5	$BaZrP_2O_8$ impurity	Dispersed poorly. Pressed poorly. Angle = 25°	4.6
871-69-3	Process 3 Variation B	3.48	2.25	1.35	9.3	$BaZrP_2O_8$ impurity	Dispersed well. Pressed poorly. Angle = 41°	2.8
871-70-3	Process 3 Variation C	3.53	2.30	0.87	12.9	$BaZrP_2O_8$ impurity	Dispersed fair. Pressed poorly. Angle = 36°	3.1
871-71-3	Process 3 Variation D	3.56	2.43	2.39	7.5	$BaZrP_2O_8$ impurity	Dispersed well. Pressed poorly. Angle = 42°	2.4

Table 2. Continued

871-85-2	Process 4 Variation A	3.44	2.27	3.28	32.3	No detectable impurities	Dispersed Poorly. Pressed fair. Angle not tested	1.84
871-94-2	Process 4 Variation B	3.19	2.23	1.73	8.56	No detectable impurities	Dispersed well. Pressed poorly. Angle not tested	2.75
871-94-*-2	Process 4 Variation C	3.27	2.24	2.64	8.12	No detectable impurities	Dispersed well. Pressed poorly. Angle not tested	2.56

Table 3. Summary of results of testing done on Catalytica's microfluidizer-based CS-50 powders.

Powder ID	Process Conditions	Particle Density, g/cc	Sintered Density, g/cc	Surface Area, m^2/g	Median Size, μm	XRD	Dispersibility, Pressability, Angle of Repose	S w
Original CS-50	Original	3.38	3.21	5.92	37.8	No detectable impurities.	Dispersed well. Pressed well. Angle not tested.	1.34
871-40-2 (amorphous)	Process 1 Variation A	3.04	Not Tested	52.75	Not Tested	Not Tested	Not Tested	-
871-40-3 (calcined)	Process 1 Variation A	3.22	2.824	4.43	4.87	No detectable impurities	Dispersed well. Pressed well. Angle = 41°	2.16
871-41-2 (amorphous)	Process 2 Variation A	3.04	Not Tested	58.99	Not Tested	Not Tested	Not Tested	-
871-41-3 (calcined)	Process 2 Variation A	3.09	2.366	1.89	8.18	No detectable impurities	Dispersed well. Pressed well. Angle = 41°	2.01
871-42-3	Process 1 Variation B	3.31	2.805	6.21	9.97	No detectable impurities	Dispersed well. Pressed well. Angle = 41°	1.82
871-43-3	Process 1 Variation C	3.30	2.875	15.42	8.48	No detectable impurities	Dispersed well. Pressed well. Angle = 47°	2.65
871-43-3a	Process 1 Variation D	3.34	1.996	8.97	8.18	ZrP_2O_7 impurity	Dispersed well. Pressed well. Angle = 50°	2.78
871-44-3	Process 2 Variation B	3.02	2.150	2.22	17.5	No detectable impurities	Dispersed poorly. Pressed poorly. Angle = 18°	3.34
871-44-3a	Process 2 Variation C	3.21	2.211	0.68	12.3	ZrP_2O_7 impurity	Did not disperse* Pressed poorly. Angle = 30°	3.81
871-59-3	Process 1 Variation E	3.24	2.55	5.67	18.4	not yet performed	Dispersed fair. Pressed well. Angle = 45°	2.26

* hydrophobic lumping of powders

Table 3. Continued.

871-60-2.5	Process 1 Variation F	3.13	2.66	74.7	23.1	semi-amorphous	Dispersed fair. Pressed well. Angle not tested.	3.82
871-60-3	Process 1 Variation G	3.23	2.86	8.89	18.7	No detectable impurities	Dispersed fair. Pressed well. Angle = 33°	2.66
871-62-3	Process 3 Variation A	3.00	not able to determine	4.65	15.5	No detectable impurities	Dispersed fair. Pressed poorly. Angle = 41°	3.07
871-87-2	Process 4 Variation A	3.28	2.23	0.57	9.07	very small amount ZrP2O7	Dispersed well. Pressed poorly. Angle = 52°	2.46
871-89-2	Process 4 Variation B	3.22	2.18	4.04	39.6	No detectable impurities	Dispersed poorly. Pressed fair. Angle = 39°	1.92

Table 4. Summary of results of testing of NexTech's hydrothermally derived BS-25 Powders.

Powder ID	Process Conditions	Particle Density, g/cc	Sintered Density, g/cc	Surface Area, m^2/g	Median Size, μm	XRD	Dispersibility, Pressability, & Angle of Repose	S w
Original BS-25	Original	3.55	2.35	12.8	24.3	good	Dispersed fair Pressed well Angle = 45°	1.83
CZPII-0-2	Phos. Route 1 Process Variation A	3.61	2.50	32.9	19.7	good	Dispersed fair Pressed well Angle = 39°	1.62
CZPII-0-3	Phos. Route 1 Process Variation B	3.57	2.56	23.1	19.5	good	Dispersed fair Pressed well Angle = 42°	1.64
CZPII-0-4	Phos. Route 1 Process Variation C	3.62	cracked	104.3	6.24	amorphous	Dispersed well Pressed well Angle = 34°	2.33
CZPII-0-4 (900 C)	Phos. Route 1 Process Variation D	3.74	2.72	36.9	7.99	good	Dispersed well Pressed well Angle = 36°	1.85
CZPII-C	Phos. Route 1 Process Variation D	3.70	2.49	14.7	2.48	very small amount of $BaZrP_2O_8$	Dispersed fair Pressed fair Angle = 38°	2.01
CZPII-1-9	Nitrate Route Process Variation A	3.57	2.48	29.2	19.5	very small amount of $BaZrP_2O_8$	Dispersed fair Pressed well Angle = 48°	1.74
CZPII-1-10	Nitrate Route Process Variation B	3.64	2.80	4.35	20.5	$BaZrP_2O_8$ impurity	Dispersed fair Pressed well Angle = 40°	1.74
CZPII-10-6a	Phos. Route 2 Process Variation A	3.54	2.71	34.5	26.0	good	Dispersed fair Pressed well Angle = 46°	1.73
CZPII-10-6b	Phos. Route 3 Process Variation A	3.53	2.74	22.5	5.14	good	Dispersed well Pressed well Angle = 47°	2.20
CZPII-10-7	Phos. Route 2 Process Variation B	3.52	2.67	41.3	10.9	$BaZrP_2O_8$ impurity	Dispersed fair Pressed well Angle = 45°	1.77

Table 4. Continued.

CZPII-10-8a	Phos. Route 2 Process Variation C	3.54	2.50	44.0	29.8	$BaZrP_2O_8$ impurity	Dispersed fair Pressed well Angle = 49°	1.71
CZPII-10-8b	Phos. Route 3 Process Variation B	3.43	2.39	25.1	13.6	good	Dispersed fair Pressed well Angle = 49°	1.68
CZPII-10-10	Phos. Route 3 Process Variation C	3.45	2.63	23.3	10.3	good	Dispersed fair Pressed well Angle = 49°	1.75
CZPII-10-11	Phos. Route 3 Process Variation D	3.31	2.57	2.18	undeter-mined	good	Dispersed poorly Pressed fair Angle = 29°	-
CZPII-10-13	LoTEC Route Process Variation A	3.27	2.14	1.08	39.4	$BaZrP_2O_8$ impurity	Dispersed poorly Pressed poorly Angle = 19°	4.47
CZPII-10-13B	LoTEC Route Process Variation B	3.53	Not enough powder to test	7.5	15.7	very small $BaZrP_2O_8$ impurity	Not enough sample	2.29

Table 5. Summary of results of testing of NexTech's hydrothermally derived CS-50 powders.

Powder ID	Process Conditions	Particle Density, g/cc	Sintered Density, g/cc	Surface Area, m^2/g	Median Size, μm	XRD	Dispersibility, Pressability, Angle of Repose	S w
Phase I CZP #2	original 1 not calcined	not analyzed	3.00	51.7	7.22	amorphous	Dispersed well Pressed well Angle not tested	1.00
Phase I CZP #4	original 1 calcined	3.20	2.89	13.5	15.8	small amount of ZrP_2O_7	Dispersed fair Pressed well Angle not tested	1.12
Phase I CZP #7	original 2 calcined	3.26	2.54	9.1	12.9	small amount of ZrP_2O_7	Dispersed fair Pressed well Angle not tested	1.18
CZPII-10-9	Phos. Route 2 Process Variation A	3.17	3.03	17.3	9.41	good	Dispersed fair Pressed well Angle = 51°	1.91
CZPII-10-14	LoTEC Route Variation A	3.07	2.46	0.37	37.4	unknown impurity	Dispersed poorly Pressed poorly Angle = 34°	4.83
CZPII-10-15	LoTEC Route Variation B	3.16	2.51	0.47	36.5	good	Dispersed poorly Pressed poorly angle = 43°	4.46
CZPII-10-16	LoTEC Route Variattion C	3.25	2.17	0.93	34.0	small amount of ZrP_2O_7	Dispersed poorly Pressed fair angle not tested	4.38

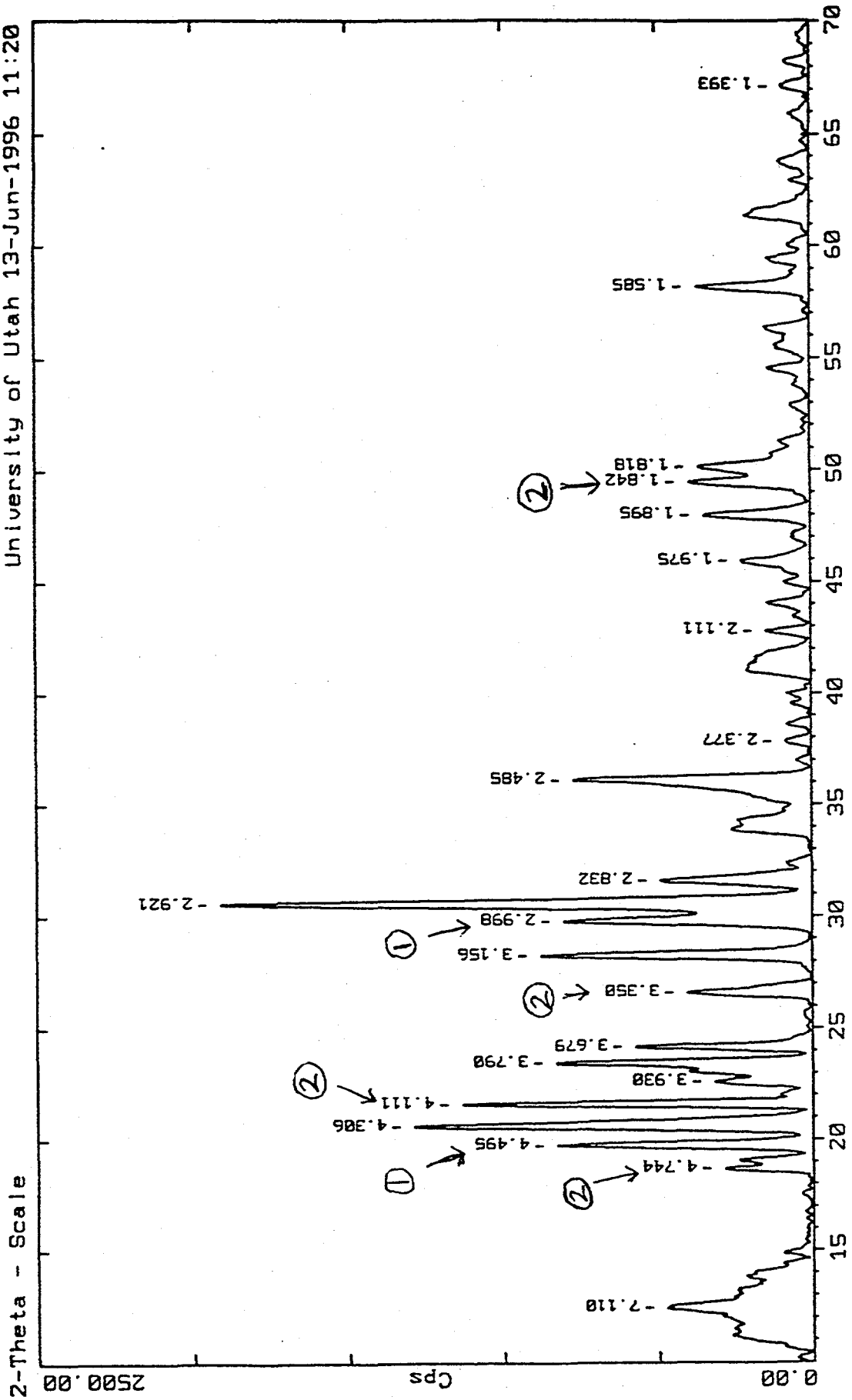

Figure 1. XRD patterns of BS-25 powder synthesized by Cerac, Inc. showing minor phases (marked 1 and 2).

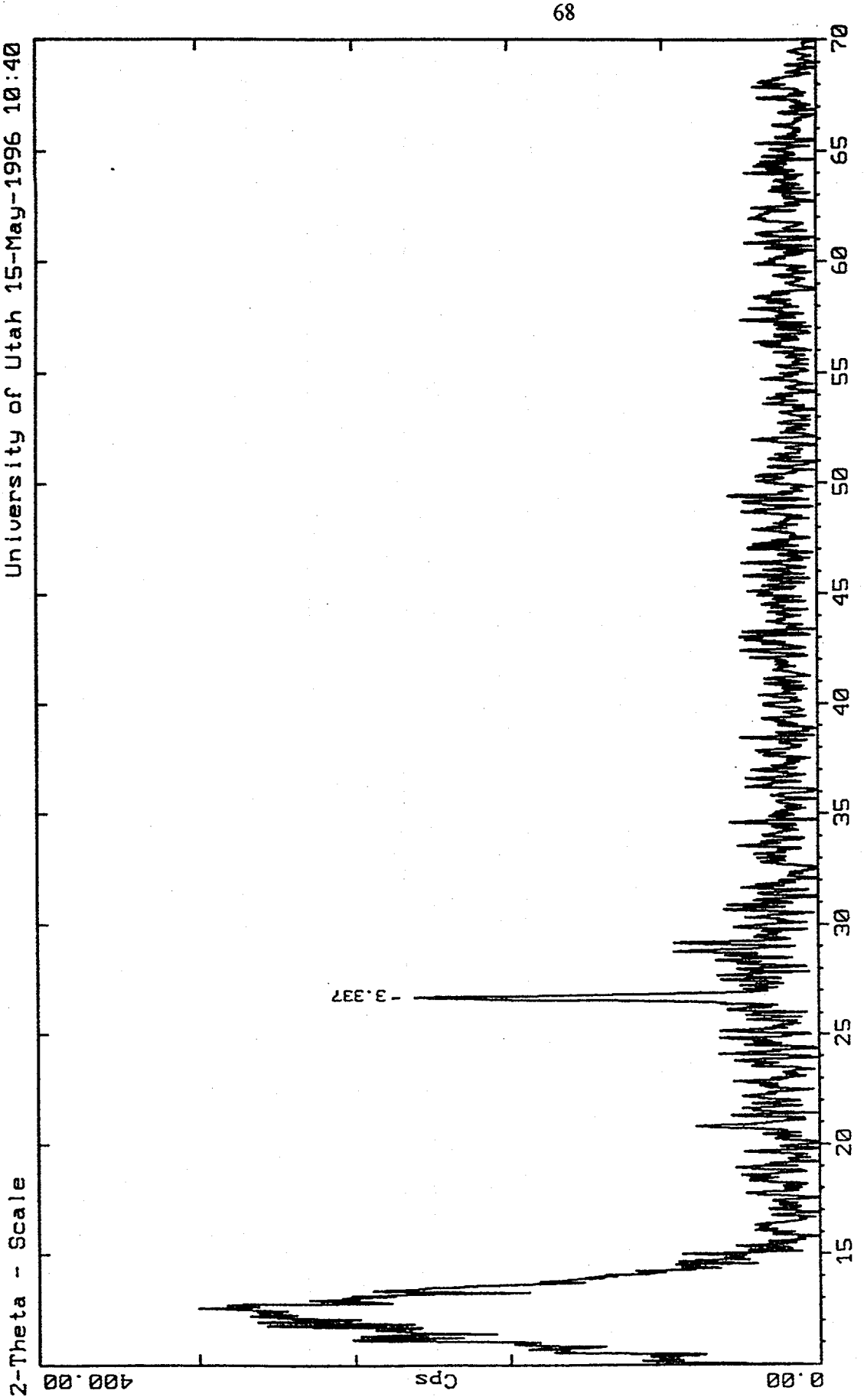

Figure 2. XRD patterns of as-reacted powders from LoTEC's acid based precipitation process showing its amorphous nature.

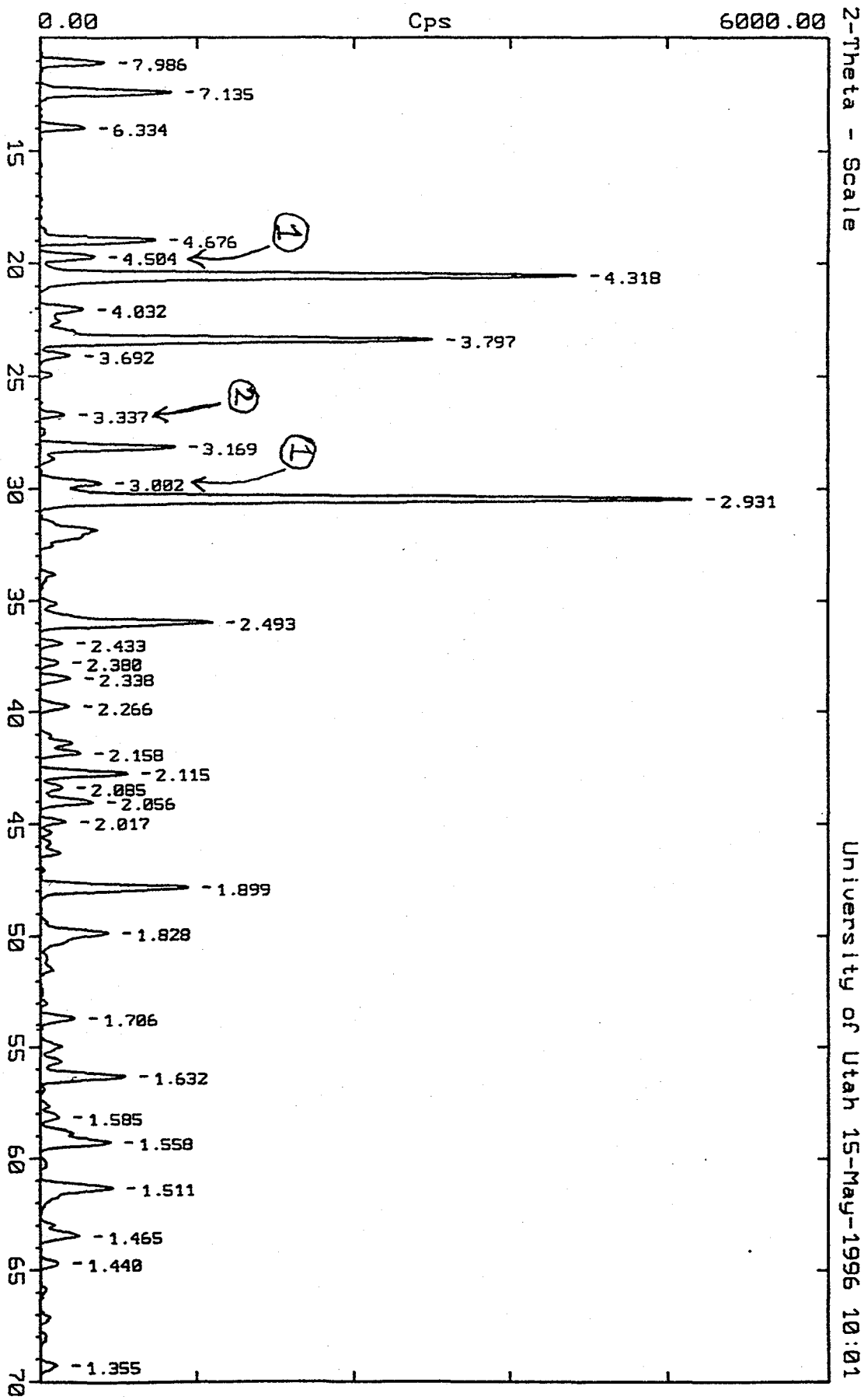

Figure 3. XRD patterns of calcined (1200°C) powders from LoTEC's acid based precipitation process showing nearly single phase BS-25.

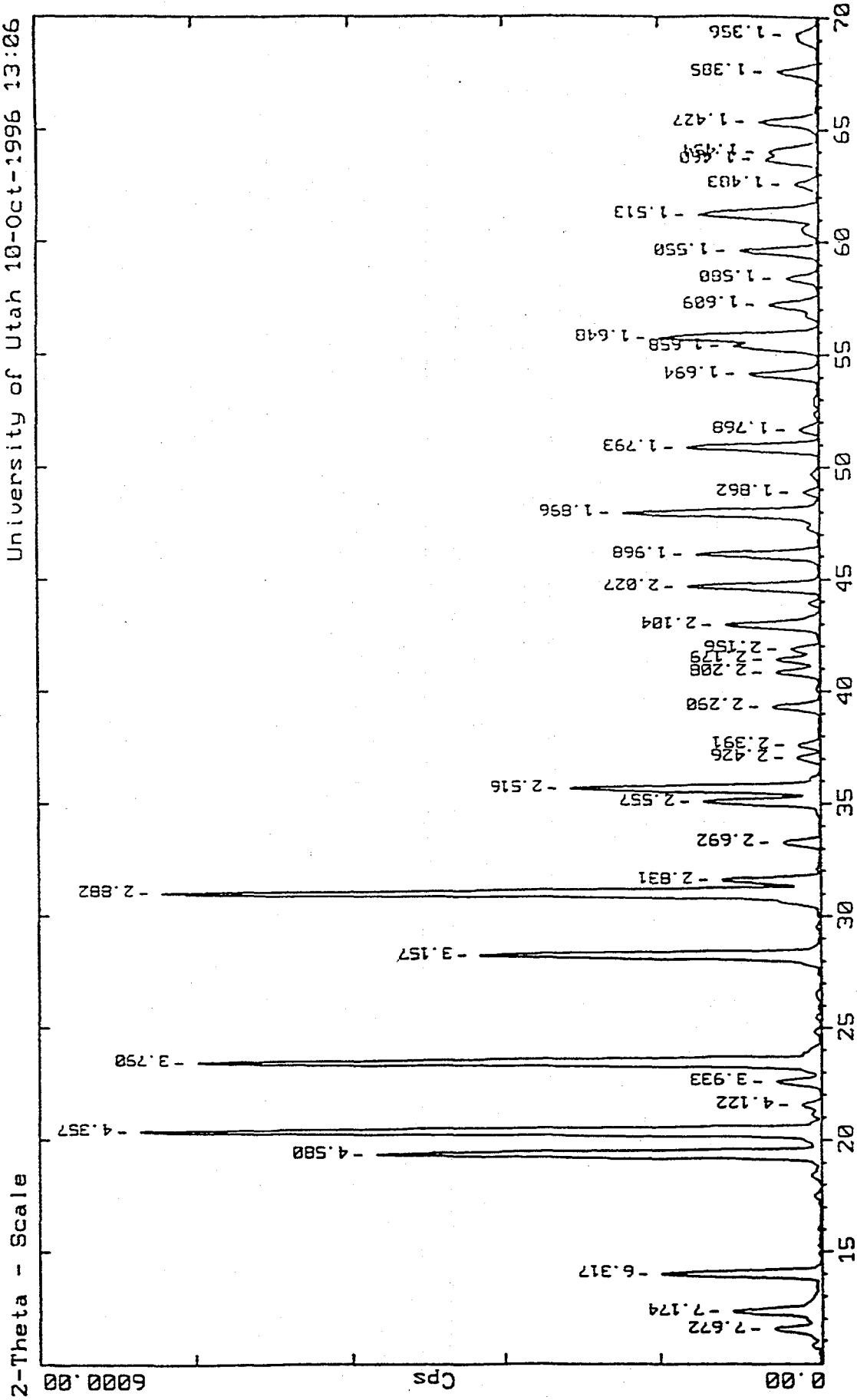

Figure 4. XRD pattern of CS-50 powder, containing no detectable impurities, which was synthesized at LoTEC using a phosphoric acid method with an adjusted pH.

ADVANCED MANUFACTURING TECHNOLOGY

DEVELOPMENT OF ADVANCED CERAMIC MANUFACTURING TECHNOLOGY

Subcontract No. 86X-SP234C

C.Burk, T.P.Leo, L.D.Lynch, B.J.McEntire - SGNICC, Norton Advanced Ceramics
Y.Kalish, R.Begin - Detroit Diesel Corporation
C.Bida, M. Mauptman, L.E.Mains - Deco Grand, Inc.
M.Tricard, D. Graham, J.Picone - Norton Company, World Grinding Technology Center
J.Kellogg - Centorr/Vacuum Industries
V.K.Pujari, W.T.Collins, R.L.Yeckley - SGNICC, Northboro R&D Center
P.Parrish - BDM Federal, Inc.
T.Zahrah, S.Ho lo - MATSYS, Inc.
A.E.Mascarin - IBIS Associates, Inc.
D.Wittmer - Wittmer Consultants

Report Prepared by
Vilmal Pujari

Saint-Gobain/Norton Industrial Ceramics Corporation
Northboro Research and Development Center
Goddard Road
Northboro, MA 01532

Semi-Annual Technical Progress Report
March 1996 - October 1996

Objective/Scope

The objectives of this program are to design, develop and demonstrate advanced manufacturing technology for the production of ceramic valves. A production manufacturing process for a ceramic exhaust valve for DDC's Series 149 diesel engine is being developed under this program. Specific objectives are: (1) To reduce manufacturing cost by a least an order of magnitude over current levels: (2) To develop and demonstrate process capability values (C_{pk}) of 0.7 or less for all critical component attributes; and (3) To validate performance, durability, and reliability of this ceramic valve in rig and engine testing.

Technical Highlights

Task 1 - Component Design and Specification

1a) Preliminary Design

This task has been completed. Based upon this activity, valves were fabricated for the 500 hours durability test described below.

1b) Final Design Analysis

The final design specifications for DDc series 149 valve has been established based upon the engine testing of preliminary design valves (Task 1a). Specifically, as per DDC's drawing DD-125232, these include the following characteristics:

- Thirty degree (30^{o}) seat angle.
- Keeper groove configuration per View B on the drawing.
- Material and inspection requirements per DDC Spec. 15T-S149.
- Part Number and Serial Number identification of each valve.
- Proof Testing requirement relaxed in number of samples to be tested based on positive durability tests.

Task 2. Component Manufacturing Technology Development

2a) Environmental Safety and Health

This task has been completed.

2b) Process Cost Modeling

The modeling effort has continued to be applied to three analysis during this reporting period. The sintering analysis has been expanded to compare continuous, batch, continuous and HIP'ing, batch and HIP'ing, and gas pressure sintering. The grinding analysis is comparing Deco's centerless process to Junker and Studer processes in order to down-select one grinding approach. The third analysis is looking at the cost reduction and efficiency improvements that can be gained as the manufacturing process is scaled up to higher volumes.

Data on the alternative sintering scenarios has been collected and incorporated into the model and is shown in Fig. 1. It is obvious from Fig.1, that continuous sintering with or without HIP offers the most cost effective alternative. However, as mentioned in section 2c) below, due to the furnace design limitations, continuously sintered valves currently show significantly higher dimensional distortion as compared to those processed in the batch furnace.

The process flow for the Studer machining approach has been defined and the Centerless assumptions have been confirmed by Deco. Grinding wheel data have also been assembled by WGTC for both the machining techniques. Based upon this data, the projected machining costs per valve for the Deco, WGTC and Junder processes have been computed as shown in Fig. 2. The centerless grinding technique seem to offer the most cost effective alternative closely followed by Junker and Studer processes.

Using the optimum Sintering (continuous Sinter +HIP) and machining procedures (centerless-Deco) outlined above, the scaled up manufacturing procedure has been defined and the production volume manufacturing cost has been estimated as shown in Figure 3. As shown in Fig. 3, a factor of 25 reduction in valve manufacturing cost is projected based upon demonstrated process improvements and economy of scale assumptions. IBIS has also completed the cost modeling activity and has submitted the draft final report to NAC.

2c) Process Control

i.) Milling and Spray Drying Process Control

As part of the optimization effort, the NT551 silicon nitride composition was processed utilizing the established S.O.P. and subsequently densified following sinter/HIP approach. The specimens were first sintered in a batch (NAC) or continuous (University of Southern Illinois) mode and subsequently HIP'ed to achieve densities $\geq$99.9% T.D.. The salient mechanical properties corresponding to these two densification approaches are summarized in Table 1. It is obvious from Table 1, that for both those conditions, the mechanical properties obtained meet and/or exceed the targeted values established by DDC.

Following the above procedures, a substantially larger quantity of specimens (75 tiles and 200 rods) have also been fabricated and delivered to ORNL. The ORNL, as planned earlier, will independently generate flexure and tensile strength data base from these specimens.

Using the sinter/HIP approach, a set of valves has also been densified and their straightness (TIR)measured. As compared to sintered SiAlON (NT451), a factor of 3 reduction in bending has been achieved. Reduced TIR is expected to reduce the machining time/cost significantly.

A large quantity of valves is currently under fabrication for delivery to Deco Grand, World Grinding Technology Center (WGTC) and Chand Technical Ceramics (CTC) in support of machining optimization.

ii) Continuous Sintering

During this reporting period, several valves, tiles, and pellets of NT-551 composition were sintered in three separate runs (designated as #66, #77, and #80). These results suggest that sintered densities which will allow complete densification by post-sinter HIP

were achieved. As reported in Section (i), acceptable mechanical properties have been achieved utilizing these test specimens.

In preparation for the final demonstration of the valve manufacture process, the S.O.P. for both the batch and the continuous sintering processes have also been defined.

Sufficient quantity of batch, as well as continuously sintered valves (NT551) followed by HIP were also evaluated for dimensional control (TIR). Overall, the batch sintered valves showed better dimensional control (Fig 4). This is not unexpected, as during the continuous sintering process, valves were not fixtured in an optimal configuration due to the limitations of the current furnace chamber design. It is essential to emphasize here that the dimensional control is extremely important for the efficient machining and the overall process yield.

iii) Machining

Development of various machining techniques for finishing DDC Series 149 blanks is progressing as planned. A total of approximately one hundred (100) NT551 valve blanks were fabricated and divided equally between the three machining approaches described below:

a) Centerless Grinding (Deco Grand)

Modifications to the LidKoping machine was completed as planned and the centerless grinding methodology was established. However, twenty centerless ground valves fabricated so far,do not meet the dimensional or the surface finish specifications. However, they will be pull tested to complete the characterization effort. In the meantime, Deco is in the process of fine tuning the truing procedure in order to improve the valve dimensions and the surface finish.

b) CNC Profile Grinding (WGTC)

During this reporting period, effort was focused on the finish grinding of the valve stem and head radius. Briefly, this involves plunging the end of the valve stem, grinding the valve stem, grinding the valve seat and CNC profiling the valve head/radius. Chronology of machining improvement in terms of total required time is highlighted in Table 2. Assuming a normalized total machining time of 100% with the (old) base line NAC process, an order of magnitude reduction has been realized with the most current process.

Table 2 Chronology of Machining Improvement

	Old Process @NAC	WGTC (10/1/95 report)	WGTC (12/1/95 report)	WGTC (4/1/96 report)	WGTC Current
Max Total Grinding Time	100%	33%	29%	19%	9%

Following the above procedures thirty valves have been rough ground and currently are in the process of being finish machined

c) Compound Centerless Grinding (Chand Kare)

This technique is also showing promise. The total machining time is estimated to be comparable to CNC profile grinding.

The evaluation data (machining time, dimensions, surface finish and pull load) from the above three techniques will be compared with the already established parameters of the Junker and baseline, NAC processes for the final down selection.

d) Intelligent Process Control

This task has been completed.

Task 3 - Inspection and Testing

Five hundred hour durability test was completed using 32 ceramic (NT451) valves. Cylinder heads were removed from the engine for examination of the valves at the conclusion of the 500 hour durability test. Upon removal of the valve springs and valves from the heads, one of the valves in position 3R was found with the tip of the valve fractured off. The valve did not drop during the engine test, both the tip and the valve being retained by the keeper.

Although the retention of the broken valve is a good indication for field operation, it prevented earlier discovery of the failure. Valve was sent to Norton for additional analysis. After the analysis it was concluded that the use of machined keepers (Norton design) and/or soft DDC keepers may help minimize the stress concentration inside the groove by providing a better fit. Consequently additional 500 hour testing was initiated at DDC in order to evaluate the two keeper designs.

Split set of 30° ceramic valves - part with soft keepers from Milwaukee Wire and part with machined keepers from Norton - was installed on an 8V-149 engine in for additional five hundred hour mine haul cycle durability test.

At 250 hours, the valve inspection was conducted. Cylinder head were pulled out of the engine and valves were removed from the cylinder heads. All valves and keepers were inspected. Valve faces and seat surfaces looked fine. Some wear marks on the keepers were detected, all within the expected range. Engine was reassembled and tested resumed.

Task 4 - Process Demonstration

4a) This task has been completed.

4b) Final Demonstration

In preparation for the final valve manufacturing demonstration, processing of approximately 200 kg. of press-ready NT551 powder has also begun. During this period, 80kg of powder was processed at NRDC and delivered to NAC's East Granby facility. The powder processing followed the S.O.P. established previously. Key salient features of the powder processing approach includes:

(a) Closed loop aqueous processing methodology previously developed in a separate DOE sponsored "Processing for Reliability" program.

(b) Intelligent Control System (ICS) based powder milling and spray drying procedure, and,

(c) SPC and Duality Assurance methodology.

Status of Milestones

Milestones No's 1-5 are complete. Milestones No's 6 through 8 are on schedule.

Communications/Visits/Travel

4/9/96 - V.K.Pujari (NRDC)and T. Mascarin (IBIS Associates) visited IMT's HIP facility to collect data for cost analysis.

5/1/96 - A Meeting was held at WGTC with Mar Tricard, K.Subramanian, Bob Benoit, Chuck Bida, Tony Mascarin, V.K.Pujari and Marc Abouaf to define detailed centerless grinding machining procedure at Deco to (a) establish grinding wheel requirements and (b) per form cost modeling.

5/24/96 - Marc Tricard (WGTC) visited Deco Technologies to discuss status of Lidkiping machine and wheel requirements.

Discussions were held between Dale Wittmer, Tony Mascarin, and VKPujari to further refine the cost modeling effort related to continous sintering.

7/10/96 - D.E.Wittmer (WCI), J.Kellogg (CVI) and V.K.Pujari, Larry Lynch, and Bill Collins (NAC) met on July 10 at USI in Carbondale, IL to discuss continuous furnace operation and design, and to observe furnace being used to continuously sinter full-sized NT551 valves.

7/11/96 - D.E.Wittmer (WCI). K/Le;;pgg)CVI) and V.K.Pujari, Larry Synch, and Bill Collins (NAC) and Bob Schulz, Ray Johnson and Arvid Pasto (DOE) met on July 11 at USI in Carbondale, IL for an informal program review and to observe and discuss continuous sintering of full-sized NT551 valves.

7/12/96 - V.K.Pujari, Larry Lynch, and Bill Collins (NAC) visited Deco Technologies, Troy,Michigan to review technical progress towards centerless grinding of valves.

7/9/96 - V.K.Pujari visited WGTC in regards to valve machining activity being performed at this facility.

9/5/96 - V.K.Pujari of NRDC and Tony Mascarin of IBIS Corp. Visited NAC's East Granby operation to help facilitate the transfer and implementation of the TCM (Technical Cost Model) for the final valve manufacturing demonstration.

9/9/96 - V.K.Pujari and Lin Broderick of NRDC, Tony Mascarin of IBIS Corp. Visited WGTC to review CNC profile grinding procedure with Dr. Subramanian, John Hogan and Doug Wakefield.

9/18/96 - V.K.Pujari of NRDC and Tony Mascarin of IBIS Corp. Visited WGTC to meet with Dr. Subramanian, John Hogan, Doug Wakefield and V. Ramanujan to finalize grinding S.O.P. for final input to the cost model.

Problems Encountered

Several minor problems were encountered with the Lidkiping Machine. These related to spindle bearing and hold down pusher mechanism's pivot device. The problems were corrected and valves were centerless ground as mentioned above.

MECHANICAL PROPERTIES OF NT551 SILICON NITRIDE

DENSIFICATION PROCEDURE	MEAN STRENGTH (MPa)	B1 (MPa)	WEIBULL MODULUS m	K_{Ic}* MPa$\sqrt{m}$	No. Of SPECIMENS
Batch + HIP Sinter	890	732	22	7.1	20
Continuous Sinter + HIP	970	866	36	7.4	10

* Measured by R-curve method of Becker et al.

Table 1

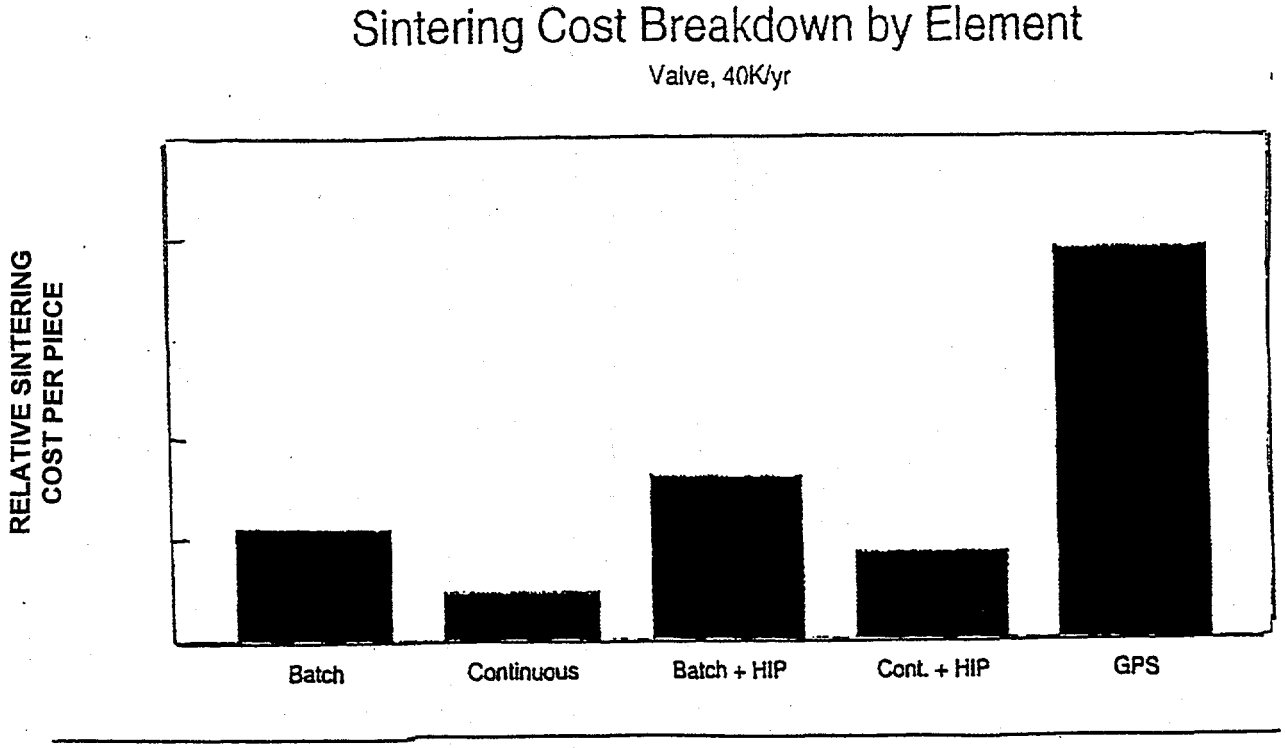

Figure 1

FIG. 2

Grinding Cost Breakdown by Element

Valve, 40K/yr

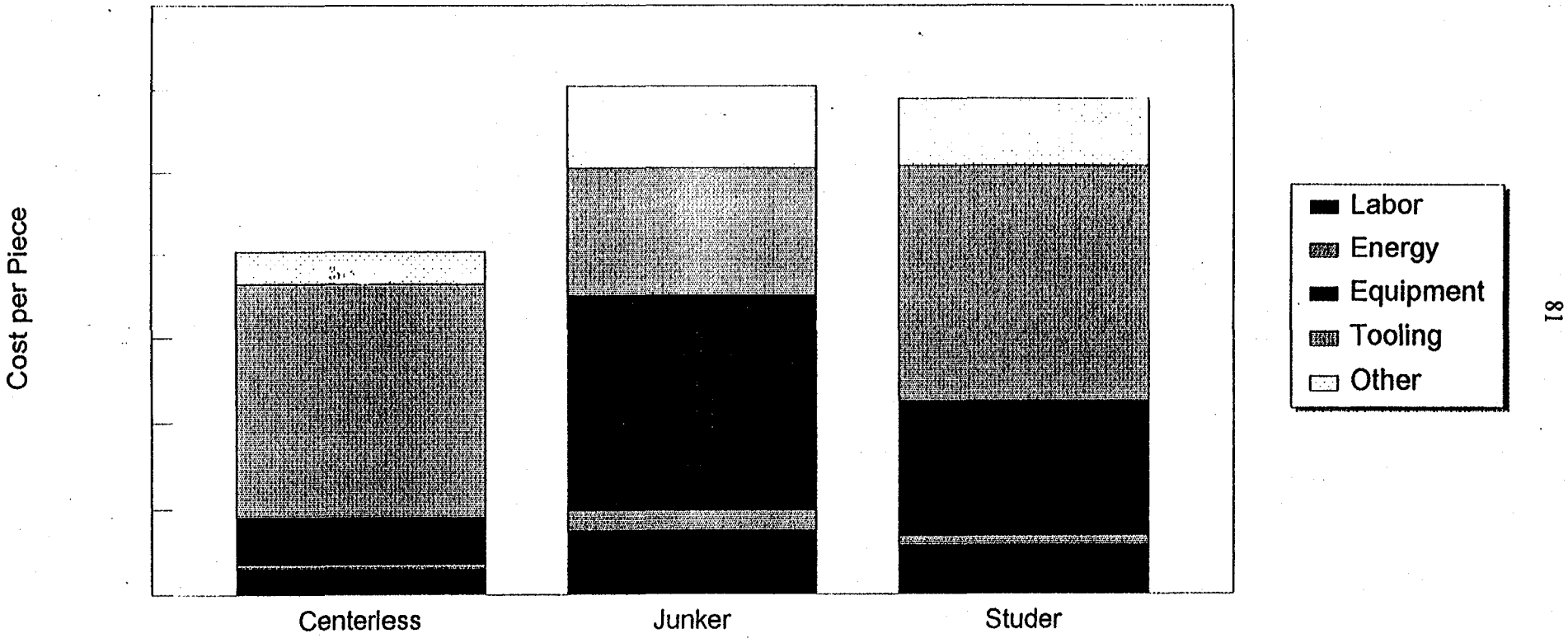

IBIS Associates

10/02/96

FIG. 3

Variable Cost vs Cumulative Production Volume

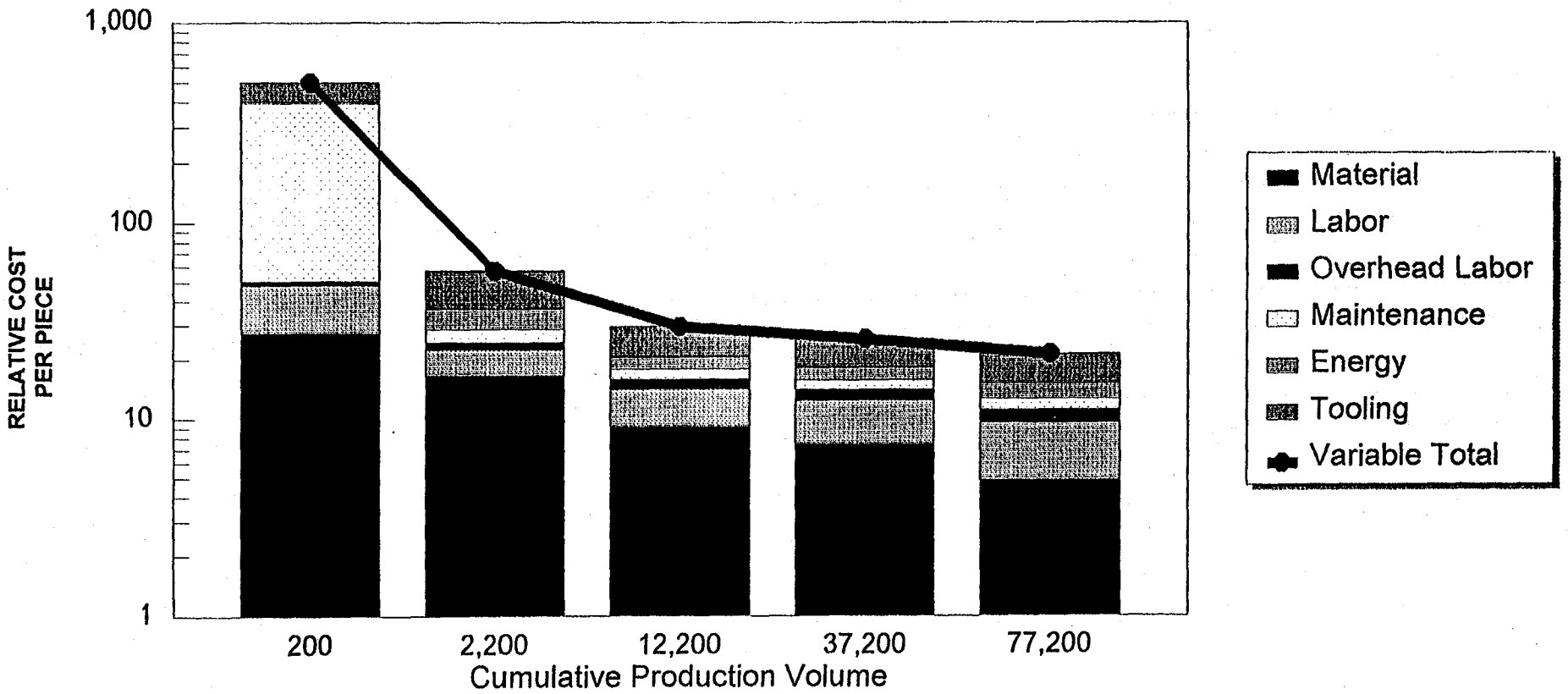

82

FIG. 4

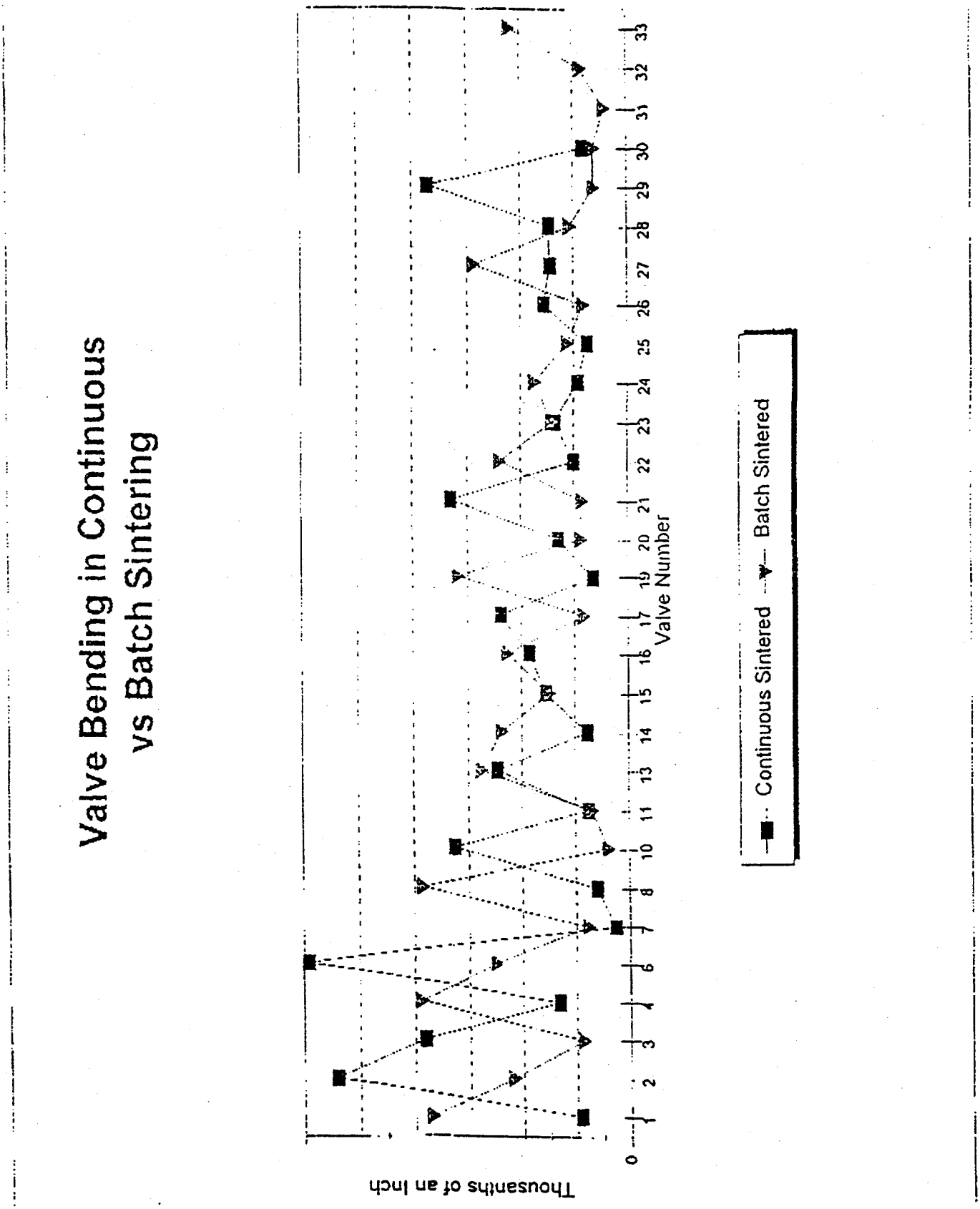
Valve Bending in Continuous
vs Batch Sintering
Thousanths of an Inch
0
2
3
4
6
7
8
10
11
13
14
15
16
17
19
20
21
22
23
24
25
26
27
28
29
30
31
32
33
Valve Number
Continuous Sintered
Batch Sintered

COST-EFFECTIVE CERAMIC MACHINING

P. J. Blau and E. S. Zanoria
Oak Ridge National Laboratory

Objective/Scope

The objective of this effort is to develop, in conjunction with U. S. industry, advanced technologies and the associated scientific and economic concepts necessary to reduce the costs associated with the machining of structural ceramics; especially, as related to the use of these materials in energy-efficient, low-emissions transportation systems. This effort consists of subcontracts to industry and in-house research at Oak Ridge National Laboratory, Argonne National Laboratory, and the National Institute of Standards and Technology. Progress reports for other than the ORNL in-house research portion of this work may be found elsewhere in this publication. The four subtasks in this effort are:

1. Technology Assessment and Future Needs
2. Advanced Machining Methods Development
3. Ceramic Machinability and Related Performance
4. Structure and Surface Quality of Machined Ceramics

ORNL in-house activities are aimed at three technical areas: (1) investigating the effects of machining practices on the durability of ceramics for valve and valve seat applications, (2) understanding and characterizing the detailed nature of machining-induced surface and sub-surface damage, and (3) developing standardized methodology for assessing the grindability of ceramics. The latter includes such methods as non-contact surface profiling, atomic force microscopy of ground surfaces, and scanning acoustic microscopy to detect subsurface flaws.

Technical Highlights

September Project Review. The annual Cost-Effective Ceramic Machining Project Review was held on September 11 and 12, 1996 in Oak Ridge, Tennessee, in the Pollard Auditorium of Oak Ridge Institute of Science and Education. The meeting program is provided at the end of this report. In addition to the projects supported under the CECM effort, three additional presentations were made to describe progress on related DOE and company-supported efforts. Approximately 65 persons registered for the day-and-a-half review, a number comparable to the attendance of the first such meeting in May 1991. Attendees were offered the opportunity to tour the High Temperature Materials Laboratory at ORNL on Thursday afternoon. This tour included demonstrations of instrumented grinding machines, precision metrology equipment, and friction and wear testing equipment in the Machining and Inspection Research User Center.

A special compilation which summarizes the progress and accomplishments of the CECM effort since its inception was prepared and distributed to attendees. It contains a list of all subcontracts and laboratory projects as well as a bibliography of CECM publications. This compilation will be also be published as an ORNL report. In addition, the five-year history of the CECM effort will be featured in the upcoming issue of the Ceramic Technology Newsletter.

Assessment of the Durability of Ground GS-44. A paper titled "Effect of Incident Angle on the Impact Wear Behavior of Silicon Nitride," has been prepared for submission to the *Journal*

of the American Ceramic Society. Based on the results of experiments involving an NBD-200 silicon nitride ball striking a polished NT-154 silicon nitride surface, the paper notes that impact wear of the latter is minimized at incidence angles between 60° and 75° (Fig. 1). The influence of normal stress which promotes brittle fracture of the parent material, increases with more normal incidence angles. Whereas, the effect of tangential stress, which enhances delamination of protective film of compacted wear debris, decreases with increasing angle of incidence. The combination of such opposing effects gives rise to a minimization of impact wear between the aforementioned angles.

Contrary to the above findings, repeated impact tests on ground GS-44 silicon nitride, using similar impact conditions, revealed a strong tendency for maximum wear at incidence angles close to 60°. Figure 2 shows that the maximization of impact wear near 60° occurs both in samples ground by an 80-grit and a 320-grit diamond wheel. The reason for such a trend, as opposed to that for polished NT-154, is yet unknown, and additional experiments are being designed to establish the reasons for these apparently contrasting phenomena. These studies are aimed at identifying the unique roles of material composition, surface topography, machining-induced surface damage, and residual stresses on the impact-wear behavior of ceramics.

Future Plans

1. Work will continue on the comprehensive surface and subsurface characterization of ground GS-44 tiles. It is hoped that key x-ray residual stress data on the two types of ground specimens can be obtained during the next reporting period.

2. Repeated impact tests will be concluded on GS-44 specimens. In addition to the recently-completed paper, cited below, another paper which looks more carefully at the mechanics of material removal differences between tests on polished and ground surfaces is in preparation.

Status of Milestones

On schedule.

Communications/Visitors/Travel

Representatives of at least ten companies visited the HTML, Machining and Inspection Research User Center during the September 11-12 CECM Project Review. They were provided handouts and explanations of how the User Program works.

Problems Encountered

None.

Publications/Presentations

"Effect of Incident Angle on the Impact Wear Behavior of Silicon Nitride," submitted to the *Journal of the American Ceramic Society*.

< < < Program > > >

Wednesday, September 11

I. Introduction and Background

Background of the CECM Effort
P. J. Blau, ORNL

Update of Changes in DOE Ceramics-Related Programs
D. R. Johnson, ORNL

II. Development of Advanced Grinding Wheels and Wheel Dressing Technology

Development of a Next-Generation Grinding Wheel: Phase II
R. Licht, P. Kuo, and S. Ramanath, Norton Company

Electrolytic In Process Dressing (ELID) for High Efficiency Precision Grinding of Ceramic Parts: An experimental study.
B. P. Bandyopadhyay, University of North Dakota

Chemically-Assisted Ceramic Grinding
S. M. Hsu, NIST

Development of a Smart Grinding Wheel: New Project
S. Malkin, C. Guo, and R. Gao, U. of Massachusetts

III. Characteristics of Machine Tools and Development of New Grinding Systems

The Effect of Machine Stiffness on the Grinding of Silicon Nitride
B. Zhang, University of Connecticut

Implementation of High-Speed Grinding Technology for Structural Ceramics
J. Kovach, Eaton Corporation and
S. Malkin, U. of Massachusetts

Next Generation Spindle for High Speed Centerless Grinding of Advanced Ceramic Components
J. Kovach, Eaton Corporation and
J. Flinchbaugh, Weldon Machine Tool Company

IV. Cost Trade-offs in Ceramic Manufacturing

Cost Modeling Analysis of Fabrication Approaches for Silicon Nitride Components
B. Draskovich, AlliedSignal Ceramic Components and
J. Schoenung, California State Polytechnic University - Pomona

V. Structure and Surface Quality of Machined Ceramics

Laser Light-Scattering and Dye Penetrant Studies
J. G. Sun and W. Ellingson, Argonne National Laboratory

Thursday, September 12

V. Structure and Surface Quality of Machined Ceramics (....continued)

In-House Research on Surface Quality and Performance in Machined Ceramics

Part 1: Multi-technique analysis of grinding damage
P. J. Blau and E. Zanoria, ORNL

Part 2: Repeated-impact studies of ground ceramics
E. S. Zanoria and P. J. Blau, ORNL

Part 3: Friction and wear studies of ground GS-44
P. J. Blau and R. L. Martin

Part 4: Grindability testing and standardization
P. J. Blau, ORNL

VI. Update on Related DOE-funded Projects

Raman Studies of Ground Ceramic Surfaces
P. Yaney and N. Hecht, University of Dayton Research Institute

Process Development for Through-feed Centerless Grinding of Zirconia Timing Plungers
A. Shih,Cummins Engine Company
M. Tricard, S. Subramanian, and D. Gust, St. Gobain/Norton Company

Recent Progress on the Manufacture of Ceramic Valves
M. Tricard, St. Gobain / Norton, Worcester, MA

VII. Tour and Presentation

Machining and Inspection Research at the ORNL High Temperature Materials Laboratory
S. McSpadden, ORNL

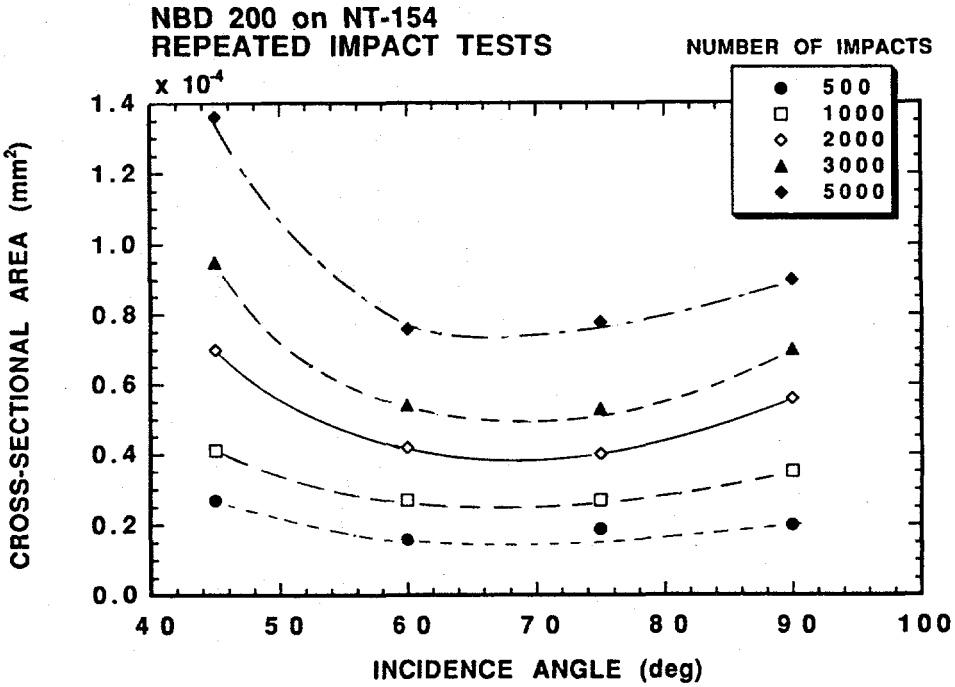

Figure 1. Cross-sectional area of impact crater in polished NT-154, plotted as a function of the angle of incidence. Each point represents an average of three tests.

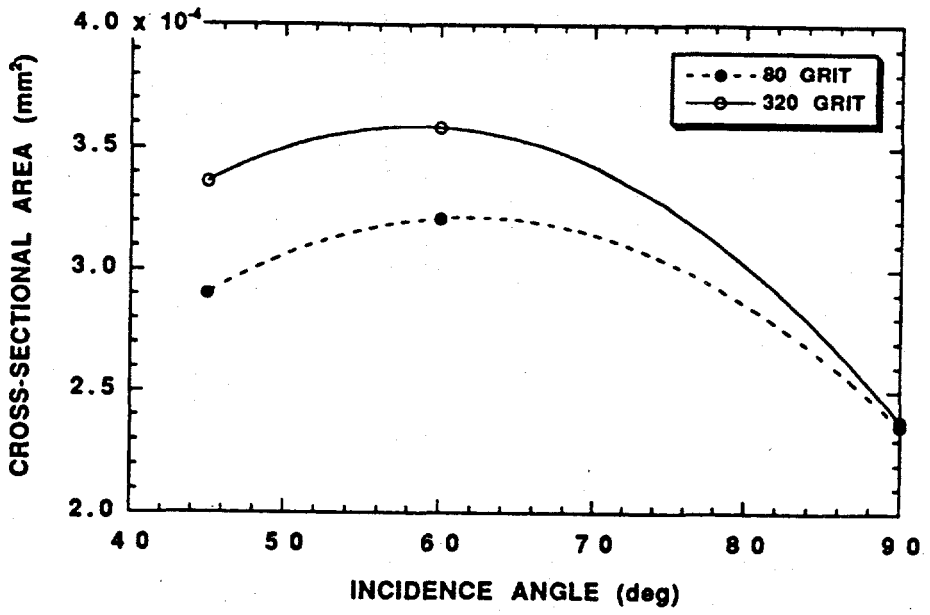

Figure 2. Cross-sectional area of impact crater in ground NT-154 plotted as a function of the angle of incidence. Each point represents an average of three tests, each with a duration of 5000 impacts.

Innovative Grinding Wheel Design for Cost-Effective Machining of Advanced Ceramics, Phase II

R.H. Licht, P. Kuo, S. Ramanath (Norton Company)

Objective/Scope

The overall objectives of this Phase II program are (1) to scale-up the manufacturing process of the Phase I experimental wheel composition in order to manufacture grinding wheels in the diameter range of 356-mm (14-in.) to 406-mm (16-in.) (expanded from the original objective of 356-mm); and (2) to validate the performance of the new wheels in cylindrical grinding of advanced ceramics at independent test sites.

In the completed Phase I, grinding test results of 76-mm (3-in.) and 203-mm (8-in.) diameter wheels indicated that a superior, next-generation grinding wheel for cylindrical grinding of ceramics had been developed[1]. Most production grinding of cylindrical ceramic parts is done on machines that use 305-mm (12-in.) to 356-mm (14-in.) diameter wheels, with more recent trends towards 406-mm diameter. A Phase II program was initiated to scale-up the new Superabrasive wheel specification to these larger diameters, to make further wheel enhancements, and to perform independent validation tests.

Task 1 of Phase II will address wheel processing and wheel variable issues to achieve grinding action for the larger wheels similar to that successfully attained for the smaller Phase I wheels. Also in Task 1, we will modify or develop the wheel core and wheel design for higher speed operation, and determine the maximum operating speed for the new wheel system.

In Task 2, we plan to fabricate large test wheels, and to perform a cylindrical in-house grinding test at Norton's World Grinding Technology Center (WGTC) prior to independent validation testing. In Task 3, large experimental test wheels will be manufactured for independent validation at ceramic manufacturers. The following organizations are scheduled to perform validation tests: Norton Advanced Ceramics (NAC); AlliedSignal Ceramic Components; Chand Kare Technical Ceramics; and Eaton Manufacturing Technologies Center. Eaton plans to test the new wheel product under high speed grinding conditions. The NAC and WGTC wheel validation activity could complement their valve grinding development efforts currently in process under the DOE Advanced Ceramic Manufacturing Technology Program. Task 4 will include more extensive evaluation of ceramic surface integrity of ground ceramic specimens from the Tasks 2 and 3 grinding tests.

Technical Progress

The Phase II contract started March 1, 1996.

TASK 1: Process Scale-Up

Task 1.A: Experimental Design and Definition

This subtask was completed. The team held a preliminary design review meeting and selected a segmented wheel approach instead of a continuous rim approach. Norton also

requested, and LMES approved, a modification to expand the SOW that changed the test wheel diameter requirement from 356-mm, to include a range of between 356-mm and 406-mm. This larger diameter capability is preferable for some of the newer OD grinding machines and current grinding trends in the ceramic industry. The successful manufacture of the larger diameter wheels will expedite new wheel commercialization at the conclusion of this Phase II contract.

Task 1.B: Strength Characterization and High Speed Core Development

This subtask was completed this period.

Bond strength tests in Phase I demonstrated that a typical metal bond has more than twice the flexural strength of a resin bond currently being used for ceramic grinding. For the smaller diameter (203-mm) Phase I wheels, a standard wheel hub composition was selected that was adequate for the required testing parameters. The wheels were speed-tested and rated for up to 61 m/s (12,000 surface ft/min.) grinding speed. Speed tests to determine the ultimate wheel speed capability of this abrasive rim-hub combination was not done in Phase I, and is being done in Phase II.

Finite element analysis was performed to estimate the minimum strength requirements for wheel core and abrasive section under various wheel designs and at a peripheral wheel speed of 200 m/s (39,370 surface ft/min.). Since stress on the wheel (σ) is proportional to the square of the wheel speed, the strength requirements for a wheel to be run at another speed (V_2) can be calculated directly from the following relationship:

$$\frac{\sigma_1}{\sigma_2} = \left(\frac{V_1}{V_2}\right)^2$$

Considering the anticipated desired testing speed at Eaton for up to 127 m/s, and with proper built-in safety factor, a core material must have a minimum yield strength of approximately 150 MPa. The actual core material chosen has a yield strength of approximately 450 MPa.

A comparison analysis of stress produced between continuous abrasive rim and segmented abrasive rim was also performed. Figures 1 and 2 shows the corresponding tangential and radial stresses at any position between arbor hole and the wheel OD under continuous rim and segmented rim wheels, respectively. The wheel model was constructed with the following dimensions: 127 mm diameter arbor hole, 392 mm outside diameter, and 6.4 mm diamond depth. The tangential stresses created at the interface between core and diamond section in a wheel with a continuous rim is at about five times of that of segmented rim wheel. For operational safety consideration, we decided to re-direct our wheel fabrication approach from continuous rim to segmented approach. This change of wheel fabrication approach also removed a physical constraint in wheel size for this program. During Phase II planning stage, we had a wheel size limitation of 356 mm (14 in.) diameter due to hot press furnace capacity. With the new segmented wheel design, we are now making larger diameter wheels, approximately 393-mm (15.5-in.). This larger size wheel is more consistent with the current needs of ceramic manufacturers.

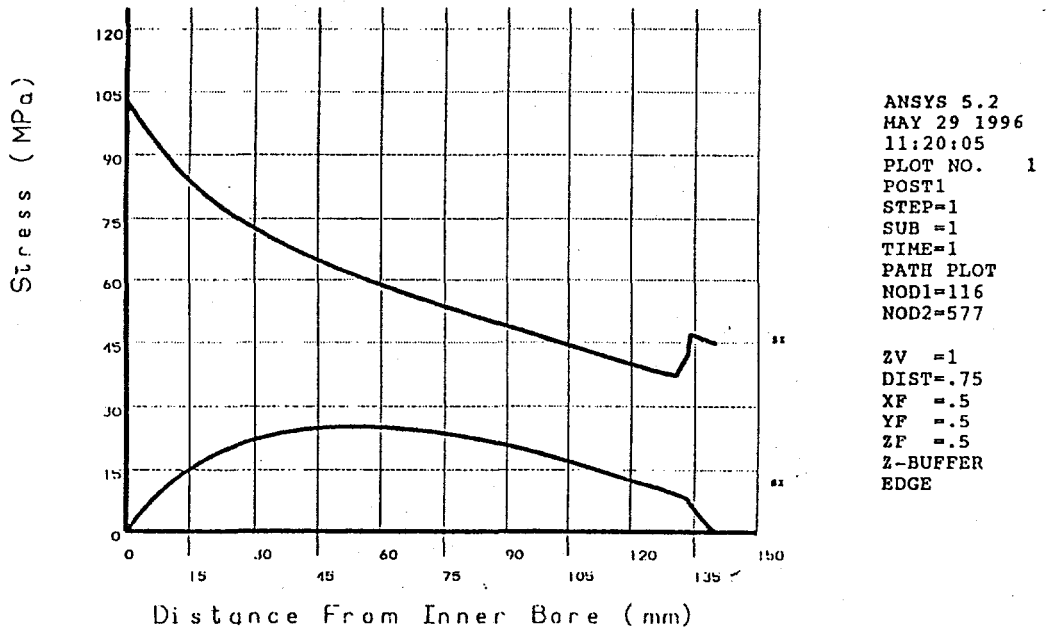

Figure 1. Tangential (SZ) and Radial (SX) Stress Distribution on a Continuous Rim Wheel. Metal Bond Wheel at 200 m/s

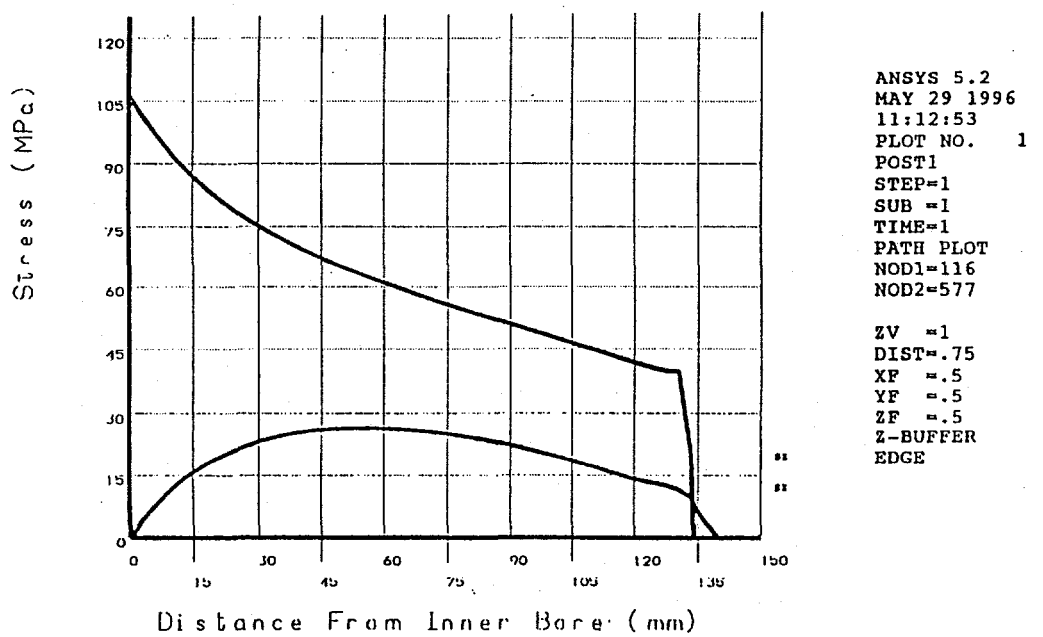

Figure 2. Tangential (SZ) and Radial (SX) Stress Distribution on a Segmented Wheel. Segmented Metal Bond Wheel at 200 m/s

For bond strength characterization, we attempted to initially do bond tensile testing. However, due to the relatively brittle nature of the specimens, we had difficulty preparing specimens that would yield required specimen gage breaks. Ultimately, we adopted a spin test method, which more closely simulates real life conditions, to verify that the experimental bond and wheel design will be sufficiently strong for anticipated high speed grinding applications. In several preliminary spin tests, described below in Task 1.C., we passed the target threshold speed for planed independent tests in Task 3 with a sufficient safety factor. We have confirmed that the core material selected for the larger wheel can pass the required speed limit with a sufficiently large safety factor.

Task 1.C: Manufacture and Characterization of Large Wheels

The general wheel design and related drawings for the large Phase II wheels were completed. All drawings for the graphite mold parts, thermocouple, and wheel core for the initial continuous rim design and the revised segment wheel manufacturing approach were completed.

Abrasive Segment Manufacturing Trials -- We characterized the relationship between fabrication control parameters and bond properties. Three different compositions and three temperatures were used to form this study matrix.

Different furnace equipment is required to make wheel segments and continuous rim wheels. Therefore, considerable emphasis was spent in correlating furnace operating parameters and final properties of the segments. This study was successfully completed. The furnace run profile and all the control parameters were identified and specified.

With the final furnace run profile, we have demonstrated that we can make very consistent segments. For example, we evaluated the hardness of laboratory made segments of the same-specification. For approximately 40, Rockwell B scale data points, both within a segment and within a batch of segments, the standard deviation was $\pm$ 0.9% and the high to low hardness range was 2.7% of the mean. This is considered very consistent. In addition, we duplicated these results in a production manufacturing environment.

The current manual furnace control procedures are sufficient to produce prototype wheels for this program. We did a preliminary assessment of automated furnace control methodologies that may be implemented later during production.

Wheel Assembly Trials -- There are several design and manufacturing objectives that we successfully meet in the scale-up of large size experimental wheels by the segmented rim approach:

1) Segment Geometry -- The objective was to make the segments to near net shape to avoid laborious machining by grinding. The design required that the segments be prepared with exact inside curvature and side angles to match with the outside diameter of core, so that the segments can be butted together tightly;

2) Segment-Core Adhesion -- To select the proper type of cement that will bond the segments to the prefabricated core, and retain sufficient strength to hold segments against centrifugal force and shear force during grinding.

(1) For near net shape control, we achieved an exact curvature match between the outside diameter of the wheel core and the inside curvature of the as-fired segments. This eliminated the need for any ID grinding.

Due to the expansion and contraction of the metal bond with process temperatures, and surface condition requirements, minor finishing grinding will still be necessary. This is particularly true for the side angle and chord length control. The angle grinding fixture was prepared and we identified a suitable grinding wheel specification for this operation. Segmented wheel expertise developed for Norton Company vitrified bonded wheel products is being applied in support of this project.

(2) Several factors that can affect the ultimate wheel assembly operation were addressed. We reviewed properties of various cementing materials for joining the diamond section to the prefabricated core. Three candidate cements were considered. Building upon the experience of the Norton vitrified wheel R&D group, two of the three candidates, namely Cement A and B, were evaluated. Shear strength, burst strength, and thermal stability are the primary considerations for the final cement selection. In addition, the surface roughness and cleanness of segment and core surfaces were considered to be critical to the retained bonding strength between the two parts at the joint line.

For obtaining proper interface adhesion, the surface roughness of wheel core and segments were monitored. Significant attention was given to cleaning the surfaces of segments and core to obtain sufficient bonding strength between the two parts at the joint line.

Wheel Assembly Burst Tests -- Three partial wheel specimens were made for burst speed study, as shown in Figure 3. Either Cement A or B was used in fastening four segments on the wheel core. Table 1 gives the burst test results, and the estimated Norton rated maximum operation speed (MOS) for similar wheels of this design based on this burst speed data.

Table 1. Burst Test Results, Four Abrasive Segments per Wheel

Wheel No.	Cement	Burst Speed (m/s)	Estimated Norton Rated MOS (m/s)	No. of Broken Segments
1	A	262	148	3
2	B	219	124	1
3	B	202	115	1

The traces of broken segments remaining on the wheel cores indicated that all the broken segments had separations initiated from the edge of the segment. The separation likely created a large bending moment on the loose end of the segment at the high burst test speeds. The bending moment eventually led to the fracture through the segment. Therefore, it is anticipated that fully assembled wheels will yield even higher burst speeds since the segments will have support from adjacent segments, unlike these partial burst test wheels. We also believe that both types of adhesives can provide sufficient strength to achieve high grinding speeds desired for this project.

In most of the cases, the separations occurred partly at the core-cement interface and partly at the segment-cement interface. Figure 4 shows a typical fracture surface appearance

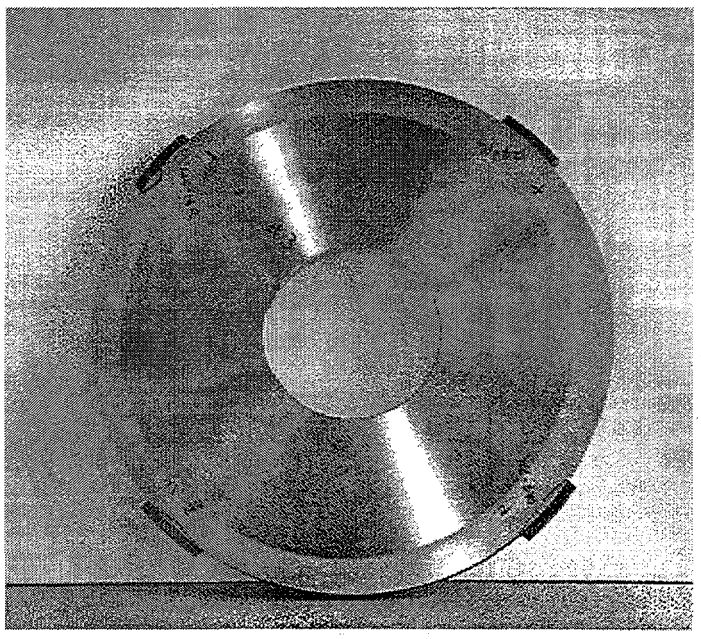

Figure 3. A preliminary burst testing wheel with four segments.

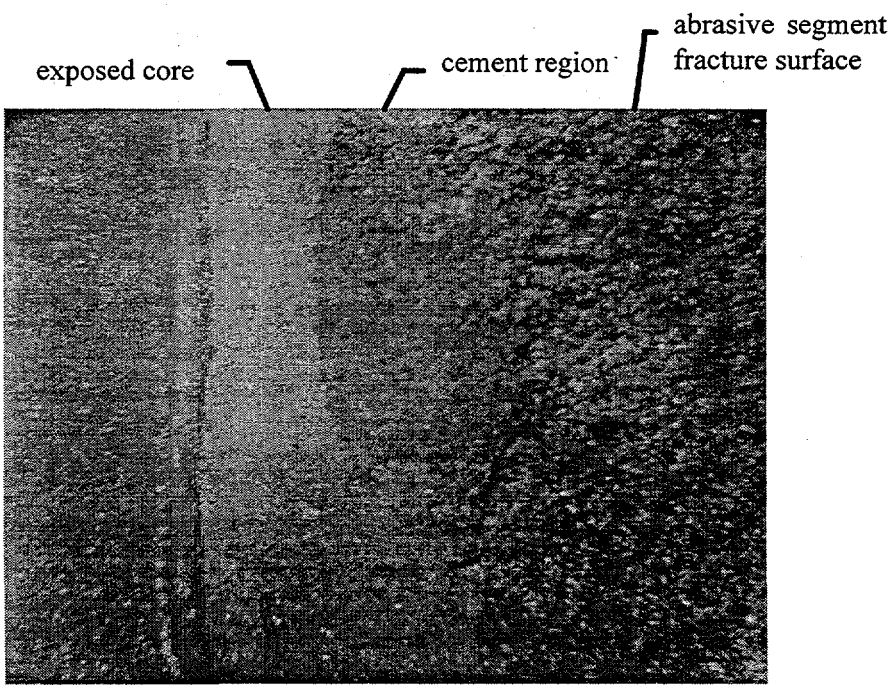

Figure 4. Typical fracture surface appearance when a segment broke off from the wheel core. The separation occurred partly at the core-cement interface and partly at segment-cement interface indicating successful interface preparation.

when one or more segments and core became separated. The fractography suggests that we have a successful surface preparation. These results also indicate that the joint line is the weakest region of the wheel. The only exception to the pattern in Figure 4 occurred for Wheel No. 1 (Table 1) where one of the three segments that broke off had separation primarily at the segment-cement interface. In this particular case, there was a clear sign of surface contamination on the ID surface of this segment prior to cementing.

During the course of adhesive strength study, we identified some manufacturability limitations in the properties of Cement A and decided to discontinue work on this cement and use only Cement B.

Full Size Test Wheel Manufacturing -- Three, 393-mm (15.5-in.) nominal diameter segmental wheels were made. Figures 5 and 6 show the first full size metal bonded segmental diamond wheel and a magnified view of a segmental rim section. These wheels will be used to run preliminary grinding test at the Norton Company Abrasives World Grinding Technology Center (WGTC) under Task 2. The three wheels were successfully speed tested to pass 120 m/s (23,622 ft/min.) peripheral speed.

The following is a summary of the manufacturing process validation trials performed during the successful manufacture of the three experimental full-size segmented wheels:

1) Temperature Control -- Furnace temperature characterization was completed.
2) Hot Press Run Profile -- Furnace run profile was re-tuned to improve the product quality and yield. When the process was transferred from R&D to production for pilot runs, some scatter in product properties were encountered. After some process modifications, the latest pilot production batch was very successful in achieving wheel properties within the tight control boundaries.
3) Segment Curvature Control -- Perfect curvature match was achieved, which eliminated the need for ID grinding on segments.
4) Angle Grinding for Butting Segment Faces -- Current process procedures and practices for grinding of segments to match one another were well defined. (See Figure 6 segment interfaces.) Operation efficiency can be further improved by making some adjustments in prior operational steps.
5) Wheel Assembly -- Procedures for segments and core surface preparation, and wheel assembly are well developed. To date, six wheels were assembled (three full wheels and three partial wheels) uniformly and without any manufacturing difficulties.

The objectives of Task 1 have been achieved. Scale-up of the Phase 1 wheel from 204 mm to 393 mm in diameter has been successfully accomplished. Note that the original project objectives were to scale-up the wheel to only 356 mm. Based on conservative speed tests, these test wheels have been qualified for grinding at speeds up to 80 m/s for the Task 2 in-house test. We expect to formally complete Task 1 by mid-October.

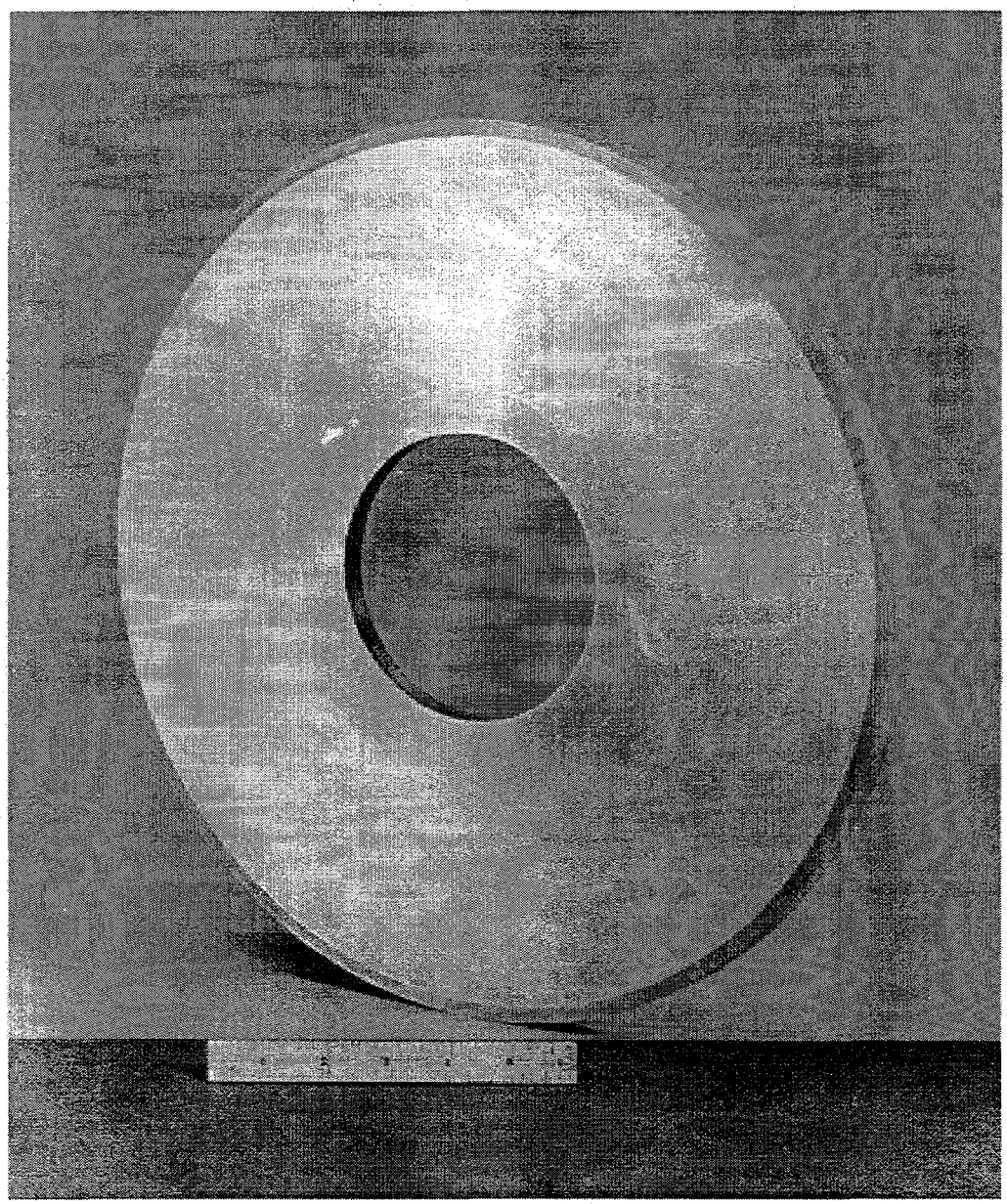

Figure 5. A full size segmental experimental metal bond wheel for the WGTC in-house grinding test. The nominal wheel size is 393 mm in diameter by 15 mm in thickness with 127 mm hole.

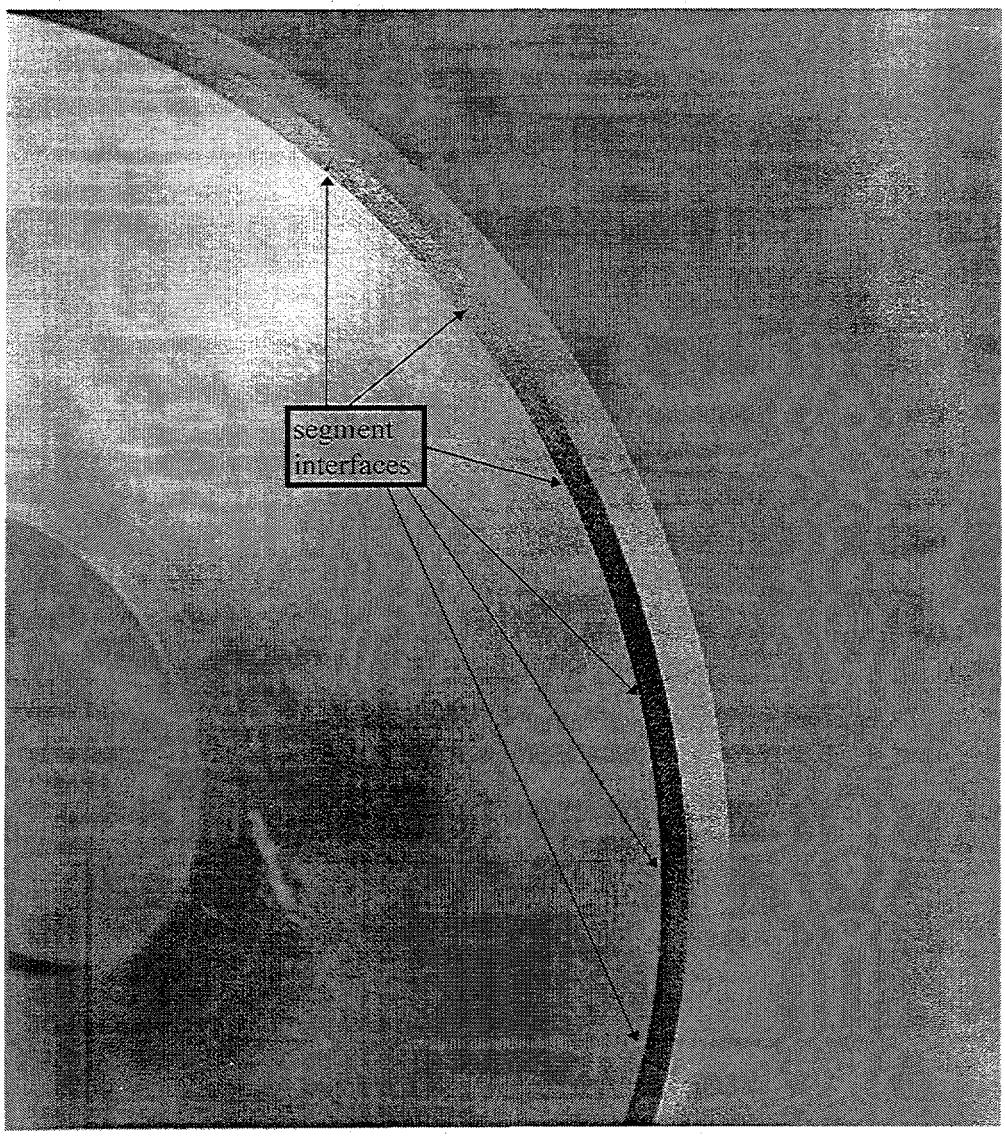

Figure 6. An enlarged view of the Figure 1 wheel to highlight the segmental rim of this experimental grinding wheel.

TASK 2: In-House Wheel Testing

Task 2.A: Ceramic Specimen Preparation

We are completing the last batch of ceramic rod specimens for this program. Approximately 200 ceramic rods are being finished for use in the Tasks 2 and 3 grinding tests. We selected Norton Advanced Ceramics' NT551 silicon nitride as the program's base material. NT551 is currently under development for diesel engine valves.

Three separate 15 kilogram powder batches were made of the NT551 silicon nitride powder composition. Each slurry batch was spray dried and the powder surface area was determined. Specimen rods were cold isostatically presses using a wet bag technique. A total of 209 green rods, (approximately 1.25 x 4 in.) and 2 tiles (2 x 2 in.) were made. All rods and tiles went through a binder burnout furnace followed by a high temperature gas pressure sinter cycle. The initial HIP run was completed and 20 rods (approximately 1 in. long x 3.5 in. diameter) were sent to the WGTC for the initial wheel tests. The remaining rods are being HIP'ed Norton Advanced Ceramics manufacturing plant in East Granby in October.

Materials characterization will be performed on the test tiles for each HIP run. These tests include room temperature 4-point flexure tests, Vicker's hardness and fracture toughness measurements.

Task 2.B. Preliminary Grinding Tests in WGTC

Three, 393-mm diameter experimental metal bonded segmental wheels were completed and successfully speed tested to 120 m/s. The wheels were delivered to the World Grinding Technology Center (WGTC) for grinding tests at 32 m/s and 80 m/s wheel speeds (6,300 and 15,750 surface feet per minute) using a Studer grinder. The in-house test is scheduled to start in October.

We plan to evaluate and select an optimized diamond concentration for the experimental bond in this in-house test. The best diamond concentration(s) will then be recommended for the proposed Task 3 independent validation tests.

The above test wheels will be re-profiled and burst tested after the preliminary in-house grinding test is completed. The burst speeds of these test wheels will be used to establish the target or anticipated MOS for the Task 3 validation test wheels.

TASK 3: Independent Validation Tests

Task 3.A. Selection of Sites and Wheel Specifications

Norton Company hosted a planning meeting with AlliedSignal Ceramic Components to finalize plans for the upcoming Task 3 validation tests. A similar meeting is scheduled at Norton with Eaton Manufacturing Technologies Center. The other scheduled validation test sites are Chand Kare Technical Ceramics and Norton Advanced Ceramics. The latter test is scheduled to be performed at the World Grinding Technology Center.

Status of Milestones

Task 1: Process Scale-Up

1.A. Experimental Design and Definition -- Completed

1.B. Strength Characterization and High Speed Core Development -- Completed

1.C. Manufacture and Characterization of Large Wheels -- In-Process. Will be completed in October (~1.5 months behind schedule)

Task 2: In-House Wheel Testing -- (~1.5 months behind schedule)

2.A. Ceramic Specimen Preparation -- In-Process. Will be completed in October

2.B. Preliminary Grinding Tests in WGTC -- Scheduled start in October

Task 3: Independent Validation Tests -- Scheduled start, December, 1996

Task 4: Ceramic Surface Integrity -- Scheduled start January, 1997.

Communications/Visits/Travel

R.H. Licht and P. Kuo to Oak Ridge, Cost-Effective Ceramic Machining (CECM) Annual Project Review and High Temperature Materials Lab (HTML) User Center, September 11-12, 1996.

James Blackmore, AlliedSignal Ceramic Components, during a visit to Norton Company Superabrasives, Worcester MA, reviewed ASCC planned independent validation test with Norton project personnel, October 4, 1996.

Publications/Presentations

R.H. Licht, P. Kuo (presenters) and S. Ramanath, "Development of a Next-Generation Grinding Wheel", presented at the Cost-Effective Ceramic Machining (CECM) Annual Project Review, Oak Ridge, September 11, 1996.

References

1. R.H. Licht, S. Ramanath, M. Simpson, E. Lilley, Innovative Grinding Wheel Design for Cost-Effective Machining of Advanced Ceramics, Phase I Final Report, Subcontract No. 87X-SM037V, published by Oak Ridge National Laboratory Ceramic Technology Project, Report Number ORNL/Sub/93-SM037/1, Publication date, Feb. 1996.

HIGH-SPEED, LOW-DAMAGE GRINDING OF ADVANCED CERAMICS

Joseph A. Kovach
Michael A. Laurich
Eaton Manufacturing Technologies Center
Willoughby Hills, Ohio 44094

Stephen Malkin
University of Massachusetts
Amherst, Mass. 01003

Objective/Scope

The overall objective of the **H**igh **S**peed **L**ow **D**amage (HSLD) grinding project is to develop a single step, roughing-finishing process suitable for producing high-quality advanced ceramic components at high material removal rates and at substantially lower cost than traditional, multi-stage grinding processes. Initial implications from Phase I have suggested that HSLD grinding of Si_3N_4 is technically feasible. Accordingly, to achieve the overall program objective, the Phase II effort is focused on:

1.0 Continued expansion of the HSLD science base

2.0 Further development of the enabling HSLD technologies required for successful implementation, and

3.0 Economic analysis of the HSLD production cost drivers.

Technical Progress

This semi-annual report summarizes technical progress achieved during the period from April 1, 1996 to September 30, 1996. The report describes activities at the University of Massachusetts and the Eaton Manufacturing Technologies Center. A technical overview is presented in the following areas:

1. Mechanisms of Material Removal
2. Hydrodynamic Forces in Grinding of Ceramics
3. Temperature Measurements and Energy Partition

1.0 Mechanisms of Material Removal

Scratched Surface Parameter

During this period, much of the effort was focused on testing the scratching energy model which included measuring forces and energies for grinding over a wide range of conditions. Four different ceramics and one glass were evaluated:

1. HPSN - Norton NC132
2. HPSN - Kyocera SN220
3. SiC - Carborundum, Hexaloy
4. SiC - Norton
5. Soda Lime Glass

Using a 180 grit resin bond wheel (DN180-N100B-1/4), three grinding parameters were varied: depth of cut, workspeed, and wheel velocity. The maximum depth of cut was increased to 76 μm, about twice that as with the 400 grit size wheel used previously. All grinding tests were carried out with a 5% solution of soluble oil applied at about 300 cm^3/s.

The measured power was found to correlate well with the scratched surface parameter. It was also found that the power increased linearly with the scratched surface parameter, except near the origin. Assuming that the total grinding energy is only associated with scratching (plowing), the slopes (in units of J/m^2) would correspond to the average energy per unit area of scratched surface generated. These slopes are listed in Table 1 together with the corresponding fracture surface energy estimated as $G_c/2$ ($G_c=K_c^2/E$). The slopes are much larger than the corresponding fracture surface energies for all materials investigated. Because the slopes are much higher than the fracture surface energies, it can be concluded that most of the material is removed via ductile flow.

	Slope (J/m^2)	Fracture Surface Energy (J/m^2) $G_c/2$
HPSN - Norton NC132	12,500	40
HPSN - Kyocera SN220	11,200	60
SiC - Carborundum, Hexaloy	8,400	26
SiC - Norton	7,600	
Soda Lime Glass	1,500	4.0

Table 1. Comparison between the values of slope and corresponding fracture surface energy.

SEM Observations of Grinding Debris, Ground Surface and Subsurface

Using the same grinding conditions associated with the scratching energy model tests, the ground and fractured surfaces of the ceramic and glass workpieces and grinding debris were analyzed with scanning electron microscopy.

Microscopic observations of ground surfaces show characteristic scratches along the grinding direction generated mainly by ductile flow. After etching with hydrofluoric acid, most of the striations on the ground silicon nitride surface were removed, which indicates a glassy layer. Additional observations to investigate the subsurface deformation were made using a fracture method. The subsurface deformation observed using the SEM under higher magnification showed a deformed layer typically 1~2 μm thick. On silicon nitride, this layer persisted after etching, implying that the microstructure of this layer is polycrystalline. Observations of the grinding debris collected for the ceramics, however, indicated that the chips were formed mainly by brittle fracture.

2.0 Hydrodynamic Forces in Grinding of Ceramics

An important consideration when utilizing high wheel speeds is the potential generation of hydrodynamic forces. This phenomenon primarily arises when using non-porous wheels which can "sustain" relatively high fluid film pressures. The following three different diamond wheels were evaluated using Safety Cool 612 (at 10:1) supplied to the workzone at 30 psi and 6 GPM:

1) 180 grit vitrified bond (D91-KZ125-VFR)
2) 180 grit resin bond (D180-100-UI841)
3) 320 grit resin bond (D320-100-UI841)

As shown in Table 2 and Figure 1, the 320 grit resin wheel produced the largest hydrodynamic force. Conversely, as the grit size is increased (i.e. by switching to a 180 grit wheel) the hydrodynamic force is reduced. When a porous vitrified wheel is used, the hydrodynamic force behavior can be considerably different. Hydrodynamic forces generated with the 180 grit vitrified wheel increase (although less than with the resin wheels) as wheel speed is increased from 5,000 to approximately 15,000 ft/min. However, as wheel speed is further increased, the magnitude of the hydrodynamic force is actually reduced.

3.0 Thermal Analysis and Temperature Measurements

Tests over the past several months have focused on measuring grinding zone temperatures and calculating the energy partition. Recall that the energy partition is the fraction of the total grinding energy which actually enters the workpiece as heat. To date, high speed temperature and energy partition measurements have now been made for the following wheels:

1. 180 grit vitrified bond (D91-KZ125-VFR)
2. 180 grit resin bond (D180-100-UI841)
3. 320 grit resin bond (D320-100-UI841)

Normal and tangential forces, power, and grinding zone temperature were all measured in-process for wheel speeds ranging from 5,000 to 25,000 ft/min (data summarized in Table 3). The material removal rate was held constant with the workpiece velocity at 100 in/min and depth of cut equal to 0.010 inches. Safety Cool 612 coolant at a 10:1 dilution ratio was supplied to the grinding zone at 30 psi and 6 GPM. Prior to each test, the wheel was dressed with a titanium roll dresser followed by conditioning with a 220 grit Al_2O_3 stick . The tests were randomly conducted using two replications per condition.

Figure 2 shows a plot of the normal force as a function of wheel speed for each of the three wheels. Moreover, for comparison purposes, data generated with the 120 grit plated wheel used in the HSLD Phase I feasibility study is also provided. Note that with the plated wheel, the normal force drops as wheel speed is increased. The bonded wheels behave similarly, to a point. At speeds above 15,000 ft/min, the normal forces developed with the resin and vitrified bonded wheels start to increase.

This increase in normal force for the resin wheels is probably associated with thermal softening of the bond. While the wheel manufacturer claimed that this was a high temperature resin (polyimide), the bond softened and required a higher normal force to achieve grit penetration into the workpiece.

As for the vitrified wheel, the bond should not be as sensitive to thermal softening. While it is possible that the glassy bond could become somewhat viscous and start to flow, two other possibilities could explain the increase in normal force as wheel speed is increased above 15,000 ft/min. First, as the wheel spins faster, it acts harder due to the generation of internal stresses proportional to the square of the rotational speed. During dressing, wheel manufacturers often suggest slowing down the wheel speed to make it behave one or two grades softer. Alternatively, it may be possible that the pumping action of the porous wheel at high speeds removed too much coolant from the workzone resulting in localized fluid starvation. This, in turn, could reduce cutting efficiency resulting in a higher normal force.

Plotted in Figure 3 are the tangential forces as a function of wheel speed for the three bonded wheels and the previously used 120 grit plated wheel. In this case, the tangential force is reduced with increasing wheel speed for all wheels, as expected.

Figure 4 shows the surface temperature of the S/RBSN workpiece as a function of wheel speed for the three bonded wheels. As wheel speed is initially increased, the temperature **decreases**. However, temperature for each of the

resin wheels only decreases to a point and then starts to increase with increasing wheel speed. Temperatures associated with the vitrified wheel decrease continuously for increasing wheel speeds over the range tested (5,000 to 20,000 ft/min). Also note that the surface temperatures are much lower than expected. Temperatures measured range from 200 to 500°F, while earlier estimates assumed that the temperature would be three to five times higher.

Why are the surface temperatures so ***low*** and why do they ***decrease*** with increasing wheel speed? As can be seen in Figure 5, the energy partition (percent of the total energy entering the workpiece as heat) for each of the wheels decreases as wheel speed is increased - meaning that the wheel is removing more heat from the workzone as wheel speed is increased.

From Figure 6, it is important to observe the "competing processes" in action here - - - While the specific energy increases with higher wheel speeds, the energy partition decreases sufficiently, thereby resulting in a nearly constant or reduced workpiece surface temperature.

Given the above workpiece temperature behavior (i.e. low surface temperatures which further decrease with increasing wheel speed) a brief discussion on "bulk" versus "flash" temperatures is mandated. Most heat transfer calculations for grinding have been historically developed for steel grinding applications - - - where the thermal grinding "damage" arises from **bulk** time/temperature effects, *not* from the localized flash temperatures at each grit/workpiece interface. However, based on the data presented above, it appears that although the gross surface temperatures may be low, the localized flash temperatures at each diamond grit can still be very high and must not be neglected. Additional investigation is required to fully understand the thermal/mechanical attributes of HSLD grinding of ceramics.

320 Grit Wheel Workpiece Surface Fragmentation Analysis

Using quantitative metalographic techniques, the percent surface fragmentation for three locations along a S/RBSN specimen was measured. Wheel speed for the 320 grit resin wheel was varied from 5,000 to 25,000 ft/min while the material removal rate was kept constant (V_w = 100 in/min, d = 0.010 in). The surface fragmentation values are summarized in Table 4 and presented in Figure 7.

Figure 7 shows the average degree of fragmentation achieved as a function of wheel speed. Note that the **lowest** fragmentation level was achieved at the **highest** wheel speed, 25,000 ft/min. The actual value or severity of the surface fragmentation may be somewhat overestimated however, due to the abundance of porosity in the workpiece. Because it is difficult to distinguish between pure "pull-out" and porosity, all surface defects have been included. Analysis of the same material ground under "ideal no damage" conditions (as in preparation for

MOR bar tests) indicates that the surface may contain between 10.5 and 17% porosity.

Status of Milestones

Program is back on schedule based on a no-cost extension through the end of March, 1997.

Milestone	Description	Completion Date
153203	Develop a two-color precision pyrometry system to accurately measure ceramic grinding zone temperatures.	Completed
153204	Using grinding zone temperature data, determine the thermal balance between the wheel and the workpiece under HSLD grinding conditions.	Completed
153205	Develop and report methods for dressing and conditioning of grinding wheels specifically intended for use in the HSLD grinding process.	Completed
153206	Conduct economic sensitivity analyses of the HSLD production cost drivers. Assess tradeoffs between cost and resulting quality under a wide range of operating conditions.	March 1997

Communications/Visits/Travel

1) The paper "Analysis of Hydrodynamic Forces in Grinding" was presented by S. Malkin at the NAMRC Conference in Ann Arbor, Michigan, May 21-23.

2) The paper "Development of Advanced Grinding Technology for Structural Ceramics" was presented by J. Kovach at the NAMRC Conference in Ann Arbor, Michigan, May 21-23.

3) J. Kovach, M. Laurich, S. Malkin participated in the Cost Effective Ceramic Machining Annual Project Review, Oak Ridge, TN September 11-12, 1996.

4) The paper, 'Development of Advanced Grinding Technology for Structural Ceramics' was presented by M. Laurich at the SME Advancements in the Application of Ceramics in Manufacturing conference in Newton, MA, October 22-23, 1996.

Problems Encountered - None

Publications

1) S. Malkin and T. W. Hwang, "Grinding Mechanisms for Ceramics", Annals of the CIRP, Vol. 45/2, 1996, Keynote Paper to appear and to be presented at CIRP General Assembly, Como, Italy, August 1996.

2) M. Ganesan, C. Guo, A. Ronen, and S. Malkin, "Analysis of Hydrodynamic Forces in Grinding", Trans. of the NAMRC/SME, Vol. 24, 1996, pp. 105-110.

3) J. Kovach, M. Laurich, K. Ziegler, et al., "Development of Advanced Grinding Technology for Structural Ceramics", Technical Papers of the NAMRC/SME, 1996, pp. 51 - 56.

4) A Ph.D. dissertation, entitled "Thermal Aspects of Ceramic Grinding", has been completed by Jonathan Bo Zhu at the University of Massachusetts. Note that as of May 28, Dr. Zhu became a full-time Eaton employee at the Manufacturing Technologies Center.

5) J. Kovach, M. Laurich, K. Ziegler, et al., "Development of Advanced Grinding Technology for Structural Ceramics", Proceedings for the SME Advancements in the Application of Ceramics in Manufacturing conference in Newton, MA, October 22-23, 1996.

Wheel Speed (ft/min)	Normalized Hydrodynamic Force 180 grit vitrified (lb/in)	180 grit resin (lb/in)	320 grit resin (lb/in)
5,000	3.5	11.6	14.0
10,000	7.5	17.3	23.1
15,000	8.7	24.6	39.9
20,000	5.2	18.8	59.7
24,000	3.9		
25,000		24.6	81.9

Table 2. Hydrodynamic forces for three wheel types.

180 grit vitrified bond

Wheel Speed (ft/min)	Normal Force (lb)	Tangential Force (lb)	Power (hp)	Specific Energy (in-lb/in³)	Surface Finish (R_a, µinch)	Surface Temperature (°F)	Energy Partition
5,000	80.7	27.3	4.9	4,734,104	33	259	4.7%
10,000	53.8	12.9	4.3	4,473,988	30	239	6.2%
15,000	54.2	11.2	5.2	5,826,590	22	209	4.7%
20,000	70.4	12.5	7.6	8,670,520	22	205	3.3%

180 grit resin bond

Wheel Speed (ft/min)	Normal Force (lb)	Tangential Force (lb)	Power (hp)	Specific Energy (in-lb/in³)	Surface Finish (R_a, µinch)	Surface Temperature (°F)	Energy Partition
5,000	98.0	13.6	3.8	2,356,522	28	448	11.6%
10,000	71.4	7.1	4.0	2,469,565	29	358	9.6%
15,000	69.6	4.4	4.2	2,269,565	28	306	8.0%
20,000	83.5	5.3	6.3	3,652,174	28	339	5.9%
25,000	96.0	5.4	7.2	4,652,174	27	328	5.0%

320 grit resin bond

Wheel Speed (ft/min)	Normal Force (lb)	Tangential Force (lb)	Power (hp)	Specific Energy (in-lb/in³)	Surface Finish (R_a, µinch)	Surface Temperature (°F)	Energy Partition
5,000	130.5	32.3	5.0	5,623,188	23	491	10.2%
10,000	71.6	15.0	4.4	5,204,522	17	230	5.3%
15,000	105.4	12.2	5.2	6,384,870	16	230	4.4%
20,000	103.0	9.8	5.7	6,782,609	19	323	5.4%
25,000	145.1	8.9	7.8	7,728,696	21	392	4.9%

120 grit plated

Wheel Speed (ft/min)	Normal Force (lb)	Tangential Force (lb)
5,000	124	34
15,000	85	11
25,000	63	11

Table 3. Data summary for high speed grinding tests on S/RBSN.

HSLD Grinding Data Summary
320 grit diamond resin (polyimide) bond wheel

Wheel Speed (ft/min)	Surface Fragmentation Location 1 (%)	Location 2 (%)	Location 3 (%)	Average (%)
5,000	12	20	15	16
5,000	14	13	24	17
5,000	15	23	18	19
10,000	31	23	10	21
10,000	17	13	24	18
15,000	15	11	26	17
15,000	16	14	19	16
15,000	23	27	20	23
20,000	31	31	18	27
20,000	21	16	18	18
20,000	21	21	14	19
25,000	16	14	11	14
25,000	13	18	18	16

Table 4. Grinding data summary for 320 grit resin bond wheel including surface fragmentation data.

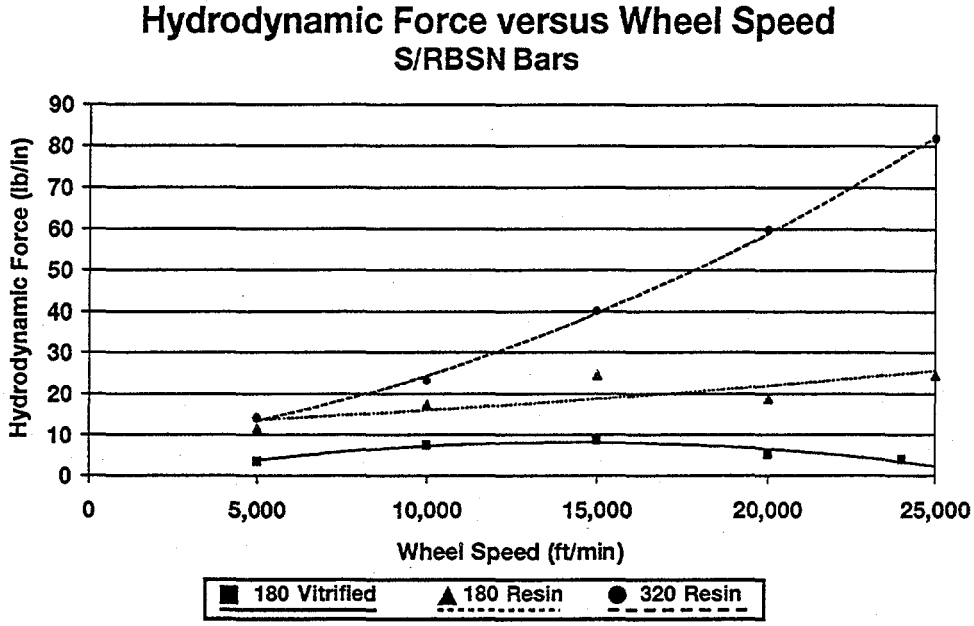

Figure 1. Hydrodynamic forces generated versus wheel speed.

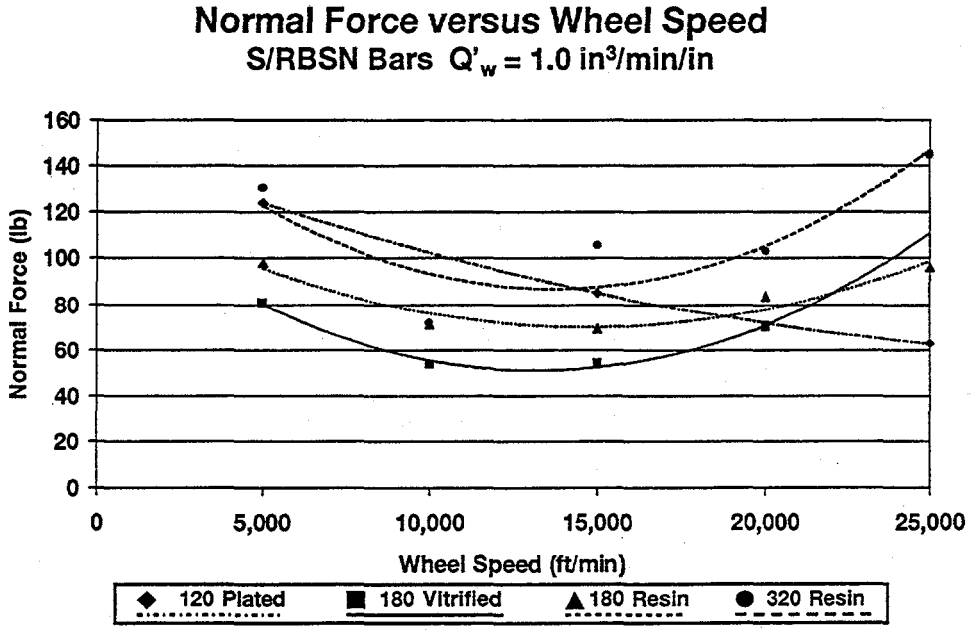

Figure 2. Normal force versus wheel speed.

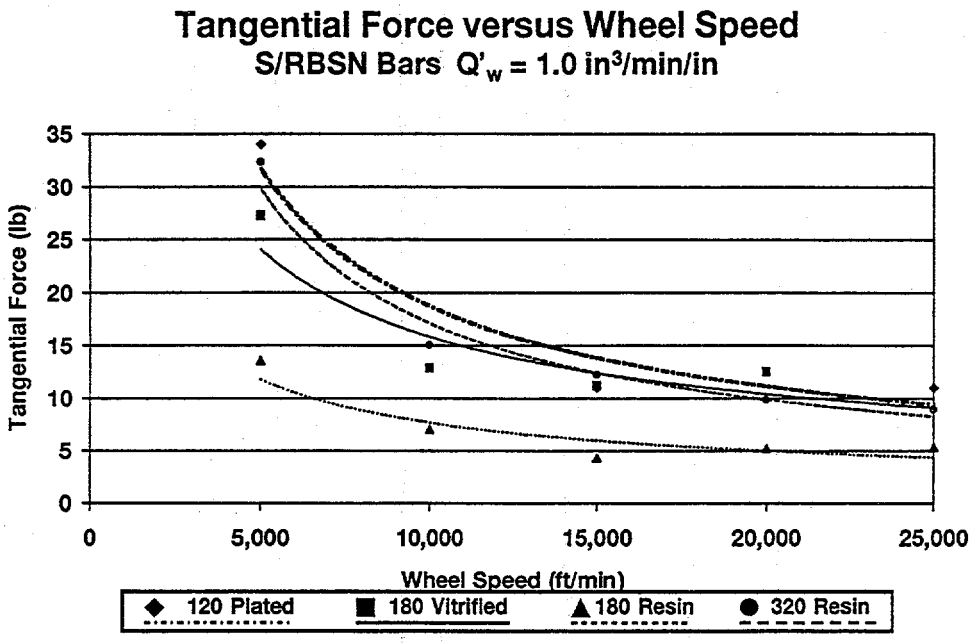

Figure 3. Tangential force versus wheel speed.

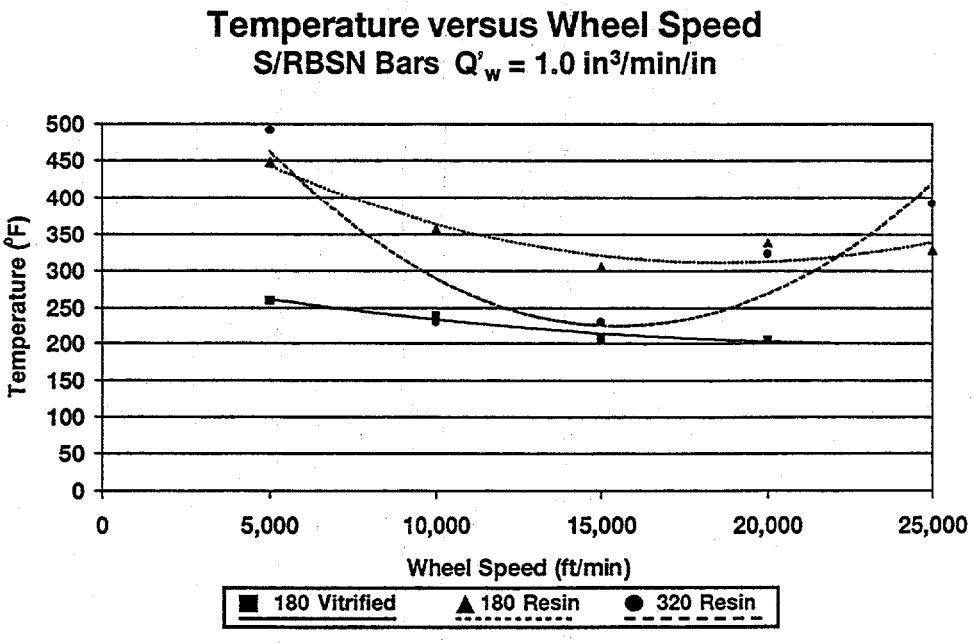

Figure 4. Surface temperature versus wheel speed.

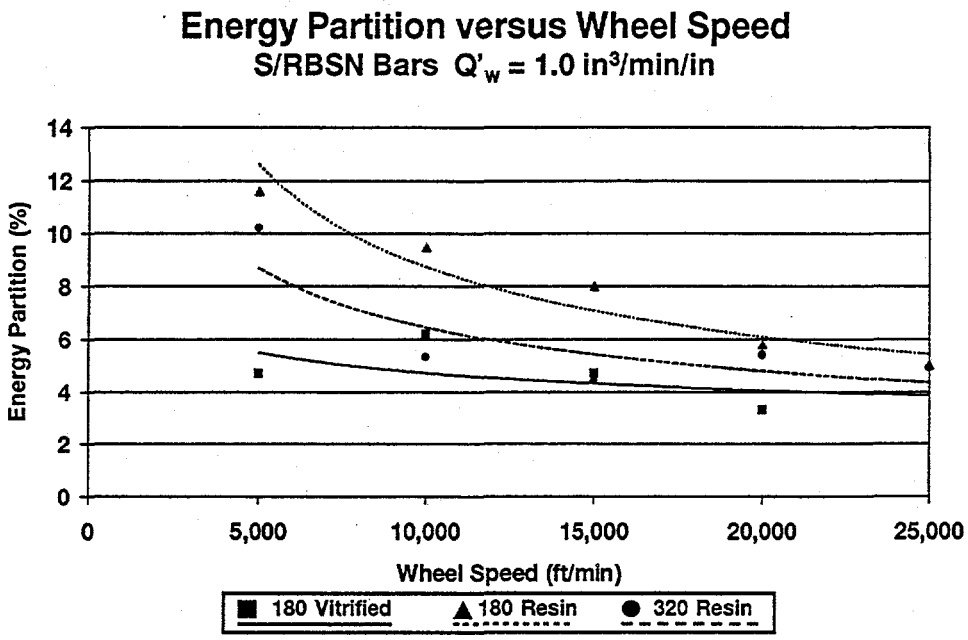

Figure 5. Energy partition versus wheel speed.

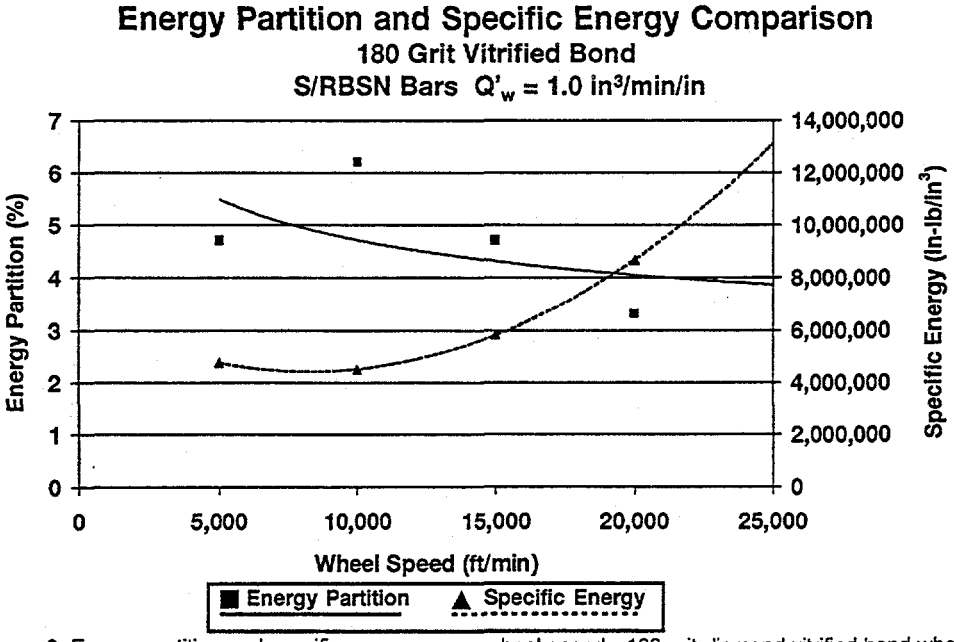

Figure 6. Energy partition and specific energy versus wheel speed - 180 grit diamond vitrified bond wheel.

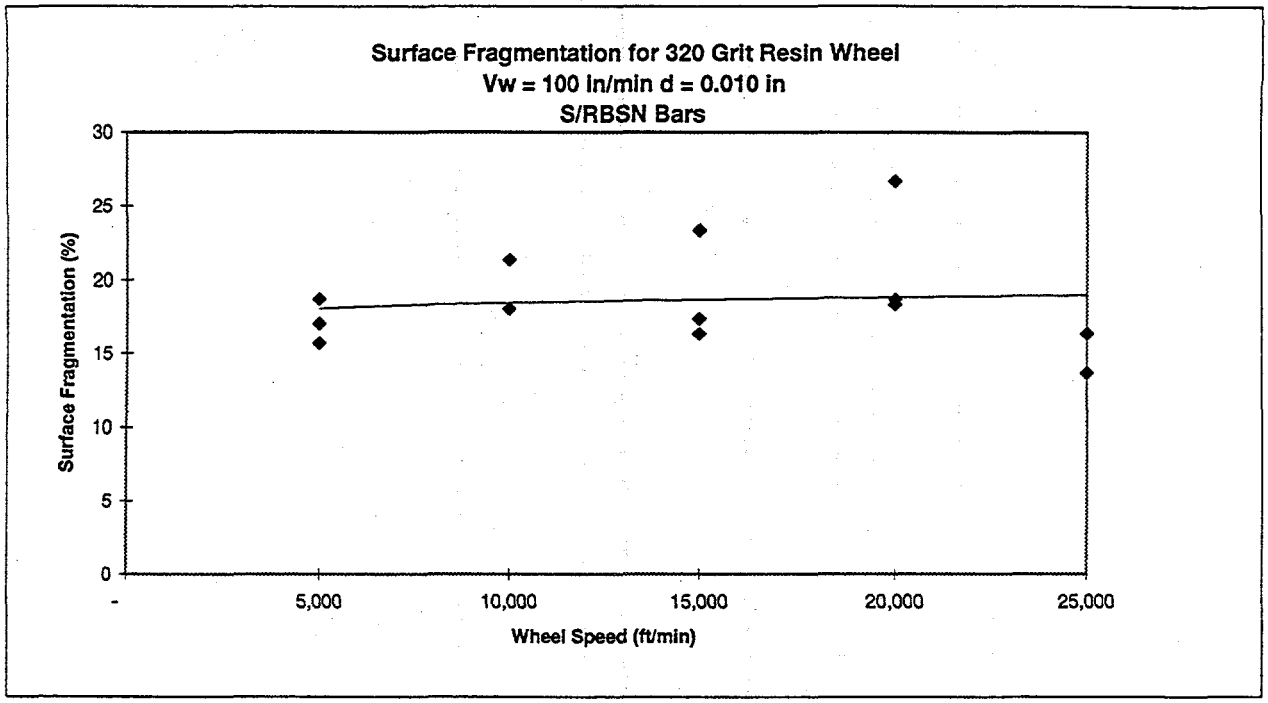

Figure 7. Surface fragmentation as a function of wheel speed (320 grit resin wheel).

Chemically Assisted Machining of Ceramics

R.S.Gates, Y.Wang, and S.M.Hsu
(National Institute of Standards and Technology)

Objective/Scope

The ceramics industry has identified the lack of a rapid low cost ceramic machining technology as a major barrier for widespread use of ceramics. Current machining technology is slow and labor intensive. Residual surface damage is a primary concern. This project aims to increase the machining rate of ceramics by using chemical reactions at the interface. The chemical reactions at the interface produce a reaction layer that may function in several ways. It may behave as a lubricating layer, barrier film, passive protective film reducing the wear of the diamond, or it may reduce the contact stresses, therefore minimizing the surface damage. Si_3N_4 is the main material of focus.

The project involves several subtasks including:

1. Develop a bench test simulation to allow screening of chemistries under well-controlled conditions.
2. Identify new chemistries that can significantly improve the machining rate of ceramics, especially for silicon nitrides.
3. Provide understanding on the working mechanisms of the chemistries identified and develop correlations with the surface quality of the machined surface.
4. Establish limits of performance and applicability of the chemistry on different material compositions and processes. Establish optimum machining conditions for each chemistry/material combination.
5. Examine the environmental impact of the chemistry and work with industrial partners to optimize the chemistry and validate the concepts and methodology in industrial practice.

Technical Highlights

Previously, we reported the results of diamond grinding tests on silicon nitride using a surface grinder. A chemistry was discovered that has high grinding efficiency on silicon nitride. This coolant was blended and shipped to a Kennametal plant in North Carolina for testing in an actual automated production grinding machine. In this period, we describe the results of the field trial after five months of continuous operation.

At the same time, grinding maps have been developed to show the performance of a particular diamond wheel-sample-coolant combination under different operating conditions.

Kennametal Plant Trial of NIST Coolant

A 100-gallon sample of the NIST experimental coolant was blended and shipped to a Kennametal plant in North Carolina for testing in an automated production grinding machine. Kennametal decided to conduct the plant trial of the NIST coolant on cemented tungsten carbide insert materials. Since the cemented tungsten carbide represents the bulk of their operations, a successful demonstration of our coolant would yield the highest economic impact for them.

The industrial grinder used for this trial was a specially designed, computer controlled, enclosed, robotic apparatus capable of grinding inserts at a rate of more than a thousand pieces a day. The details of the operation were described in the previous semi-annual report.

Over a period of five months, from March 1996 to August 1996, 170,000 inserts were successfully ground using the experimental fluid. Reject rates for parts were less than 0.8%, despite attempts to push the coolant to its operating limits. The most dramatic effect of the experimental coolant was to increase the number of inserts that could be ground before dressing of the diamond grinding wheel becomes necessary. The commercial coolant is usually dressed after 30 to 40 inserts have been ground. The experimental NIST coolant was capable of grinding over 500 inserts per dressing cycle.

During the course of the trial, the number of tungsten carbide inserts ground per dressing cycle was observed to gradually decreased from 500 less than 100 inserts per cycle. Careful analysis of the used sample of coolant indicated that one of the components of the coolant, present initially at only 2% (w), had degraded. A concentrated sample of the component was blended and sent to Kennametal to see if the performance could be boosted back up to previous levels. After blending the concentrate into the existing fluid, the number of inserts per dressing cycle was boosted back to 200 inserts per cycle without incident. It may have been possible to go back to the original 500 inserts per cycle; however, other operational considerations prevented the attempt. The components for a second large batch of experimental coolant have been ordered and will be blended for future collaborative efforts.

Ceramic Grinding Maps

We have been investigating the effect of different operating conditions on grinding of silicon nitride using both commercial and experimental (NIST) coolants. Previously, we demonstrated the benefits of the experimental grinding fluid in enhancing the grinding rate under a single set of grinding conditions in order to optimize the formulation of the experimental fluid. In the past six months, we have expanded testing to include different test severities and different grit size diamond grinding wheels. Further refinement of data analysis procedures have also resulted in development of terms to more clearly describe the performance of the grinding operation.

The most striking attribute of our grinding tests has been the observation of degradation in grinding performance with time with the commercial grinding coolant. This is commonly

observed in a very qualitative way with any grinding operation and is the prime motivation for re-dressing of diamond wheels. In order to be more quantitative, we have calculated a retained grinding efficiency (RGE) for diamond grinding of silicon nitride. This term more clearly demonstrates the performance loss during grinding operations. The loss in grinding efficiency can be attributed to the dulling of the diamond by chemical reactions.

The retained grinding efficiency is calculated from the surface grinder data as demonstrated in Figure 1 for a commercial coolant. By taking the slope of the displacement curve in Figure 1, at the beginning and end of the test, we can calculate the instantaneous grinding rate for that portion of the test. The percent retained diamond grinding efficiency at the end of the test is determined by taking the difference in final and initial grinding rates and normalizing to the initial rate as shown below:

$$\textit{Retained Grinding Efficiency} = 100 - \frac{R_{final} - R_{initial}}{R_{initial}} * 100 \qquad \textbf{(1)}$$

A value of 100% indicates that the grinding rate is the same at the end of the test as the beginning. A value of 0% indicates that the grinding rate dropped to zero at the end of the test.

Data from the surface grinder tests indicates that the major difference between the commercial coolant and the NIST experimental grinding coolant lies in the drop in retained grinding efficiency during a test (Figure 2). Using an 80 grit diamond wheel and a 2 kg feed load, the commercial coolant retains approximately 50% to 70% retained grinding efficiency for small depth of cut (<0.8 mm) in which less than 300 mm^3 total silicon nitride material is removed. As the depth of cut is increased, there are two effects on the grinding conditions: lower feed pressures, and higher total silicon nitride material removed during the test. At a depth of cut of 1.0 mm, almost 400 mm^3 of silicon nitride material is removed by the end of the test. At this point in the testing, the diamond has become dull and a transfer film has been produced on the grinding wheel. As a result, retained grinding efficiency has dropped to near zero. At higher depths of cut, the diamond grinding wheel actually fails to grind further into the sample and the grinding rate drops to zero. The NIST experimental coolant does not display this kind of decay in grinding efficiency. The retained grinding efficiency stays in the region of 50% to 80% throughout the test series. Similar results were observed at higher feed load of 5 kg. In this case, the decay in the performance of the commercial fluid takes place at a depth of cut of 2.0 mm.

A comparison of commercial and experimental coolant performance at 80 grit and 400 grit for 2 kg feed load is provided in Figure 3. The commercial coolant (triangle symbols) shows loss of grinding efficiency to zero in both cases. With smaller diamonds (400 grit) the loss is very rapid, occurring at only 0.4 mm depth of cut. This is expected since the diamond dulling process observed with the commercial coolant should have a more pronounced effect on smaller diamond grains. The NIST coolant does not experience much of a change in retained grinding efficiency with the 80 grit diamond. The smaller 400 grit diamond does display some reduction in grinding efficiency at depth of cut of 0.8 mm. Grinding efficiency has dropped to 20% to 30%.

During this period, we have further refined the process of data analysis to provide calculation of instantaneous grinding rates throughout each grinding test. Using data from a series of tests conducted with different depth of cut for a grinding wheel allowed us to develop three dimensional grinding maps to clearly identify regions of operation where maximum grinding rates can be achieved.

One critical element of grinding map generation is the calculation of the instantaneous grinding rate for all times during a test. This is accomplished through a mathematical treatment of the original raw data of sample displacement as a function of time generated from the surface grinder tests. The process is demonstrated for a single experiment conducted using a commercial coolant, an 80 grit diamond wheel, and a depth of cut of 0.8mm and a feed load of 20 N (Figure 4). First, for each overlap, there are regions of grinding in which steady-state grinding conditions do not exist. Within the steady-state condition region, one can estimate the grinding rate at any point in time by taking the slope of the displacement versus time curve and multiplying by the cross sectional area of contact (width of wheel x depth of cut). This can be achieved for all points in our curve by fitting the data to an expression and taking the derivative of the expression to provide a new expression of instantaneous grinding rate versus time.

The raw data for the steady-state region is fitted to a mathematical expression:

$$y = f(t) = a(1-e^{-bt}) + C \qquad \textbf{(2)}$$

where t is the time in seconds and y is the displacement in mm. The instantaneous grinding rate is obtained from the derivative:

$$Grinding\ Rate = \frac{dy}{dt} * X_{area} = (abe^{-bt}) * X_{area} \qquad \textbf{(3)}$$

and is in mm^3/s. By developing expressions for each run at different depth of cut, we can generate multiple curves for each grinding wheel-sample-coolant combination. Multiple curves can be combined to provide a grinding map of grinding rate versus time and depth of cut.

The three dimensional grinding map shown in Figure 5 for the commercial coolant demonstrates the concept. It clearly shows the strong effect of grinding time resulting in a decrease in grinding rate as the test progresses. A secondary effect is also observed for large depth of cut in which the grinding rates have dropped to zero for the longest test durations. In comparison, the NIST experimental grinding coolant (Figure 6) has a very flat response to both time and depth of cut. High grinding rates are maintained throughout the tests.

The grinding map concept can also be applied to the normal force data. By combining data from different runs at different depth of cut, we can generate a map of normal force as a function of both time and depth of cut. Figure 7 shows that the commercial coolant has a distinctive increase in normal grinding force with time that is associated with the reduced grinding rates. It is due to the dulling of the diamond that takes place with this coolant in these tests. The NIST coolant (Figure 8) does not show any variation of normal grinding force with time or depth of cut. Normal grinding forces are consistently low throughout the tests.

Status of Milestones

On schedule

Communications/Visits/Travel

Three visitors from Insaco Inc. came to NIST in October to discuss possible collaborations in evaluating the experimental NIST coolant in ceramic grinding operations.

Three visitors from Kennametal Inc. came to NIST in October to discuss further collaborations in diamond grinding of ceramics.

Problems Encountered

None

Publications

None

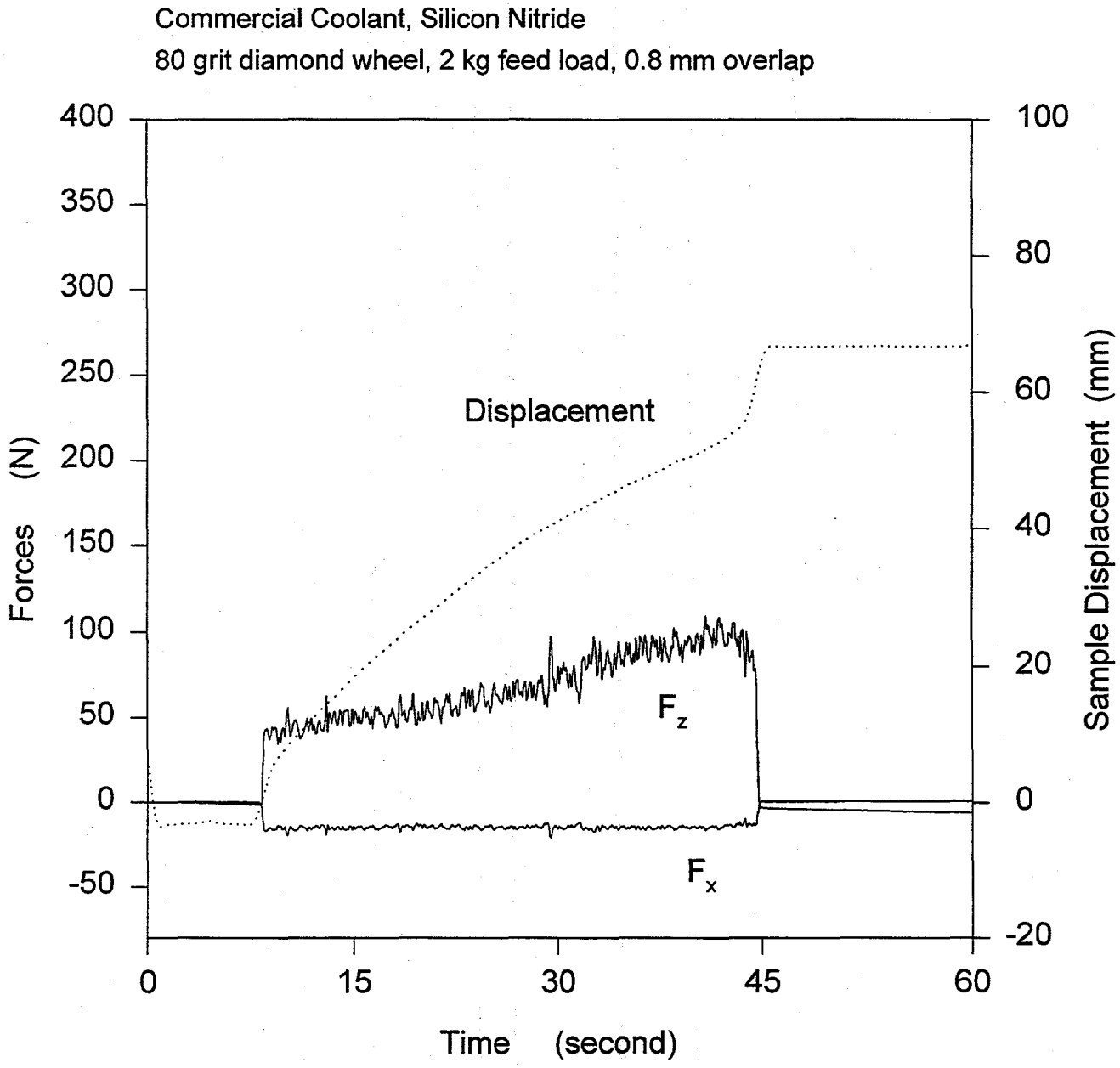

Figure 1. Raw data collected from NIST-instrumented surface grinder.

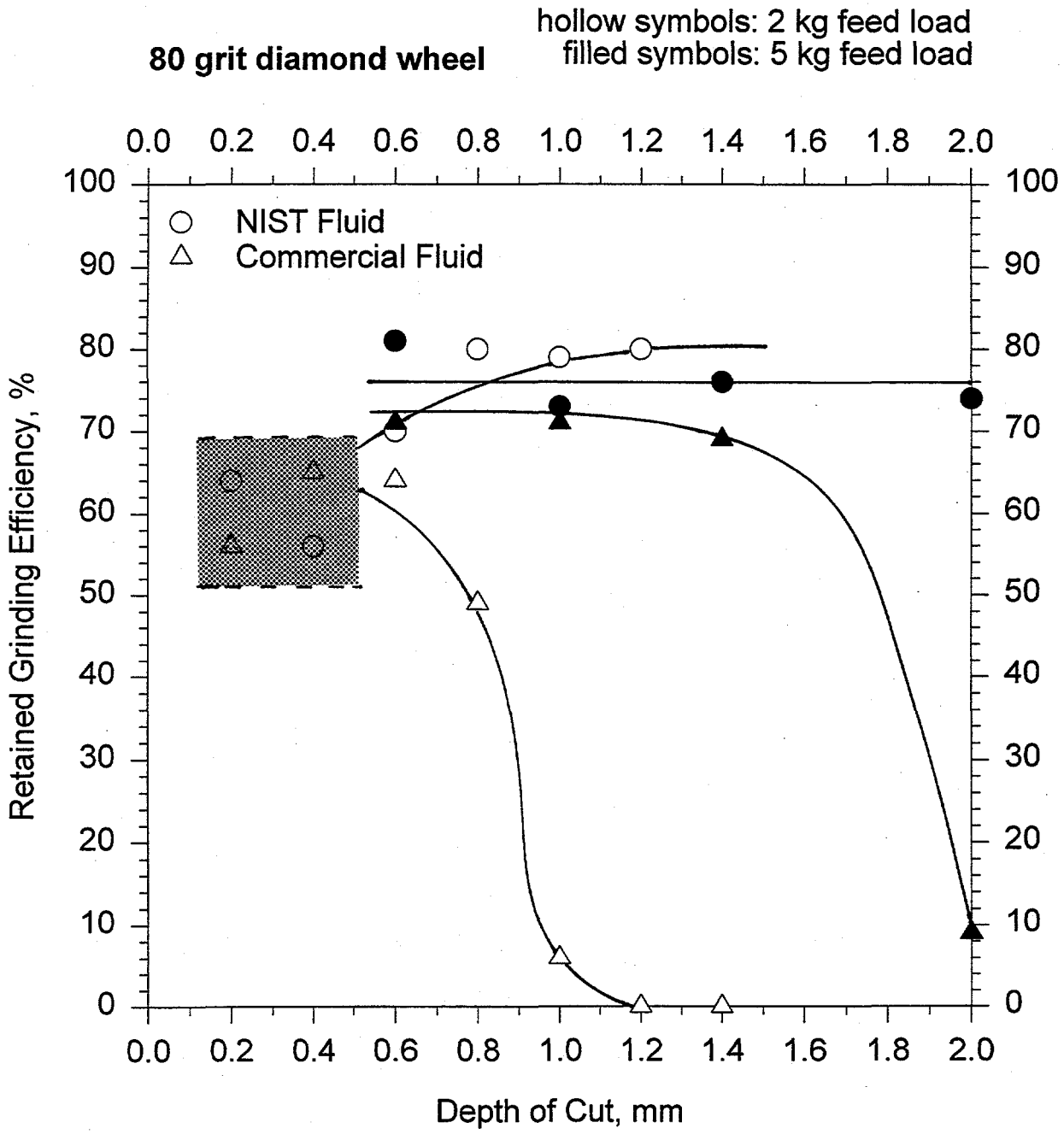

Figure 2. Comparison of retained grinding efficiency of grinding coolants with 80 grit Diamond wheel at different feed loads.

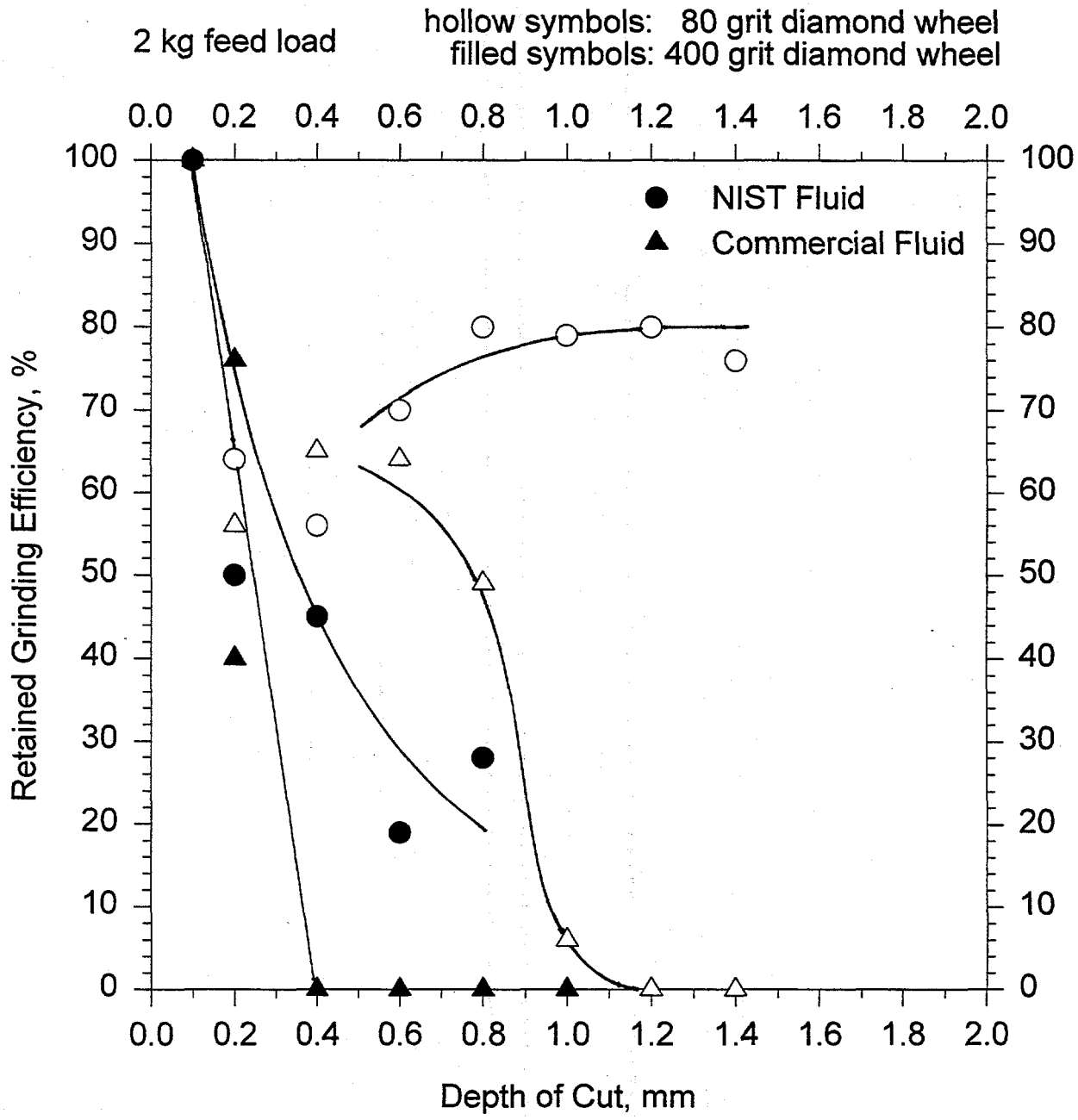

Figure 3. Comparison of retained grinding efficiency of grinding coolants with different Diamond grit wheels and 2 kg feed load.

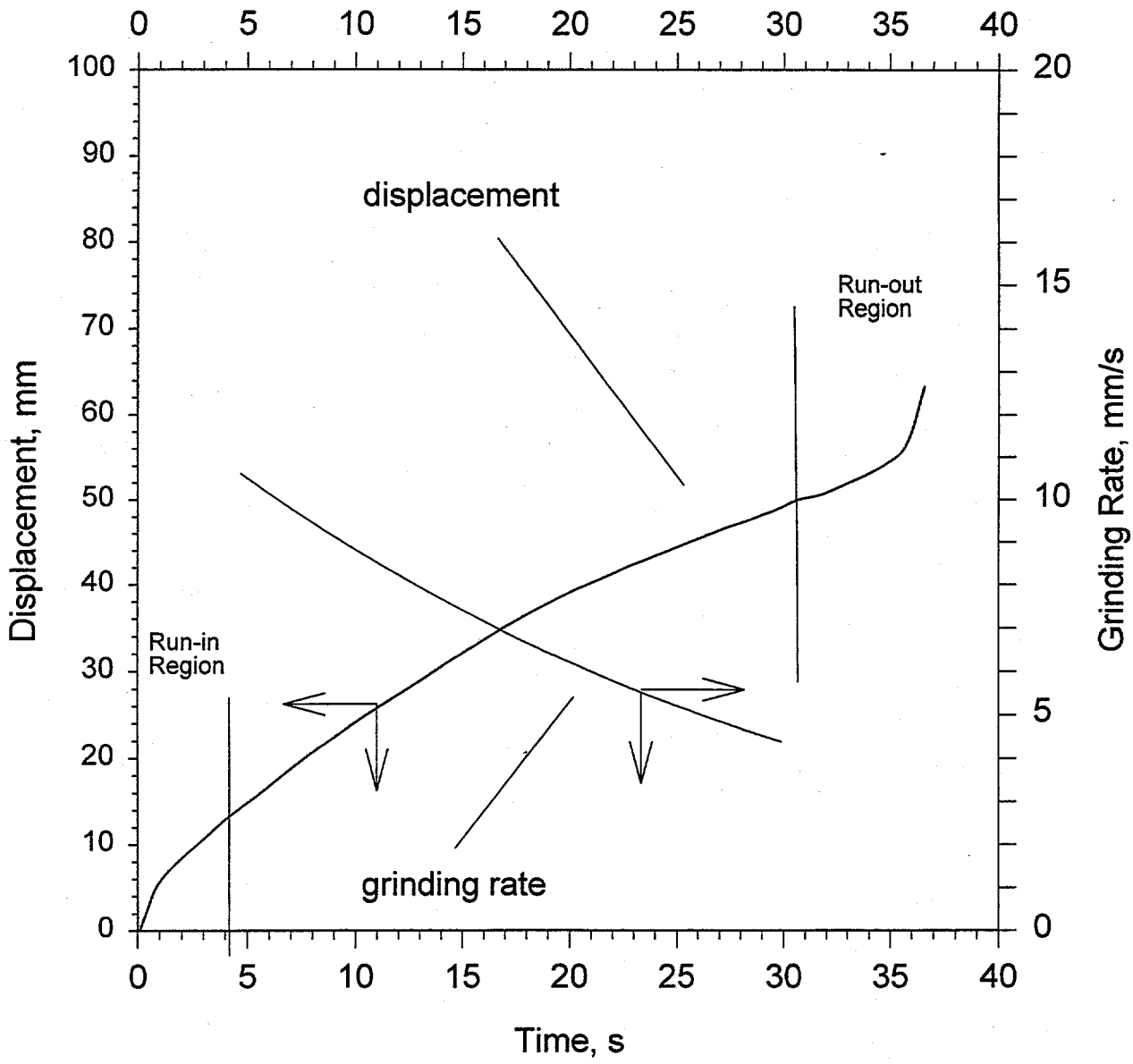

Figure 4. Example of displacement and calculated grinding rate data for a surface grinder test using the commercial coolant, 80 grit diamond wheel, 2 kg feed load, and 0.8 mm depth of cut.

Grinding Map: Commercial Coolant

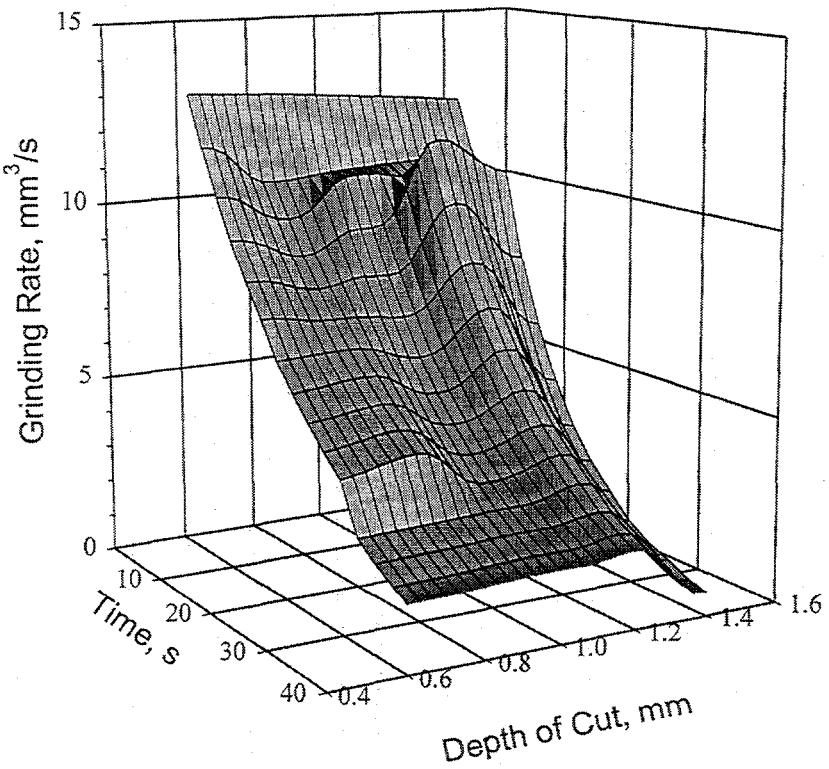

80 grit diamond wheel, 2 kg feed load

Figure 5. Grinding rate map for commercial coolant: surface grinder, 80 grit diamond wheel, 2 kg feed load.

Grinding Map: NIST Coolant

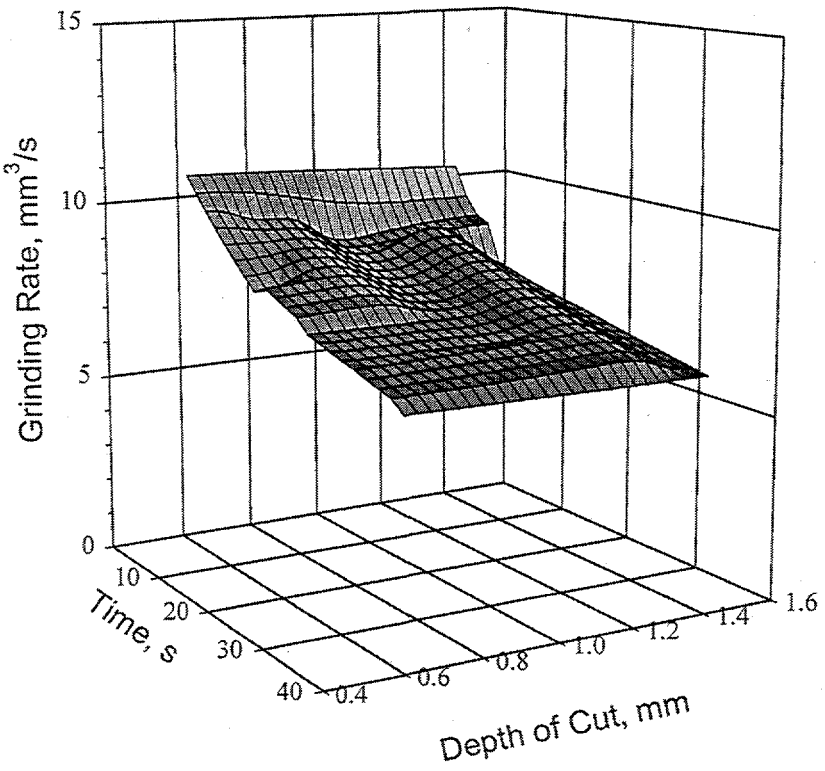

80 grit diamond wheel, 2 kg feed load

Figure 6. Grinding rate map for NIST coolant: surface grinder, 80 grit diamond wheel, 2 kg feed load.

Grinding Force Map: Commercial Coolant

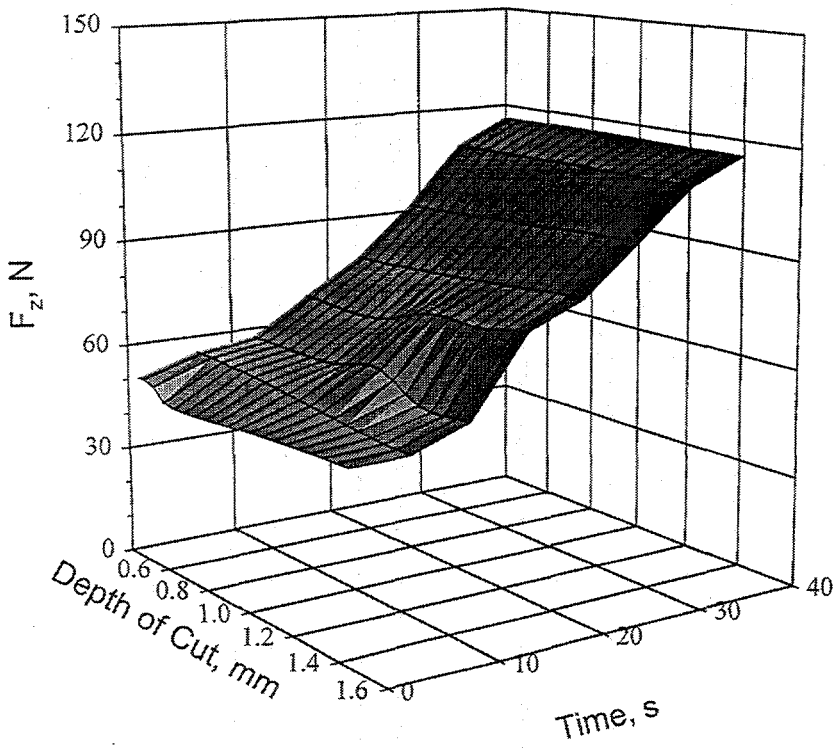

80 grit diamond wheel, 2 kg feed load

Figure 7. Grinding normal force map for commercial coolant: surface grinder, 80 grit diamond wheel, 2 kg feed load.

Grinding Force Map: NIST Coolant

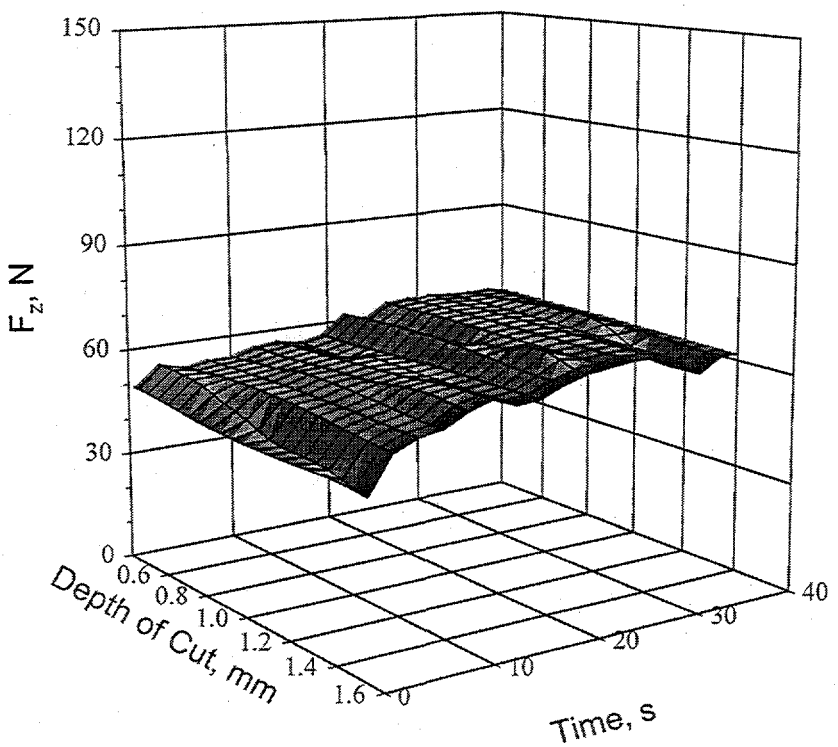

80 grit diamond wheel, 2 kg feed load

Figure 8. Grinding normal force map for NIST coolant: surface grinder, 80 grit diamond wheel, 2 kg feed load.

Laser Scatter Methods for Detecting Subsurface Machining Damage in Ceramics – Jiangang Sun, William A. Ellingson, George A. Forster (Argonne National Laboratory), Michael H. Haselkorn, and Charles J. Anderson (Caterpillar Inc.)

Objective/scope

The primary objective of this program is to develop a laser scattering procedure that would provide a direct (near-real-time) indication of changes in the subsurface (and surface) during machining. These changes include machining-induced damage (such as median crack formation) and surface roughness. A second objective is to evaluate dye penetrant technology as an off-line indicator of surface-breaking cracks. The laser program is being executed in three steps. The first is evaluating optimization of the laser scattering procedure to examine specimens machined by innovative techniques. The second step will involve correlation of the laser scattering results with mechanical properties in "real" machined ceramic specimens. The final step will be to develop a prototype instrument to be evaluated for on-line implementation in a production environment. The investigation into dye penetrants for surface-defect detection is being conducted in three steps: review of literature, off-site visits to appropriate current users (e.g., Norton) and vendors (e.g., Sherwin, Inc.), and laboratory experiments.

Technical progress

A. Elastic Optical Scattering

A1. Elastic Optical Scattering results

Elastic optical scattering data have been acquired for the 16 diamond-ground flat specimens obtained from Dr. M. H. Haselkorn of Caterpillar Inc. in the last period. These specimens are part of the original specimen test matrix and are listed in Table 1. Figure 1 shows the typical elastic optical scattering ratio and sum images (for Specimen S125AAA1). The resolution was 10 μm with an image size of 2.56x2.56 mm^2 for the images. Figure 2 shows optical photomicrograph for the specimen surface at a magnification of 100X.

The scattering ratio and sum images in Fig. 1 show suspected machining damage and machine marks. The gray scale of these marks in the images indicates the severity of the suspected damage, i.e., a brighter region in sum images and a darker region in ratio images represents more severe damage. Two observations can be made from the scattering images. First, the suspected machining damages occur predominantly along the feed direction (vertical direction in the images) and are represented as machine marks. It is seen that the machine marks or damages are consistent along the whole length (vertical) in the images and some are more severe than others. Secondly, there are distributed dark spots in the ratio images and bright spots in the corresponding sum images. Those damaged spots are not associated with machine marks and

they appear in various sizes and distribution densities for different specimens. The scattering images also show some additional defects in the specimens which may or may not be due to the machining process, e.g., the curved line at upper-right corner in the scattering images in Figs. 1a and 1b may be a scratch that caused damage in the subsurface. The curved mark is visible in the photomicrograph in Fig. 2 which correlate well with the scattering images. However, the photomicrograph does not provide information on the severity of the damage or if the damage occurs in the subsurface.

Table 1 List of the 16 diamond-ground GS44 specimens and their machining conditions

Specimen ID	diamond concentration (%)	bond	diamond type	depth of cut (inch)	feed rate (inch/sec)	run No.
S125AAA1	125	soft	friable	0.001	40	1
S125AAA2	125	soft	friable	0.001	40	2
S125AAA3	125	soft	friable	0.001	40	3
S125AAB2	125	soft	friable	0.002	20	2
S125AAB3	125	soft	friable	0.002	20	3
S50ABA2	50	soft	non friable	0.001	40	2
S50ABA3	50	soft	non friable	0.001	40	3
S125BAA1	125	hard	friable	0.001	40	1
S125BAA2	125	hard	friable	0.001	40	2
S125BAA3	125	hard	friable	0.001	40	3
S50BAA2	50	hard	friable	0.001	40	2
S50ABB1	50	soft	non friable	0.002	20	1
S50ABB2	50	soft	non friable	0.002	20	2
S125BAB1	125	hard	friable	0.002	20	1
S125BAB2	125	hard	friable	0.002	20	2
S50BAB3	50	hard	friable	0.002	20	3

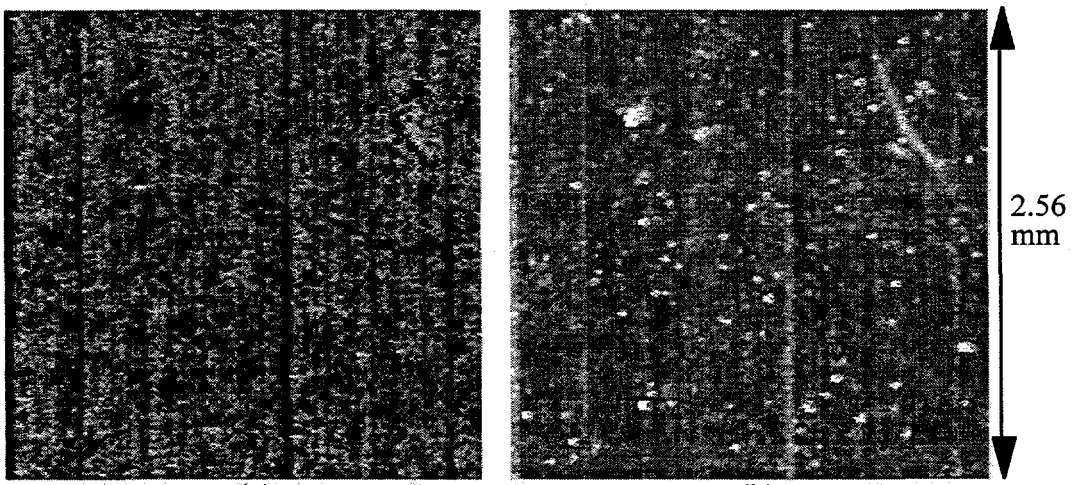

Fig. 1 Laser scatter (a) ratio and (b) sum images showing machine marks and suspected damage for specimen S125AAA1

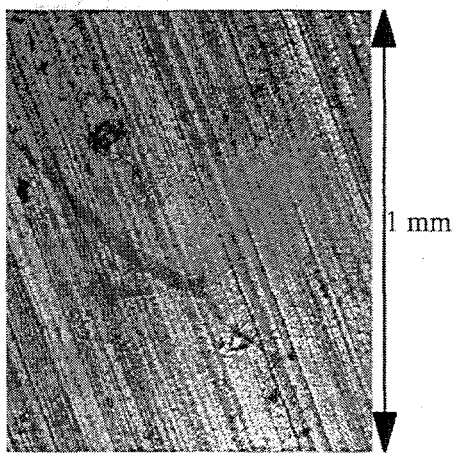

Fig. 2 Photomicrograph of the surface of diamond ground specimen S125AAA1 at magnification of 100X

During this period, two diamond ground GS-44 coupons were received from Dr. E. Zanoria of ORNL, and they were studied by elastic optical scattering for subsurface defect detection. The machining conditions for the GS-44 coupons are listed in Table 2. Six surface areas of 1.28 x 6 mm^2 each with a resolution of 10 μm were scanned on each specimens, as illustrated in Fig. 3. Sample elastic optical scattering ratio and sum images [at location (a) in Fig. 3] are shown in Figs. 4 and 5 for specimens 10102 and 10202, respectively. In the sum images the white speckles represent surface regions with excessive light scattering which is due to subsurface defects or cracks. Correspondingly, the damaged regions are shown as dark speckles in the ratio images. Because of the special method used for data acquisition, the ratio and sum images are sensitive respectively to the median and lateral cracks in the specimen subsurface.

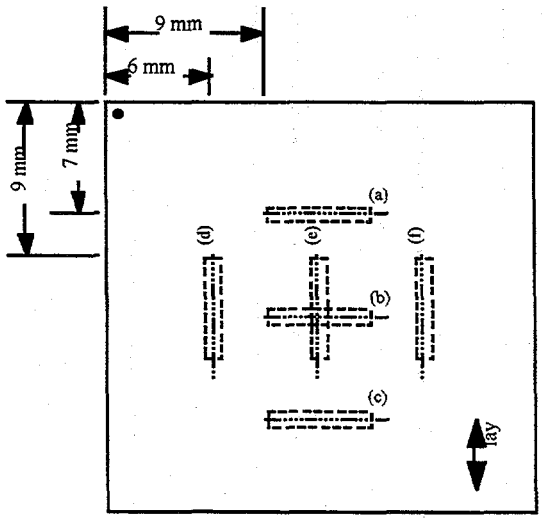

Fig. 3 Laser scanned areas (dashed line rectangles) were 6 mm long and 1.28 mm wide with 10 μm resolution.

Table 2 Machining conditions for GS-44 coupons

Coupon ID	10102	10202
Wheel grit number	80	320
Surface wheel speed (m/s)	35	74
Down feed (mm)	0.018 (0.0007")	0.018 (0.0007")

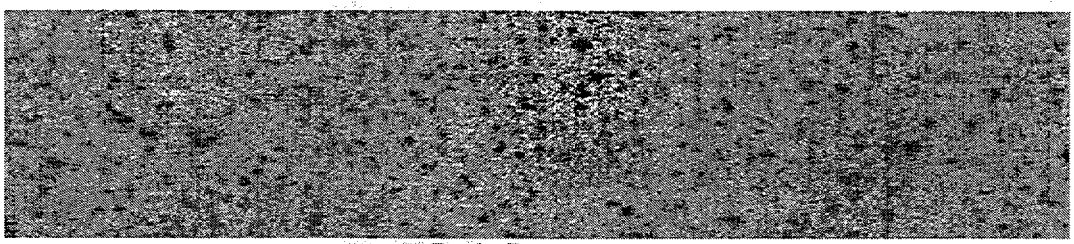

Ratio Image

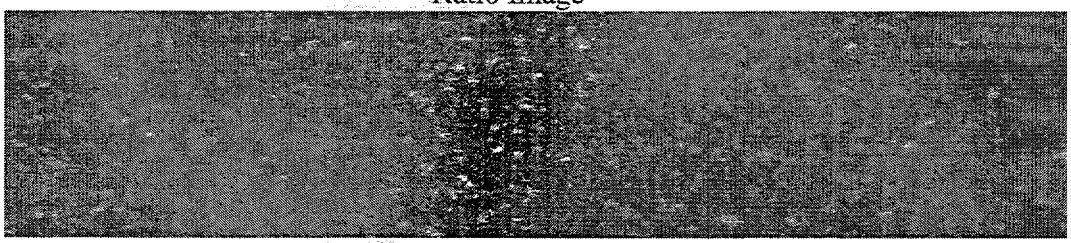

Sum Image

Fig. 4 Elastic optical scattering images of ORNL GS-44 coupons 10102 at location (a) shown in Fig. 1

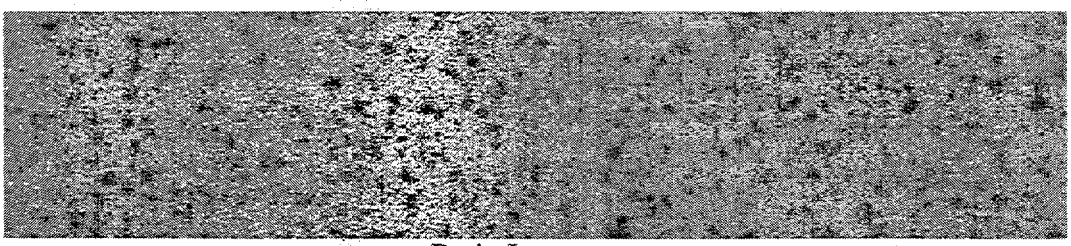

Ratio Image

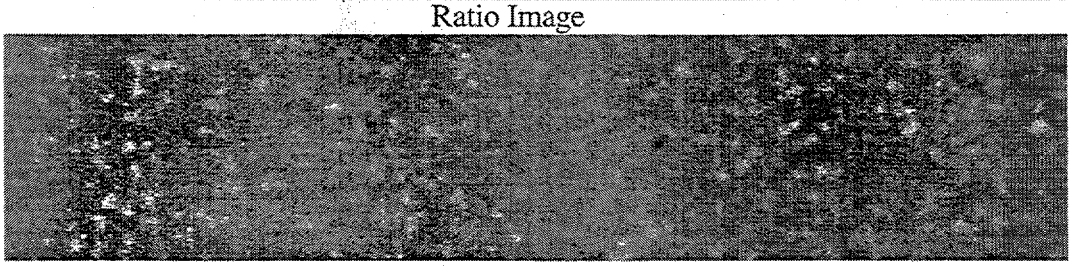

Sum Image

Fig. 5 Elastic optical scattering images of ORNL GS-44 coupons 10202 at location (a) shown in Fig. 3

From the scattering images in Figs. 4 and 5, two types of machining-induced damage can be determined. First, machining marks are represented by damage lines, darker lines in ratio images and whiter lines in sum images. These marks are most likely the median cracks generated

when the grinding particles pass through the specimen surfaces. Second, individual damaged areas, or individual speckles, are distributed all over the specimen subsurfaces. The scattering images show different speckle patterns between the two specimens. The frequency of these speckles can be found from the Fast Fourier Transform (FFT) of the images. Figure 6 shows the averaged central horizontal and vertical profiles of the 2-D FFT images from the scattering ratio images at all locations (a)-(f) on the two specimens. The horizontal direction is the direction across the lay in the specimen and the vertical is along the lay. The central spike at pixel 64 in the profiles represent the zero frequency and the frequency increases toward both sides. It is seen that the lower frequencies are generally dominant. The speckles across the lay direction in specimen 10102 have a dominant period (inverse of frequency) at about 213 μm while those in specimen 10202 have a dominant period at 320 μm. In addition, all horizontal profiles (across the lay) in Fig. 5 show characteristic periods at about 213 μm and 107 μm which are not present in the vertical profiles (along the lay). Therefore, the suspected machining-induced damage is not same in the two directions on the specimen subsurface, but the general pattern is similar in both specimens.

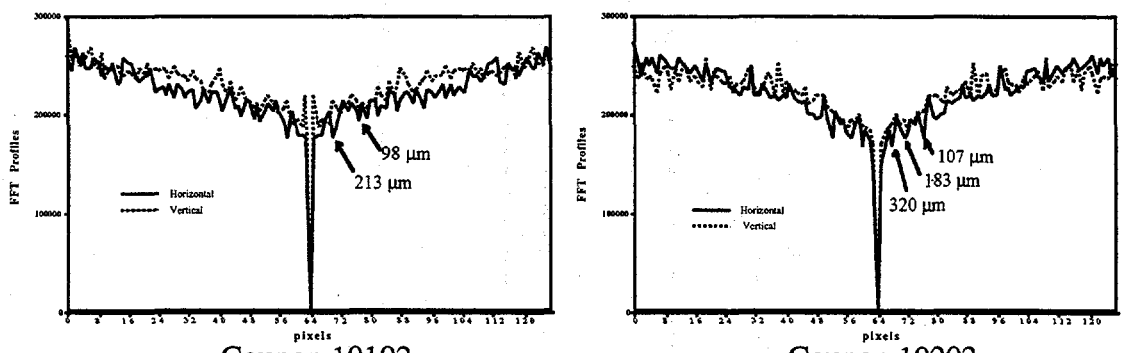

Coupon 10102 Coupon 10202

Fig. 6 Averaged FFT profiles of scattering ratio images of ORNL GS-44 coupons

Figure 7 shows gray scale histograms of the scattering ratio images shown in Figs. 4 and 5 for the two specimens. For specimen 10102, a characteristic cut is present with a higher intensity above the cut at a lower gray scale (corresponding to dark speckles in the scattering ratio images), which may indicate a certain defect pattern, probably the machine marks. On the other hand, the histogram of ratio images for specimen 10202 is relatively symmetric.

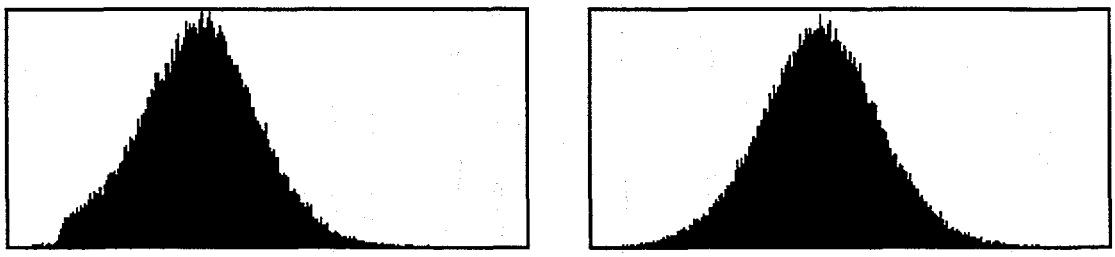

Coupon 10102 at location (a) Coupon 10202 at location (a)

Fig. 7 Histograms of gray scales of scattering ratio images of ORNL GS-44 coupons

A2. Automation for on-line inspection

Development continued this period for implementation of the elastic optical scattering technique to on-line inspection of machining induced damage. A portable prototype laser scattering system has been assembled, and a computer controlled rotation/translation stage has been build for scanning of cylindrical specimens. The laboratory set up of the complete system is illustrated in Fig. 8. Figure 9 shows initial scattering ratio and sum images of a tensile rod obtained with the new system.

The portable prototype laser scattering system has been mounted on the Brown & Sharpe grinding machine at ANL for on-line machining inspection demonstration. Figure 10 shows a picture of the system setup on the grinding machine. However, because the data acquisition speed in the current system is low, a simulation of the on-line inspection was demonstrated. Figure 11 shows a test result of a tensile rod mounted on the lathe. A 2 mm wide tape was attached on the rod to simulated a band of a damaged region, and the lathe was operated at a rotational speed of 128 rpm and translational speed of 7.7"/min. To increase the data acquisition speed for real-time, on-line machining inspection, a fast data acquisition board has been ordered, and it is expected to be received in the next period.

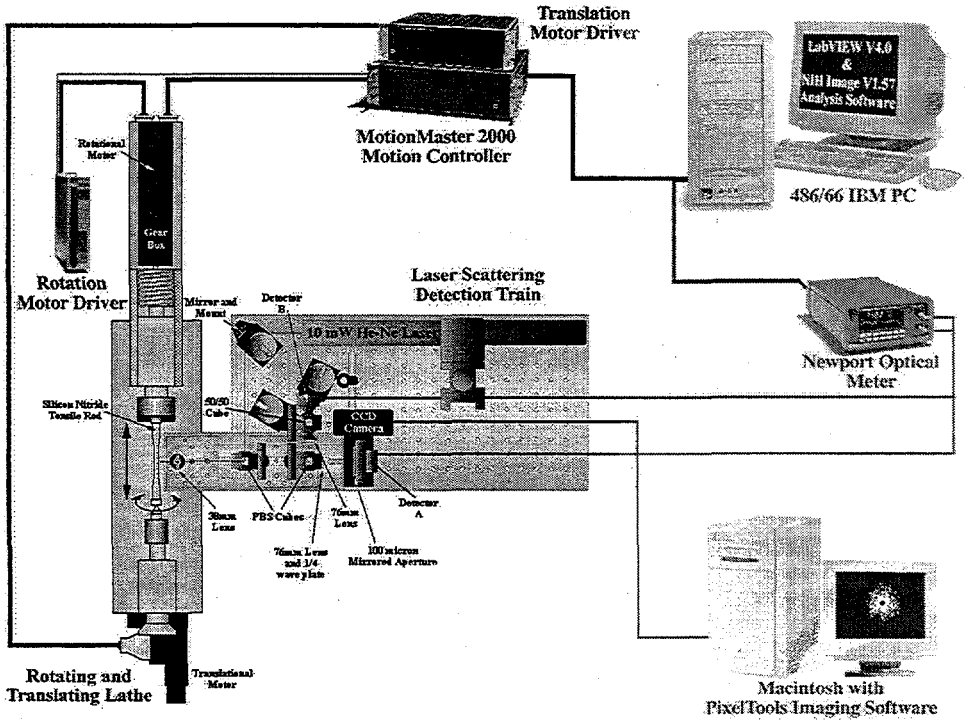

Fig. 8 Laboratory set up of a portable scattering system for scanning of cylindrical specimens

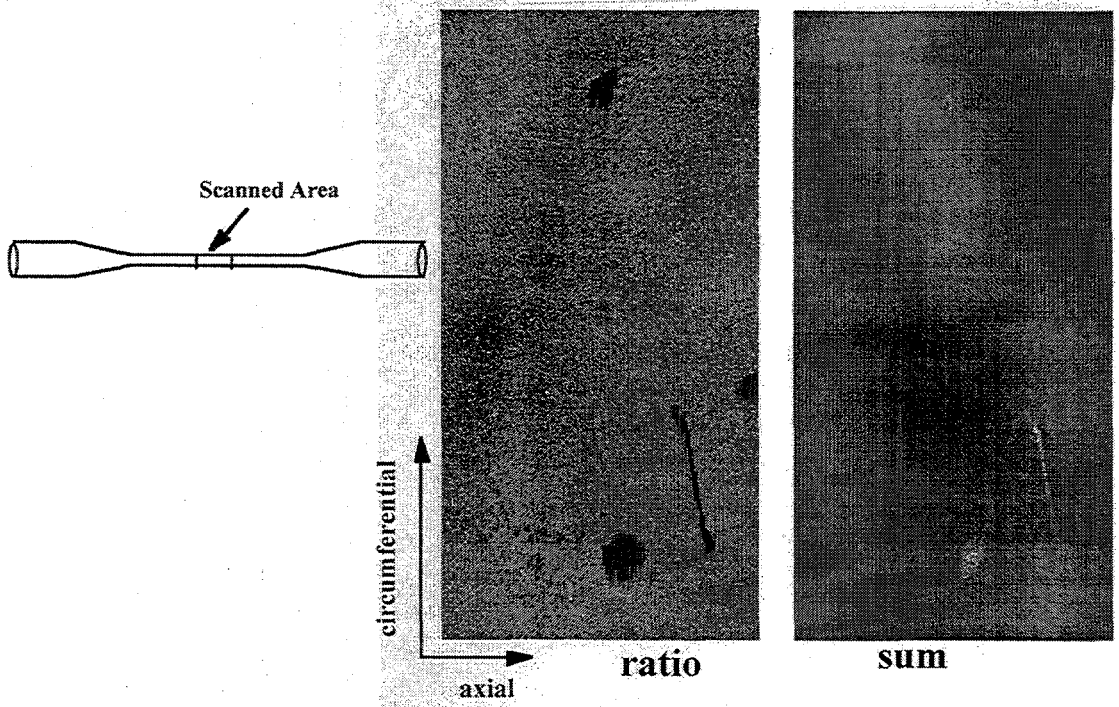

Fig. 9 Elastic optical scattering ratio and sum images of a tensile rod

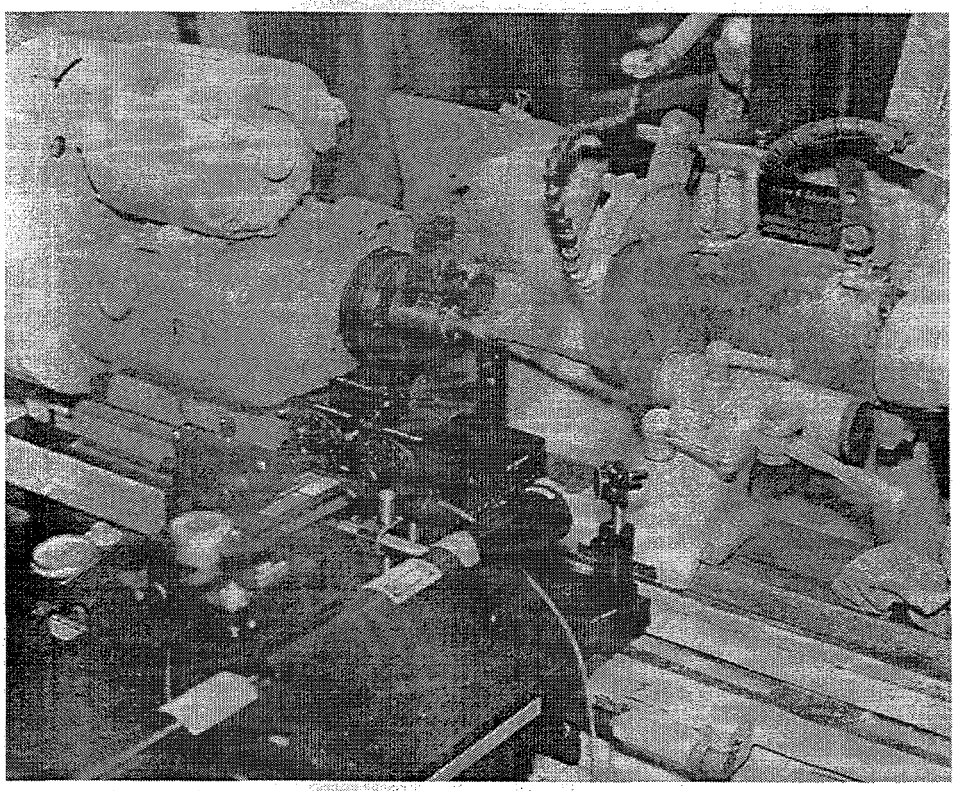

Fig. 10 A portable laser scattering system mounted on the Brown & Sharpe grinding machine at ANL

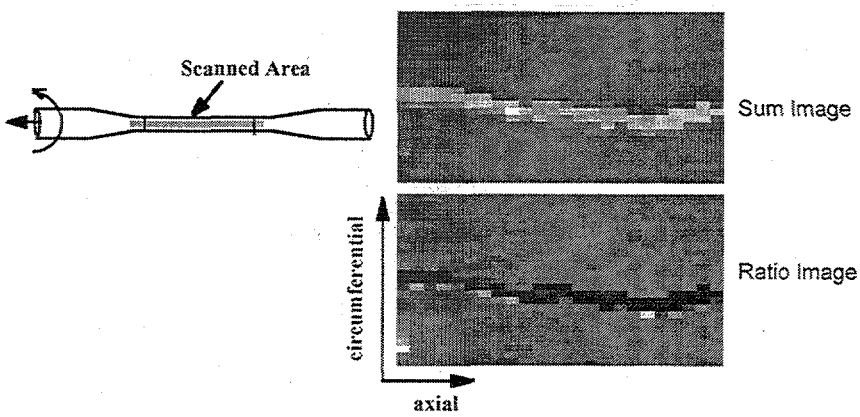

Fig. 11 Simulated on-line inspection result of a ceramic tensile rod on a grinding machine

B. Dye Penetrant

B1 Report

The final report on Phase I has been submitted.

B2. Technology Transfer

The development of the initial aspects of the dye penetrant work were successfully transferred.

Status of Milestones

Milestone 150701 is complete. Milestone 150702 (Correlate Argonne National Laboratory (ANL) laser scatter results with Caterpillar (CAT) mechanical properties) has begun by receipt of specimens from Caterpillar, Inc. Communication continues with CAT on the delivery of additional specimens. All other ANL milestones are on or ahead of schedule.

Communications/Visits/Travel

J. G. Sun attended the QNDE conference in Jul. 28-Aug. 2, 1996 at Brunswick, ME.

J. G. Sun attended the annual review of Cost-Effective Ceramic Machining projects in Sep. 11-12 at ORNL.

Problems Encountered

We are now out of funds and we request that our FY97 funds be released as soon as possible.

Publications

None this period.

Milestone Schedule

Milestone	Date	Status
1. Determine optical properties of SiAlON and GS-44 for optimum optical detection parameters (polarization, wavelength, angle of incidence, etc.).	Feb. 28, 1994	**Completed**
2. Conduct exploratory studies of dye penetrant on machined surfaces.	May 31, 1994	**Completed**
3. Submit report on dye penetrants.	Dec. 1, 1994	**Completed**
4. Correlate laser scatter analysis (ANL) of contoured specimens with mechanical properties, residual stress measurements, and mechanical surface roughness measurements (CAT).	Dec. 1, 1996	Rescheduled date
5. Correlate laser scatter results (ANL) with mechanical properties (CAT): Flat Specimens	Dec. 1, 1996	Rescheduled date
6. Install and demonstrate prototype laser scatter device.	Aug. 31, 1996	**Completed**
Phase II: Proposal under review. Tentative Milestone:		
7. Quantify laser scatter data with severity of machining damage or defects	May 30, 1997	
8. Develop high-speed data acquisition system for on-line inspection	Dec. 1, 1997	
9. Correlate laser scatter data with machining damage and mechanical properties of flat ceramic specimens	Sep. 30, 1998	

THE EFFECT OF MACHINE STIFFNESS ON THE GRINDING OF SILICON NITRIDE

Bi Zhang, Trevor D. Howes, and Zhenqi Zhu
Precision Manufacturing Center
University of Connecticut
Storrs, CT 06269-5119

(Report Period: Feb. 1 to Sept. 30, 1996)

Objectives/Scope

This research project seeks to determine the minimum required machine stiffness to satisfactorily grind ceramics. This in turn will determine the suitability of existing machinery for use in grinding of ceramics. A grinding machine having the minimum required stiffness will suppress surface and subsurface damage of a ceramic workpiece to a level at which residual strength, surface finish and quality, and dimensional accuracy are acceptable. The ceramic material chosen for study is High Pressure Sintered Silicon Nitride.

Grinding experiments have been done on the Dover grinding machine using a specially designed work holder with variable static and dynamic compliances. This design simulates more compliant machines, and thus, the effect of machine stiffness can be isolated by using otherwise identical conditions. Grinding tests have been conducted on the workpieces while using the work holder under various conditions. Surface and subsurface damage will be evaluated using etching, taper polishing, fracture techniques, and scanning electron microscopy. A four-point transverse rupture strength testing method is used to validate the damage evaluation techniques.

An analytical relationship will be established to predict the minimum required machine stiffness for grinding ceramic materials with known properties. The analytical relationship will be compared with the results obtained in the experiments. The results will help us (1) understand the fundamental physics involved in grinding of ceramics, and (2) facilitate grinding of ceramics in a deterministic way.

Technical Highlights

The project focus was first on the preparation of the experimental needs for the grinding test, flexural strength test and workpiece evaluation; then on setting up the ELID system and enhancing the stiffness of the grinding machine, and on grinding experiments using both vitrified bond diamond wheels and Cast Iron Fiber Bond (CIFB) diamond wheels.

Grinding Wheels

Two types of diamond wheels are obtained for this research: vitrified bond and Cast Iron Fiber Bond. Each type of the diamond wheels has two different grain sizes. The chosen mesh numbers are #120 and #1,000 for vitrified bond diamond wheels, and #1,000 and #10,000 for the CIFB diamond wheels because electrolytic in-process dressing (ELID) grinding prefers fine grains. All of these diamond wheels have a concentration of 100%. The two different grain sizes for each bond type allow us to examine the grain size effect on the minimum machine stiffness required for grinding silicon nitride. Meanwhile, the bond type effect on the minimum machine stiffness can be investigated on the #1,000 wheels. Much of the silicon nitride grinding research has been done with resin bond wheels, but vitrified bond diamond wheels offer a longer life, and a higher dimensional accuracy, and are recently experiencing a wider use, particularly in Japan. All the

grinding wheels have a diameter of 180 mm and a rim of 5 mm in width, and are 11A2 flaring cup wheels.

Fabrication of Precision Quills for Grinding Wheels

Surface grinding using a cup-type wheel has been performed on the Dover grinding machine. A new quill was designed and fabricated for each of the four grinding wheels to ensure a high interface stiffness of the wheel mounting. Each set of the quill and wheel was properly balanced in order to reduced the motion errors induced by the wheel mounting. Figure 1 shows the dimensions of the quills fabricated.

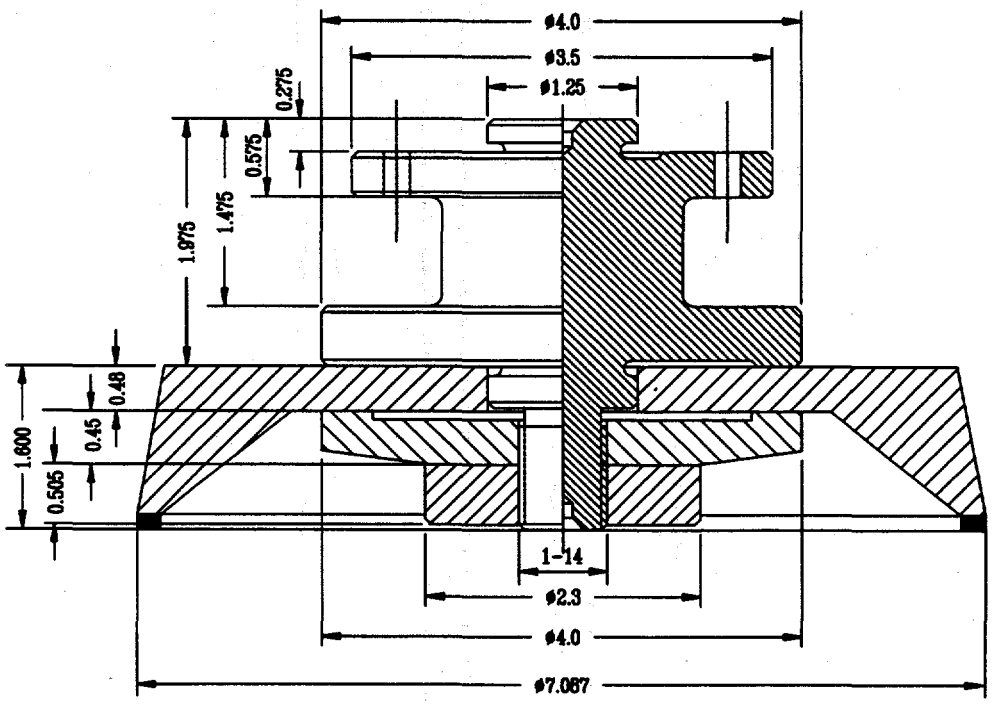

Figure 1 Dimensions of quill and grinding wheel (unit: inch)

Preparation of Silicon Nitride Test Bars

The GS-44 silicon nitride test bars (from AlliedSignal Inc.) have the following physical properties

Maximum use temperature	1,100 °C
Flexural strength	1,051 MPa at room temp. 655 MPa at 1,100 °C
Fracture toughness	8.25 MPa$\sqrt{m}$
Thermal conductivity	35 W/mk
Density	3.2 g/cm^3
Elastic modulus	300 GPa
Vickers hardness	14.6 GPa
Thermal expansion	3.4 $\times 10^{-6}$ /°C (20-1,000 °C)

The test bars were prepared and ground based on the ASTM Standard: C1161-94. The process is highlighted as follows:

Specimen size: Width (b) : 4.0 mm, Depth (d): 3.1 mm, Length (L): 45 mm (minimum).

Specimen Preparation: All grinding was done with an ample supply of appropriate filtered coolant to keep workpiece and wheel constantly flooded and particles flushed. Grinding was in at least two stages, ranging from coarse to fine rates of material removal. All machining was in the surface grinding mode, and was parallel to the specimen long axis. No Blanchard or rotary grinding were used.

The stock-removal rate did not exceed 0.03 mm (0.001 in.) per pass to the last 0.06 mm (0.002 in.) per face. Final (and intermediate) finishing was performed with a diamond wheel that was between #400 and #1,000. No less than 0.06 mm per face was removed during the final finishing phase, and at a rate of not more than 0.002 mm (0.0001 in.) per pass. Approximately equal stock was removed from opposite faces.

The four long edges of each specimen were uniformly chamfered at 45°, a distance of 0.12 ± 0.03 mm. Edge finishing are comparable to that applied to the specimen surfaces. In particular, the direction of machining are parallel to the specimen long axis.

Construction and Testing of Work Holder

The machine stiffness will be varied by adding a compliance via the work holder to simulate a more compliant machine. The basic requirements for the work holder are variable compliance, high sensitivity, and high accuracy. Variable compliance can be achieved by sliding two compliance modulators along a flexural plate as shown in Fig. 2. High sensitivity can be obtained by an appropriate design of the spring plate, and high accuracy is ensured by rigid modulators, and a rigid base, and by applying a large preload to all the mechanical interfaces of the work holder. A three-channel piezoelectric force transducer and a capacitance displacement sensor are attached to the work holder. The workpiece is mounted on the top of the work holder.

The static stiffness of the work holder was tested using capacitance sensors and a piezoelectric force transducer. The capacitance sensors (from Lion Precision) were used to measure the elastic deformation of the work holder and the force transducer (from Kistler) was used to detect the load applied to the holder. The test result is also shown in Fig. 2. The thickness of the flexural plate is 3 mm. The dynamic response of the work holder is being tested and will be reported next time according to the timeline of the project.

Flexural Strength Testing Machine

A stand-alone servo hydraulic fatigue test system equipped with a fully articulated four-point bend fixture was obtained from Instron Corporation. The testing machine, model 8511, satisfies ASTM Standard C1161-94. The full articulation of the four-point bend fixture is accomplished via arched ceramic pieces and hardened steel pins that permitted to roll, which ensures uniform loading of test bars. The fixture can be changed to a non-articulated version by replacing these ceramic arched pieces with rectangular ceramic pieces. The testing machine is closed-loop controlled by a computer with the feedback signals from a force and displacement sensors. LabView software and a data acquisition board (National Instruments) were used in the flexural strength testing. The hydraulic universal testing machine has the following features:

System Accuracies	
Load	±0.005% of load cell capacity or ±0.5% of indicated load, whatever is greater
Strain	channel and sensor are included
Stroke	±0.5% of full scale actuator travel.
Load frame	
Capacity, fatigue	25 kN (5.5 Kip)
Stiffness	245 kN/mm (1.4×10^6 lb/in)

Load cell	20 kN (4.9 Kip)
Actuator	
Force rating	20 kN (4.9 Kip)
Dynamic rating	18 kN (4 Kip)
Stroke	±50 mm (±2 in)
Velocity	0.05 to 3050 mm/min (0.002 to 120 in/min)
Dynamic performance	20 Hz, 0.56 mm (0.022 in) P-P.
Electronics	Closed-loop controller with Front panel display Data acquisition board and software.

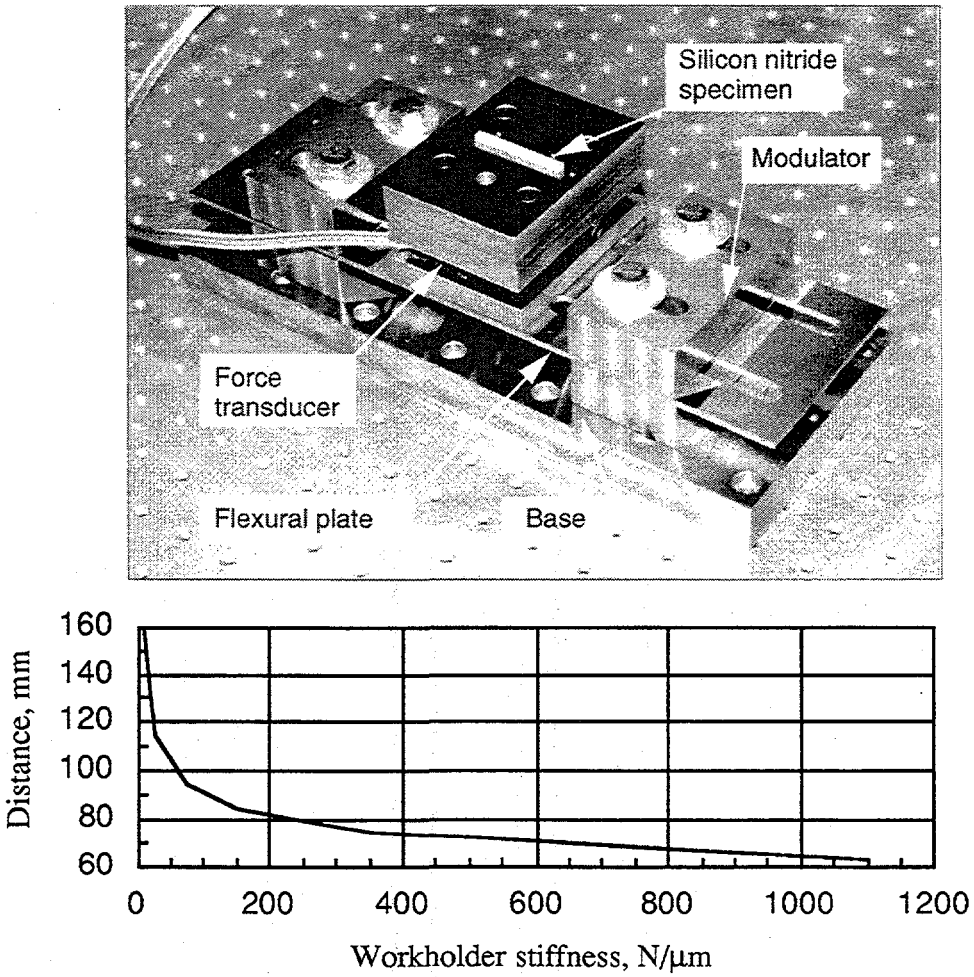

Figure 2 Work holder with its stiffness adjustable by sliding two modulators along a flexural plate

The ELID Grinding System Setup

FUJI ELIDER ED-910 ELID system (Fuji Die Co. Ltd.) was used for CIFB diamond wheel dressing. The system removes the metal bond of the wheel by applying power between the wheel and an electrode. The grinding coolant, Rustlick G-1066D from ITW Fluid Products Group, is a synthetic, water soluble coolant for diamond wheel grinding, slicing and dicing of nonmetallics including semiconductor wafers. Since it is electro-conductive, the coolant acts as an electrolyte

which allows current to flow, ionizing the bond material at the surface, and producing an oxide layer. Figure 3 shows the setup of the ELID system. The metal bonded grinding wheel is connected to the positive pole of a power supply using a smooth brush contact, and a fixed electrode is made negative. The electrode is made from copper having 1/6 of the wheel periphery length and a width of 2 mm more than the wheel rim thickness of 5 mm. The gap between the wheel and electrode can be adjusted by a mechanical means. A clearance of approximately 0.1 mm is kept between the positive pole (the grinding wheel) and the negative pole. The coolant flows through the clearance. The combination of current and electrolyte chemistry controls the grain layer exposed, and the thickness of the oxide layer. Once the oxide layer is formed, the bond removal process is stopped because the oxide layer acts as an electric insulator. Grinding can proceed until the exposed abrasives become worn sufficiently so that the chips produced erode the oxide layer, which results in bond erosion.

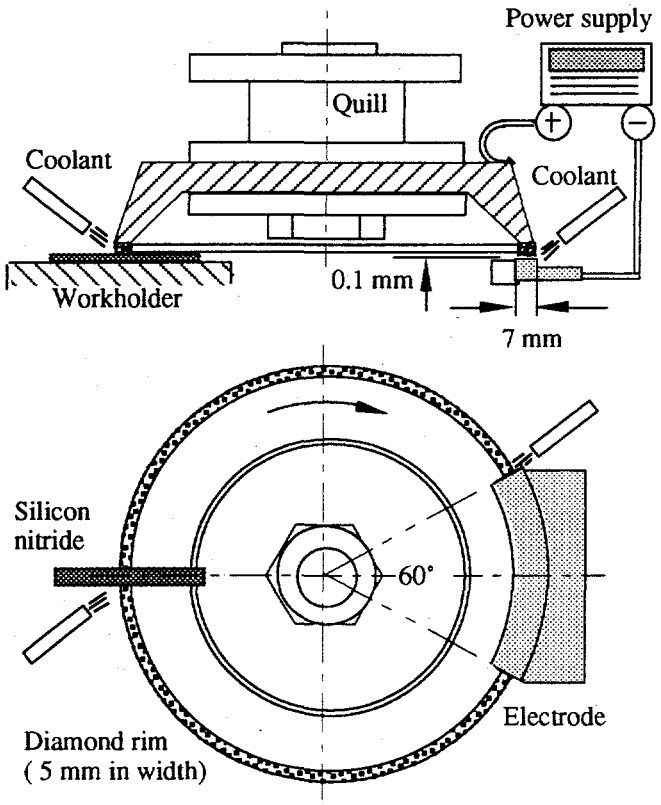

Figure 3 CIFB diamond wheel and ELID system setup

Enhancing the Stiffness of the Grinding Machine

Experimentation was performed on the Dover grinding machine shown in Fig. 4. This machine was designed for applications requiring sub-micron tolerances. It is equipped with a granite base and column, and an aerostatic spindle and aerostatic slideways. The granite structure provides a high stability and a good damping effect. The X-axis is an air-vacuum puck mounted on lapped granite rails that are directly mounted to the granite base. The Y-axis, also an air-vacuum puck, is mounted on top of the X-axis, and is guided by two hardcoated aluminum rails. All axes have a straightness error of 4 μin/in, and are driven by precision ball screws with integrally mounted brush type DC motors with tachometer feedback, and laser interferometer

system for positioning feedback with a resolution of 3 μin. The overall system accuracy is 60 μin. The spindle is configured to mount vertically, and is directly mounted to the Z-axis slideway. However, as the spindle is mounted outside the Z-slide, a cantilever exists which reduces the loop stiffness of the machine structure.

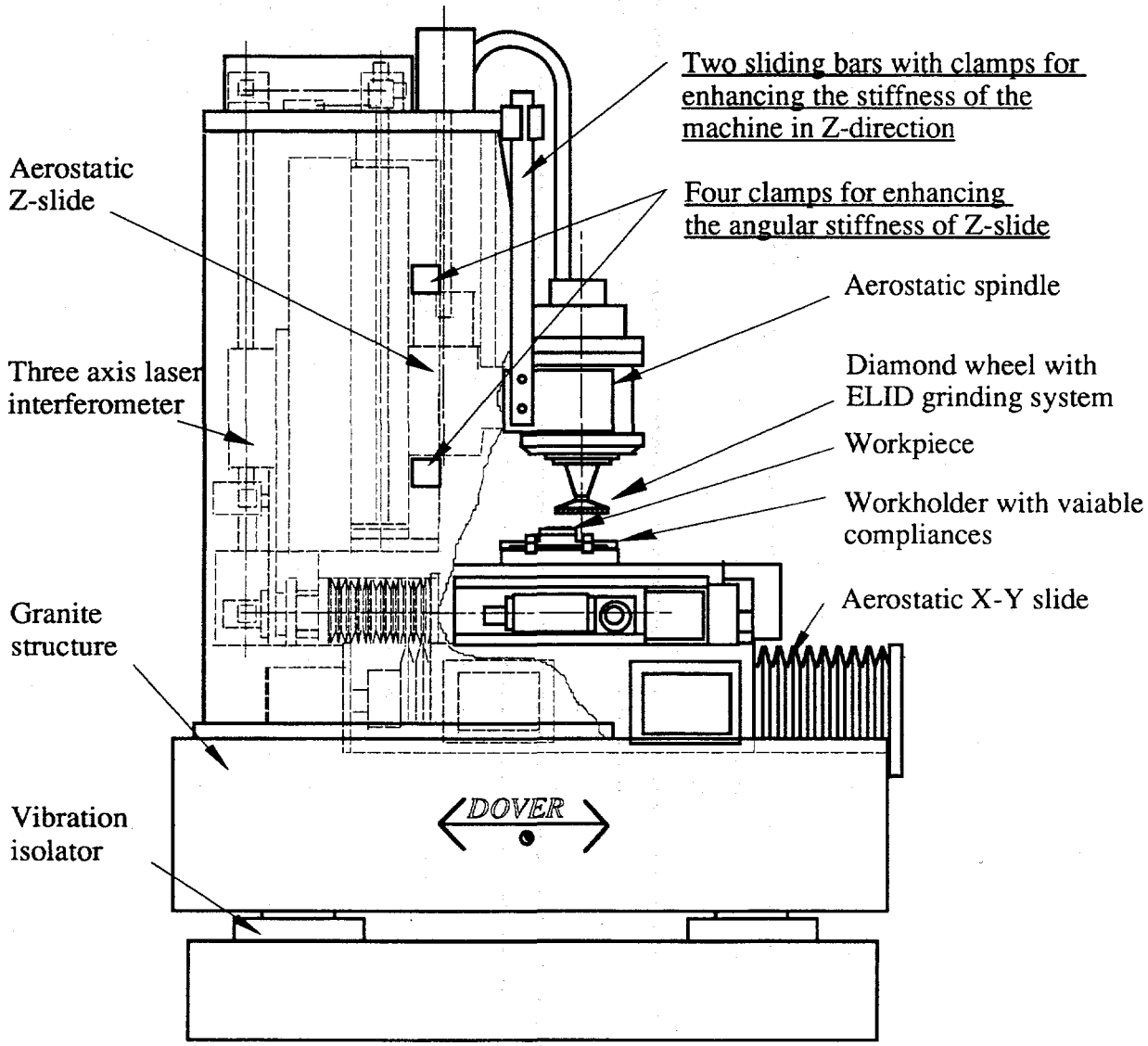

Figure 4 Four Clamps are added to the aerostatic Z-slide to enhance its angular stiffness and two sliding bars with clamps are attached to the spindle housing to enhance the stiffness in Z-direction

To overcome the cantilever effect, two sliding bars with clamps were fabricated and added to the spindle housing to increase the machine structure stiffness. The aerostatic Z-slide, which is driven by a ballscrew-rotary motor, had a limited stiffness in the travel direction. Therefore, four clamps were designed and added to the Z-slide to increase its stiffness in Z-direction. After feeding a small step, the clamps lock both the Z-slide and the spindle housing. These clamps can be used when a very high stiffness is needed in this research.

To measure the loop stiffness, a force was applied between a specimen and the grinding wheel rim. A piezoelectric transducer built in the specimen holder is used to measure the force.

Capacitance sensors were used to detect the displacement between the specimen and spindle. For a cup type diamond wheel of vitrified bond, the loop stiffness was measured as follows:

Without clamping		
Average force:	227 N	Displacement: 5.5 μm
Loop stiffness:	41 N/μm	
With clamping		
Average force:	80 N	Displacement: 0.8 μm
Loop stiffness:	100 N/μm.	

Testing the ELID

Figure 5 shows the experimental results of the ELID working voltage and current in a time period of 38 minutes. The spindle speed was 1000 rpm and the sampling rate was 5 Hz. The grinding wheel surface was a metallic color before dressing, and turned brown after dressing. It was observed that the dressing voltage and current did not vary much in the first five minutes. Dressing proceeded in the second five minutes and began slowing down in the third five minutes. After 30 minutes of dressing both voltage and current became stable. No grinding was conducted in this period. It was also determined that the spindle speed and coolant flow rate affected the rate of dressing significantly. As shown in Fig. 6, at different spindle speeds, the dressing voltage and current varied significantly. As the spindle speed increased, the coolant could not thoroughly fill up the gap between the CIFB diamond wheel and electrode, which might be caused by both centrifugal force acting on the coolant and air flow in the gap. For this reason, the effective area of the electrode was reduced from one-sixth of the surface area of the grinding wheel covered by the electrode and the conductivity between the wheel and electrode was reduced.

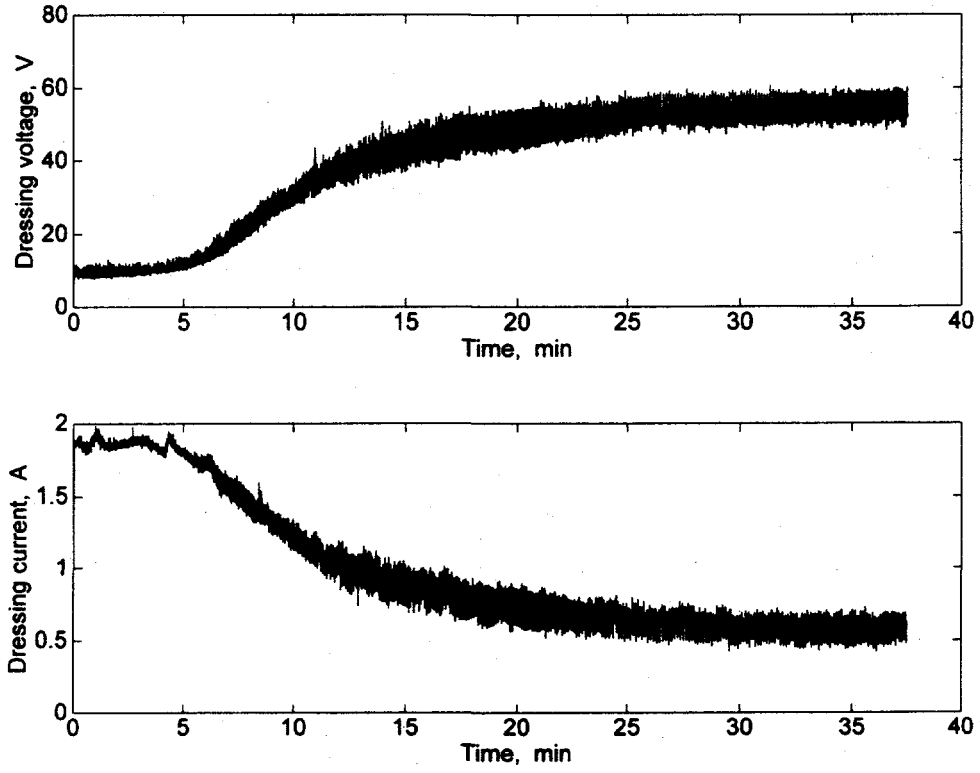

Figure 5 Electrolytic dressing of CIFB diamond wheel (#10,000CIFB-D, D=180 mm, W=5 mm, spindle speed=1,000 rpm, E_0=80 V, I_p=5 A, $\tau_{on}=\tau_{off}$=2 μs)

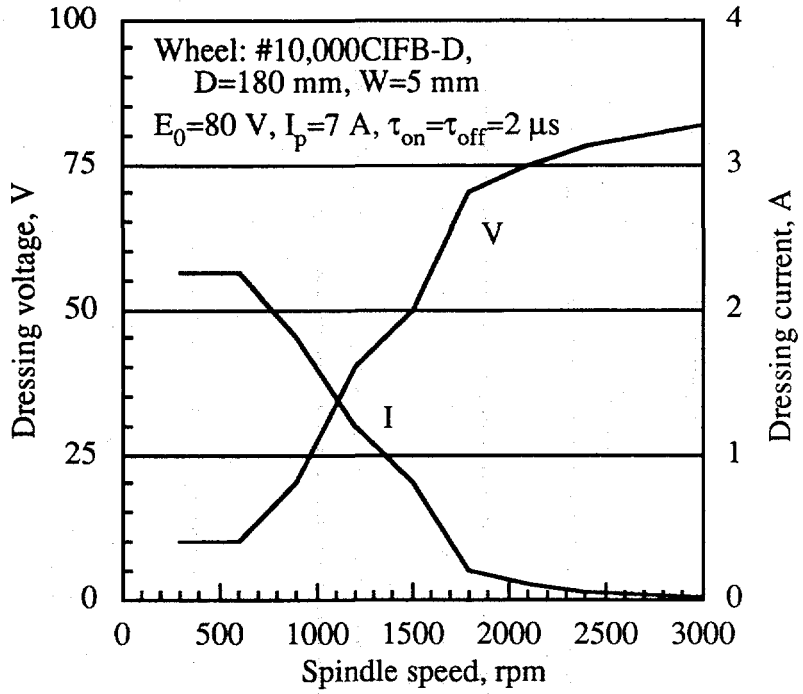

Figure 6 Effect of spindle speed on ELID voltage and current (measured at the beginning of dressing)

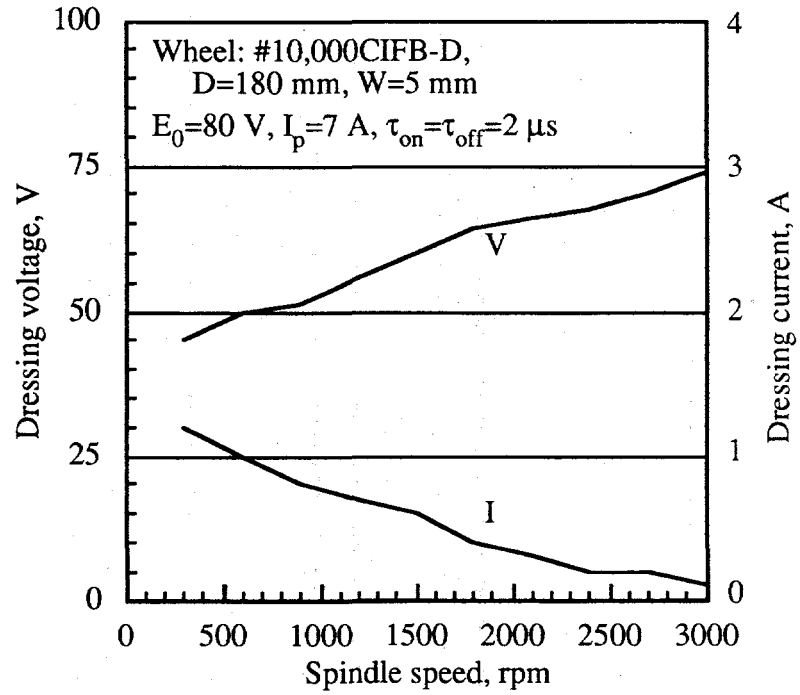

Figure 7 Effect of spindle speed on the ELID voltage and current with a larger coolant flow rate than that of Fig. 2 (measured after 10 minutes dressing with a spindle speed of 1,500 rpm)

To increase the conductivity, a larger coolant flow rate was effective. The result shown in Fig. 7 was obtained after 10 minutes ELID dressing with a spindle speed of 1,500 rpm. At different spindle speeds and with a larger coolant flow rate, dressing voltage and current were recorded. The result showed that at a speed ranging from 2,000 to 3,000 rpm a lower dressing voltage and a larger dressing current were established compared with those shown in Fig. 6. This indicated that a larger coolant flow rate was effective in speeding up the dressing process.

Grinding Experiments

The grinding were done under the following conditions:

Method:	Surface grinding using cup-type diamond wheels
Workpiece:	Silicon nitride (45×4×3.1 mm)
Wheel surface speed:	25 m/s (82 ft/s)
Grinding width:	5 mm (0.2 in)
Coolant application:	chemical solution type grinding coolant
ELID open voltage:	80 V
ELID peak current:	5 A, 7 A
ELID on/off time:	2 μs
ELID pulse wave:	square

Table 1 specifically shows the wheel type, machine loop stiffness, depth of cut and feed rate of each test run. The table was initially designed as a four-factor, three-level experiment with 9 test runs based on Taguchi methods. During grinding tests, the table was modified by reducing the depth of cut of the #10000CIFB-D wheel to 0.25 μm and using only one feed rate. Grinding forces were measured every ten passes.

Table 1 Experimental conditions and results (one specimen for each test run)

Run	Wheel Type	Stiffness (N/μm)	DOC (μm)	Feed Rate (mm/s)	Fz (N)	ΔFz (N)	Ra (μm)	Strength (MPa)
1	SD120-N100V	20	0.5	1	20.12	10.74	52	1,213
2	SD120-N100V	40	2.5	5	45.70	18.37	94	858
3	SD120-N100V	75	4.5	10	52.23	24.19	88	900
4	#1,000CIFB-D	20	2.5	10	120.23	44.76	42	946
5	#1,000CIFB-D	40	4.5	1	71.29	27.94	46	1,145
6	#1,000CIFB-D	75	0.5	5	108.61	17.62	46	1,139
7	#10,000CIFB-D	20	0.25	5	106.10	21.26	28	1,145
8	#10,000CIFB-D	40	0.25	5	85.81	17.71	28	1,225
9	#10,000CIFB-D	75	0.25	5	113.69	30.99	28	1,097

After grinding, surface roughness was measured over a length of over 43 mm for each specimen. Figures 8a, 8b, and 8c show the surface profile of specimens ground using the SD120-N100V, #1,000CIFB-D and #10,000CIFB-D wheels respectively, these profiles were measured over a length of 1 mm. The surface roughness decreased by a small amount as the wheel mesh number increased in an order of magnitude. Figure 8c shows the stiffness effect on the surface profiles ground by a single wheel. Though the surface roughness data of all the three specimens are close, the profile patterns are different, which may be caused by the machine stiffness variation.

Flexural strength at ambient temperature was tested according to ASTM Standard C1161-94. The four-point bend fixture was used for testing the specimens (configuration B). A crosshead speed of 0.5 mm/min was used for the four-point-1/4 point loading under displacement-control. In most cases, the loading span of a specimen was broken into several pieces.

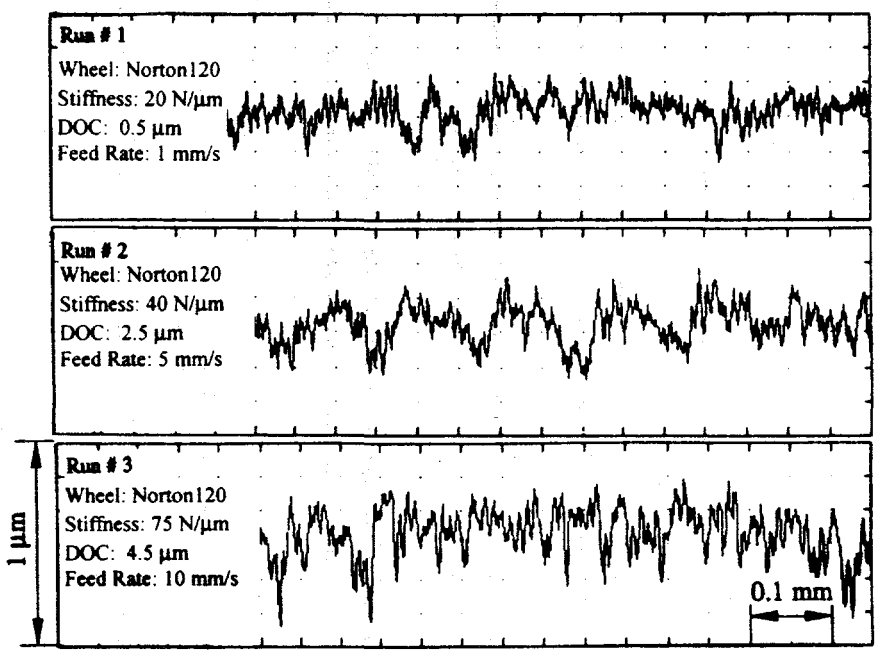

Figure 8a Surface profiles of specimens ground using the SD120-N100V wheel

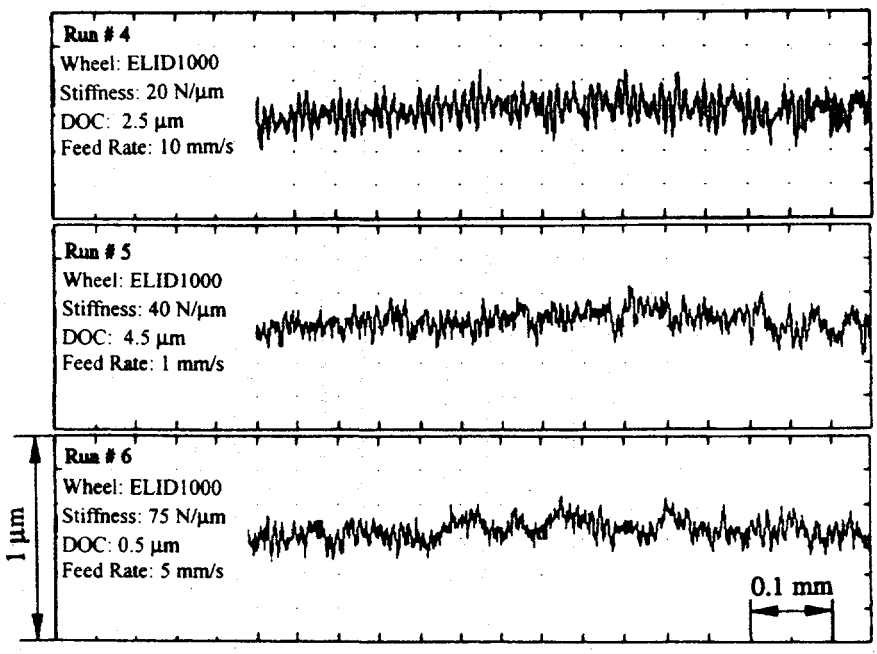

Figure 8b Surface profiles of specimens ground using the #1,000CIFB-D wheel

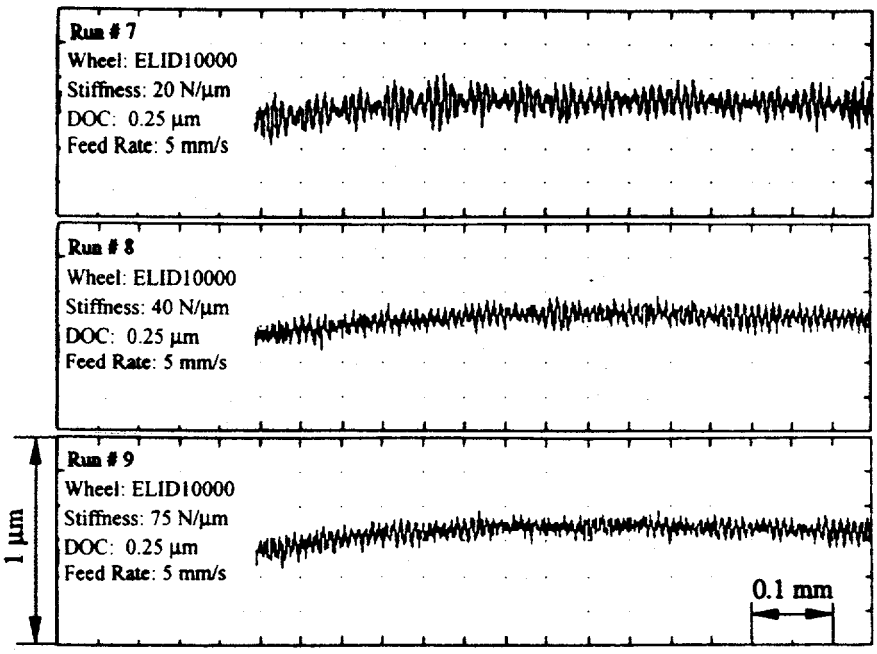

Figure 8c Surface profiles of specimens ground using the #10,000CIFB-D wheel

The measured surface roughness Ra and flexural strength data shown in Table 1 were further analyzed using Taguchi methods and the results are shown in Fig. 9. Although for each test run 10 specimens will be ground for a reliable result. At this stage only 1 specimen was ground for each test run, and the test results of the 9 specimens did show that the wheel type, machine loop stiffness, depth of cut and feed rate affected surface roughness and flexural strength. For surface roughness, the wheel type was the dominant factor while the other three factors had nearly the same effect. For flexural strength, the stiffness had the smallest effect and the other three factors showed a stronger effect. Figure 9 suggests that for the smallest surface roughness and the highest flexural strength, the #10000CIFB-D wheel, a smaller depth of cut, and a smaller feed rate should be used. It is interesting to note that machine stiffness has the least effect on surface roughness and flexural strength but more specimens have to be ground and tested in order to draw a conclusion on the role of machine stiffness.

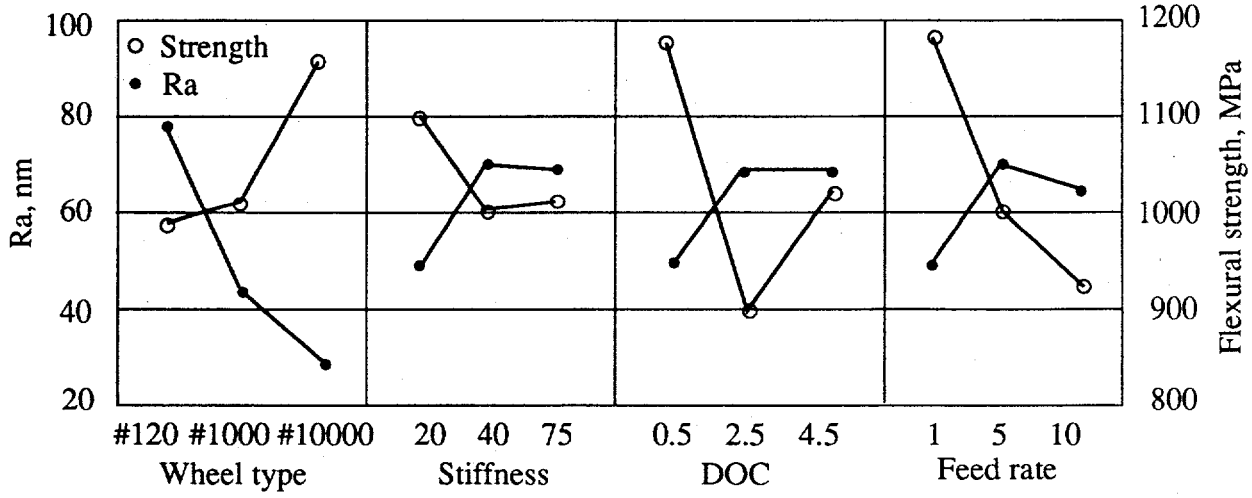

Figure 9 Analysis of experimental data from test runs 1 to 6 showing the effects of stiffness, depth of cut and feed rate, and from test runs 1 to 9 for analyzing the effect of grinding wheels on surface roughness and flexural strength

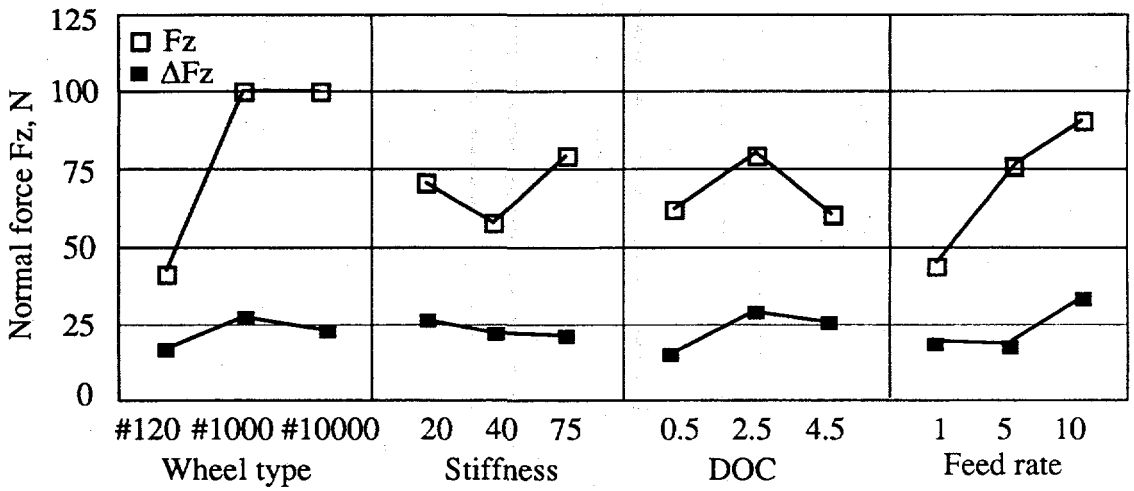

Figure 10 Analysis of experimental data from test runs 1 to 6 showing the effects of stiffness, depth of cut and feed rate, and from test runs 1 to 9 showing the effect of wheel type on the normal grinding force Fz and its variation ΔFz

The normal grinding force Fz and its variation ΔFz were also measured. Table 1 shows such a trend, i.e., for a specific grinding wheel, a smaller normal grinding force corresponds to a higher flexural strength. For the SD120-N100V wheel, the smallest Fz of 20.12 N corresponds to the highest flexural strength of 1,213 MPa. For the #1,000CIFB-D wheel, the largest Fz of 120.23 N corresponds to the lowest flexural strength of 946 MPa. For the #10,000CIFB-D wheel, the smallest grinding force corresponds to the highest flexural strength of 1,225 MPa. This is also true for the normal force variation ΔFz. Figure 10 shows the data analysis of the effects of factors on the normal grinding force Fz and its variation ΔFz. The data from test runs 1 to 6 are used for examining the effects of stiffness, depth of cut and feed rate, and the data from test runs 1 to 9 are used for examining the effect of wheel types. It appears that the feed rate and wheel type have larger influence on normal grinding force than stiffness and depth of cut do.

Status of Milestones

Milestone 1, April 29, 1996 Conducting the design of the work holder, the test of Dover grinding machine, the design of the quills for grinding wheels, the progress on the literature search, and an update on the procurement of materials for the work holder, wheels, workpieces, coolant, and dressers. (**Completed**)

Milestone 2, August 31, 1996 Carrying out the fabrication and testing of the work holder, and the baseline strength tests of a representative sample of workpieces. (**Completed**)

Milestone 3, December 31, 1996 Reporting the grinding tests, the four-point bending strength tests, subsurface inspection, surface measurements, and SEM studies of surfaces and subsurfaces of the ground workpieces. (**On schedule**)

Communications/Visits/Travel

Prof. Bi Zhang and Dr. Zhenqi Zhu went to Oak Ridge National Lab for the Annual Project Review meeting (Sept. 11 to 12, 1996).

The UConn team are cooperating with Dr. J.G. Sun of Argonne National Laboratory on evaluating surface and subsurface damage of silicon nitride specimens ground by the Dover grinding machine and ELID system using the laser scattering technique developed by the team at Argonne National Laboratory.

Problems Encountered

Our SEM does not function well and was under repair. Meanwhile, SEM inspection of specimen surfaces is done using the SEM of another research group at the university.

Publications (None.)

TESTING AND CHARACTERIZATION

X-RAY COMPUTED TOMOGRAPHIC IMAGING*

W. A. Ellingson, E. R. Koehl, H. P. Engel, J. B. Stuckey,
J. P. Pollinger and H. C. Yeh*

Objective/Scope

The original objectives of the Phase III work of this project were to: (1) study the utilization of high-spatial-resolution 3-D X-ray micro computed tomography techniques to study density distributions (X-ray densitometry) in composite green-state (as cast) pressure slip-cast ATTAP rotors; and (2) correlate destructive density analysis (to be conducted by Allied-Signal Ceramic Components) of the as-cast ATTAP rotors with the 3-D microtomography density data. Because the large ATTAP rotors are no longer of technical interest, a change was made to refocus the work to AS-800 Si_3N_4 using special billets with final data acquisition on Series 85 nozzles being produced by Allied-Signal Ceramic Components.

Technical Highlights

a) Software development

The image reconstruction software has been ported to the 133 Mhz dual Pentium computer and executes under the Microsoft Windows NT operating system. Debugging of this software suite was required to accommodate the more stringent nature of the 32-bit compiler in the Microsoft Fortran Powerstation for Windows NT. Such activities occur on an "as needed" basis.

A demonstration routine in the data display software package, IDL 4.0, has been modified by the vendor, Research Systems, Inc., at Argonne's request, to enhance the data manipulation tools for analyzing the cross-sectional and axial density profiles of reconstructed images. The resulting package is now being applied to Allied Signal ceramic components data sets.

b) Hardware Improvements

The HOMX-161 micro-focus X-ray machine has been modified to allow vertical positioning of samples 12 cm (4-1/2 inches) or less, in height. Positioning accuracies of 50 μm (0.002 in.) with a repeatability to 25 μm (0.001 in.) are now possible.

*Allied Signal Ceramic Components, Torrance, CA.

c) Densitometry

Densitometry data have been obtained from all three Allied Signal ceramic components AS800 samples (see Fig. 1). Initial data sets were used to assess the quality of the images and determine techniques to improve image quality. These initial sets have been superseded by more recent data.

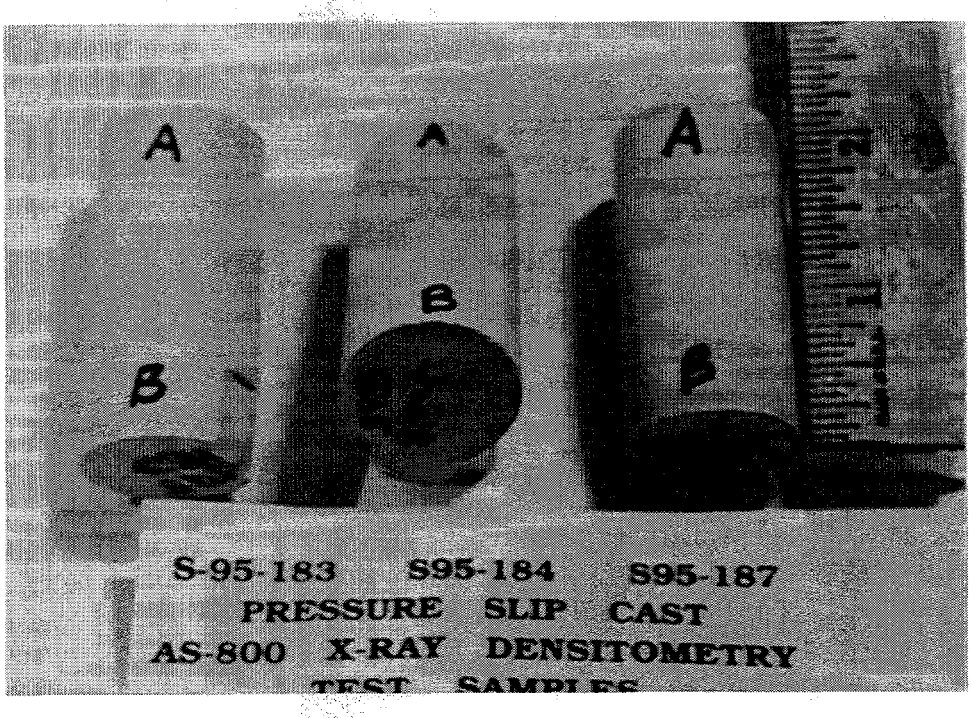

Fig. 1. Photograph of three pressure slip cast AS800 billets used to study X-ray CT densitometry.

An initial density profile has been generated for Allied Signal ceramic components sample S95183 (see Fig. 2). Note the chip seen in Fig. 1. The profile was obtained from a gray scale histogram function using a graphical display package, Adobe Photo Shop. The vertical axis is the average gray-scale value (range 0 - 255) for a slice. The horizontal axis is the slice number (location within the sample). This data indicates two anomalous occurrences: one at the midpoint, the other at the lower "B" end of the sample. Due to the length of the sample 50 mm, full 3D data could not be acquired in a single scan. Two 3D scans were made, each 2.5 cm in height. A step appears at the junction of the 2 data sets data probably due to a difference in scale factors which are selected automatically during the

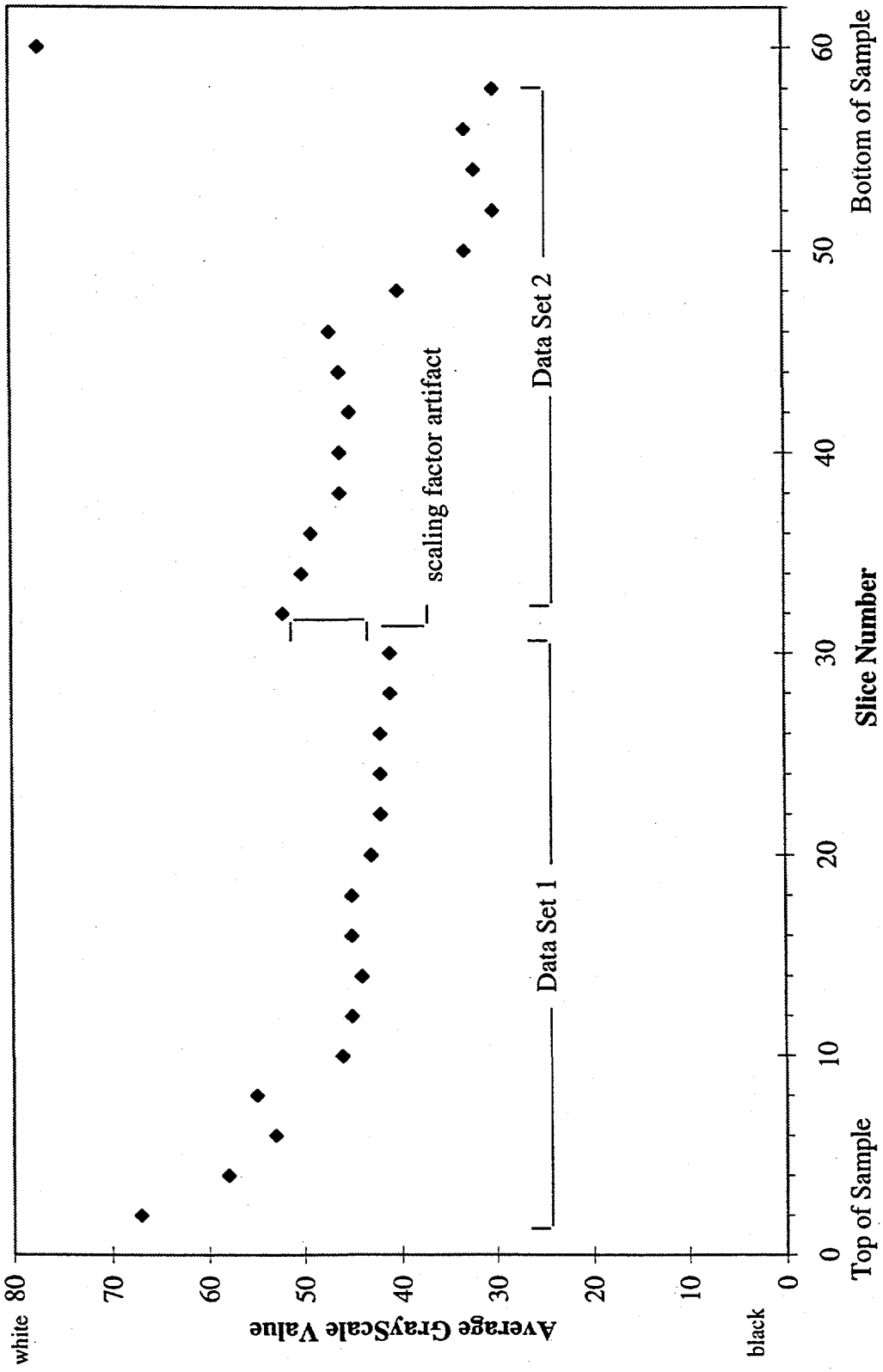

Figure 2. Initail axial density profile of Allied Signal Ceramic specimen S95183

reconstruction process. In addition, both ends of the sample are chipped. The bottom end of the sample has a sizable chip which extended through several slices. Since the gray scale values if averaged over the cross-section, a chip would suggest a lower average density. The end-points of the graph indicate that those CT slices include some data outside the physical boundary of the sample, i.e., air. This is an unavoidable result of the physical setup and the manner in which the reconstructed CT slices are obtained. These outer slices must be discarded when analyzing the sample density at the ends.

These data will be further analyzed with the new version of Interactive Data Language (IDL) by Research Systems Inc., and DIS by SMS. IDL is a data visualization and analysis computing environment. Both systems are able to perform batch operations on large data sets.

Figure 3 shows a typical reconstructed slice. The light line lying outside the left side of the slice is an external marker added to indicate the direction of the X-ray source.

Figure 4 shows a line (gray scale) profile through the center of the slice shown in Fig. 3.

This profile indicates that the edges of the sample are denser than the center region. The wavy variations occurring in the central region are ring artifacts from the reconstruction. The scale has been normalized with 0 (white) indicating saturation, and 1 (black) indicating maximum attenuation.

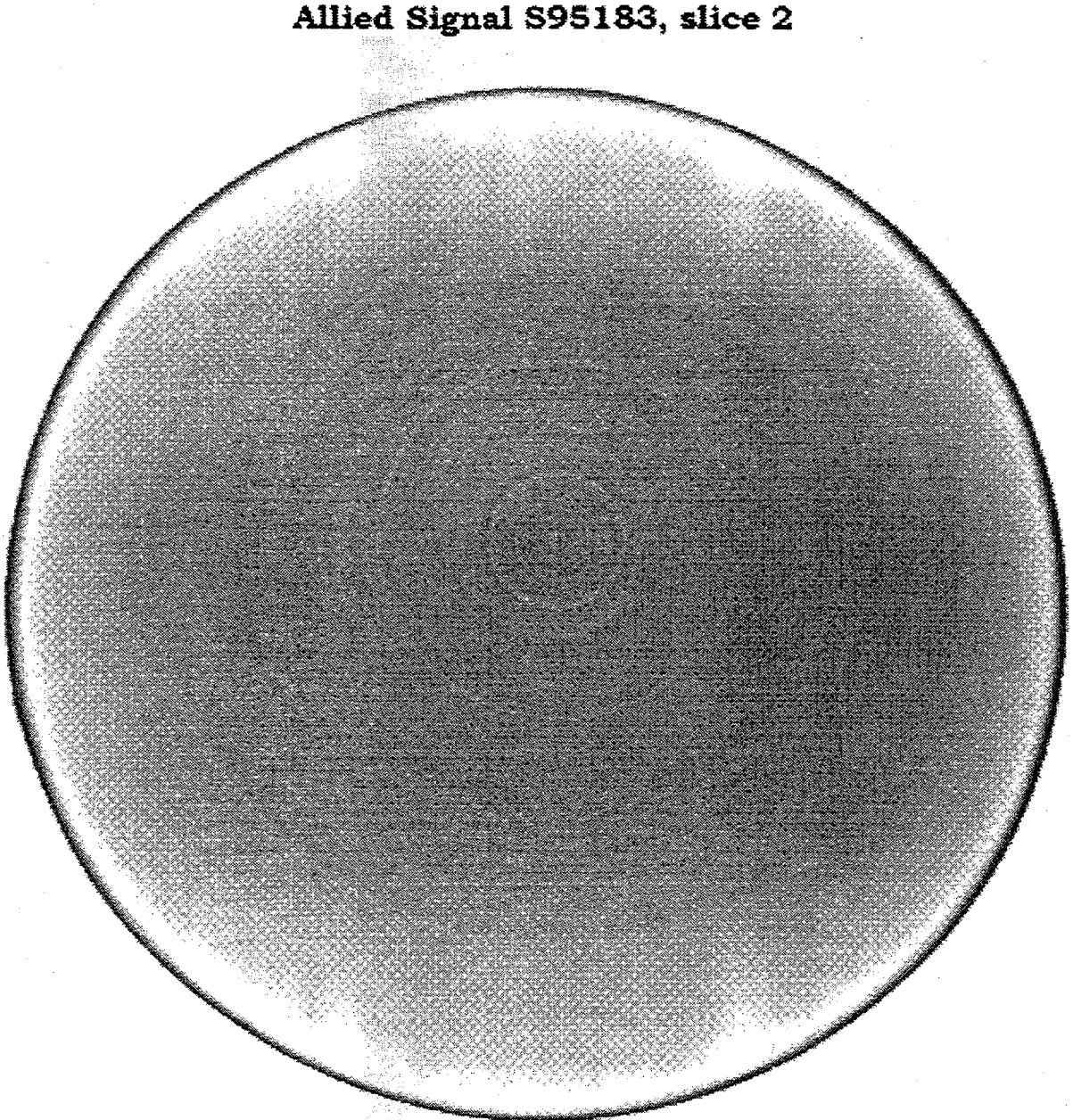

Figure 3. Typical X-ray reconstructed image of sample S95183 (Image from Slice 2)

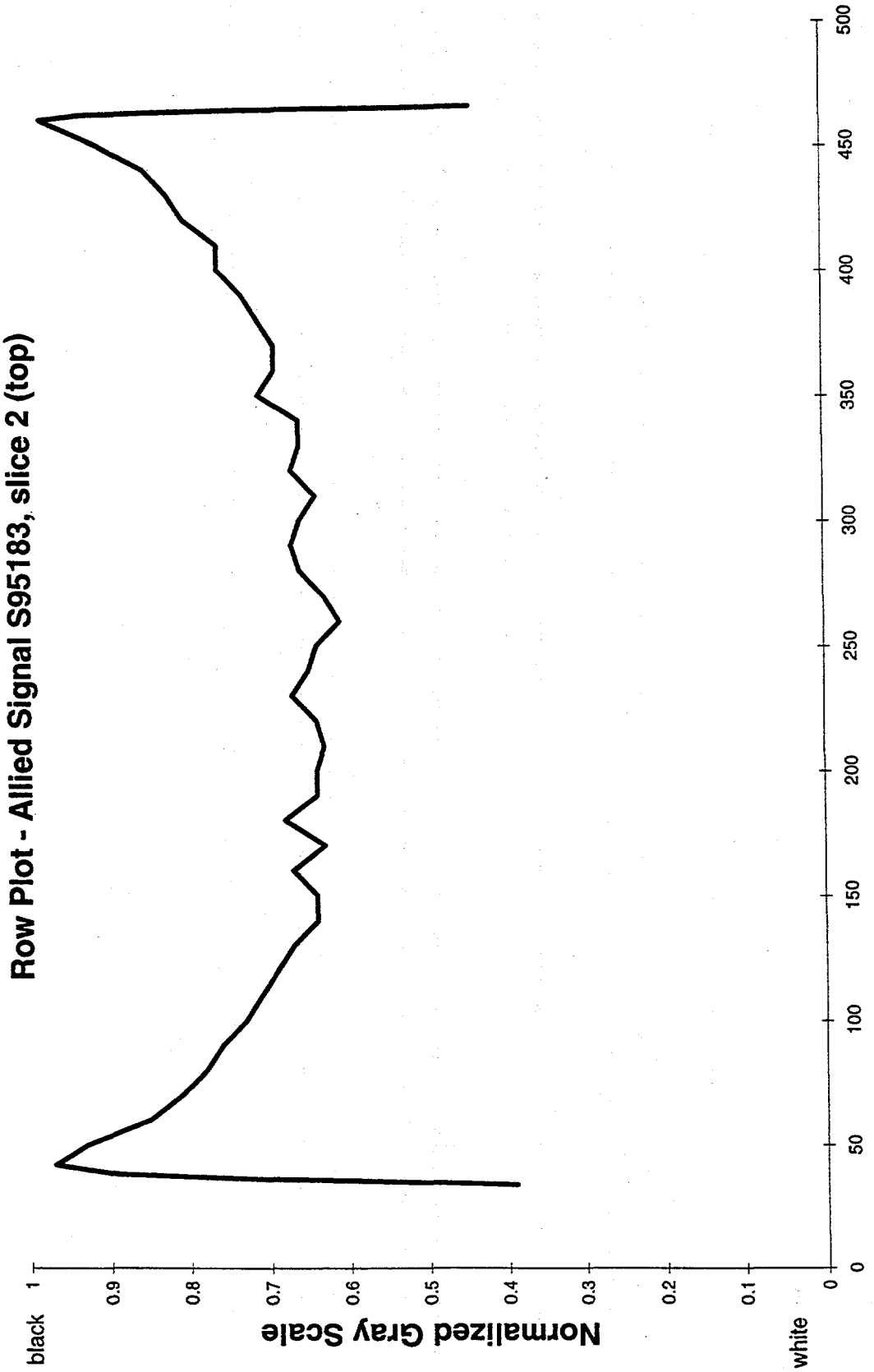

Figure 4. Diametral line plot across the reconstructed image shown in figure 2

Nuclear Magnetic Resonance Imaging

S. L. Dieckman, O. O. Omatate* , A. C. Raptis,
and W. A. Ellingson

Objective/Scope

The purpose of this work is to evaluate the potential of NMR imaging to impact the development and process control of near-net-shape gel-cast ceramic composites. The specific objectives of this work are to determine the utility of NMR imaging for: (1) 3D mapping of polymerization homogeneity; (2) real-time imaging of the polymerization process; (3) nondestructive evaluation of voids and flaws in the resultant components; and (4) measurement of physical properties such as degree of polymerization, viscosity, and specimen strength via correlation of these properties with measurable NMR parameters (T_1, T_{1r}, and T_2). This work will be performed in conjunction with Dr. Ogbemi O. Omatete from the Materials and Ceramics Division at Oak Ridge National Laboratory.

Technical Highlights

In previous reporting periods experimental NMR studies have been conducted on the methacrylamide-N,N'-methylene bisacrylamide (MAM-MBAM) copolymer system. These studies have included both spectroscopic and imaging experiments. The results have shown that NMR relaxation times are directly indicative of polymerization extent, and can therefore be used as an imaging modality showing polymerization rate and homogeneity. Experiments to date were performed on the spectrometer system in the Chemistry Division at ANL. This system however had distinct geometric and experimental operating constraints that has limited the utility of this system for applications to small specimens that are less than 1 inch in diameter. To overcome these restrictions, the Energy Technology Division at ANL has been installing a commercial NMR spectrometer and imaging system for the past several reporting periods. This system is capable of imaging large (6" diameter rotors) ceramic gelcast specimens with high resolution and speed.

In this reporting period, we are pleased to report that the installation of the Energy Technology Division's NMR imaging system has been completed, and that initial experimental results pertinent to this program have been obtained. These results include experimental studies on both gel MAM-MBAM polymer matrixes and MAM-MBAM polymer - Al_2O_3 matrix ceramic systems. These set of experiments were chosen to establish the efficacy of the NMR techniques for monitoring polymerization reactions, and the concentration of water in drying gel-Al_2O_3 matrix specimens. It has been established by ORNL that these phenomena are of considerable importance for the further development of the ceramic gel cast processing technology.

Initial studies were performed on a standard specimen (often termed phantom) containing water, polymerized MAM-MBAM polymer gel, and unpolymerized MAM-MBAM polymeric reactants as presented in the photo (see Figure 1A) and a representative high-resolution axial image obtained from the specimen is shown (Figure 1B). Additional images from the same area in the specimen that

*Metals and Ceramics Division, Oak Ridge National Laboratory

were acquired with increasing temporal delays in the imaging sequence are presented in Figure 2. The tubes in the middle and at the top contain polymerized MAM-MBAM gel and thus exhibit a decrease in image intensity as a function of imaging delay. Furthermore the top tube was polymerized with a large excess of initiator while the nonpolymerized reactants (in the tube at roughly 2 O'clock) show no difference in image intensity than the water viles in the other four sample locations. Further application of these techniques will allow direct monitoring of polymerization extent throughout the gel matrix.

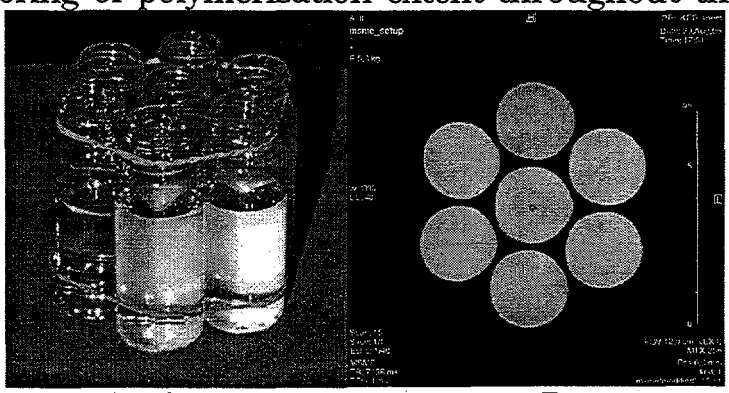

A. B.

Figure 1. A) Imaging specimen consisting of a series of glass viles containing polymer, unpolymerized gel reactants (monomer and cross-linking agent, and water) and water. A high resolution axial image obtained from the specimen is shown in B.

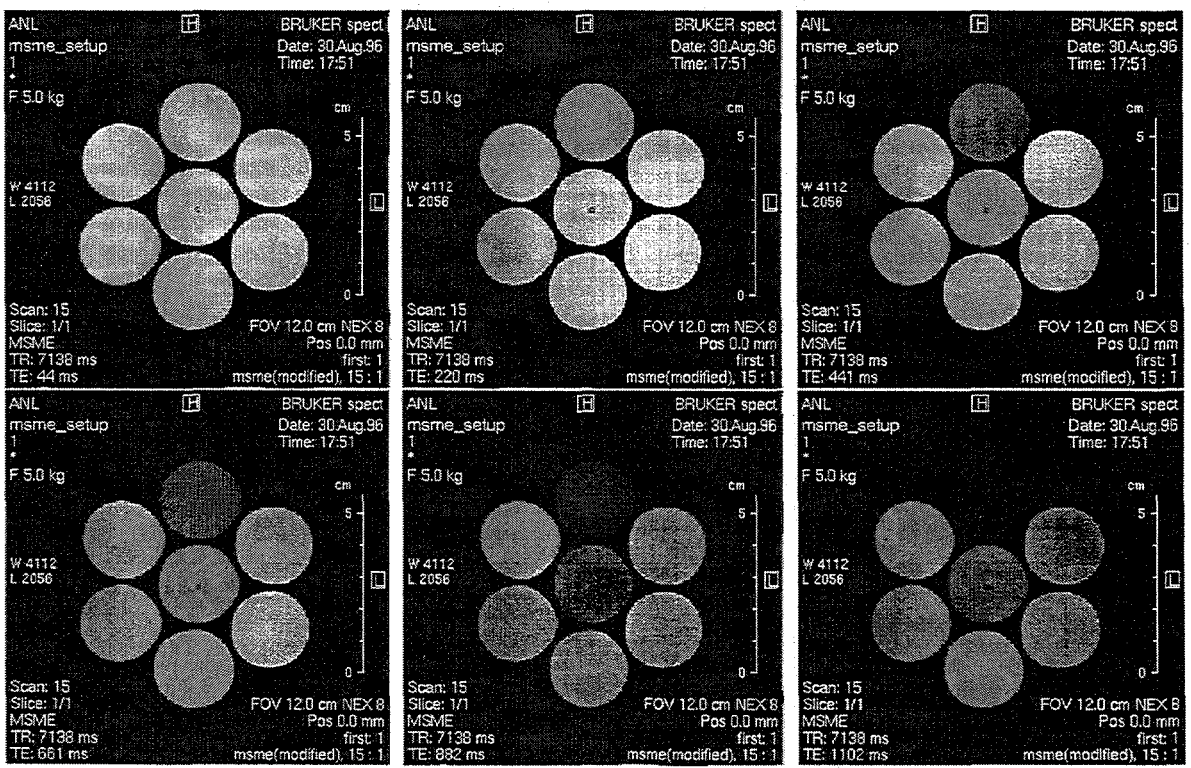

Figure 2. A series of axial images obtained with increasing temporal delays from the specimen shown in Figure 1.

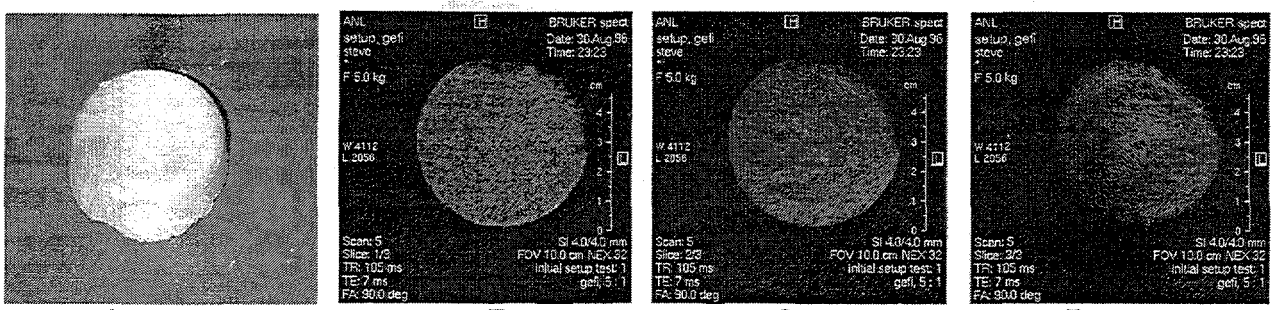

Figure 3. A) Photo of a gel-cast specimen composed of 15% polymer (by weight) and 50% Al_2O_3 solids loading by volume. B-D) Axial images obtained nondestructively from three locations throughout the specimen.

A third set of imaging experiments was performed on the gel-cast specimen shown in Figure 3A. This specimen consisted of a 2.5 inch diameter disk containing 15% polymer matrix with 50% by volume Al_2O_3 solids loading. Initial experimental studies were performed 24 hours after polymerization was initiated and with subsequent storage of the specimen in 100 % relative humidity at ambient (laboratory) temperature. Variations in image intensity indicate free water content in the composite. These experiments pave the way for future studies which will focus on determining water distribution and shrinking in drying ceramic specimens.

Considerable effort has been devoted to developing composite sample molding and polymerization techniques. This is a necessary step to support the composite polymerization and drying NMR studies that ORNL has determined will aid the development of the ceramic gel-cast technology. Technical efforts have therefore focused on developing suitable molds, finding appropriate mold release agents, establishing chemical reaction conditions, and discovering optimal reactant concentrations. A set of representative photographs of the molds and process is presented in Figure 4. Several mold materials were evaluated including two types of plastics, glass, and aluminum. The use of the plastic materials produced mixed success, often characterized by incomplete reaction at the mold surface. It is thought that the reaction interference results from bound oxygen on the mold surface, or competing polymerization reactions near the plastic surface. The glass and aluminum molds provided a more complete polymerization reaction at the surface, however, they produced a poor specimen-mold release. At the suggestion of ORNL the aluminum surfaces were anodized. Anodizing the surface produced a much smoother mold surface and noticeably improved the specimen release. Additionally, we are in the process of evaluating several types of mold release agents. Degassing of the molded specimens using a rough vacuum and a vacuum desiccator showed significant increase in reaction rate and extent. Future experiments will be performed in a nitrogen atmosphere using a glove box environment. In this manner, we will minimize the dissolved and entrained oxygen in the

specimens. Furthermore we have established a series of relative humidity chambers using saturated salt solutions. These environments range from 51% to 97% RH at ambient temperatures. We are also in the process of manufacturing six standard molds. The molds will allow the simultaneous casting of multiple specimens from the same sample mix for the drying studies. Additional work will contunue on both real-time polymerization monitoring, and on matrix drying as a function of relative humidity and time.

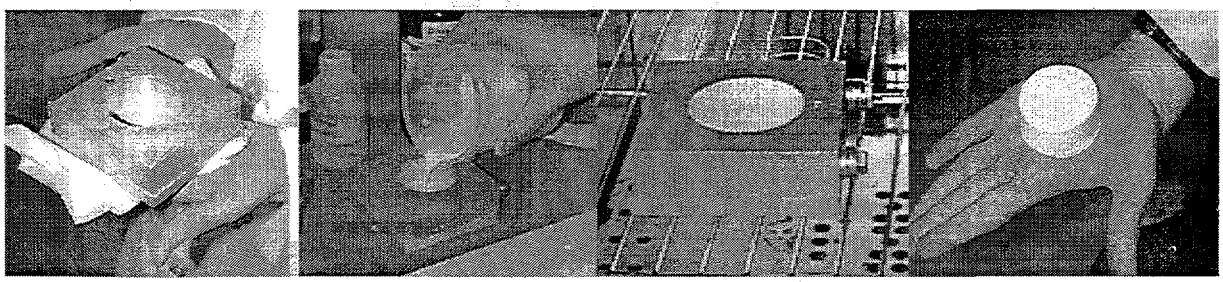

Figure 4. Photographs documenting an experimental series showing from left to right ANL's anodized aluminum mold, casting of gel-Al_2O_3 matrix, curing of reactants at 40°C , and the resultant cast 1" high by 2" diameter green-state gel-cast ceramic composite specimen.

TESTING AND EVALUATION OF ADVANCED CERAMICS AT HIGH TEMPERATURE

J. Sankar, A. D. Kelkar, V. Vijayrao and Q.Wei (Department of Mechanical Engineering, North Carolina A & T State University, Greensboro, NC 27406).

Objective/Scope

The objective of this research is to test and evaluate the long-term mechanical reliability of a Si_3N_4 at temperatures up to 1300^{o}C.

The required research includes four (4) major tasks:

Task 1. Cyclic Fatigue Testing of PY6

Cyclic fatigue of GTE-PY6 silicon nitride shall be performed at lower temperatures to investigate 500^{o} -1100^{o}C characteristics of the material at this temperature range. At these lower temperatures, there may be a true cyclic fatigue effect which enhances failure compared with the static load case.

Task 2. Stress - Rupture Study of PY6

Stress-rupture testing of GTE PY6 silicon nitride shall be performed at a lower temperature range of 500^{o} - 1100^{o}C. Since there is little information about the time dependent behavior of this material is available at this temperature regime, this task should provide some valuable data.

Task 3. Tensile Testing of GS 44

Pure Uniaxial tensile testing of GS 44 silicon nitride will be carried out at both room and elevated temperature up to 1200^{o}C. The obtained data will be compared with other silicon nitride materials.

Task 4. Stress - Rupture Study of GS 44

Stress-rupture testing of GS 44 silicon nitride will be performed at various temperatures and stresses.

Technical Highlights

Creep testing:

During this reporting period, high temperature tensile creep tests were performed on PY-6 hot isostatically pressed (HIped) silicon nitride material. The testing temperature was maintained at 900 ^{o}C. The test was also performed for different loading conditions, namely 267Mpa and 313MPa. creep strain vs time graphs were plotted, the creep curves are shown in Figure 5. Further, some tests were stopped during the secondary creep stage and will be tested for tensile residual strength. All the residual strength tests will be carried out at room temperature.

Table 1: Summary of Creep Tests

Room Temp Strength		= 631MPa
Strength @ 900°C		= 470MPa
Condition		Result
1	Creep : 900°C, 267MPa - 510hrs	Did not fail
2	Creep : 900°C, 313MPa - 0.1 hrs	Failed

Morphology Changes Accompanying Creep Of Sintered Si_3N_4

This section addresses the investigation of morphological changes upon creeping of a sintered silicon nitride (Allied Signal GS44) for hot turbine application. Transmission electron microscopy (TEM)(both high resolution and normal), field emission scanning electron microscopy (SEM) and energy dispersive spectroscopy are employed to study the grain boundary and triple junction glassy phases, the dislocation structure, fractography and surface deterioration of the samples. The results are discussed in combination with the creep behavior of the material. Further studies are suggested at the end of this work.

TEM samples were cut from the virgin (as-received) sample and from the gage section of the creeped samples and then mechanically thinned to 50-80 μm. The creep tests were carried out at 1275 and 1200°C, respectively, under various loads. The samples were subsequently dimpled to get a thin area of about 5 μm of thickness using a precision dimple grinder. The dimpled samples were then loaded into a double gun ion milling machine to mill the samples to make them electron transparent. TEM observations were carried out on TOPCON 002B. The as-ruptured surfaces were analyzed in SEM (JEOL 6400F) for fractographic observations. The EDS was initially

done on the cross section of a sample thermally soaked in air at 1200°C for 32 hours with a windowless mode in the SEM with a field emission electron source.

Fatigue Testing:

PY-6 HIPed (hot isostatically pressed) Si_3N_4 material was also tested for failure under cyclic loading at high temperature.. The tests were performed in tension/tension (T/T) mode. A cyclic triangular waveform was used to determine and control the frequency and stress amplitude during testing. All the tests were performed until failure occurred. The temperature during the test was maintained at 1000°C. Maximum loads of 65% - 80% of the UTS were applied in order to obtain the S-N curve for the material. The S-N curve obtained was compared to that of GS-44. Following these tests, microstructural investigations will also be performed on the material.

Cyclic fatigue tests were also performed on GS-44 Si_3N_4. The temperature during the test was maintained at 1100 °C. All tests were performed until failure occurred. The fatigue limit of the sample was determined using the empirical formula:

$$\sigma_{fl} = 70\%\sigma_{uts} .$$

where σ_{fl} is the maximum fatigue stress limit and σ_{uts} is the ultimate tensile strength at that temperature.

Also, the tests were performed at various stress levels including $70\%\sigma_{uts}$,$60\%\sigma_{uts}$ and $50\%\sigma_{uts}$ to enable us to determine the S-N curve for GS-44 at 1200°C.

Fatigue loading conditions -- Tension-tension cyclic triangular waveform:

Frequency :	0.1 Hz
Total number of cycles :	Until failure occurred
Temperature :	1000°C
R-Ratio (min. stress/max. stress) :	0.1

Effect of Oxidation on Sintered Silicon Nitride

Since the source of the specimen failure during creep testing is due to the stress oxidation damage zone which occurs when the test temperature is increased and the stresses are kept relatively low. Only 15-35% of the tensile strength was applied at high temperatures for the creep tests performed. In order to find the effect of oxidation the creep tested specimens were cut within their gage sections and metallographically polished to a 0.30μm finish. The polished cross-sections of the creep specimens tested at 1200 °C and 1275 °C are shown in Figure 6. To study the effect of oxidation alone without any creep stress the specimens were thermally soaked for different periods of time at 1275 °C. Figure 7 shows the effect of oxidation for 16,24,32 and 40 hrs.

RESULTS AND DISCUSSION

1. Creep Test Results

A creep curve was plotted from the data obtained from the above tests The creep curve shows the creep strain vs time at 900 °C and 267 Mpa of PY-6. It can be observed that the creep strain is steadily increasing during the test. Also , the tested sample did not fail even after 510 hrs of loading. However the tests conducted at 1200°C and above showed failure. This may indicate that the mechanical properties of PY-6 maybe temperature sensitive. The results of the tests performed are shown in Table 1.

2. Microstructural Investigations

Fig. 1a is a general view (TEM) of the microstructure of the as-received silicon nitride. Triple junction and grain boundary having amorphous phase are indicated with arrows in Fig. 1b and Fig. 1c, and the insert diffraction pattern in Fig. 2b corresponds to the triple junction amorphous phase; while Fig. 1d shows the dislocation networks (dark field) representative of sintered silicon nitride. Fig. 2a shows the gap between two grains which is formed during the creeping process, indicating grain boundary sliding as a deformation mechanism. This kind of gaps can play as cracks and their further development can lead to failure of the whole sample. The so-called strain whorls are frequently observed, as shown in Fig. 2b, suggesting that some large grains might have accommodated the total strain of the sample during the deformation process. The dislocation pile-ups observed in some large grains, as shown in Fig. 2c, also supports the occurrence of this secondary deformation mechanism. Here it is considered to be secondary because the creep deformation could not be dominated by the dislocation mechanism since the stress exponential component calculated based on the experimental results is close to unity. This is indicative of a diffusion mechanism and the creep activation energy is ca. 540KJ/Mol, typical of grain boundary diffusion of oxygen in silicon nitride.

SEM shows (Fig. 3) no cavitation as is typical for HIPed silicon nitride. Therefore, the creep mechanism of sintered silicon nitride is significantly different from that of HIPed silicon nitride.

Though a number of investigations have been reported of oxidation of single crystal silicon nitride films for semiconductor applications, much less has been known for bulk silicon nitride material. It can be predicted that the mechanism for oxidation

would be very different since in the case of bulk material, either sintered or HIPed, a large number of pores can be expected as well as a large amount of amorphous grain boundary phase which can remarkably enhance the diffusion of the reactants. Therefore, Wagner's parabolic law of oxidation may not be applicable anymore. We have studied with EDS, the compositional changes of silicon nitride due to high temperature soaking in air. A piece of *ca.* 6mm in diameter was cut from the soaked sample. Fig. 4a shows the energy dispersive spectrum from the center of the sample. It shows a huge peak of Si and some Al, Mg, and oxygen due to the presence of the sintering aids. The peak of nitrogen is absurdly small because of the serious absorption of the characteristic lines from nitrogen. Fig. 4b is the energy dispersive spectrum from the edge, viz. the surface scales of the sample. The depletion of Si and Mg elements in the scales is obvious. It is then clear that material loss occurred during thermal soaking in air. Since the enroachment of the surface of the sample will decrease its effective cross sectional area and hence raise the stress intensity level, and even initiate cracks, the surface deterioration will make the high temperature performance in corrosive atmosphere degrade with time. A way to apply a protective surface coating of strong oxidation resistance may be helpful in promoting the performance of the material under service.

A large amount of amorphous phase in the grain boundaries and triple junctions were observed and gaps between the silicon nitride grains formed because of creep. Dislocation pile-ups indicate the deformation of some grains, but it's a secondary deformation mechanism in the creep of this material since the stress component is close to unity, suggesting that the creep is dominated by the diffusion mechanism. SEM fractography shows no cavities. Surface deterioration of the samples occurred at high temperatures in corrosive atmosphere and the scales thus formed are depleted of Si and Mg, indicative of material loss because of chemical enroachment. Protective surface coating to promote the high temperature performance of the material is recommended for further investigations.

Fatigue Test Results:

Figure 8 shows the S-N curves for PY-6 (HIPed) and GS-44 (sintered silicon nitride). The data obtained from the high temperature fatigue tests for both materials were plotted and the S-N curves were compared. It is evident that fatigue under tension/tension mode is detrimental to both materials at high temperature. However, GS-44 shows more resistance to fatigue failure at 1100°C than PY-6 at 1000°C. Also, stress levels below 65% of the ultimate tensile strength may not lead to failure in PY-6. In the case of GS-44, stress levels below 50% of the UTS need to be applied to ensure that there is no failure. This however, is due to the fact that GS-44 has a much higher UTS than PY-6. Currently more tests are being performed at temperatures of 900 °C and below to determine the fatigue behavior of PY-6 at these temperatures.

Status of Milestones

On schedule

Communications/Visitors/Travel

None

Problems encountered :

None

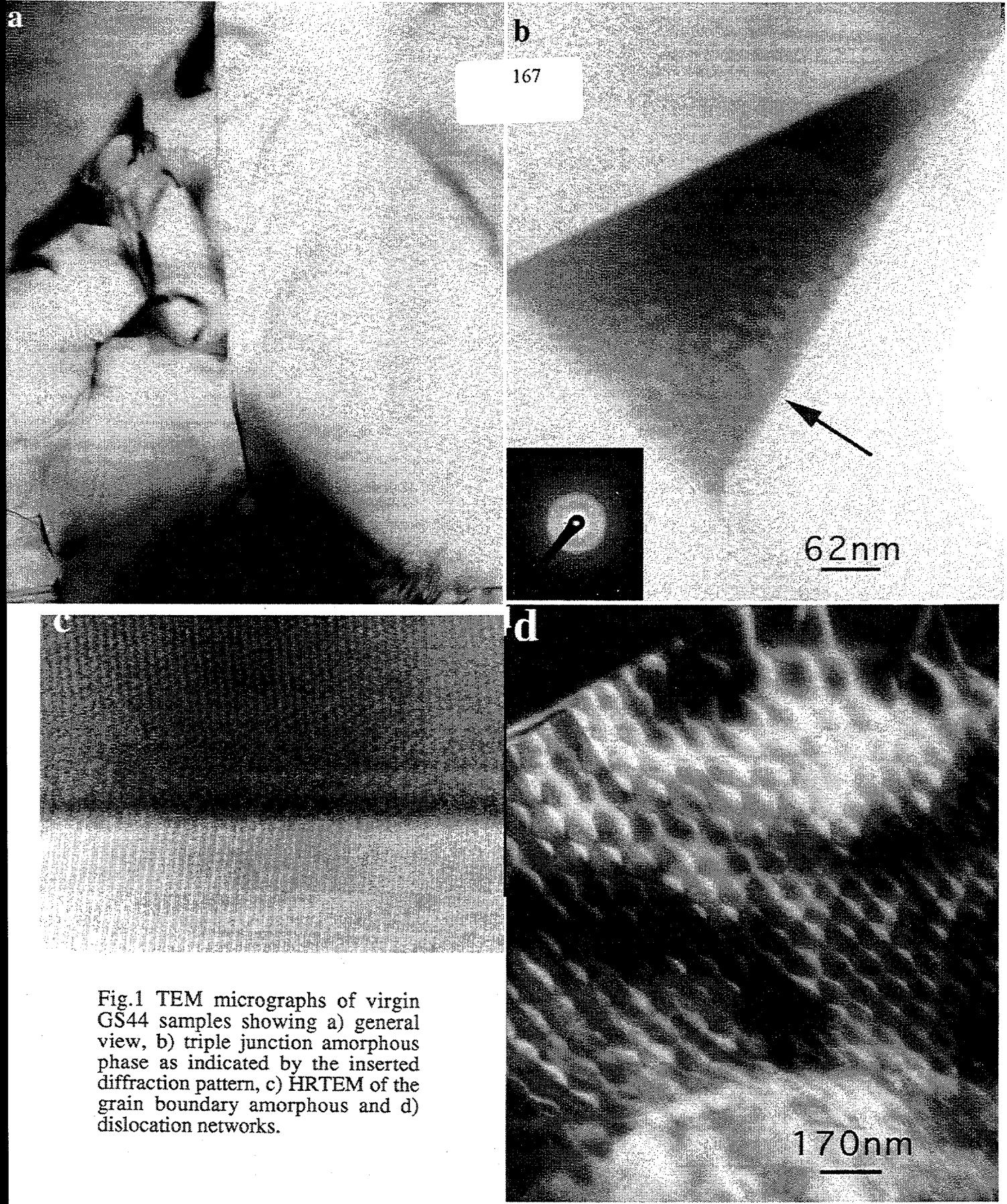

Fig.1 TEM micrographs of virgin GS44 samples showing a) general view, b) triple junction amorphous phase as indicated by the inserted diffraction pattern, c) HRTEM of the grain boundary amorphous and d) dislocation networks.

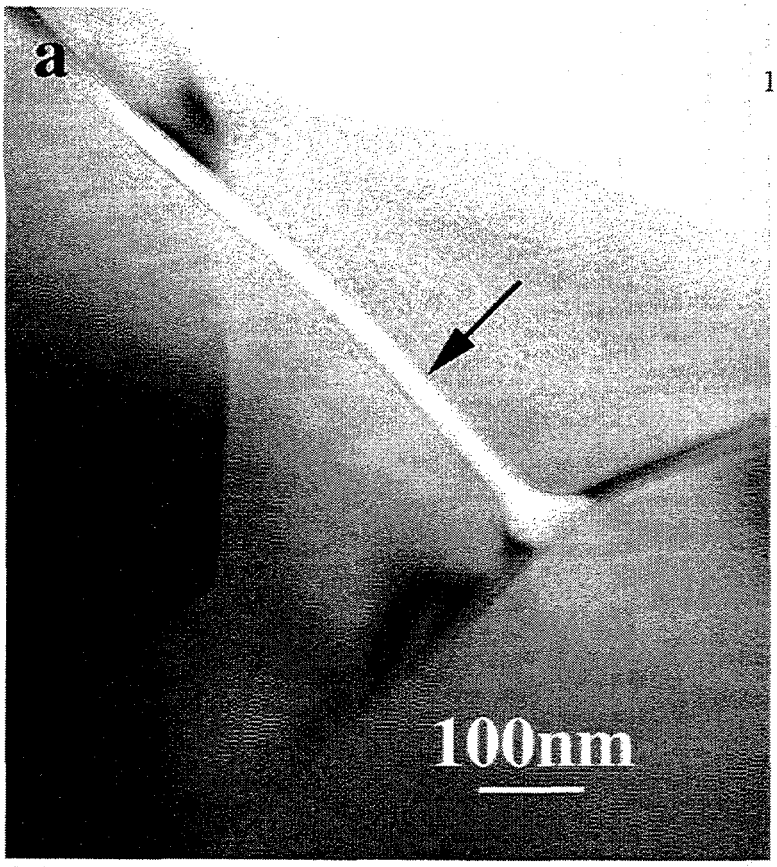

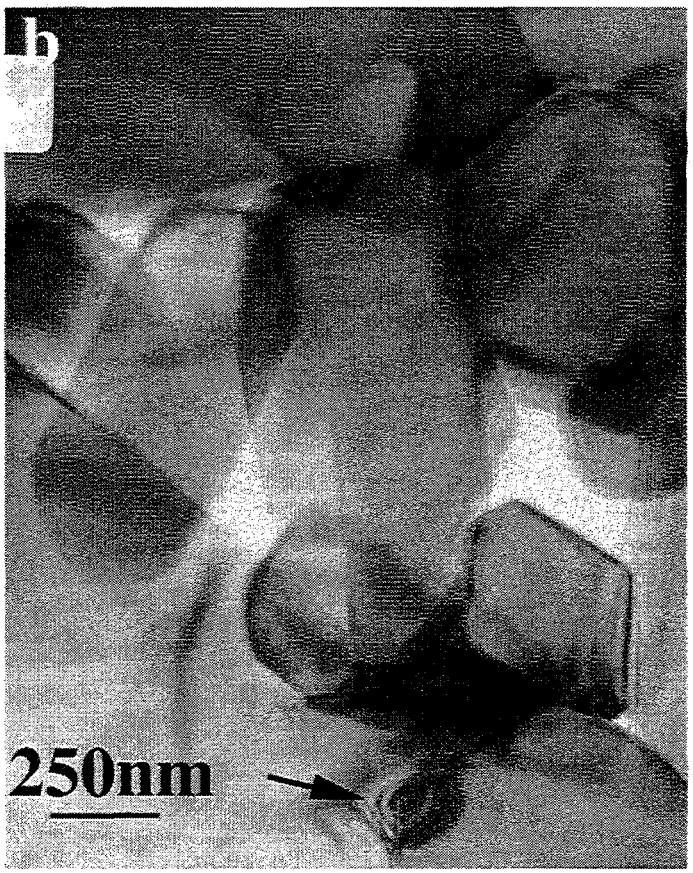

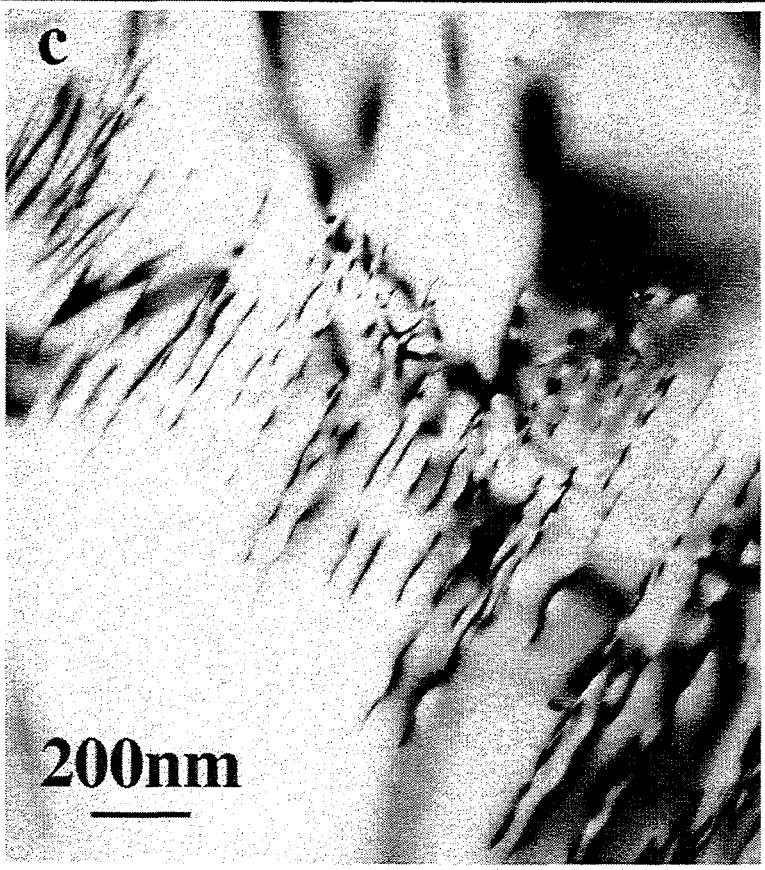

Fig.2 TEM micrographs of creeped GS44 samples showing a) gap between two silicon nitride grains, b) strain whorls formed during creeping and c) dislocation pile-ups formed due to deformation of the grain.

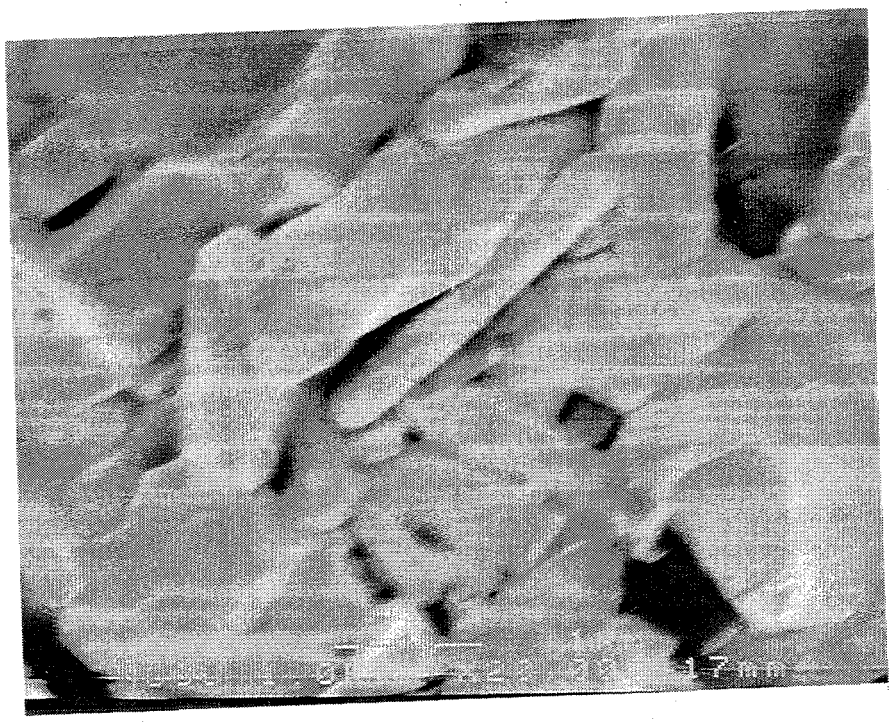

Fig.3 SEM micrograph showing no cavitation due to creep.

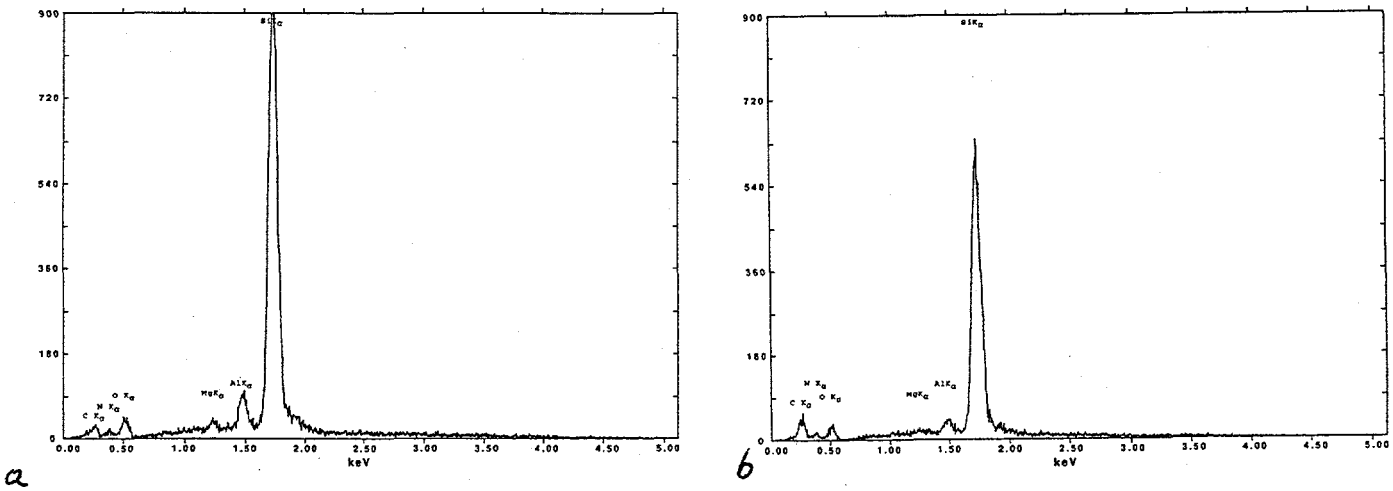

Fig.4 EDS of the cross section of GS44 thermally soaked at 1200°C for 32 hours. Explanations are referred to the text.

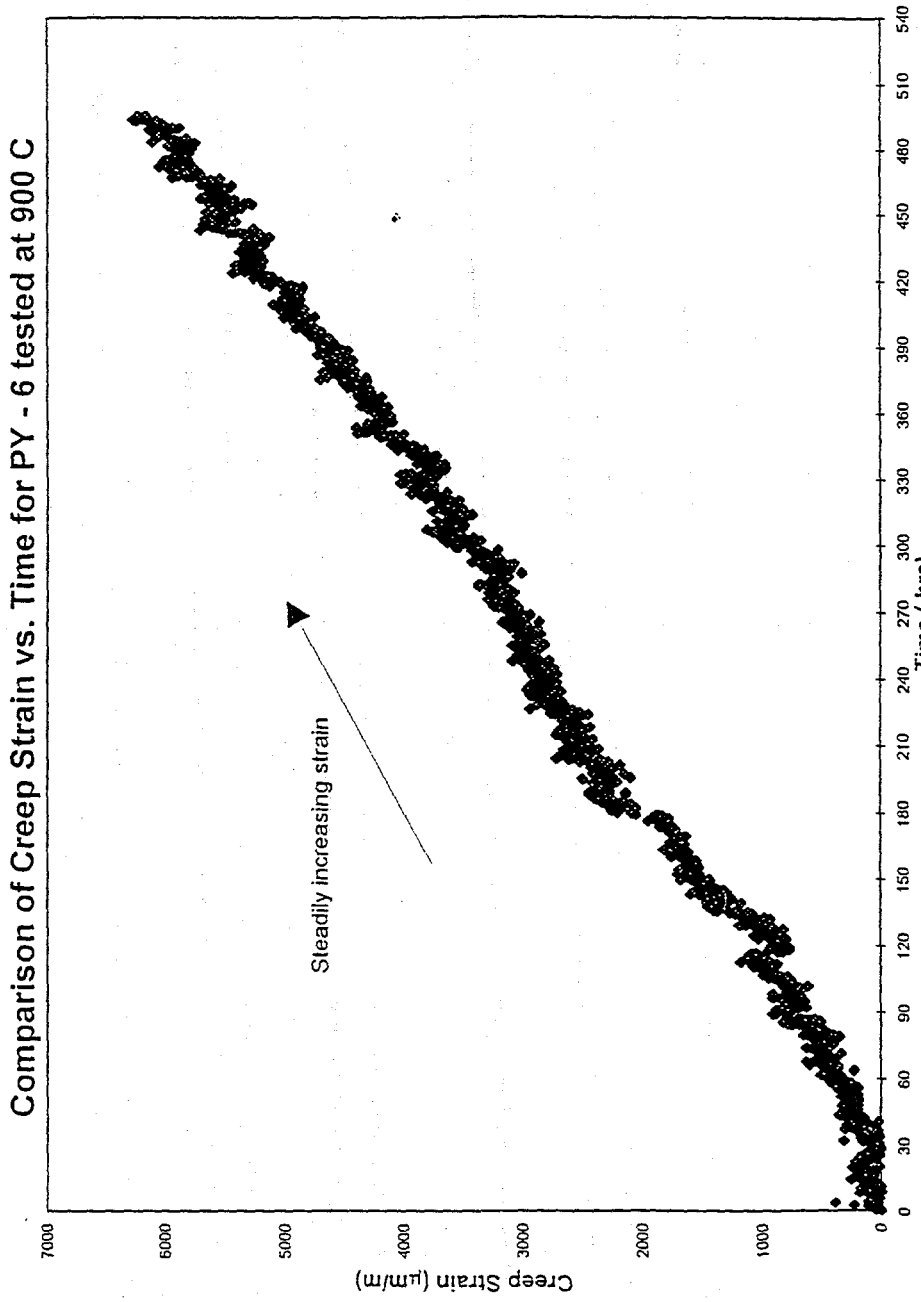
Comparison of Creep Strain vs. Time for PY - 6 tested at 900 C
Steadily increasing strain
Creep Strain (μm/m)
Time (hrs)
0
1000
2000
3000
4000
5000
6000
7000
0
30
60
90
120
150
180
210
240
270
300
330
360
390
420
450
480
510
540

Figure 5

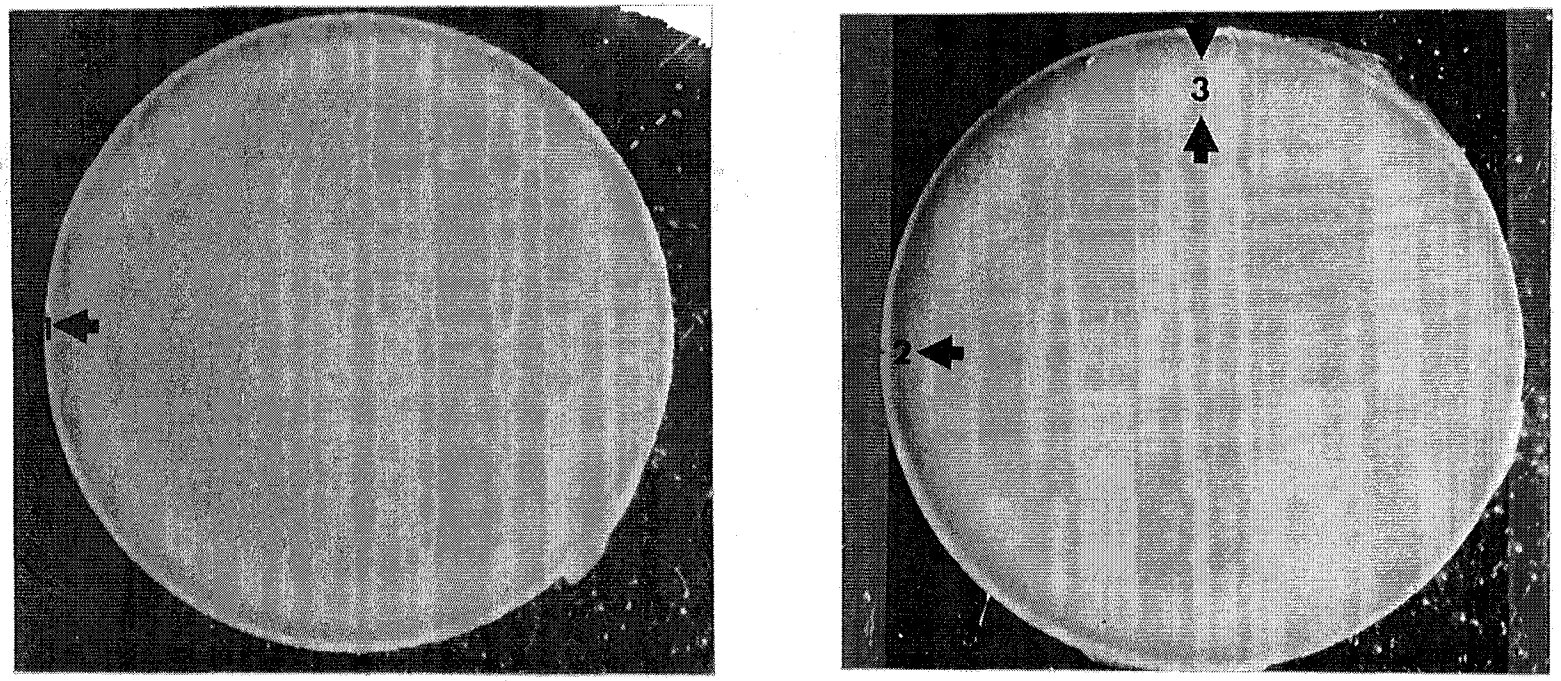

Figure 6: Polished cross sections of GS 44 tested at a)1200oC and b) 1275oC showing annular regions.

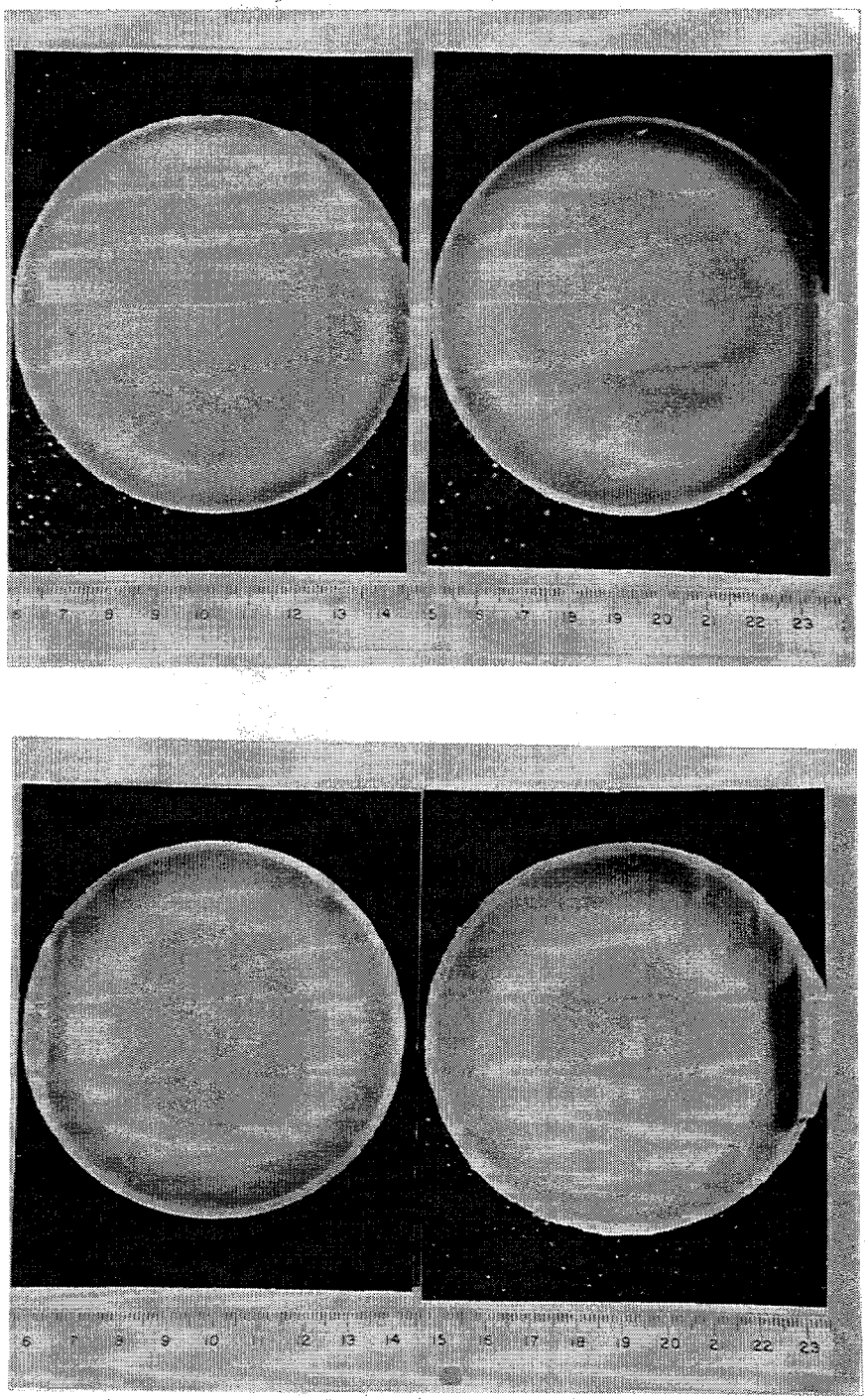

Figure 7: Polished cross sections of GS 44 which were thermally soaked for 16, 24, 32, and 40hrs

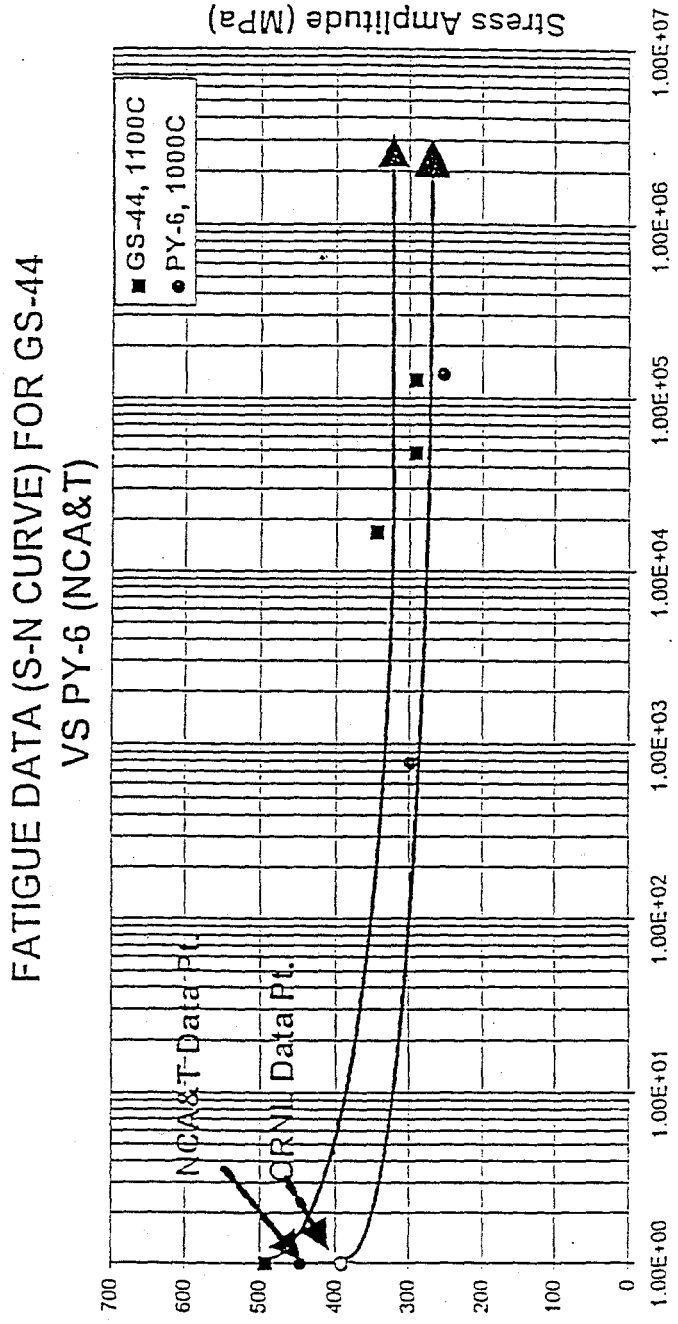
FATIGUE DATA (S-N CURVE) FOR GS-44
VS PY-6 (NCA&T)
Stress Amplitude (MPa)
Number Of Cycles To Failure
GS-44, 1100C
PY-6, 1000C
NCA&T Data Pt.
ORNL Data Pt.
700
600
500
400
300
200
100
0
1.00E+00
1.00E+01
1.00E+02
1.00E+03
1.00E+04
1.00E+05
1.00E+06
1.00E+07

Figure 8

3.2.1.6 *Life Prediction Verification*

A. A. Wereszczak, M. K. Ferber, T. P. Kirkland, and M. J. Andrews (ORNL)

Objective/Scope

There are three central goals of the proposed research program: the generation of engineering data from high temperature mechanical testing; microstructural characterization of failure phenomena; and the implementation and verification of life prediction methods involving structural ceramics. Ultimately, the prediction of the high temperature mechanical performance and service life is information that is critical for the progress towards implementation of structural ceramics as components in internal combustion and automotive gas turbine engines.

The systematic study of the high temperature mechanical performance of a silicon nitride and a SiAlON is undertaken as a function of temperature and time. A different temperature regime will serve as an independent parameter for each material. Studies on both SiAlON and silicon nitride will be conducted at temperatures ≈ <1000°C, while studies with only silicon nitride will be at temperatures ≈ >1000°C; these are likely operating temperature thresholds for internal combustion and automotive gas turbine engines, respectively. For the lower temperature regime, properties such as strength and fatigue life will be measured in the SiAlON and silicon nitride material as a function of temperature. For the higher temperature regime, tensile stress-rupture data will be generated on silicon nitride by measuring fatigue life at a constant or cyclic stress. The time-dependent deformation will also be monitored so that high-temperature creep and its effects may be studied.

The second goal of the program is to characterize the evolution and role of damage mechanisms associated with high temperature deformation. The damage will be examined using established ceramographic, SEM, TEM, and non-destructive acoustic techniques. Several microstructural aspects of high-temperature failure will be examined:

(1) the extent of slow crack growth;
(2) the evolution of cavitation-induced damage and fracture;
(3) the transition between brittle crack extension and cavitation-induced growth;
(4) crack blunting; and
(5) the evolution and role of oxidation-assisted damage.

Lastly, available analytical and numerical models will be utilized to predict the life of complex-shaped components and prototype engine parts (e.g., valves). The applicability of analytical models such as the Monkman-Grant and the Sherby-Dorn models to

structural ceramics will be examined, and modifications will be made where necessary to refine the models and improve their predictive capabilities. Numerical models (i.e., life prediction codes) will also be used in conjunction with generated strength data from standard test specimens to predict the failure probability and reliability of complex-shaped components subjected to mechanical loading, such as a SiAlON or silicon nitride diesel engine valve. As a consequence of these efforts, the data generated in this program will not only provide a critically needed base for component utilization in internal combustion and automotive gas turbine engines, but also facilitate the development of a design methodology for structural ceramics subjected to mechanical loading in general.

Technical Progress

During the present reporting period, work continued to generate the necessary information required for the life prediction of the S149 NT451 SiAlON valves. This included the generation of an "input" tensile specimen geometry for the utilization of AlliedSignal's CERAMIC and ERICA codes, the continued refinement of the valve finite element analysis model which is also needed for these two codes, and the continuation of fractography of the bend bars and tensile specimens tested to date. In addition, insight was gained into what advantages and disadvantages the AlliedSignal's codes have compared with NASA's CARES/LIFE program.

In order to use tensile strength data from tests conducted with the modified ORNL buttonhead specimen used in these life prediction exercises, input data that was uniquely characteristic to this geometry needed pre-defining. The CERAMIC code already recognizes several standard geometries including Mil-Std bend bars, and the conventional ORNL buttonhead specimen. If strength or fatigue data is generated using one of these standard geometries, then the CERAMIC code may be readily used to predict life and confidence bounds on life with this data. However, the tensile specimen used in these studies was machined from stems in supplied valve blanks (whose diameter was approximately 10mm), so it was required that the whole ORNL buttonhead geometry be modified and scaled down from its conventional size. In order for CERAMIC to allow input from tensile strength tests from these specimens, the stress gradient factor (I) needed to be determined as a function of Weibull Modulus (m); this step was performed using AlliedSignal's ERICA code. An axisymetric finite element model of this modified ORNL buttonhead specimen (subjected to uniaxial tensile stress via a copper-collet loading system) was constructed in ANSYS, and the results file from it were inputted into ERICA. A range of Weibull Moduli were independently varied, and the I was determined as a

function of m for surface and volume integrations. This tensile specimen has no edges that are parallel to the uniaxially applied stress, so I for edge integrations was not needed. This function of I vs. m was then stored, and will be used whenever tensile strength data generated from this geometry is inputted into CERAMIC to predict the life of an arbitrary component made from the same ceramic material. As a verification check to the I vs. m definition of this modified ORNL tensile specimen, the failure probability of this modified ORNL specimen was then "predicted" and compared with experimental data; if the described process was successful, then the tensile strength data and the predicted probability of failures should be in agreement.* The probability of failure as a function of tensile stress for this modified ORNL buttonhead geometry is shown in Fig. 1, and the agreement in "prediction" and data show that the described process proceeded correctly.

A substantial amount of time was spent during the present reporting period in obtaining convergent solutions to the ANSYS finite element model of the SiAlON valve in frictional contact with the steel valve seat. The goal is to obtain the dependence of the maximum principal tensile stress as a function of the friction coefficient between the valve and the seat, and the applied pressure as well. The stress solution reported in a previous report [1] was for a coefficient of friction between the valve and seat of 0.3 at a pressurized face loading of 16 MPa; however, because friction is present in this model, the maximum principal tensile stress does not linearly scale with applied pressure. Being that the valves will be loaded to failure in future mechanical tests, the knowledge of larger-valued pressures and corresponding maximum principal tensile stresses is required to predict the probability of failure of the valves in these tests. The search for convergent solutions to the finite element model for higher pressures (and coefficients of friction too) have resulted in numerous trials and errors involving the search for the optimum adjustment of gap/friction element stiffness and numerical iterations. After this (and numerous conversations with ANSYS technical support staff members) progress was being made at the time of this writing in quantifying the maximum principal tensile stress as a function of friction and pressure loading.

Fractography during the present reporting period showed evidence that there are two-size classifications of volume pores in NT451; this will have important ramifications in the life prediction of the valves. The volume pores that caused failure in some flexure strength tests (results reported in [2]) were approximately 10μm in diameter. However, the volume pores and inclusions that caused failure in the tensile strength tests were *at least* four to

---

* The word *predicted* is in quotes because here in this exercise the inputted tensile strength data is being used to predict *itself*. If the described process was incorrectly conducted, then the predicted performance and the tensile strength data would not be in agreement.

five times larger. Fractography from valves that have been strength tested for another program [3] typically failed from volume flaws similar to those exploited by the tensile strength tests. Examples of these flaw types are shown in Fig. 2. Life predictions of the valves will be made using both types of flaws to examine how the probability of failure is affected by them; however, it is expected that the performance affected by each type will be quite different.

As a future study of comparison, life predictions using NASA's CARES/LIFE program will be conducted using the same NT451 data that is being used in the AlliedSignal codes. During the present reporting period a tutorial was given to A. A. Wereszczak by CARES-support staff at NASA-Lewis. Both the CARES system of codes and the CERAMIC/ERICA system codes have some advantages over one other. Although this is by no means an exhaustive comparison, some example differences in the two series of codes are: the CARES series of codes have been available much longer and they enjoy more recognition in the structural ceramic community; the CARES is inter-usable with several commercially available finite element packages (e.g., ABAQUS, PATRAN/NASTRAN, COSMOS/M, and ANSYS), while CERAMIC/ERICA codes may only presently be used with ANSYS; the CARES codes have provisions to consider specialized loading-waveforms, such as cyclic fatigue, while CERAMIC/ERICA presently only considers fast fracture and static fatigue conditions; censored volume, surface, and corner failures may be considered in CERAMIC/ERICA, while CARES does not consider corner failures; and a "bootstrapping" statistical technique is used in CERAMIC/ERICA to calculate any arbitrary confidence bounds on the predicted failure probability or design stress, while CARES/LIFE presently does not have this capability. These differences and others will be further explored in future studies for this subtask, and will be reported on in a future article submitted to a journal.

Fast-fracture failure probability of a prototype NT451 SiAlON diesel exhaust valve was predicted using volume-censored flexure and tensile strength data. AlliedSignal's CERAMIC and ERICA codes were used to make these predictions in this exercise; these codes also yielded 95% confidence estimates on determined two-parameter Weibull distributions and failure probabilities. The prediction of fast-fracture failure probability was compared to actual NT451 SiAlON valve fast-fracture strengths. All the valves failed from volume-flaws, so volume-censored input strength data were required for the fast-fracture failure probability predictions. In addition to the failure probability predictions, the effects of several independent parameters on strength, and ultimately on the failure probability were also examined in this exercise: the specimen geometry tested; and specimen machining parameters consisting of grinding direction and grinding wheel grit size; and

the utilization of a post-machining anneal. Within 95% confidence estimates, all predictions of fast-fracture valve failure probability (independent of specimen geometry and machining parameters investigated) were found to correlate quite well with NT451 SiAlON valve fast-fracture strengths.

For this study, five sets of test specimens were tested, and are summarized in Table 1. The uncensored two-parameter Weibull distributions for these sets were described in previous bimonthly reports [2], and the Weibull Moduli and 95% confidence estimates for each are shown in Table 2. All strength data was censored though, and Weibull parameters were determined using CERAMIC, along with 95% confidence estimates; these results are shown in Tables 3-5.

Within 95% confidence estimates, it may be concluded that none of the test sets listed in Tables 2-5 are statistically different. Firstly, the uncensored m is not statistically different among the sets as shown in Table 2. Because the sets in Table 2 contain data generated from flexure and tensile specimens, and exhibited failures caused by various types of flaws, a comparison of scaling parameters or characteristic strengths is inappropriate among the sets. Likewise, Table 3 shows that the m and σ_0 for corner-failures are not statistically different either among the sets; it is evident that the few numbers of corner failures resulted in wide confidence bounds for these parameters. From Table 4, it is not conclusive that any of the machining conditions resulted in statistically significant differences in the surface failure-censored Weibull parameters, although the numbers of surface failures were greater in all flexure strength sets (which resulted in narrower confidence bounds). It may be argued that set 4 has a lower surface failure - censored m than set 2; however, all the 95% confidence estimate bounds overlap somewhat for sets 1-4, so this cannot be conclusively asserted. To examine this further, additional flexure tests would have to be conducted in order to increase the numbers of censored data, which in turn would lessen the 95% confidence estimates, and perhaps show statistical differences among the four sets of Weibull parameters generated. Lastly, the various grinding parameters and the use of post-machining anneal did not statistically affect the volume failure-censored Weibull parameters, as evidenced by Table 5. Volume failure -censored data generated from either flexure or tensile strength testing of NT451 was statistically equivalent; this shows that there is no statistically significant specimen-size effect on the Weibull parameters for this material. Set 4 did not have any volume-flaws that caused failure, and all specimens from this set failed from surface and corner flaws. As a consequence of this, set 4 was not used for any of the fast-fracture failure probability predictions of the valves because the valves all failed from volume flaws.

In parallel, finite element analysis (FEA) was performed using ANSYS with the SiAlON valve seated on the valve-seat insert at the moment of combustion. Axisymetric analysis was used with friction/sliding gap elements incorporated between the valve and seat insert. A friction coefficient of 0.3 was used [4]; it was found that maximum principal stresses did not significantly vary for coefficients between 0.1 to 0.5 for equivalent face pressures. A Young's Modulus of 291 GPa was measured for the NT451 using a strain-gaged specimen, and a Poisson's ratio of 0.28 [4] were used in the FEA. Elastic properties for the seat insert were taken to be 240 GPa and 0.31 for Poisson's ratio [4]. A service combustion pressure of 16 MPa (2.3 ksi) was modeled, and the resultant maximum principal tensile stress (MPTS) was 164 MPa. The MPTS was also determined as a function of combustion pressure, MPTS did not strictly scale linearly with face pressure because of friction between the valve and seat insert; however, their relation was very close to being linear.

The fast-fracture failure probabilities of the NT451 SiAlON valves for each of the four sets containing volume-censored input data listed in Table 3 are respectively shown in Figs. 3-6 as a function of MPTS in the valve. The fast-fracture failure probability predictions (represented by the thick lines) are shown with the 95% confidence estimates of these predictions (represented by the thin lines) that were calculated by CERAMIC, and are compared with experimental NT451 SiAlON valve strengths [4]. The MPTS in service is shown as well in these figures. Although the authors know of no quantifiable "acceptable" fast fracture failure rate for these valves, it is evident that there is essentially no likelihood of valve fast-fracture occurring during the first cycle of service. All the failure probability predictions correlated well with the experimental results, with sets 2, 3, and 5 [Figs. 4-6, respectively] matching particularly well.

Fracture toughness data was generated and analyzed for NT451 during the present reporting period. Chevron-notched bend bars were loaded in 3-point flexure at room temperature. Appropriate compliance calibration curves and analysis were applied [5], and the average K_{Ic} was found to be 6.0 MPa$\sqrt{m}$ with a standard deviation of 0.4 MPa$\sqrt{m}$ for eight specimens. K_I as a function of crack length was determined as well, and was found to be independent of it (i.e., flat R-curve behavior). Implications of this on the fatigue performance of this material is under investigation.

Rotary bend fatigue data was also further analyzed during the present reporting period. Much of the results were reported on in a previous bimonthly [6], but additional tests were performed since that earlier presentation. A fatigue exponent equaling 37 was arrived at (see Fig. 7), and is being compared with that of other silicon nitrides and SiAlONs in the literature. It is interesting to note that all specimens failed from small volume flaws that

were located at, or near, the gage section surface of the specimen. These volume flaws were much the same as those causing failure in some of the bend bars; an example of this flaw was shown in a previous bimonthly report [7].

Efforts were made to organize the mechanical testing effort for the newly arrived NT551 Si_3N_4 from Norton. A proposed NT551 test matrix was described in a previous report [3], but it agreed upon after discussions with UDRI staff that it should be altered so that less independent test conditions would be examined but that more specimens would be tested per condition. More confident statistical results would be a consequence of this change.

The mechanical and physical properties of NT551 that will be determined are summarized in Tables 6-15. Testing involving flexure bars are described in Tables 6-10. The fast-fracture strength and fatigue performance of NT551 will be examined as a function of temperature (Table 6), machining direction (comparing Table 6 with Table 7), and environment (comparing Table 8 with Tables 6-7). The cyclic performance on NT551 will be examined according to Table 9, and the physical properties according to Table 10. Test plans to characterize NT551's tensile strength and fatigue performance are shown in Tables 11-13. The test matrix for generating high cycle fatigue data for NT551 is shown Table 14. Lastly, the tests that are planned for NT551 valves are listed in Table 15, with these experimental results on these valves ultimately being compared with predictions made from data that was generated in Tables 6-14.

The NT551 valves are to be transversely machined using a 320 grit diamond grinding wheel [9], so almost all flexure specimens, and all tensile specimens, will be machined using the same procedure. The exception to this will be to examine what effect flexure results will have on the strength of NT551 if bend bars are longitudinally machined (Table 2). Grinding direction for 320 grit longitudinally machined NT451 SiAlON flexure bars did not yield statistically significant different results than transversely machined sets (Figs. 3-6); however, only 30 bars per set were tested in that study, and the confidence estimates on the censored Weibull statistics were not as narrow as desired. By testing 50 NT551 flexure specimens, it is hoped that the confidence estimates on the censored Weibull statistics will lead to narrow bounds, and more conclusive comparisons on the effects of machining.

Machining requests have been made to have additional flexure bars machined, and during the next reporting period, orders for tensile and rotary bend fatigue specimens will be submitted for commercial machining.

Status of Milestones

The deadline for milestone 3.2.1.6.12 was extended to 31 July 1996 due to repeated delivery delays in machined tensile specimens from an outside machine shop vendor. The title of milestone 3.2.1.6.12 was "Complete mechanical testing of NT451 S149 valves and submit open literature publication on results." An article on life prediction of NT451 valves was then completed during the present reporting period to satisfy this milestone.

The deadline for milestone 3.2.1.6.13 was extended to 30 September 1996 due to shipment delays of the expected NT551 silicon nitride from the vendor. The title of milestone 3.2.1.6.13 was "Issue letter report to CTP Program Manager regarding life prediction of NT551 S149 diesel engine valves." The first set of machined NT551 longitudinally machined flexure bars were not delivered until 4 October 1996; subsequently the September 30 deadline for this milestone was not able to be met, but will be completed during the next reporting period.

Communications / Visitors / Travel

A. A. Wereszczak attended the 98th Annual Meeting of the American Ceramic Society, Apr. 15-18, Indianapolis, IN, and presented two papers entitled "Reliability Prediction of Thin Alumina Plates Using AlliedSignal's CERAMIC and ERICA Life Prediction Codes," and "Mechanical Performance of a Candidate SiAlON Ceramic for Diesel Engine Applications."

A. A. Wereszczak traveled to NASA-Lewis on May 16 to meet with Lynn Powers, and others in their structural materials group, and received an introduction and tutorial to CARES.

A. A. Wereszczak traveled to AlliedSignal Engines, Phoenix, AZ, on May 30-31 to: work with Alonso Peralta using AlliedSignal's CERAMIC and ERICA codes; to discuss slow crack growth and creep-damage dominated failure mechanisms (and effects associated with their transition) in silicon nitride with Nanu Menon; and to attend research-relevant portions of the ATTAP meeting held there at that time.

A. A. Wereszczak traveled to Laurel, MD, June 3-5, to take an ANSYS finite element analysis training course offered at Mallett Technologies.

58 tiles and 36 rods of SGNIC's new NT551 silicon nitride were received from Vimal Pujari during the present reporting period.

Dr. N. Hecht visited the HTML during the week of September 9-13 to discuss commencement plans for the NT551 test matrix.

Problems Encountered

None.

Publications

An article entitled "Failure Probability Prediction of Fast-Fractured NT451 SiAlON Diesel Exhaust Valves" by A. A. Wereszczak, T. P. Kirkland, M. K. Ferber, J. M. Corum, and Alonso Peralta was submitted to the *Journal of the American Ceramic Society*.

An abstract entitled "Prediction of SiAlON Diesel Valve Failure Probability Using AlliedSignal's CERAMIC and ERICA Life Prediction Codes" by A. A. Wereszczak, T. P. Kirkland, and M. K. Ferber was submitted for inclusion in the 21st Annual Conference on Composites and Advanced Ceramic Materials, to be held Jan. 97 in Cocoa Beach, FL.

References

[1] A. A. Wereszczak, H. Cai, M. K. Ferber, and T. P. Kirkland, "Life Prediction Verification," pp. 52-62 in *Ceramic Technology Project Bimonthly Technical Progress Report to DOE Office of Transportation Technologies, Apr. - May 1995.*

[2] A. A. Wereszczak, T. P. Kirkland, and M. K. Ferber, "Life Prediction Verification," pp. 52-58 in *Ceramic Technology Project Bimonthly Technical Progress Report to DOE Office of Transportation Technologies, Feb. - Mar. 1996.*

[3] Used with permission of J. M. Corum, P.I. on the LMES/DDC CRADA involving the demonstration of cost-effective ceramic components in the Series 149 heavy duty diesel engine.

[4] J. M. Corum, R. L. Batiste, R. C. Gwaltney, and C. R. Luttrell, *Design Analysis and Testing of Ceramic Exhaust Valve for Heavy Duty Diesel Engine*, U.S. DOE Report ORNL/TM-13253, July 1996.

[5] A. A. Wereszczak, M. K. Ferber, R. R. Sanders, M. G. Jenkins, and P. Khandelwal, "Fracture Toughness (K_{Ic} and γ_{wof}) of a HIPed Si_3N_4 at Elevated Temperatures," *Ceramic Engineering and Science Proceedings*, Vol. 14, No. 7-10, pp. 101-112, 1993.

[6] A. A. Wereszczak, H. Cai, M. K. Ferber, and T. P. Kirkland, "Life Prediction Verification," pp. 51-55 in *Ceramic Technology Project Bimonthly Technical Progress Report to DOE Office of Transportation Technologies, Oct. - Nov. 1995.*

[7] A. A. Wereszczak, T. P. Kirkland, and M. K. Ferber, "Life Prediction Verification," pp. 56-67 in *Ceramic Technology Project Bimonthly Technical Progress Report to DOE Office of Transportation Technologies, Dec. 1995 - Jan. 1996.*

[8] A. A. Wereszczak, H. Cai, M. K. Ferber, and T. P. Kirkland, "Life Prediction Verification," pp. 61-69 in *Ceramic Technology Project Bimonthly Technical Progress Report to DOE Office of Transportation Technologies*, Dec. 1994 - Jan. 1995.

[9] Personal communication, Vimal Pujari, Norton Advanced Ceramics.

Table 1. Summary of Machining Parameters Used to Machine Test Specimens.

Set	Specimen Geometry	Grinding Direction	Grit Size of Wheel Used for Finish Grinding	Post-machining Anneal?
1	Flex (Mil-B)	Longitudinal	320	No
2	Flex (Mil-B)	Longitudinal	700	Yes
3	Flex (Mil-B)	Transverse	700	Yes
4	Flex (Mil-B)	Transverse	700	No
5	Tensile	Longitudinal	320	No

Table 2. Uncensored Maximum Likelihood Estimates of Weibull modulus with 95% confidence estimates.

Set (# of specimens)	Weibull Modulus *m* (± 95% Conf. Est.)
1 (32)	19.0 (14.1, 24.4)
2 (35)	21.9 (16.3, 28.5)
3 (35)	16.9 (12.6, 22.0)
4 (30)	13.1 (9.8, 16.9)
5 (7)	11.1 (5.9, 19.1)

Table 3. Corner failure - censored Maximum Likelihood Estimates of Weibull parameters with 95% confidence estimates.

Set (# of specimens)	Weibull Modulus *m* (± 95% Conf. Est.)	Scaling Parameter, σ_0 [MPa•mm$^{1/m}$] (± 95% Conf. Est.)
1 (6)	14.0 (6.2, 25.1)	1409 (1194, 2313)
2 (2)	47.5 (12.6, 102.8)	1131 (1063, 1641
3 (6)	18.1 (8.4, 32.5)	1284 (1133, 1823)
4 (1)	14.8 (1.4, 44.4)	1390 (1046, 1390)
5 (0)	Not Applicable	Not Applicable

Table 4. Surface failure - censored Maximum Likelihood Estimates of Weibull parameters with 95% confidence estimates.

Set (# of specimens)	Weibull Modulus m (± 95% Conf. Est.)	Scaling Parameter, σ_0 [MPa•mm$^{2/m}$] (± 95% Conf. Est.)
1 (23)	20.5 (14.6, 27.4)	1099 (1060, 1173)
2 (19)	33.6 (23.0, 46.2)	1061 (1037, 1108)
3 (22)	19.9 (13.8, 27.4)	1096 (1051, 1183)
4 (29)	13.1 (9.7, 16.9)	1046 (993, 1142)
5 (0)	No Surface Failures	No Surface Failures

Table 5. Volume failure - censored Maximum Likelihood Estimates of Weibull parameters with 95% confidence estimates.

Set (# of volume-failures)	Weibull Modulus m (± 95% Conf. Est.)	Scaling Parameter, σ_0 [MPa•mm$^{3/m}$] (± 95% Conf. Est.)
1 (3)	19.9 (6.3, 40.7)	985 (933, 1473)
2 (14)	13.4 (7.9, 20.5)	949 (907, 1071)
3 (7)	10.8 (5.1, 19.3)	1018 (922, 1487)
4 (0)	No Volume Failures	No Volume Failures
5 (7)	11.1 (5.9, 19.1)	1013 (906, 1412)

Table 6. Test matrix for determining fast-fracture and dynamic fatigue flexure strengths of NT551. All specimens are to be transversely machined, and tested at the HTML/ORNL.

Temperature (°C)	Stressing Rate (MPa/s)	# of Specimens
20	30	50
20	0.3	50
20	0.003	50
700	30	50
850	30	50
850	0.3	50
850	0.003	50
		Total = 350

Table 7. Text matrix for determining the effect of machining direction on the fast-fracture strength of NT551. All specimens are to be longitudinally machined, and tested at the HTML/ORNL.

Temperature (°C)	Stressing Rate (MPa/s)	# of Specimens
20	30	50
850	30	50
		Total = 100

Table 8. Test matrix for determining the effect of environment on the fast-fracture and dynamic fatigue strengths of NT551. All specimens are to be transversely machined, and tested at 850°C at the UDRI.

Environment	Stressing Rate (MPa/s)	# of Specimens
N_2	30	10
N_2	3	10
N_2	0.3	10
N_2 + 10%H_2O	30	10
N_2 + 10%H_2O	3	10
N_2 + 10%H_2O	0.3	10
N2 + SO_2	30	10
N2 + SO_2	3	10
N2 + SO_2	0.3	10
		Total = 90

Table 9. Test matrix for determining the physical properties of NT551. Properties are to be measured by UDRI using flexure specimens.

Property	Temperature (°C)	# of Specimens
Density	20	5
Elastic Constants	20-850	5
Thermal Expansion	20-850	5
Fracture Toughness	20, 700, 850	15
		Total = 30

Table 10. Text matrix for determining the cyclic fatigue performance of NT551 flexure bars. All specimens to be tested at 10Hz, and at the HTML/ORNL.

Temperature (°C)	Number of Stress Levels	# of Specimens
20	20	50
850	20	50
		Total = 100

Table 11. Test matrix for determining the tensile fast-fracture strength of transverse machined NT551 specimens. Testing to be performed at the HTML/ORNL.

Temperature (°C)	# of Specimens
20	26
850	26
	Total = 52

Table 12. Test matrix for determining the tensile dynamic fatigue performance of NT551. Specimens to be tested at the HTML/ORNL.

Temperature (°C)	Number of Stressing Rates	# of Specimens
20	3	12
850	3	12
		Total = 24

Note: The fastest rate is the same used for the tensile strength tests.

Table 13. Test matrix for determining the cyclic tensile fatigue performance of NT551. Testing to be performed at the HTML/ORNL.

Temperature (°C)	Frequency (Hz)	R	Number of Stress Levels	# of Specimens
20	10	0.1	1	3
850	10	0.1	3	9
850	1	0.1	1	3
850	10	0.55	1	3
				Total = 18

Table 14. Text matrix describing rotary beam fatigue testing, which is to be performed at the HTML/ORNL.

Temperature (°C)	Frequency (RPMs)	Number of Stress Levels	# of Specimens
20	6000	1	6
850	600	1	6
850	6000	6	36
			Total = 48

Table 15. Test matrix of NT551 valve performance, to be conducted at the HTML/ORNL.

Temperature (°C)	Type of Test	# of Specimens
20	Fast-fracture	5
20	Dynamic fatigue	10
20	Cyclic fatigue	5
850	Fast-fracture	5
850	Dynamic fatigue	10
850	Cyclic fatigue	5
		Total = 40

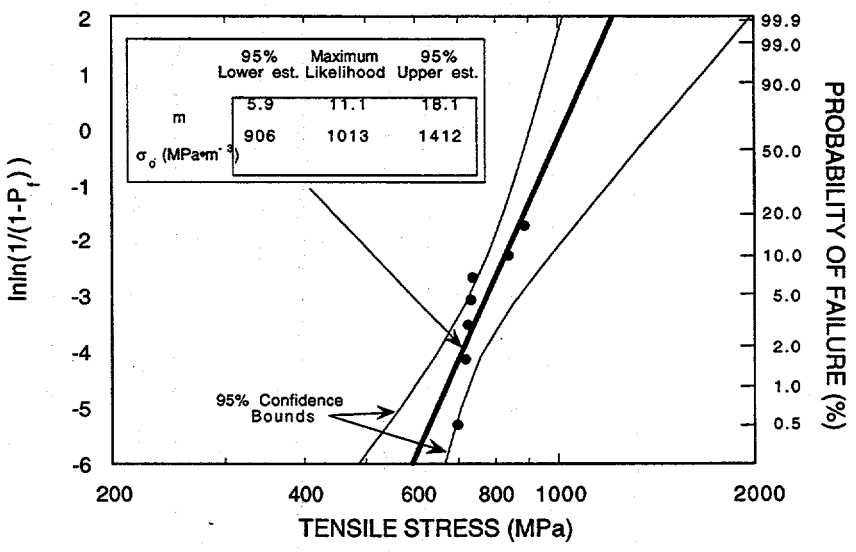

Fig. 1. Weibull analysis of tensile data generated from the modified ORNL buttonhead tensile specimen. All specimens failed from volume pores or inclusions; were longitudinally ground using a 320 grit diamond grinding wheel; and were not subjected to a post-machining anneal.

Volume flaw (pore) from a flexure strength test

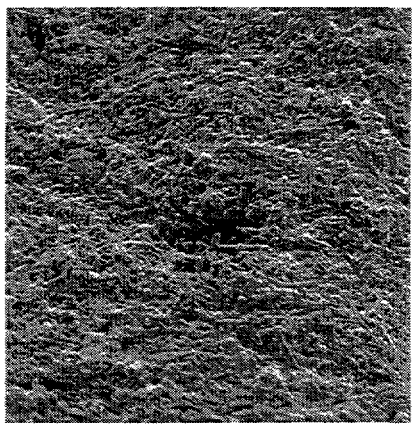

20 μm

Volume flaw (iron inclusion) from a tensile strength test

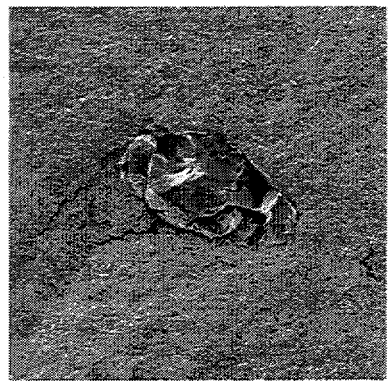

20 μm

Volume flaw (pore) from a valve strength test

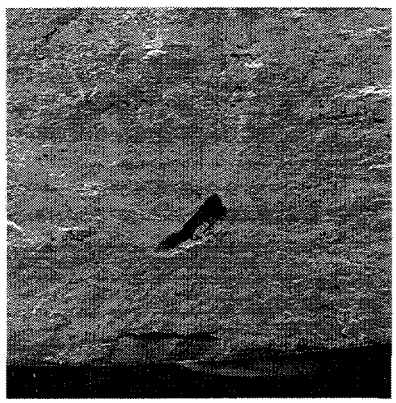

100 μm

Fig.2 Volume flaw types in NT451 SiAlON causing failures in flexure, tensile, and valve tests. Note that the volume flaw in flexure failures is much smaller than that in the tensile and valve failures.

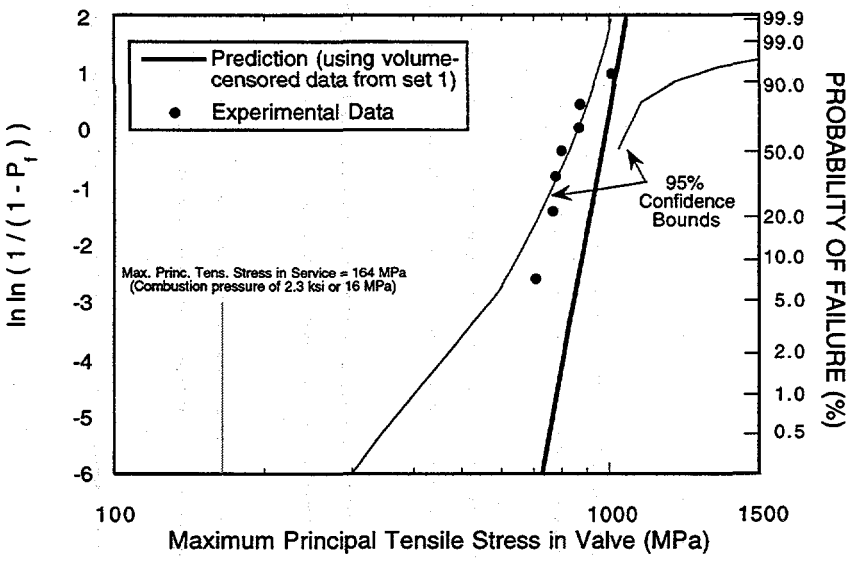

Fig. 3. Predictions of probability of failure as a function of maximum principal tensile stress for the NT451 SiAlON valves using volume-censored input from set 1.

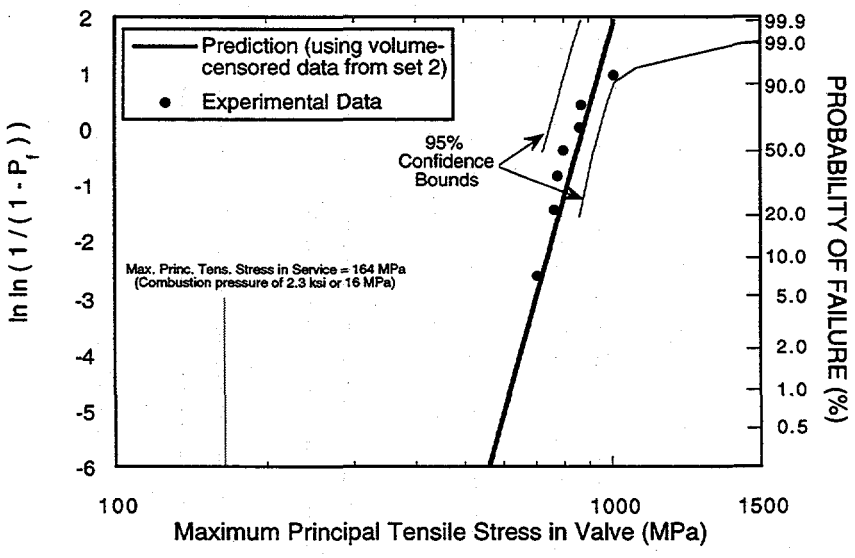

Fig. 4. Predictions of probability of failure as a function of maximum principal tensile stress for the NT451 SiAlON valves using volume-censored input from set 2.

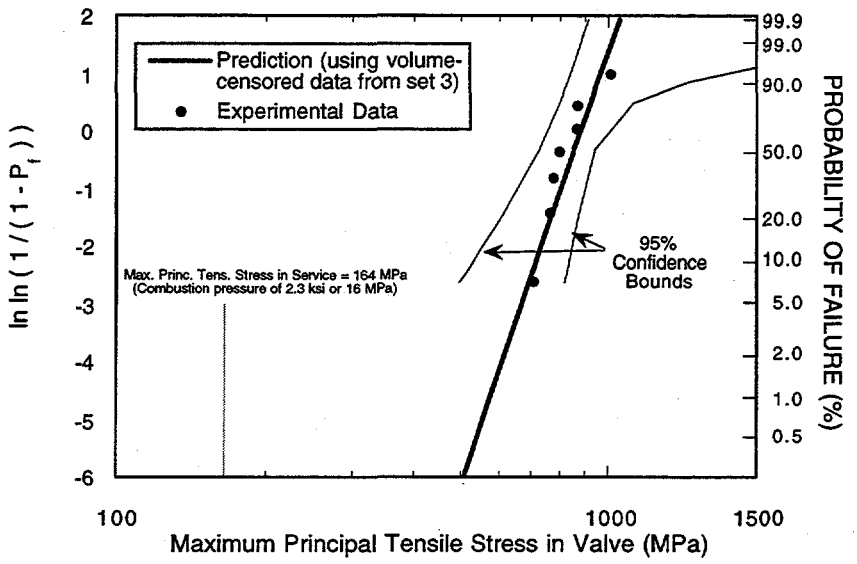

Fig. 5. Predictions of probability of failure as a function of maximum principal tensile stress for the NT451 SiAlON valves using volume-censored input from set 3.

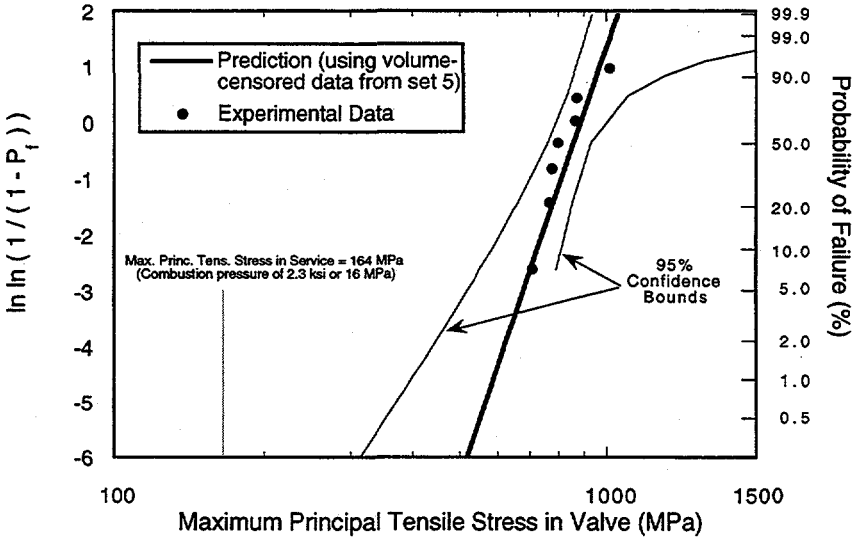

Fig. 6. Predictions of probability of failure as a function of maximum principal tensile stress for the NT451 SiAlON valves using volume-censored input from set 5.

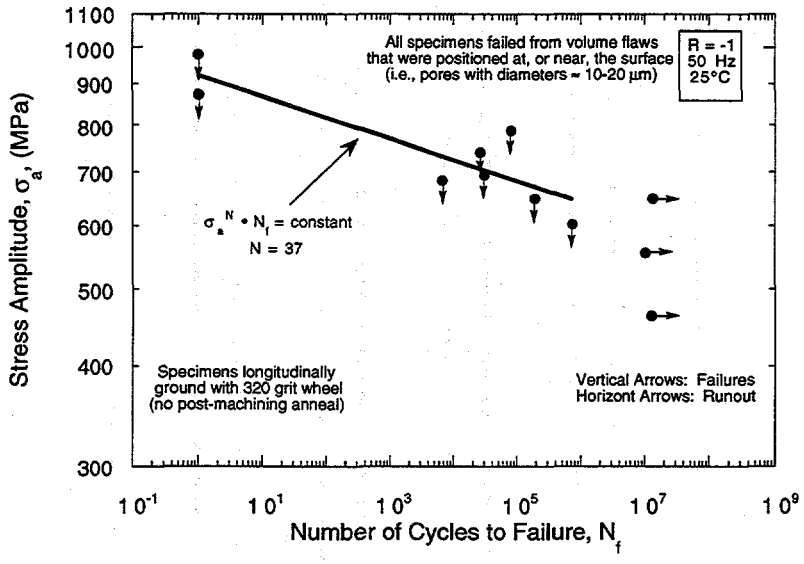

Fig. 7. Relationship of number of cycles to failure and the applied stress amplitude from rotary bend fatigue tests for NT451. The results show NT451 appears to be susceptible to cyclic fatigue.

Field Emission Analytical Electron Microscopy for Characterization of Catalyst Microstructures

L. F. Allard and T. A. Nolan

OBJECTIVE/SCOPE

The objective of the research is to use analytical and high resolution electron microscopy to characterize the microstructures of emission control catalysts. Emphasis is placed on relating microstructural changes to performance, as tested using a newly developed. "ex-situ" reactor designed to expose transmission electron microscopy (TEM) catalyst specimens to gas mixtures at temperatures that simulate actual use. Materials to be studied include nobel metals such as Pt and Pd on oxide substrates such as Al2O3 and TiO2, prepared at Ford Research using novel methods that have been shown to improve the behavior of the catalysts in preliminary tests of their ability to reduce NOx emissions from diesel exhausts. Other experimental diesel oxidation catalysts comprising rare earths on these supports will also be studied. The efficacy of the new reactor for use in these studies is highlighted.

TECHNICAL HIGHLIGHTS

The optimization of currently available catalysts and the development of new ones requires a detailed understanding of the effects of both microstructure and composition on their function. Previous work has demonstrated that information at the atomic-scale on heterogeneous catalysts can be derived using high resolution transmission electron microscopy. Under favorable conditions, the morphology of heavy metal catalytic particles can be related to catalytic activity. In order to study the changes in morphology and chemistry that are related to exposure of the catalyst to standard use conditions, we have completed the construction and testing of the operation of a new reactor system designed to permit catalyst materials to be reacted under conditions that simulate actual use conditions (i.e. atmospheric pressure, high temperature, varying gas compositions etc.). A primary feature of this reactor and the associated specimen holder for the electron microscope is that it permits the sample to be transferred from the reactor into the microscope (and back again) without exposure to the atmosphere. This is important for most specimens which may need to be treated initially under reducing conditions to serve as a starting point for systematic studies of reaction behavior. Also, the sequential observations to be made are supposed to mimic "snapshots" of the structure at different times during the reaction, so minimizing atmospheric exposure during transfers is considered important in maintaining the integrity of the specimen throughout the reaction process.

Figure 1 is an example of the ability to react a specimen and examine it in the microscope uncorrupted by atmospheric exposure. We chose a specimen for this test

that is highly reactive: fine Fe particles. However, pure Fe particles do not exist in nature, so we reversed the process and began with Fe catalysts that had a thin passivation layer of Fe2O3, as shown in Fig. 1a. These particles were reduced in the reactor to remove the oxide layer, then transferred into the microscope. The specimen is encapsulated within a protective inert atmosphere such as Ar during transfer. Figure 1b shows the reduced particle, which clearly has no residual oxide layer, thus the sample can indeed be transferred in a manner that maintains its integrity during the transfer process. These techniques are currently being applied to studies of lean burn NOx catalysts.

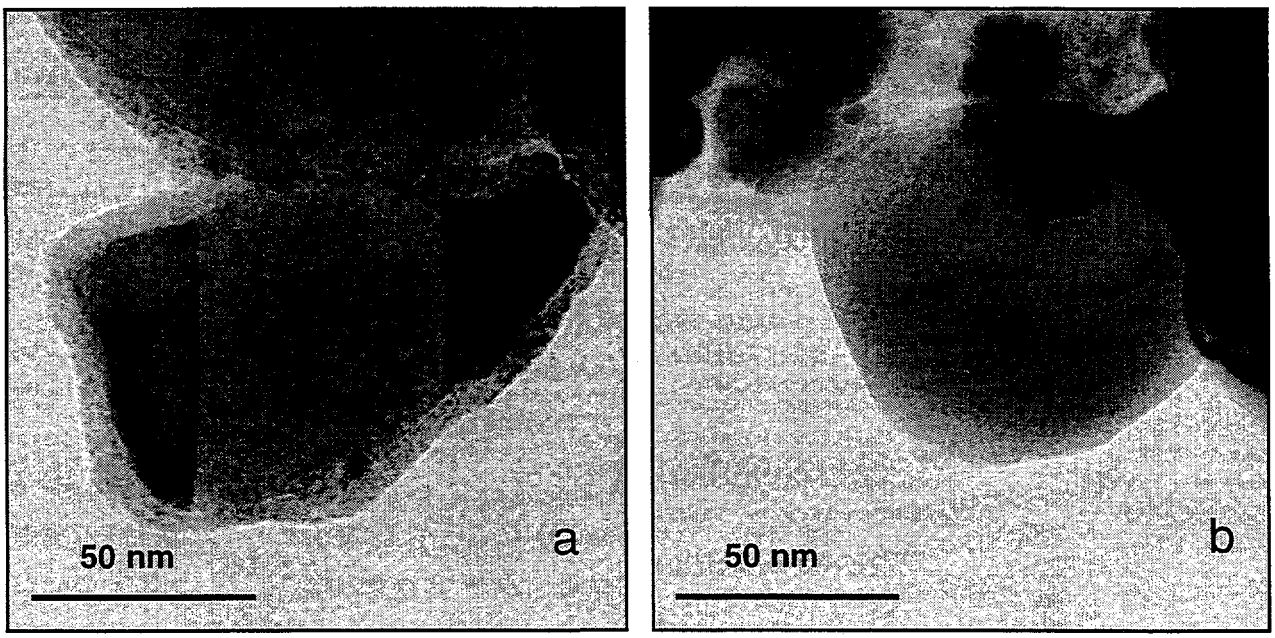

Fig. 1 a) Fe particles passivated by thin layer of Fe2O3, prior to reduction reaction in new catalyst reactor; b) Particles after reduction reaction and transfer into microscope. Absense of oxide layer is evidence that transfer process can be done while maintaining sample integrity.

Publications:

1. "The Performance of a Reactor Systems for TEM Studies of Catalyst Reactions", L. F. Allard, K. S. Ailey, A. K. Datye and W. C. Bigelow, submitted to Applied Catalysis

Trips and Presentations:

1. L. F. Allard, "Modern Field Emission Electron Microscopy Techniques Applied to Catalyst Characterization", Invited Talk at Catalyst Club of Philadelphia, Jan. 18, 1996.

2. L. F. Allard, P. A. Teague and T. A. Nolan, "Catalyst Research at the High Temperature Materials Laboratory", Seminar at Dupont Experimental Station, Wilmington, DE, Nov. 3, 1995.

3. L. F. Allard, "Catalyst Research at the High Temperature Materials Laboratory", presentation to Hoescht-Celanese researchers as part of H-C Government Day, Nov. 2, 1995.

4. L. F. Allard, K. S. Ailey, W. C. Bigelow and A. K. Datye, "The Performance of an Ex-Situ Catalyst Reactor System", Frontiers of Electron Microscopy in Materials Science, Oak Brook, Il, June, 1996.

MATERIALS AND TESTING STANDARDS

IEA ANNEX II Management (April 1, 1996-September 30, 1996)

M. K. Ferber and K. Breder (Oak Ridge National Laboratory)

Objective/Scope

The purpose of this task is to organize, assist, and facilitate international research cooperation on the characterization of advanced structural ceramic materials. A major objective of this research is the evolution of measurement standards. This task, which is managed in the United States by ORNL, now includes a formal IEA Annex agreement identified as Annex II between the United States, Germany, Sweden, Japan, and Belgium. The original annex included four subtasks: (1) information exchange, (2) ceramic powder characterization, (3) ceramic chemical and physical characterization, and (4) ceramic mechanical property measurements. In the United States, a total of 13 industrial and government laboratories have participated and contributed their resources to this research. The research in Subtasks 2, 3, and 4 is now complete. In 1990, research in two new subtasks was initiated, including Subtask 5, Tensile and Flexural Properties of Ceramics, and Subtask 6, Advanced Ceramic Powder Characterization. The research in Subtasks 5 and 6 was completed in 1993 and the reports were distributed. Two new tasks (Subtask 7 on Ceramic Machining and Subtask 8 on Ceramic Powder Characterization) were proposed in late FY 1993 and have now been accepted by all member countries, and the research is nearly complete. Subtask 7 in the United States includes eight companies and three federal laboratories. Subtask 8 includes six companies.

The United States will host the 1996 Executive Committee Meeting in Dearborn, Michigan, on October 30, 1996, in conjunction with the Annual CCM Meeting. The addition of two new Subtasks (9 and 10) will be discussed at that meeting. Subtask 9 examines reproducibility of advanced thermal shock techniques while Subtask 10 expands the work on the earlier powder effort (Subtask 8).

Recent Developments

Technical Highlights

Working Group Meeting

A summary of the Subtask 7 Working Group Meeting held in Indianapolis, Indiana, on Monday, April 15, 1996, follows. The attendees were: Belgium, J. P. Erauw -Germany, T. Hollstein - Japan, M. Mizuno - Sweden, L. Carlsson and R. Pompe - United States, K. Breder, M. Ferber, F. Foust, R. Ott, R. Schulz, and V. Tennery. The following sections summarize the major highlights from that meeting.

Subtask 9, Thermal Shock

Dr. Ferber wished everybody welcome to Indianapolis and thanked all for coming to the working group meeting. There was no formal agenda for this meeting, and the main purpose was to discuss results in Subtask 7 which is nearing completion.

First, Dr. Ferber briefly summarized the status of Subtask 9, Thermal Shock. He confirmed that all participating countries now were ready to start. Dr. Erauw mentioned that the finances in Belgium were unclear but they would like to participate in future tasks on a minimum basis. They had laser equipment in-house at VITO, but lacked temperature hardware. He said that one company had expressed an interest in participating in Subtask 9. He also expressed interest in using the water quench test as this would be closer to a practical test in use. The laser thermal shock would be more considered a basic research tool.

Mr. Schulz expressed hope that this work would be considered as an area of science in which we would be able to do research without getting into proprietary work.

Dr. Hollstein indicated that they had good industrial response in Germany on Subtask 9. Many companies were willing to participate at least with specimens, and Siemens has now two thermal shock apparati set up. Dr. Hollstein also hoped they would succeed in identifying a larger German effort, however, that would depend on the funding situation. He expressed the importance of the national support or there will be no funding for Subtask 9.

Mr. Schulz remarked that there are many changes and financial difficulties in the U.S. federal government now. The Department of Energy (DOE) is reorganizing and they are emphasizing customer focus. The heavy vehicle propulsion materials program is being managed by Schulz, but the Partnership for a New Generation Vehicle (PNGV) is now the largest group and given high priority in funding. IEA remains in the budget this year and in the request for 1997, but we are under budget pressure and the future is uncertain.

Mr. Schulz also said that our IEA agreement is part of end use sector of the IEA. Our agreement will come to an end with this Annex (June 1997) and we will be part of a new agreement. Mr. Schulz would find out more about a new agreement and come back with more information at the next Executive Committee Meeting. The need for visibility with our own governments was also stressed by Mr. Schulz.

Dr. Carlsson requested background information on Sweden's involvement in the IEA. Current managers of their research programs will have to be convinced that this is a good investment for their research money. He would like to get a copy of the agreement which shows who signed for Sweden and

any other pertinent information which would be useful to him in presenting request for continued support for this project in Sweden. Mr. Schulz and Ms. Foust took responsibility for getting the needed information out to Dr. Carlsson. (This information has been sent to Dr. Carlsson.)

Dr. Mizuno handed out a collection of information about the Japanese thermal shock set-up and some results.

Subtask 7, Machining Effects on Strength of Structural Ceramics

Each country's representative then gave a summary of the status of their work in Subtask 7. Dr. Erauw summarized the status of the Belgian work. The strength comparison for the SN73 machined in the participating countries showed a variation in strength from 850 to 950 MPa. This variation was partly between the machining countries and partly between the testing countries. The Weibull moduli measured for the SN73 also showed similar variability. The results of the foreign materials machined in Belgium were summarized. Grinding forces recorded for the GS44 were of the same order of magnitude as those measured in the United States. The grinding forces measured for the Japanese material were higher, and the supporting material from Belgium clearly illustrates some of the problems associated with measuring forces over the small area as cross grinding of four flexure bars represent. The Belgian work included an attempt on correlating strengths and grinding forces for specific flexure bars, but no clear conclusions could be drawn at present. All the machining in Belgium was complete, only fractography remaining of the work. Dr. Hollstein summarized the German work which is also complete with the exception of the fractography. The comparison of the German material machined abroad showed a large strength variation - from 950 to 1265 MPa. Further, the Weibull moduli showed relatively large variability. Dr. Carlsson briefly summarized the Swedish work and discussed the shape of some of the Weibull graphs generated. Dr. Mizuno summarized the Japanese work showing that the Japanese machining consistently resulted in high strengths for all the foreign materials; however, the Weibull moduli were often low, a result of a few specimens in each set breaking at unusually low stresses. The reason for this was discussed at the meeting, and it is the hope that fractography can help clarify this issue. Dr. Breder summarized the U.S. work, indicating that the variability in the strengths of the GS44 machined abroad was not very different from the variations seen for the various batches machined in the United States under the same conditions. The measurement of forces was illustrated and discussed, especially the problem of measuring high forces on very small cross sections. All machining in the United States is complete and the fractography is ongoing.

Dr. Breder led the wrap up discussion and some issues of information exchange were discussed.

It was agreed that reports should be exchanged by the end of July,

It was agreed that domestic reports from each country would be ready by the end of July and that Dr. Breder will compile the final report using these individual reports. The draft of this should be ready by the next Executive Committee Meeting in Dearborn in October 1996.

Current Subtask 7 Technical Efforts

The sets of GS44 machined and tested abroad (from Germany and Sweden) have been returned to the United States for fractography, and strength results for performing a full comparison of the interlaboratory exchange are being compiled.

The two fractography reports have been published (January 1996) and distributed to the International partners and the U.S. participants (May 24, 1966).

Subtask 7 final report is in preparation.

Current Subtask 9 Technical Efforts

In Subtask 9, advanced thermal shock techniques for structural ceramics will be examined by each of the participating countries. All of the thermal shock methods will utilize a thin disk specimen which is centrally heated by either a laser (Fig. 1), a shaped heating element (Fig. 2), or a high intensity lamp (Fig. 3). The resulting radial temperature gradient generates high tensile stresses along the specimen edge. The temperature profile at fracture can be used to calculate the thermal fracture stress. In order to compare the data produced by the various heating approaches, specimens fabricated from at least two candidate structural ceramics will be distributed to each of the participating countries. The resulting values of the fracture stress will be used as the primary correlating parameter.

Figure 2 illustrates the proposed thermal shock facility to be used in the U.S. effort. To date, disk specimens of aluminum oxide, silicon nitride, and silicon carbide have been thermally shocked using a silicon carbide heating element to provide the heat flux. As shown in Fig. 4a, the maximum temperature arising from the shaped heating element generates is confined to a centrally located rectangular region. The resulting stresses cause the specimen to fracture into two pieces (Fig. 4b). Current effort is focused on modifying the shape of the heating element to generate a circular hot spot.

In order to better understand the evolution of the temperature gradients which are responsible for the thermal stresses, a commercially available heat transfer program, Heating 7.2 (K.W. Childs, Computing Applications Division, ORNL), was used to develop a model to simulate the temperature profiles as a function of time. Heating 7.2 is a multifaceted program that allows the user to choose from a variety of coordinate axes in one- two- or three-dimensions to describe the physical model. Many of the material properties necessary for the heat transfer calculations can be input as a constant, or as a function of either time, temperature, or position. Using the method of finite time difference, transient heating profiles are calculated using either an explicit or implicit solution technique. The required input is read from a file resembling a set

of Fortran punch cards, relying on keywords to identify the input data. The program output can be readily formatted as an ASCII file which then can be read by many available plotting programs.

Figure 5 shows the model used to simulate the centrally heated disk. Because of symmetry, a two-dimensional r-z coordinate system is appropriate. Figure 6 shows the temperature distribution in a centrally heated SiC disk after 0.4 seconds. Because the thickness of the disk is small compared with the diameter, the through-the-thickness temperature gradients are insignificant. Efforts are currently underway to calculate the stress distribution arising from the radial temperature gradients.

Subtask 8, Characterizing Ceramic Powders

Major responsibility for this subtask in the United States is at NIST, and a detailed report of progress on this subtask is provided in the section of this report submitted by NIST.

Status of Milestones - Milestones 411520 (publish powder final report - Subtask 8) and 411521 (publish mechanical properties final report - Subtask 7) have been changed from August 30, 1996, to December 31, 1996. The reason for this change is due to delay in receipt of all specimens and the fractography work is taking longer than anticipated. Other milestones are on schedule.

Communications/Visits/Travel - Kristin Breder, Matt Ferber, and Felicia Foust attended the IEA Subtask 7 Working group meeting in Indianapolis, Indiana, on Monday, April 15, 1996, held in conjunction with the Annual American Ceramic Society Meeting.

Publications and Presentations - J. P. Erauw and W. Hendrix, Vlaamse Instelling voor Technologisch Onderzoek (VITO), Mol, Belgium; K. A. Drüsedau and T. Hollstein, Fraunhofer-Institut für Werkstoffmechanik (IWM), Freiburg, Germany; Y. Nagano and M. Mizuno, Japan Fine Ceramics Center (JFCC), Nagoya, Japan; L. Carlsson, Swedish National Testing and Research Institute (SP), Borås, Sweden; K. Breder and M. K. Ferber, Oak Ridge National Laboratory (ORNL), Oak Ridge, Tennessee, U.S.A., "Round Robin Comparison of Fractography of Three Different Silicon Nitrides - Topical Report - Subtask 7," IEA Annex II Report, Lockheed Martin Energy Research Corporation, Oak Ridge National Laboratory, January 1996.

Kristin Breder and Mattison K. Ferber, "Round Robin Comparison of Fractography of Three Different Silicon Nitrides - U.S. Results," Lockheed Martin Energy Research Corporation, Oak Ridge National Laboratory, Oak Ridge, Tennessee, U.S.A., January 1996.

"Status of Work in USA," presented by Kristin Breder and Matt Ferber at the Working Group Meeting, Indianapolis, April 15, 1996.

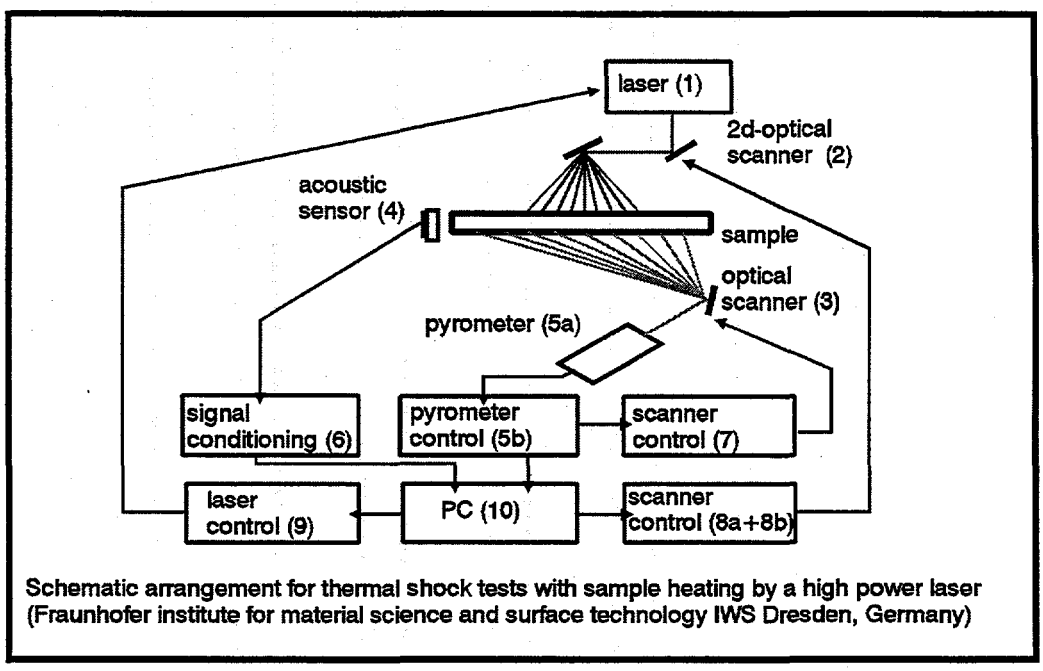

Figure 1. Laser-based system used to measure thermal upshock in structural ceramics. This system is currently in use in Germany.

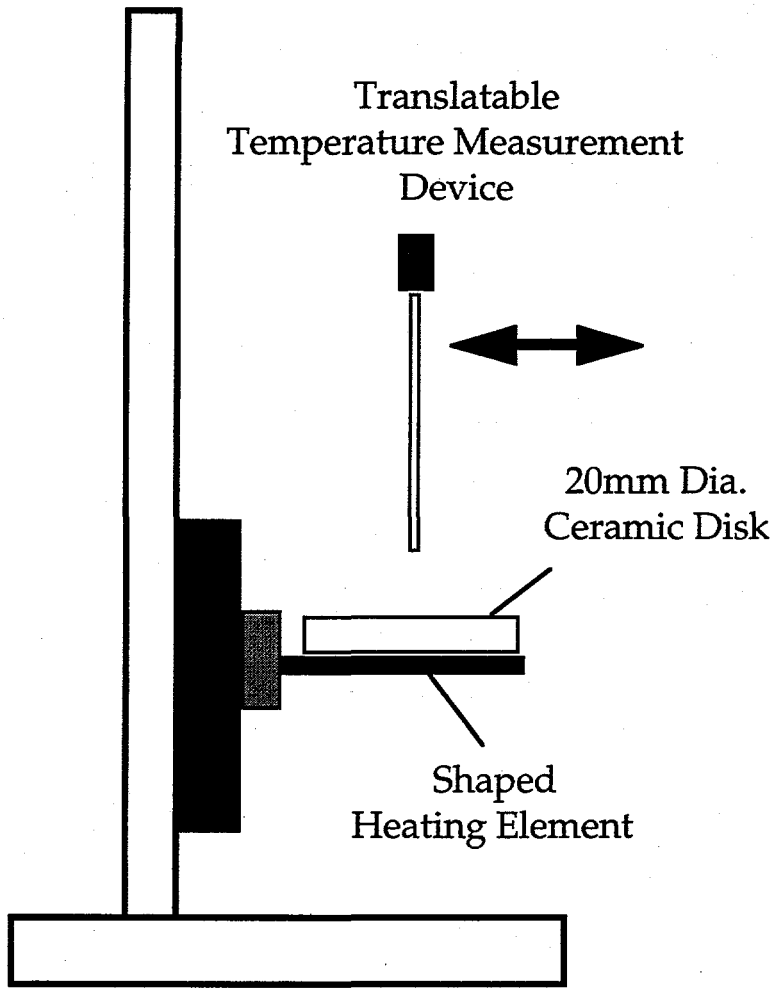

Figure 2. Thermal upshock system proposed by the United States. The current design utilizes a heating element to centrally heat the disk.

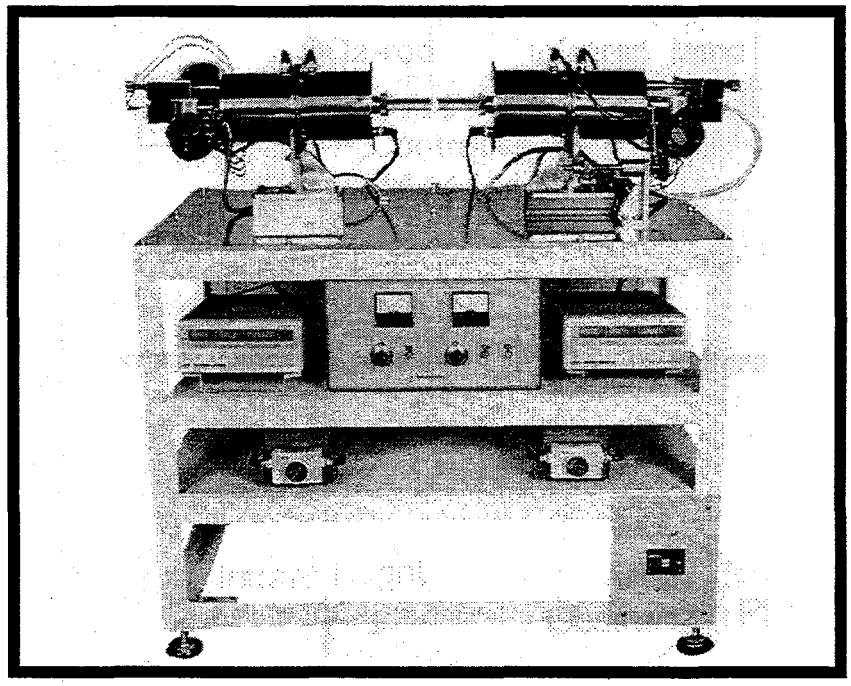

Figure 3. Thermal upshock system proposed by Japan. The current design utilizes a high intensity lamp to centrally heat the disk. A similar system may be used by both Sweden and Belgium.

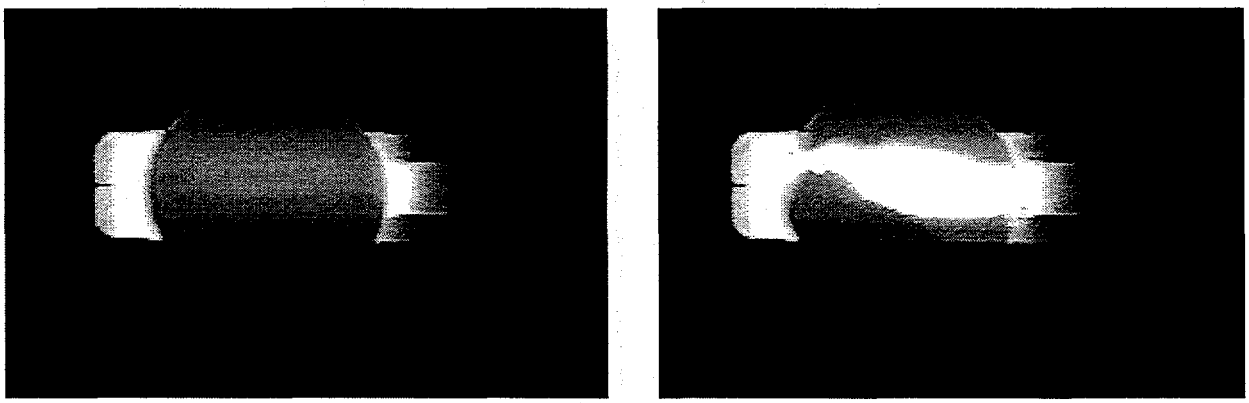

(a) (b)

Figure 4. Silicon carbide specimen heated by shaped heating element just prior to (a) and preceding (b) fracture.

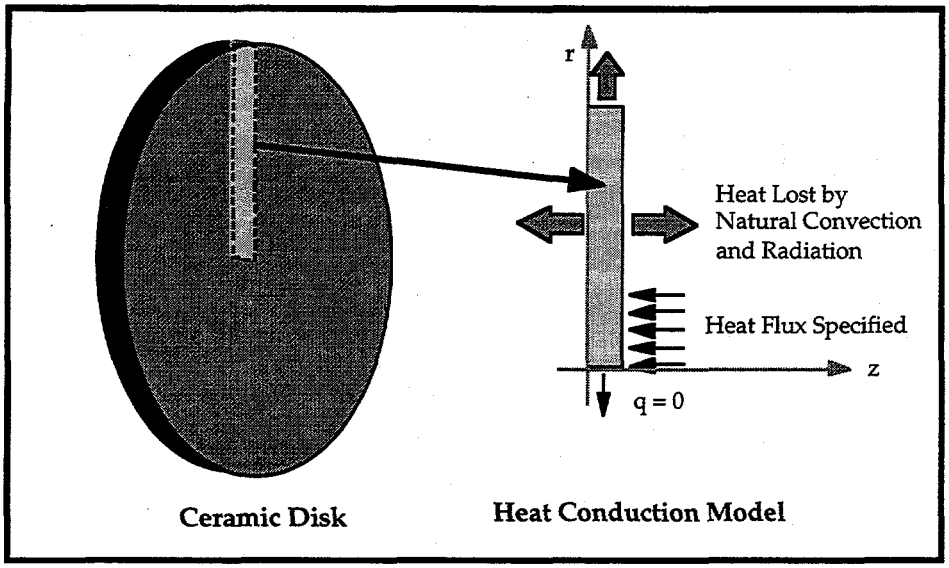

Figure 5. Two dimensional element used to model the temperature distribution in the ceramic disk subjected to fixed heat flux.

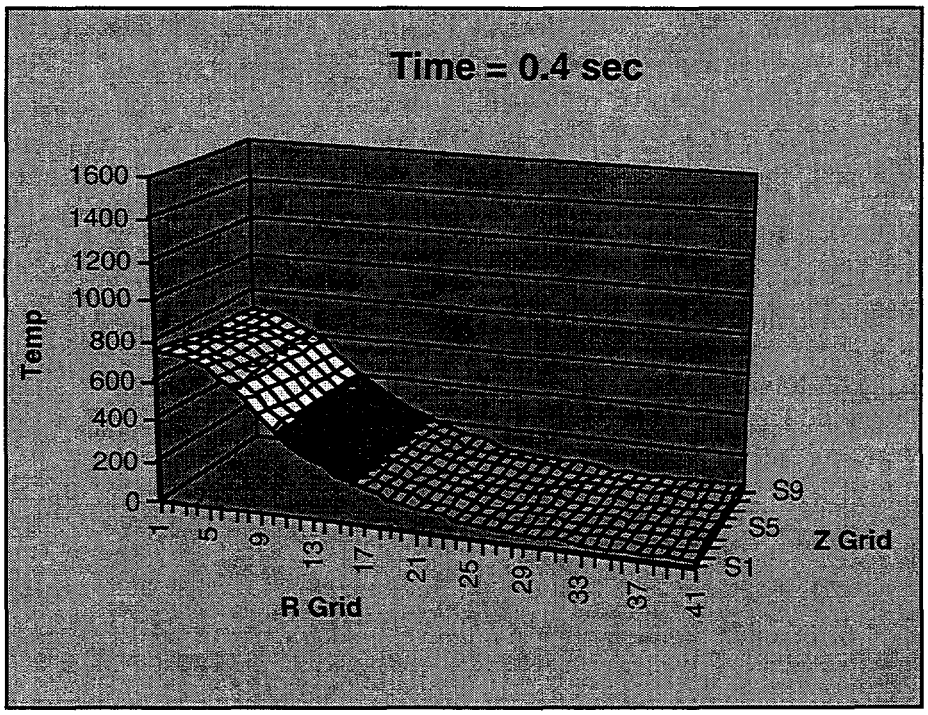

Figure 6. Temperature distribution in centrally heated SiC disk after 0.4 seconds.

NDE Standards for Advanced Ceramics

R. W. McClung

The development of standards is important for the establishment of reliability and acceptance of advanced structural materials. Committee C-28, on Advanced Ceramics, has been organized in the American Society for Testing and Materials (ASTM) to address this issue. One of the activities of the C-28 committee is nondestructive examination (NDE). The Section C-28.02.02 on NDE is reviewing existing standards on NDE (primarily developed for metals) to determine potential applicability for ceramics, as well as drafting original standards. Use of existing or modified standards, if available, is more efficient that generation of new documents and will assure the input of a large body of NDE expertise. Close liaison has been established with ASTM Committee E-7 on Nondestructive Testing, and documents are in various stages of review, recommendations for change, modification, and balloting. R. W. McClung is a subcommittee chairman in both committees and the official liaison.

Technical Highlights

Liaison and technical support have been continued between ASTM committees C-28 and E-7. To date, thirty-six E-7 NDE standards identified as having potential relevance to ceramics have been reviewed in detail with recommendations made to E-7 for modifications to identified documents. Successful action is complete on 32 documents; others require action by C-28.

Two new standards have successfully passed committee ballots and gained society approval. They are

> C-1331-96, Standard Test Method for Measuring Ultrasonic Velocity in Advanced Ceramics with the Broadband Cross-Correlation Method, and
>
> C-1332-96, Standard Test Method for Measurement of Ultrasonic Attenuation Coefficients of Advanced Ceramics by the Pulse Echo Contact Technique.

A new proposed standard, "Standard Practice for Fabricating Non-Oxide Ceramic Reference Specimens Containing Seeded Inclusions" was balloted successfully as concurrent subcommittee and committee levels. Affirmative comments were considered and incorporated into the text. The numerical designation for this standard is now C-1336.

Standard C-1212 (on fabricating reference specimens with seeded voids) was reviewed with the intent of incorporating improvements from C-1336. A proposed revised draft was reviewed at the June 1996 meeting and approved for a concurrent subcommittee/committee ballot.

A limited amount of data has been identified for establishing radiographic equivalence factors for advanced ceramics. Additional specimens will be sought for experimental radiography to

develop additional data. A volunteer for the radiography has been recognized. The intent of this action is to provide data for a table in an E-7 standard E-94 on the radiographic method. Other work in progress includes an amplified outline for a draft standard for reference specimens containing laser-drilled holes and a possible standard on determination of porosity in ceramics using ultrasonic velocity.

An advisory ballot is planned for the NDE section to obtain consensus on applicability to advanced ceramics of additional standards on radiography, ultrasonics, radioscopy, and computed tomography.

During meetings of Committee E-7 in June, participation by McClung as C-28 liaison included meetings of the subcommittees on radiology and ultrasonics. Significant activity is ongoing in both subcommittees that will result in standards of interest and value for advanced ceramics. Radiographic standards in progress include a standard on low-energy X-ray focal spots and several standards in various stages of development of balloting on radiographic film including system performance, film processing control, and storage of film. Radioscopic standards in various ballot stages include a guide, a practice, a guide for data transfer and storage, and a standard on back-scatter tomography. New computed tomography (CT) standards in progress include calibration and measurement of density by CT and a planned document on beam-hardening artifacts. Approved documents on CT imaging and CT examination are being submitted for consideration as international standards by ISO. Expansion of the radiological glossary includes adding terms on back-scatter imaging and review of European terms.

Subcommittee E7.06 on Ultrasonic Methods has many standards in different stages of preparation on ballot. Those relevant to ceramics will be highlighted. A new draft guide has completed subcommittee ballot for the detection and evaluation of discontinuities by the contact method. A new draft guide has been started on the ultrasonic resonance technique. [R. W. McClung served as negotiator to establish meaningful communication between the proponent (of the Quattro Corporation) and the ultrasonic subcommittee.] A new standard on sizing of surface breaking cracks has been balloted at subcommittee level. Several draft standards are in progress on the evaluation of ultrasonic search units including beam profile and beam angle of focused units. Work is ongoing for an international standard on characterization of sound fields of contact search units. Other ultrasonic standards are in the ISO mill.

Ceramic Mechanical Property Test Method Development

George D. Quinn
(National Institute of Standards and Technology)

Objective/Scope

This task is to develop mechanical test method standards in support of the Propulsion Systems Materials Program. Test method development should meet the needs of the DOE engine community but should also consider the general USA structural ceramics community as well as foreign laboratories and companies.

Draft recommendations for practices or procedures shall be developed based upon the needs identified above and circulated within the DOE ceramics engine community for review and modification. Round-robins will be conducted as necessary, but shall be well-focussed, limited in scope, and complementary to IEA round-robins. Procedures developed in this program will be standardized by ASTM.

Technical Highlights and Results

Summary

Work on hardness and fractography is winding down following the adoption of the two hardness standards C 1326 and C 1327 and the fractography standard C 1322. Time permitting, we will prepare a comprehensive paper on hardness measurements methodology. We will continue to refine our fracture toughness test procedures with the goal of improving the draft ASTM fracture toughness standard. New work is underway on the diametral compression strength test which we feel is a strong candidate for early standardization.

Earlier work in this project has contributed to the following completed standards:

1. ASTM C 1161-90 "Standard Test Method for Flexural Strength of Advanced Ceramics at Ambient Temperature," G. Quinn, NIST.
2. ASTM C 1198-91 "Dynamic Young's Modulus, Shear Modulus, and Poisson's Ratio for Advanced Ceramics by Sonic Resonance," by S. Gonczy, Allied-Signal; G. Quinn, NIST; and J. Helfinstine, Corning.
3. ASTM C 1211-92 "Standard Test Method for Flexural Strength of Advanced Ceramic at Elevated Temperature," by G. Quinn in cooperation with Mr. M. Foley, Norton; Mr. T. Richerson, Allied-Signal; and Dr. M. Ferber, ORNL.
4. MIL HDBK 790 "Fractography and Characterization of Fracture Origins in Advanced Structural Ceramics," with J. Swab and M. Slavin, U.S. ARL.
5. ASTM C 1239-94a "Standard Practice for Reporting Strength Data and Estimating Weibull Distribution Parameters," by S. Duffy, NASA-Lewis; G. Quinn, NIST; and C. Johnson, G.E.
6. ASTM C 1322-96 "Standard Practice for Fractography and Characterization of Fracture Origins in Advanced Ceramics," in cooperation with Mr. J. Swab, U.S. ARL.
7. ASTM C 1326-96 "Standard Test Method for Knoop Indentation Hardness of Advanced Ceramics."
8. ASTM C 1327-96 "Standard Test Method for Vickers Indentation Hardness of Advanced Ceramics."

In addition, work on this task has contributed to the following draft standard:

1. ASTM C-xxxx "Standard Test Methods for the Determination of Fracture Toughness of Advanced Ceramics," in cooperation with Prof. Isa Bar-on, WPI; Prof. M. Jenkins, University of Washington, and J. Salem, NASA-Lewis.

Fracture Toughness

Work in this element was devoted to preparing the draft ASTM fracture toughness standard and conducting new surface crack in flexure (SCF) experiments to refine this test method.

Unfortunately, Prof. Bar-on was unable to prepare a new draft for the Spring 1996 C 28 ballot, but in May, an intensive four-party conference telephone call helped solve some of the problems with the draft. Mike Jenkins agreed to prepare the next draft for review at the June, 1996 C-28 meeting in ASTM headquarters, West Conshohoken, PA. Earnest discussions about the nature of the next rendition ensued at this meeting. Mike prepared drafts in June and July, yet there were still some outstanding technical and editorial matters that had to be reconciled among the task group members. Therefore G. Quinn organized a multihour telephone conference call on August 28, 1996. This conference call was productive and paved the way for Mike Jenkins to prepare an August 29, 1996 draft. In the first week of September, G. Quinn reviewed this draft and furnished six pages of detailed revisions and corrections as well as some polished illustrations. G. Quinn refined a scheme for reporting the specimen and crack plane orientation for fracture toughness specimens relative to component axes. This was sent to M. Jenkins who incorporated it into a new draft of the toughness document. Having received this and other input from Prof. Bar-on and Mr. Jon Salem, Michael Jenkins proceeded to make a final draft, dated September 21, 1996 which was submitted to ASTM in September for the October, 1996.

As of the writing of this semiannual report, at least three negative ballots had been received which will have to be considered at the next C-28 meeting scheduled in January at Cocoa Beach, FL. It is not surprising that this document, which is fairly comprehensive and deals with a complicated property, will have to be balloted a number of times. (For example, C 1161, the original flexure strength at room temperature standard, required five ASTM ballots before it was adopted.) The consensus is that the fracture toughness draft document is in good shape and the negatives primarily deal with details that need to be polished up. We are optimistic that the standard will be adopted in 1997.

Experimental work in this task continues to refine the surface crack in flexure (SCF) method. The goals of this work are to reinforce and refine the procedures already specified in the draft ASTM standard. Specifically, in this six month interval we have:

a. Conducted a series of experiments to study the halo which is visible on the fracture surface around precracks in some ceramics.
b. Conducted some experiments in dry-nitrogen to compare apparent fracture toughness values in air versus inert atmospheres.
c. Conducted many experiments on new materials to broaden the data base.
d. Conducted some preliminary experiments with the goal of preparing a Standard Reference Material for fracture toughness.

The SCF method requires fractographic measurements of the precrack size on fracture surfaces. Sometimes there are interpretation problems due to the existence of a halo around the precrack. The halos may be detected with optical and/or scanning electron microscopy. The dilemma is whether to include the halo as part of the crack size. The halo may be caused by:

1. crack realignment to the direction of maximum principal stress during catastrophic fracture. This is a geometrical effect and the halo is due to variable light reflection or electron emission off the surfaces, or
2. stable crack extension either due to residual stresses, R-curve, or slow crack growth phenomena.

For case 1, the correct fracture toughness should be calculated using the crack size without the halo. For case 2, the crack size should include the halo. In the last semiannual report, we summarized experiments on sintered alumina, Coors grade AD 999 which conclusively proved that the halos in this material were due to water-assisted slow crack growth (SCG). There were no halos in specimens tested in dry nitrogen. A paper on this finding is in preparation for the American Ceramic Society meeting in Cocoa Beach in January, 1997.

In order to investigate further the effects of SCG on apparent toughness as measured by the SCF method, we conducted experiments on a material that is highly susceptible to SCG at room temperature in lab ambient conditions: Schott BK-7 borosilicate crown glass. We previously had reported fracture toughness in air and inert conditions but we recently expanded our data base. All specimens were from one batch of material and were 3 x 4 x 45 mm tested in 4-point fixtures (20 x 40 mm) at 0.5 mm/min. All were Knoop indented at 5 kgf. Some were tested in laboratory ambient conditions and there could be SCG from the water vapor in lab ambient air. Some were tested without the removal of the residual stresses. We expected that there would be a big difference due to the residual stresses from the indent.

1. Indent in lab ambient conditions, indent polished away to a depth of 4.5 x indent depth, lab ambient conditions:
   $K_{Ic} = 0.88 \pm 0.09$ 3 specimens.
   Evidence of slow crack growth on fracture surface. Use largest ellipse.

2. Indented in lab ambient, indent polished away to a depth of 4.5 x indent depth, tested in dry nitrogen:
   $K_{Ic} = 0.97 \pm 0.09$ 5 specimens

3. Indented with silicone oil immediately applied, then **8** x indent depth polished off (to eliminate residual stress *and* some deep lateral cracks, tested in inert nitrogen gas:
   $K_{Ic} = 1.06 \pm .08$ 5 specimens

4. Indented with silicone oil immediately applied, **no** removal of residual stresses, tested in lab normal conditions, but with silicone oil still on indent:
   $K_{Ic} = 1.04 \pm .07$ 5 specimens
   No correction for residual stresses.

5. Indented in lab ambient conditions, **no** removal of residual stresses, tested lab ambient conditions

Material	Code and/or source	Processing	ρ (Mg/m^3)	E (GPa)	characterization of precracks						success rate	K_{Ic} $\pm 1\sigma$ ($MPA\sqrt{m}$)
					Optical or SEM	halo?	brightness?	hackle lines?	overall amenity	crack size a, 2c (μm)		
Si_3N_4	Dow, self reinforced	sintered	3.20	306	SEM stereo	No	No	No	moderately difficult	77, 266	5/5	6.75 ±.29
Si_3N_4	Ceradyne, 147-3 Needlelok	Sintered, RBSN	3.2*	320*	SEM stereo	No	No	Slight	too difficult	-	0/5	(5.4 - 7.5?)
Si_3N_4	Cercom CIW15	hot pressed?	-	335*	SEM stereo	No	Sometimes	Slight	very difficult	44, 208	2/4	7.33 ±.34
Si_3N_4	Wesgo SNW 1000	sintered	3.29	281	SEM stereo	No	No	Yes	difficult	134, 354	3/6	6.37 ±.27 ★
Si_3N_4	NKK toughened	sintered?	3.26	307	SEM stereo	No	No	No	too difficult	?	0/4	-
SiC	Cercom PAD-B	hot pressed?	3.20*	455*	SEM stereo	No	No	Slight	very difficult	164 382	3/6	4.47 ±.37
B_4C	Ceradyne	hot pressed	2.48*	441-469*	SEM	No	Yes	Yes	easy	163, 299	5/5	3.08 ±.07
AIN	Dow	hot pressed	3.26	323	Optical	Yes	Yes	No	easy	133, 302	6/6	2.79 ±0.35
SiON	U.S. ARL	sintered?	-	-	SEM	No	No	Yes	easy	62, 169	3/5	1.53 ±.04
Glass ceramic	Pyroceram 9603	melt, heat treat	2.59	132	Optical, + SEM	Maybe	Yes	Yes	easy	138, 381	4/5	2.19 ±.21 &

* Company furnished data - Data unavailable & Tested in nitrogen ★ 10 kg indentations

Table 1
SCF fracture toughness results

K_{Ic} = 0.84 ± .01 MPa$\sqrt{m}$ 3 of 5 specimens attempted;
No correction for residual stresses. 2 specimens fractured from lateral cracks and were not used. Lab ambient conditions means some possibility of slow crack growth during the fracture test. Slow crack growth on fracture surface. Use largest ellipse.

These results are somewhat disappointing since a simple, clear answer for what is K_c is elusive. Is it 0.88, 0.97, or 1.06 MPa$\sqrt{m}$? We hoped to discern distinct trends for the effects of inert versus lab ambient test conditions and/or the influence of the residual stresses. Unfortunately the data scatter is high. We take some consolation in the findings of other related studies on the identical material. Theo Fett and Dietrich Munz at the Nuclear Research Center at Karlsruhe report (1988, 1991, 1993) exactly the same scatter (K_c averages of 0.8, 0.9, 1.05 MPa$\sqrt{m}$ depending on exact test conditions) in their fracture toughness values by the same test method. Similarly, Sheldon Wiederhorn in his original work (1972) on the Skylab windows measured the fracture toughness of BK-7 by precracked beam specimens and double cantilever beam specimens obtained toughnesses from 0.84 - 0.93 in vacuum. All the data were collected under careful testing conditions. It is not likely that residual stresses existed in any of the material since the plates in all three studies were carefully annealed to ensure perfect optical performance. We conclude that this material has scatter in fracture toughness measurements due to: variability in the material, subtle variability in the test methods, and lastly and most likely, that the methods are all measuring apparent toughness values that are really different points on the Region III curve on a K-V (stress intensity versus crack velocity) diagram. Region III has a slope (SCG exponent) of about 105 for BK-7 in vacuum at room temperature (Wiederhorn, 1972) which is so steep that one would not expect much apparent K_c toughness variability.

New test data has been collected on ten new materials and will be presented in a paper at the American Ceramic Society conference in January, 1997 at Cocoa Beach. The last four materials in Table 1 were chosen in order to expand our data base to verify that the test method is applicable to low toughness materials. With the sole exception of SNW 1000 (for which 10 kg was used) all precracks were made with 5 kg Knoop indentation with 4.5 times the indentation depth polished away to remove residual stresses. All testing was in lab ambient conditions with the exception of the glass ceramic which was tested in nitrogen. The information in the fractographic characterization columns pertains to the detectability of the precracks. A paper on these findings is in preparation for the Cocoa Beach meeting of the American Ceramic Society in January, 1997.

Dow sintered silicon nitride is a self-reinforced material. Five specimens were tested successfully and gave an average toughness of 6.75 MPa$\sqrt{m}$ which is in good agreement with chevron notch results of 6.8 reported by Dow. Fractography was difficult, but stereo scanning electron microscope pictures were able to show the precracks.

Cercom CIW15 is a hot-pressed silicon nitride with 15% silicon carbide whiskers. From four test specimens, only three specimens fractured from the precrack. Two valid test results were obtained with an average toughness of 7.33 MPa$\sqrt{m}$. Fractographic/ interpretation was difficult and there was some evidence of stable crack extension prior to fracture.

Ceradyne 147-3 is a sintered, reaction-bonded silicon nitride with a tailored

microstructure of elongated, interlocking grains. SCF specimens did fracture from the surface cracks, but interpretation of the precrack boundary was too speculative to permit a fracture toughness calculation. The complex microstructure, which gives rise to the enhanced toughness, causes difficulty in fractographic interpretation.

We received a four specimens of NKK silicon nitride from Jon Salem at NASA-Lewis. Salem and Choi previously had reported SEPB and CN results for this material, and we wanted to compare results from the three methods in the draft ASTM standard on this very tough silicon nitride. Unfortunately, only two of the specimens fractured from our SCF precracks and in these we could not see or measure the precracks reliably due to the rough, complex microstructure.

Clearly these findings point out the need to develop a simple dye-penetration procedure to highlight SCF precracks, a task we intend to commence in 1997. We were also handicapped in many instances in having only five or fewer specimens to test for a material. The ASTM draft recommends that ten or more be prepared, from which four valid tests should be obtained.

A Standard Reference Material for fracture toughness would be a excellent support for the ASTM draft standard and would be a giant step in improving fracture toughness testing in general. Two materials are under consideration for this role: hot-pressed silicon nitride, grade NC 132, or sintered alpha silicon carbide. An enormous data base exists for the former and it was featured in an international round robin in which superlative results were obtained. It has negligible R-curve behavior, but may be susceptible to slight SCG at room temperature in ambient air. During this semiannual period, experiments have started to assess the sensitivity of our NC 132 SCF fracture toughness results to such SCG. The alternative material, sintered silicon carbide, has a flat R-curve and experiences no SCG at room temperature. The data base is less complete for this material, but exceptionally consistent SCF fracture toughness data has been generated by several labs.

Hardness

The two ASTM hardness standards were adopted by ASTM in January, 1996 as:

ASTM C 1326-96	"Standard Test Method for Knoop Indentation Hardness of Advanced Ceramics."
ASTM C 1327-96	"Standard Test Method for Vickers Indentation Hardness of Advanced Ceramics."

Knoop hardness certified hardness blocks, SRM #2830, were prepared in a parallel program at NIST. These have passed the review and statistical evaluation process at NIST and were put on sale in January, 1996 at a unit cost of $555. Hardness is *certified to within 1% at a 95% confidence level.* The Knoop standard, SRM #2830, uses NBD 200 hipped silicon nitride and an indentation load of 2 kgf (19.6 N). SRM #2831, Vickers Indentation Hardness at 1 kgf (9.8 N), has been delayed.

During this semiannual period, corrections and refinements to the two ASTM hardness standards were prepared for the Fall 1996 ASTM ballot. The revisions were: clarifications to several minor technical points, inclusion of several new references, and a

major new addition to clarify the proper utilization of microscope crosshairs. The latter is one of the biggest problems in making hardness measurements. Test machine operators (novices and pros alike) often use the machine crosshairs improperly.

We are gratified that preliminary results of a new VAMAS hardness of ceramics round robin have been released. The round robin was organized by the Japan Fine Ceramic Center and featured a silicon nitride with 0, 10, and 20% SiC whiskers additives. Testing was done with Vickers indentations at 1 and 10 kg, and Knoop at 1 and 2 kg. *The best results (within-lab repeatability and between-lab reproducibility) were obtained with the Knoop 2 kg condition, which is the preferred procedure specified in our new ASTM standard C 1326-96.* These results vindicate our stance of using a higher than normal load for Knoop indentations. We expect that this will have a big impact on ISO standardization and may cause other national groups to reconsider their earlier hardness standards.

Fractography

"Standard Practice for Fractography and Characterization of Fracture Origins in Advanced Ceramics," was adopted by ASTM as Standard Practice C 1322-96 in January, 1996. This work is a collaboration between G. Quinn of NIST and J. Swab of U. S. Army Research Laboratory (ARL).

A "Revision to C 1322" was prepared for a subcommittee C 28.05 ballot in August, 1996. The revisions corrected paragraph 7.2.4.4.2 pertaining to the mirror to flaw size ratio and also added new citations to a paper by Quinn and Swab on comparing calculated to measured flaw sizes. Finally, the revision included a new clause pertaining to the characterization of different types of external surfaces (e.g., side surface versus tensile surface on bend bars) on specimens or components in paragraph 7.2.3.2.

During this semiannual report we prepared several fractographic terms that were balloted and subsequently adopted for inclusion into the C-28 master terminology standard, C 1145. These were:

fractography:	means and methods for characterizing a fractured specimen or component.
fracture origin:	the source from which brittle fracture commences.

We are pleased to report that a new activity to standardize fractographic analysis in the European Community will borrow heavily from C 1322-96, in no small part due to the success of a VAMAS fractography round robin and the success of an IEA Subtask 7 fractography exercise.

On the matter of technology transfer, we are also pleased to report that MIL HDBK 790 and ASTM C 1322 are distributed and presented as parts of fractography courses offered by the American Ceramic Society (topical course) and Alfred University (special summer course). Review of other progress reports in this semiannual progress report volume will likely reflect elements of the fractographic procedures standardized in C 1322. We appreciate and thank the help offered to us on this task from other DOE subcontractors.

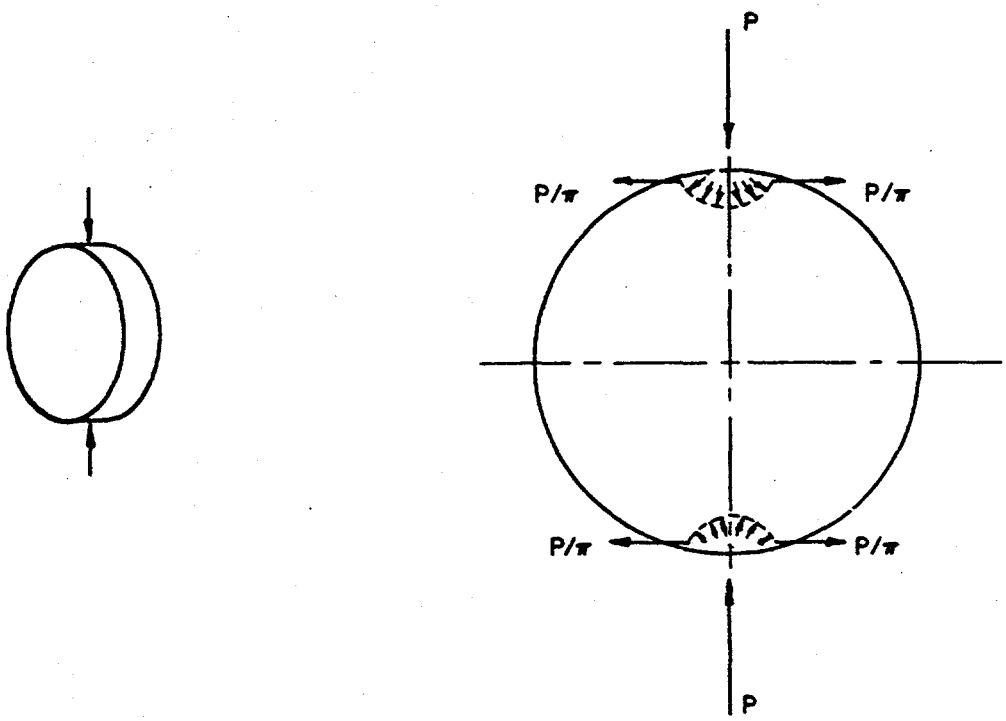

Figure 1

The diametral compression strength test. A cylindrical specimen is loaded on its ends Fracture commences from tensile stresses in the middle of the disk.

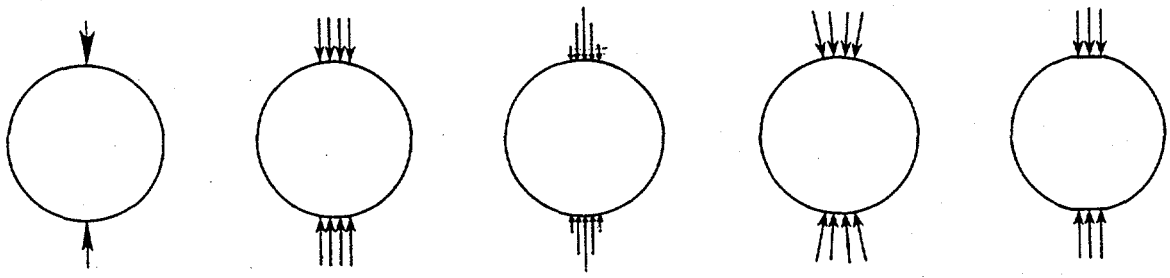

Figure 2

Many stress solutions have shown that the tensile stresses in the center of the disk are insensitive to the details of loading at the rim. Provision must be made to distribute the load, however, otherwise shear stresses will cause fractures from the contact points.

This fractographic element of this project is now complete.

Diametral Compression

The diametral compression test method, also known as the Brazilian disk method, is occasionally used to measure the strength of brittle materials. Figure 1 illustrates the testing configuration. A right circular cylindrical specimen is loaded on its ends and compressed. Provided that the load is distributed somewhat on the ends (to prevent crushing or shear fractures) a tensile stress in the middle of the disk will cause fracture. The stress state is biaxial, with the tension stress accompanied by compression stresses than are three times as large. The compression stresses do not have a significant effect upon the fracture, however. Hence, the method is suitable for measuring the tensile strength of ceramics.

This method is *ideally suited for determination of strength of cylindrical parts* such as valves or fuel injection pins, or for small specimens cut from larger components. The highest stresses in the specimen exist both at the surface and in a large part of the volume of the specimen. The fixtures and the specimens are *extremely simple and cheap*.

Mr. Quinn and Mr. Swab of the U. S. ARL will evaluate this method and prepare an ASTM draft standard.

During this six month interval, we completed some preliminary tests of diametral compression strength specimens and conducted a comprehensive literature survey of all diametral compression strength tests reported on ceramics over the last 30 years. The literature survey found 65 papers or articles that were relevant, ranging from materials evaluation papers to theoretical studies of the stress states in the specimens. There are some amazing conclusions that we draw from the review:

1. The *theoretical, classical solutions* for the state of stress in disk have been devised by Hertz (1880's), Mitchell (1900), Timoshenko (1934), and Timoshenko and Goodier (1951) are completely consistent and yield simple, elegant solutions for the stresses in the disk.
2. Subsequent analytical studies by *theory of elasticity* (Hondros, 1959); (Peltier, 1954); Davidson, Wadley, Pindera, 1994); (Awaji and Sato, 1979) all agree with the classical solution over nearly the entire volume of the disk.
3. *Strain gage studies* (Rosenfield, Shetty, McGuire, Bansal, Duckworth, 1979); (Hondros, 1959); (Fessler and Fricker, 1976); and (Shetty et al., 1986) all confirm the classical solutions are correct and very precisely so.
4. Modern *finite element (FEM)* analysis (Love, 1967); (Price and Murray, 1973); and Rosenfield, Shetty, McGuire, Bansal and Duckworth, 1979); (Fahad, 1996) also confirm that the classical stress solutions are correct.
5. Comprehensive *photoelastic studies* (Frocht, 1941 and 1948), (Rudnick, Hunter, and Holden, 1963); and (Price and Murray, 1973) also confirm the stress state for almost the entire volume of the body.

Such a convergence of solutions by all these studies is remarkable. That so many investigators analyzed and confirmed the stress solutions suggests a widespread skepticism

that the simple classical solution could be correct. It appears it is. Many of the subsequent analyses started by confirming the classical solutions, but then expanded them to cover cases of distributed loads such as shown in Figure 2. Distributed loads are essential to preclude premature fracture due the extreme concentrated loading at the anvils. Indeed, it is common in the ceramics community to utilize shims or load spreaders do distribute the loads a bit at the loading points. The next remarkable finding is that these studies have confirmed that the *exact details of the load distribution* (whether it is uniform, with a Hertzian distribution, or even over a machined flat on the end of the disk as shown on the right of Figure 2) *are inconsequential*. The stress state in the disk middle is hardly affected at all provided that the breadth of the contact area is within limits. This is evidently a consequence of St. Venant's principle. In other words, the stress state in the middle of the disk is very robust and does not depend very much on the details of the loading.

There are limits to this finding, however. Shims must not be too thin or too thick and or too broad. The shim material should also have a low Poisson's ratio to avoid lateral stresses. Most studies empirically have converged on pieces of thin manila folders, file index cards, or even old IBM cards. These materials have low Poisson's rations, whereas metallic foils or shims do not. This has been widely overlooked by many testers.

Another remarkable conclusion is the almost complete paucity of fractographic analysis. There are only three papers that we are aware of that actually discuss the fracture origins. Most papers merely state that the fracture was in a classic triple-cleft mode which is characteristic of a properly-conducted test.

The method has been applied to many ceramics, plastics, and concrete and credible results have been obtained. In most instances, the diametral compression strength is less than three- or four-point flexure strength of the exact same material. Data is very sparse, but diametral strengths are often similar to direct tension strength (Spriggs, Brisselle, and Vasilos, 1964). Several studies attempted to relate the different strengths by conventional Weibull analysis. Results have been mixed, but several successful examples have been reported (e.g. Vardar and Finnie, 1975) and (Fessler, Fricker, and Godfrey, 1983). In all probability, the lower strengths of the diametral compression strength specimens is attributable to the larger volume that is under high stress in diametral compression specimens than in flexure specimens.

We conclude that the lower strengths obtained in diametral compression specimens and the uncertainty about the meaning of the test results have curbed widespread acceptance of this test method in the general ceramics community. That is a shame, since it appears to be a very suitable test for a range of ceramic materials and components, and exceptionally rigorous stress solutions are in existence. Work in the last 20 years on the mixed-mode fracture problem (Mode I and Mode II loadings on cracks) or multiaxial stress states (tension-compression stress quadrant) have shown that the second component of stress in diametral compression specimens will have *very little or no effect* upon fracture behavior or strength.

So, it is our intent to capitalize on this set of circumstances and advance this test

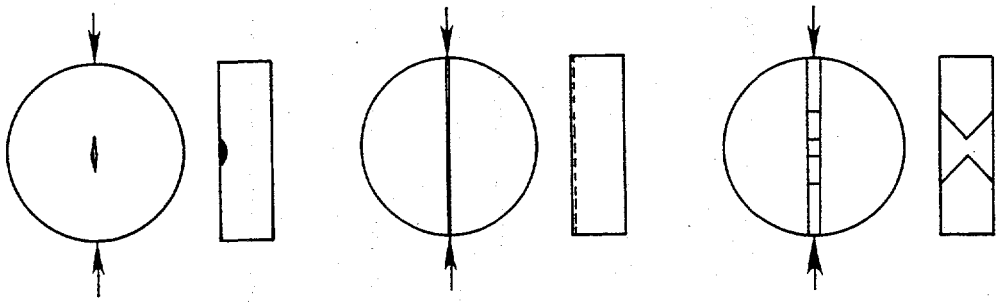

Figure 3

The diametral compression test has been adapted to measure fracture toughness.

method. Emphasis will be on applying sound fractographic techniques to the fractured disks. This may help clear up the question of why diametral compression strengths are different than results from other methods.

In this six month period, we did some preliminary testing to reacquaint ourselves with the method, to obtain some simple data, and to produce some fractured specimen suitable for fractographic analysis. Hardened steel compression anvils were prepared and then used for preliminary diametral compression experiments on simple Coors AD 99 alumina rods. The alumina rods were extruded and were very inexpensive. We prepared 1/4" and 3/8" diameter disks with diameter to thickness ratios of 2:1 and 4:1. Similarly, specimens from a partially-stabilized zirconia were also prepared and tested. In all cases we used simple index cards as inserts.

Fractures were in the conventional triple cleft fracture mode, and the origins were volume distributed defects in the cores of the AD 99 alumina rods. Indeed, the alumina specimens had a higher porosity concentration in the core which is not surprising considering that the rods were extruded and sintered. This points out one of the reasons that could account for differences in flexure and diametral compression strengths in earlier studies: different flaw populations or flaw distributions were activated. Strength results are being analyzed.

New specimens are being fabricated from sintered alumina AD-999 plates which should not have the core-porosity problem and which will better enable us to compare flexure to diametral compression strengths. Sintered alpha silicon carbide specimens are also on order. The objective will be to correlate results to flexure data for specimens cut from the identical billet. Emphasis will be on fractography to confirm that the same flaws are activated in the respective test methods.

Finally, we would be remiss if we did not point out that the diametral compression specimen is attractive as a potential fracture mechanics test specimen. Figure 3 illustrates several testing configurations that have been reported already in the literature.

Other Activities

It is important that our ASTM documents, which were so painstakingly prepared, be represented adequately and defended in the ISO forum.

A draft International Standards Organization Technical Committee TC 206 fracture toughness standard was prepared by Dr. T. Nose and presented at the ISO meeting in July. Mr. Quinn assisted Prof. Bar-on in presenting the USA response to this draft. The draft is built around the Single-Edge Precracked Beam (SEPB) method. On behalf of ASTM C-28, we are attempting to have Dr. Nose refine his draft and bring it more into harmony with the draft ASTM C-28 document.

A draft flexure strength standard was prepared in April, 1996 for International Standards Organization Technical Committee 206. Following a meeting of TC 206 in July, a revised draft was prepared on November 22, 1996 and distributed to ASTM C-28 ISO

Technical Advisory Group members for review. This draft standard incorporates nearly all the critical elements of ASTM C 1161 and thus is harmonious with USA interests.

Draft hardness standards from ISO TC 206 were reviewed and vigorously reviewed. Our input and results from a new VAMAS round robin are causing the Japanese conveners to rewrite extensively their hardness document in order to bring it more into line with the ASTM standards C 1326 and C 1327.

At the ISO TC 206 meeting, Mr. Quinn represented the United States in the task groups for hardness, flexure strength, tension strength of monolithics, and tension strength of CFCC's.

Status of Milestones

412123 Conduct preliminary diametral compression strength tests.
Completed October 1996.

412124 Prepare comprehensive paper on hardness testing of ceramics.
Postpone due to delays associated with preparing SRM 2831, Vickers hardness of ceramics, and also shift of work to other priorities.

412125 Prepare draft ISO Flexure Strength Standard.
Completed April 1996

412126 Prepare and distribute to ASTM Committee C-28 members a simple statistical analysis package for interlaboratory round robin test data.
Completed, June 1996

412127 Participate in a ceramic whisker-reinforced composite round robin
Completed May 1996.

Other milestones are on schedule with the exception of the following:

412128 Conduct dye-penetrant experiments on SCF fracture toughness specimens (to develop a simpler, lower cost fracture toughness evaluation method).
Delay to June, 1997 so that an effort can be made to finish the Vickers hardness SRM #2831.

Publications/Presentations

1. C. R. Brinkman, G. D. Quinn, and R. W. McClung, "Overview of ASTM Standard Activities in Support of Advanced Structural Ceramics Development," pp. 97 - 108 in Challenges in Ceramic Product Development, Manufacturing and Commercialization, Ceramic Transactions, Vol 66, American Ceramic Society, Westerville, OH, 1996.
2. G. D. Quinn and R. J. Gettings, "Fractography and the Surface Crack in Flexure (SCF) Method for Evaluating Fracture Toughness of Ceramics," pp 107 - 144 in "Fractography of Glasses and Ceramics," Ceramic Transactions, Vol. 64, ACS,

Westerville, OH, 1996.
3. J. J. Swab and G. D. Quinn, "Findings of the VAMAS Fractography Round Robin Exercise," idem, pp 55 -70.
4. G. D. Quinn and J. J. Swab, "Fractography and Estimates of Fracture Origin Size from Fracture Mechanics," presented at Cocoa Beach, Jan. 1996, to be publ. Ceram. Eng. and Sci. Proc., 1996.
5. M. G. Jenkins and G. D. Quinn, "ASTM Standards for Monolithic and Composite Advanced Ceramics: Industrial, Governmental and Academic Cooperation," American Society of Mechanical Engineers paper 96-GT-270, June 1996. Presented at the International Gas Turbine and Aerospace Congress, Birmingham, UK, June 10, 1996.

Communications/Visits

G. Quinn consulted with S. Wiederhorn and W. Leucke on the topic of statistical analysis of interlaboratory test data. W. Leucke will come to the Cocoa Beach January, 1997 C-28 meeting and make a presentation on the round robin results to C-28.01.

Jon Salem of NASA-Lewis kindly furnished us a few specimens of NKK silicon nitride in support of our K_c work.

G. Quinn attended the Customers Coordination Meeting in October and helped Charles Brinkman prepare and present a poster paper:

"Standardization of Mechanical Properties Tests for Advanced Ceramics."

H. D. Cai of Allied-Signal Engine Company requested information on SCF fracture toughness testing.

Mr. Quinn attended the ASTM C-28 meeting in West Conshohocken, Pennsylvania in June.

Mr. Quinn exchanged correspondence with a Dr. Koichi Yasuda of the Tokyo Institute of Technology regarding SCF testing. Dr. Yasuda is an advocate of SCF testing and has new results regarding application of the method to materials with rising R-curve behavior.

A draft dynamic fatigue standard was received from Mr. S. Choi of NASA-Lewis. Mr. Quinn reviewed this and recommended a few minor changes prior to C-28 balloting in October.

G. Quinn helped Michael Jenkins prepare an overview article on C-28's activities for an ASME Turbine conference.

INTERNAL DISTRIBUTION

Central Research Library (2)
Document Reference Section
Laboratory Records Department (2)
Laboratory Records, ORNL RC
ORNL Patent Section
L. F. Allard, Jr.
P. F. Becher
T. M. Besmann
P. J. Blau
R. A. Bradley
K. Breder
C. R. Brinkman
A. Choudhury
D. D. Conger
R. H. Cooper, Jr.
S. A. David
M. K. Ferber
R. L. Graves
H. W. Hayden, Jr.
C. R. Hubbard
M. A. Janney
D. R. Johnson (5)
R. R. Judkins
M. A. Karnitz
H. D. Kimrey, Jr.
R. J. Lauf
W. Y. Lee
K. C. Liu
W. D. Manly
S. B. McSpadden
T. A. Nolan
A. E. Pasto
M. H. Rawlins
M. L. Santella
A. C. Schaffhauser
D. P. Stinton
T. N. Tiegs
S. G. Winslow
R. E. Ziegler

EXTERNAL DISTRIBUTION

Pioneering Research Info. Ctr.
E.I. Dupont de Nemours & Co.
Experimental Station
P.O. Box 80302
Wilmington DE 19880-0302

Jeffrey Abboud
U.S. Advanced Ceramics Assoc.
1600 Wilson Blvd., Suite 1008
Arlington VA 22209

Joseph E. Amaral
Instron Corporation
Corporate Engineering Office
100 Royale Street
Canton MA 02021

Edward M. Anderson
Aluminum Company of America
N. American Industrial Chemical
P.O. Box 300
Bauxite AR 72011

Joseph Annese
Bomas Machine
334 Washington Street
Somerville MA 02143

Frank Armatis
3M Company
Building 60-1N-01
St. Paul MN 55144-1000

V. S. Avva
North Carolina A&T State Univ.
Dept. of Mechanical Engineering
Greensboro NC 27411

Bob Baker
Ceradyne, Inc.
3169 Redhill Avenue
Costa Mesa CA 92626

Frank Baker
Aluminum Company of America
Alcoa Technical Center
Alcoa Center PA 15069

Clifford P. Ballard
AlliedSignal Aerospace Company
Ceramics Program
P.O. Box 1021
Morristown NJ 07962-1021

B. P. Bandyopadhyay
University of North Dakota
Box 8359 University Station
Grand Forks ND 58202-8359

Renald D. Bartoe
Vesuvius McDanel
510 Ninth Avenue
Box 560
Beaver Falls PA 15010-0560

David L. Baty
Babcock & Wilcox - LRC
P.O. Box 11165
Lynchburg VA 24506-1165

Donald F. Baxter, Jr.
ASM International
Advanced Materials & Processes
Materials Park OH 44073-0002

M. Brad Beardsley
Caterpillar Inc.
Technical Center Bldg. E
P.O. Box 1875
Peoria IL 61656-1875

Larry D. Bentsen
BFGoodrich Company
R&D Center
9921 Brecksville Road
Brecksville OH 44141

Ram Bhatt
NASA Lewis Research Center
21000 Brookpark Road
Cleveland OH 44135

William D. Bjorndahl
TRW, Inc.
One Space Park, MS:R6-2188
Building 01, Room 2040
Redondo Beach CA 90278

Keith A. Blakely
Advanced Refractory Technologies, Inc.
699 Hertel Avenue
Buffalo NY 14207

Edward G. Blanchard
Netzsch Inc.
119 Pickering Way
Exton PA 19341

Bruce Boardman
Deere & Company Technical Ctr.
3300 River Drive
Moline IL 61265-1792

Tom Booth
AlliedSignal, Inc.
AiResearch Los Angeles Division
2525 West 190th Street
Torrance CA 90509-2960

Steven C. Boyce
Air Force Office of Scientific Research
AFOSR/NA Bldg. 410
Bolling AFB DC 20332-6448

Steve Bradley
UOP Research Center
50 E. Algonquin Road
Des Plaines IL 60017-6187

Michael C. Brands
Cummins Engine Company, Inc.
P.O. Box 3005, Mail Code 50179
Columbus IN 47201

Raymond J. Bratton
Westinghouse Science & Technology
1310 Beulah Road
Pittsburgh PA 15235

John J. Brennan
United Technologies Corporation
Silver Lane, MS:24
East Hartford CT 06108

S. L. Bruner
Ceramatec, Inc.
2425 South 900 West
Salt Lake City UT 84119

Walter Bryzik
U.S. Army Tank Automotive Command
R&D Center, Propulsion Systems
Warren MI 48397-5000

David A. Caillet
Ethyl Corporation
451 Florida Street
Baton Rouge La 70801

David Carruthers
Kyocera Industrial Ceramics
5713 East Fourth Plain
Vancouver WA 98661

Ronald H. Chand
Chand Kare Technical Ceramics
2 Coppage Drive
Worcester MA 01603-1252

William J. Chmura
Torrington Company
59 Field Street
Torrington CT 06790-4942

William S. Coblenz
Adv. Research Projects Agency
3701 N. Fairfax Drive
Arlington VA 22203

Gloria M. Collins
ASTM
1916 Race Street
Philadelphia PA 19103

William C. Connors
Sundstrand Aviation Operations
Materials Science & Engineering
4747 Harrison Avenue
Rockford IL 61125-7002

Shawn Cooper
FEV Engine Technology
2285 Opdyke Road, Suite F
Auburn Hills MI 48326

Normand D. Corbin
Norton Company
SGNICC/NRDC
Goddard Road
Northboro MA 01532-1545

Douglas Corey
AlliedSignal, Inc.
2525 West 190th Street, MS:T52
Torrance CA 90504-6099

Keith P. Costello
Chand/Kare Technical Ceramics
2 Coppage Drive
Worcester MA 01603-1252

Ed L. Courtright
Pacific Northwest Laboratory
MS:K3-59
Richland WA 99352

J. Wesley Cox
BIRL
1801 Maple Avenue
Evanston IL 60201-3135

Art Cozens
Instron Corporation
3414 Snowden Avenue
Long Beach CA 90808

Mark Crawford
New Technology Week
4604 Monterey Drive
Annandale VA 22003

Les Crittenden
Vesuvius McDanel
Box 560
Beaver Falls PA 15010

M. J. Cronin
Mechanical Technology, Inc.
968 Albany-Shaker Road
Latham NY 12110

Gary M. Crosbie
Ford Motor Company
20000 Rotunda Drive
MD-3182, SRL Building
Dearborn MI 48121-2053

Floyd W. Crouse, Jr.
U.S. Department of Energy
Morgantown Energy Tech. Ctr.
P.O. Box 880
Morgantown WV 26505

John Cuccio
AlliedSignal Engines
P.O. Box 52180, MS:1302-2Q
Phoenix AZ 85072-2180

Raymond A. Cutler
Ceramatec, Inc.
2425 South 900 West
Salt Lake City UT 84119

Sankar Das Gupta
Electrofuel Manufacturing Co.
9 Hanna Avenue
Toronto Ontario MGK-1W8
CANADA

George C. DeBell
Ford Motor Company
Scientific Research Lab
P.O. Box 2053, Room S2023
Dearborn MI 48121-2053

Michael DeLuca
RSA Research Group
1534 Claas Ave.
Holbrook NY 11741

Sidney Diamond
U.S. Department of Energy
Office of Transportation Technologies
EE-33, Forrestal Building
Washington DC 28505

Douglas A. Dickerson
Union Carbide Specialty Powders
1555 Main Street
Indianapolis IN 46224

John Dodsworth
Vesuvius Research & Development
Technical Ceramics Group
Box 560
Beaver Falls PA 15010

Alan Dragoo
U.S. Department of Energy
ER-131, MS:F-240
Washington DC 20817

Barry Draskovich
AlliedSignal, Inc.
Ceramic Components
P. O. Box 2960, MS:T-21
Torrance CA 90509-2960

Kenneth C. Dreitlein
United Technologies Res. Ctr.
Silver Lane
East Hartford CT 06108

Ernest J. Duwell
3M Abrasive Systems Division
3M Center
St. Paul MN 55144-1000

Robert J. Eagan
Sandia National Laboratories
Engineered Mater. & Proc.
P.O. Box 5800
Albuquerque NM 87185-5800

Harvill C. Eaton
Louisiana State University
240 Thomas Boyd Hall
Baton Rouge LA 70803

J. J. Eberhardt
U.S. Department of Energy
Office of Transportation Technologies
EE-33, Forrestal Building
Washington DC 20585

Jim Edler
Eaton Corporation
26201 Northwestern Highway
P.O. Box 766
Southfield MI 48037

G. A. Eisman
Dow Chemical Company
Ceramics and Advanced Materials
52 Building
Midland MI 48667

William A. Ellingson
Argonne National Laboratory
Energy Technology Division
9700 S. Cass Avenue
Argonne IL 60439

Anita Kaye M. Ellis
Machined Ceramics
629 N. Graham Street
Bowling Green KY 42101

Art Erdemir
Argonne National Laboratory
9700 S. Cass Avenue
Argonne IL 60439

E. M. Erwin
Lubrizol Corporation
17710 Riverside Drive
Lakewood OH 44107

W. L. Everitt
Kyocera International, Inc.
8611 Balboa Avenue
San Diego CA 92123

John W. Fairbanks
U.S. Department of Energy
Office of Transportation Technologies
EE-33, Forrestal Building
Washington DC 20585

Ho Fang
Applied Materials
2727 Augustine Drive, MS-0727
Santa Clara CA 95054

Tim Fawcett
Dow Chemical Company
Advanced Ceramics Laboratory
1776 Building
Midland MI 48674

Robert W. Fawley
Sundstrand Power Systems
Div. of Sundstrand Corporation
P.O. Box 85757
San Diego CA 92186-5757

Jeff T. Fenton
Vista Chemical Company
900 Threadneedle
Houston TX 77079

Raymond R. Fessler
BIRL
1801 Maple Avenue
Evanston IL 60201-3135

Michael Foley
Norton Company
Goddard Road
Northboro MA 01532-2527

Renee G. Ford
Materials and Processing Report
P.O. Box 72
Harrison NY 10528

Edwin Frame
Southwest Research Institute
P.O. Drawer 28510
San Antonio TX 78284

Marc R. Freedman
NASA Lewis Research Center
21000 Brookpark Road, MS:49-3
Cleveland OH 44135

Douglas Freitag
Bayside Materials Technology
17 Rocky Glen Court
Brookeville MD 20833

Brian R.T. Frost
Argonne National Laboratory
9700 S. Cass Avenue, Bldg. 900
Argonne IL 60439

Lawrence R. Frost
Instron Corporation
100 Royall Street
Canton MA 02021

J. P. Gallagher
University of Dayton Research Institute
300 College Park, JPC-250
Dayton OH 45469-0120

Richard Gates
NIST
Bldg. 223, Rm. A-256
Rt. 270 & Quince Orchard Road
Gaithersburg MD 20899

John Ghinazzi
Coors Technical Ceramics Co.
1100 Commerce Park Drive
Oak Ridge TN 37830

Robert Giddings
General Electric Company
P.O. Box 8
Schenectady NY 12301

W. M. Goldberger
Superior Graphite Company
R&D
2175 E. Broad Street
Columbus OH 43209

Allan E. Goldman
U.S. Graphite, Inc.
907 W. Outer Drive
Oak Ridge TN 37830

Frank W. Gorman
Astro Met, Inc.
9974 Springfield Pike
Cincinnati OH 45215

Robert J. Gottschall
U.S. Department of Energy
ER-131, MS:G-236
Washington DC 20585

G. A. Graves
U. of Dayton Research Institute
300 College Park
Dayton OH 45469-0001

Lance Groseclose
Allison Engine Company
P.O. Box 420, MS:W-05
Indianapolis IN 46206

Thomas J. Gross
U.S. Department of Energy
Office of Transportation Technologies
EE-30, Forrestal Building
Washington DC 20585

Mark F. Gruninger
Union Carbide Corporation
Specialty Powder Business
1555 Main Street
Indianapolis IN 46224

John P. Gyekenyesi
NASA Lewis Research Center
21000 Brookpark Road, MS:6-1
Cleveland OH 44135

Nabil S. Hakim
Detroit Diesel Corporation
13400 Outer Drive West
Detroit MI 48239

Philip J. Haley
Allison Engine Company
P.O. Box 420, MS:T12A
Indianapolis IN 46206-0420

Judith Hall
Fiber Materials, Inc.
Biddeford Industrial Park
5 Morin Street
Biddeford ME 04005

Y. Harada
IIT Research Institute
10 West 35th Street
Chicago IL 60616

Norman H. Harris
Hughes Aircraft Company
P.O. Box 800520
Saugus CA 91380-0520

Alan M. Hart
Dow Chemical Company
1776 Building
Midland MI 48674

Pat E. Hart
Battelle Pacific Northwest Labs
Ceramics and Polymers Development
P.O. Box 999
Richland WA 99352

Michael H. Haselkorn
Caterpillar Inc.
Technical Center, Building E
P.O. Box 1875
Peoria IL 61656-1875

Deborah A. Haught
U.S. Department of Energy
Off. of Transportation Technologies
EE-32, Forrestal Bldg.
Washington DC 20585

N. B. Havewala
Corning Inc.
SP-PR-11
Corning NY 14831

John Haygarth
Teledyne WAA Chang Albany
P.O. Box 460
Albany OR 97321

Norman L. Hecht
U. of Dayton Research Institute
300 College Park
Dayton OH 45469-0172

Peter W. Heitman
Allison Engine Company
P.O. Box 420, MS:W-5
Indianapolis IN 46206-0420

Hendrik Heystek
Bureau of Mines
Tuscaloosa Research Center
P.O. Box L
University AL 35486

Robert V. Hillery
GE Aircraft Engines
One Neumann Way, M.D. H85
Cincinnati OH 45215

Arthur Hindman
Instron Corporation
100 Royall Street
Canton MA 02021

John M. Hobday
U.S. Department of Energy
Morgantown Energy Tech. Ctr.
P.O. Box 880
Morgantown WV 26507

Stephen M. Hsu
NIST
Bldg. 223, Rm A256
Rt. 270 & Quince Orchard Road
Gaithersburg MD 20899

Hann S. Huang
Argonne National Laboratory
9700 S. Cass Avenue
Argonne IL 60439-4815

Gene Huber
Precision Ferrites & Ceramics
5576 Corporate Drive
Cypress CA 90630

Fred R. Huettic
Advanced Magnetics Inc.
45 Corey Lane
Mendham NJ 07945

Robert M. Humrick
Dylon Ceramic Technologies
3100 Edgehill Road
Cleveland Heights OH 44118

Said Jahanmir
NIST
Materials Bldg., Room A-237
Gaithersburg MD 20899

Curtis A. Johnson
General Electric Company
P.O. Box 8
Schenectady NY 12301

Sylvia Johnson
SRI International
333 Ravenswood Avenue
Menlo Park CA 94025

Thomas A. Johnson
Lanxide Corporation
P.O. Box 6077
Newark DE 19714-6077

Walter F. Jones
AFOSR/NA
110 Duncan Ave., Ste. B115
Washington DC 20332-0001

Jill E. Jonkouski
U.S. Department of Energy
9800 S. Cass Avenue
Argonne IL 60439-4899

Adam Jostons
Materials Division
ANSTO
PMB 1 Menal NSW 2234
AUSTRALIA

Yury Kalish
Detroit Diesel Corporation
Mechanical Systems
13400 Outer Drive West
Detroit MI 48239-4001

Lyle R. Kallenbach
Phillips Petroleum
Mail Drop:123AL
Bartlesville OK 74004

Roy Kamo
Adiabatics, Inc.
3385 Commerce Park Drive
Columbus IN 47201

Keith R. Karasek
AlliedSignal Aerospace Company
50 E. Algonquin Road
Des Plaines IL 60017-5016

Allan Katz
Wright Laboratory
Metals and Ceramics Division
Wright-Patterson AFB OH 45433

R. Nathan Katz
Worcester Polytechnic Institute
100 Institute Road
Worcester MA 01609

Lisa Kempfer
Penton Publishing
1100 Superior Avenue
Cleveland OH 44114-2543

Frederick L. Kennard, III
Delphi Energy & Engine Mgmt. Systems
Division of General Motors
1300 N. Dort Highway
Flint MI 48556

David O. Kennedy
Lester B. Knight Cast Metals
549 W. Randolph Street
Chicago IL 60661

Thomas Ketcham
Corning, Inc.
SP-DV-1-9
Corning NY 14831

Pramod K. Khandelwal
Allison Engine Company
P.O. Box 420, MS:T10B
Indianapolis IN 46206

W. C. King
Mack Truck, Z-41
1999 Pennsylvania Avenue
Hagerstown MD 21740

Carol Kirkpatrick
MSE, Inc.
P.O. Box 3767
Butte MT 59702

Tony Kirn
Caterpillar Inc.
Defense Products Dept., JB7
Peoria IL 61629

James D. Kiser
NASA Lewis Research Center
21000 Brookpark Road, MS:49-3
Cleveland OH 44135

Stanley J. Klima
NASA Lewis Research Center
21000 Brookpark Road, MS:6-1
Cleveland OH 44135

Richard A. Kole
Z-Tech Corporation
8 Dow Road
Bow NH 03304

Joseph A. Kovach
Eaton Corporation
32500 Chardon Road
Willoughby Hills OH 44094

Edwin H. Kraft
Kyocera Industrial Ceramics
5713 E. Fourth Plain Boulevard
Vancouver WA 98661

Arthur Kranish
Trends Publishing Inc.
1079 National Press Building
Washington DC 20045

Edward J. Kubel, Jr.
ASM International
Advanced Materials & Processes
Materials Park OH 44073

Oh-Hun Kwon
North Company
SGNICC/NRDC
Goddard Road
Northboro MA 01532-1545

Hari S. Lamba
General Motors Corporation
9301 West 55th Street
LaGrange IL 60525

Richard L. Landingham
Lawrence Livermore National Lab
P.O. Box 808, L-369
Livermore CA 94550

James Lankford
Southwest Research Institute
6220 Culebra Road
San Antonio TX 78228-0510

S. K. Lau
Carborundum Corporation
Technology Division
22 Acheson Drive
Niagara Falls NY 14303

J. Lawrence Lauderdale
Babcock & Wilcox
1525 Wilson Blvd., #100
Arlington VA 22209-2411

Jean F. LeCostaouec
Textron Specialty Materials
2 Industrial Avenue
Lowell MA 01851

Stan Levine
NASA Lewis Research Center
21000 Brookpark Road, MS:49-3
Cleveland OH 44135

David Lewis, III
Naval Research Laboratory
Code 6370
Washington DC 20375-5343

Robert H. Licht
Norton Company
SGNICC/NRDC
Goddard Road
Northboro MA 01532-1545

E. Lilley
Norton Company
SGNICC/NRDC
Goddard Road
Northboro MA 01532-1545

Laura J. Lindberg
AlliedSignal Aerospace Company
Garrett Fluid Systems Division
P.O. Box 22200
Tempe AZ 85284-2200

Ronald E. Loehman
Sandia National Laboratories
Chemistry & Ceramics Dept. 1840
P.O. Box 5800
Albuquerque NM 87185

L. A. Lott
EG&G Idaho, Inc.
Idaho National Engineering Lab
P.O. Box 1625
Idaho Falls ID 83415-2209

Raouf O. Loutfy
MER Corporation
7960 S. Kolb Road
Tucson AZ 85706

James W. MacBeth
Carborundum Corporation
Structural Division
23 Acheson Drive
Niagara Falls NY 14303

George Maczura
Aluminum Company of America
3450 Park Lane Drive
Pittsburgh PA 15275-1119

David Maginnis
Tinker AFB
OC-ALC/LIIRE
Tinker AFB OK 73145-5989

L. E. Mains
Deco-Grande
4850 Coolidge Highway
Royal Oak MI 48073-1023

Kenneth M. Maillar
Barbour Stockwell Company
83 Linskey Way
Cambridge MA 02142

S. G. Malghan
NIST
I-270 & Clopper Road
Gaithersburg MD 20899

John Mangels
Ceradyne, Inc.
3169 Redhill Avenue
Costa Mesa CA 92626

Russell V. Mann
Matec Applied Sciences, Inc.
75 South Street
Hopkinton MA 01748

William R. Manning
Champion Aviation Products Div.
P.O. Box 686
Liberty SC 29657

Robert A. Marra
Aluminum Company of America
Alcoa Technical Center
Alcoa Center PA 15069

Steve C. Martin
Advanced Refractory Technologies
699 Hertel Avenue
Buffalo NY 14207

James P. Mathers
3M Company
3M Center, Bldg. 201-3N-06
St. Paul MN 55144

F. N. Mazadarany
General Electric Company
Bldg. K-1, Room MB-159
P.O. Box 8
Schenectady NY 12301

Colin F. McDonald
McDonald Thermal Engineering
1730 Castellana Road
La Jolla CA 92037

B. J. McEntire
Norton Company
10 Airport Park Road
East Granby CT 06026

James McLaughlin
Sundstrand Power Systems
4400 Ruffin Road
P.O. Box 85757
San Diego CA 92186-5757

Matt McMonigle
U.S. Department of Energy
Office of Industrial Technologies
EE-234, Forrestal Building
Washington DC 20585

J. C. McVickers
AlliedSignal Engines
P.O. Box 52180, MS:9317-2
Phoenix AZ 85072-2180

Joseph J. Meindl
Reynolds International, Inc.
6603 W. Broad Street
P.O. Box 27002
Richmond VA 23261-7003

Michael D. Meiser
AlliedSignal, Inc.
Ceramic Components
P.O. Box 2960, MS:T21
Torrance CA 90509-2960

David J. Michael
Harbison-Walker Refractories
P.O. Box 98037
Pittsburgh PA 15227

Ken Michaels
Chrysler Motors Corporation
P.O. Box 1118, CIMS:418-17-09
Detroit MI 48288

Biljana Mikijelj
Ceradyne, Inc.
3169 Redhill Avenue
Costa Mesa CA 92626

Carl E. Miller
AC Rochester
1300 N. Dort Highway, MS:32-31
Flint MI 48556

Charles W. Miller, Jr.
Harper International
West Drullard Avenue
Lancaster NY 14086-1698

R. Mininni
Enichem America
2000 Cornwall Road
Monmouth Junction NJ 08852

Michele V. Mitchell
AlliedSignal, Inc.
Ceramic Components
P.O. Box 2960, MS:T21
Torrance CA 90509-2960

Howard Mizuhara
WESGO
477 Harbor Boulevard
Belmont CA 94002

Helen Moeller
Babcock & Wilcox
P.O. Box 11165
Lynchburg VA 24506-1165

Francois R. Mollard
Concurrent Technologies Corp.
1450 Scalp Avenue
Johnstown PA 15904-3374

Phil Mooney
Panametrics
221 Crescent Street
Waltham MA 02254

Geoffrey P. Morris
3M Company
3M Traffic Control Materials
Bldg. 209-BW-10, 3M Center
St. Paul MN 55144-1000

Thomas W. Mullan
Vapor Technologies Inc.
345 Route 17 South
Upper Saddle River NJ 07458

Theresa A. Mursick-Meyer
Norton Company
SGNICC/NRDC
Goddard Road
Northboro MA 01532-1545

Curtis V. Nakaishi
U.S. Department of Energy
Morgantown Energy Tech. Ctr.
P.O. Box 880
Morgantown WV 26507-0880

K. S. Narasimhan
Hoeganaes Corporation
River Road
Riverton NJ 08077

Malcolm Naylor
Cummins Engine Company, Inc.
P.O. Box 3005, Mail Code 50183
Columbus IN 47202-3005

Timothy A. Nielsen
Williams International Corp.
2280 W. Maple Road
Walled Lake MI 48390-0200

Dale E. Niesz
Rutgers University
Center for Ceramic Research
P.O. Box 909
Piscataway NJ 08855-0909

Paul W. Niskanen
Lanxide Corporation
P.O. Box 6077
Newark DE 19714-6077

David M. Nissley
United Technologies Corporation
Pratt & Whitney Aircraft
400 Main Street, MS:163-10
East Hartford CT 06108

Don Ohanehi
Magnetic Bearings, Inc.
1908 Sussex Road
Blacksburg VA 24060

Robert Orenstein
General Electric Company
55-112, River Road
Schenectady NY 12345

Richard Palicka
Cercom, Inc.
1960 Watson Way
Vista CA 92083

Pellegrino Papa
Corning Inc.
MP-WX-02-1
Corning NY 14831

Terry Paquet
Boride Products Inc.
2879 Aero Park Drive
Traverse City MI 49684

Soon C. Park
3M Corporate Research
3M Center, Bldg. 251-3B-13
St. Paul MN 55144-1000

Vijay M. Parthasarathy
Caterpillar/Solar Turbines
2200 Pacific Highway
P.O. Box 85376
San Diego CA 92186-5376

James W. Patten
Cummins Engine Company, Inc.
P.O. Box 3005, Mail Code 50183
Columbus IN 47202-3005

Robert W. Pepper
Textron Specialty Materials
2 Industrial Avenue
Lowell MA 01851

John J. Petrovic
Los Alamos National Laboratory
Group MST-4, MS:G771
Los Alamos NM 87545

John P. Pollinger
AlliedSignal, Inc.
Ceramic Components
P.O. Box 2960, MS:T21
Torrance CA 90509-2960

Bob R. Powell
General Motors Corporation
Metallurgy Department
Box 9055
Warren MI 48090-9055

Stephen C. Pred
Pred Materials International, Inc.
Lincoln Bldg.
60 East 42nd Street, Suite 1456
New York NY 10165

Karl M. Prewo
United Technologies Res. Ctr.
411 Silver Lane, MS:24
East Hartford CT 06108

Vimal K. Pujari
Norton Company
SGNICC/NRDC
Goddard Road
Northboro MA 01532-1545

Fred Quan
Corning Inc.
Sullivan Park, FR-02-08
Corning NY 14831

George Quinn
NIST
Quince Orchard & Clopper Road
Ceramics Division, Bldg. 223
Gaithersburg MD 20899

Charles F. Rapp
Owens Corning Fiberglass
2790 Columbus Road
Granville OH 43023-1200

Wilfred J. Rebello
PAR Enterprises, Inc.
12601 Clifton Hunt Lane
Clifton VA 22024

Harold Rechter
Chicago Fire Brick Company
7531 S. Ashland Avenue
Chicago IL 60620

Robert R. Reeber
U.S. Army Research Office
P.O. Box 12211
Research Triangle Park NC 27709-2211

Paul E. Rempes
McDonnell Douglass Aircraft Co.
P.O. Box 516, Mail Code:0642263
St. Louis MO 63166-0516

Gopal S. Revankar
John Deere Company
3300 River Drive
Moline IL 61265

David W. Richerson
2093 E. Delmont Drive
Salt Lake City UT 84117

Tomas Richter
J. H. France Refractories
1944 Clarence Road
Snow Shoe PA 16874

Michael Rigdon
Institute for Defense Analyses
1801 N. Beauregard Street
Alexandria VA 22311

W. Eric Roberts
Advanced Ceramic Technology
990 "F" Enterprise Street
Orange CA 92667

Michael Rossetti
Arthur D. Little, Inc.
15 Acorn Park
Cambridge MA 01240

Barry Rossing
Lanxide Corporation
P.O. Box 6077
Newark DE 19714-6077

Steven L. Rotz
Lubrizol Corporation
29400 Lakeland Boulevard
Wickliffe OH 44092

Robert Ruh
Wright Laboratory
WL/MLLM
Wright-Patterson AFB OH 45433

Robert J. Russell
Riverdale Consulting, Inc.
24 Micah Hamlin Road
Centerville MA 02632-2107

Jon A. Salem
NASA Lewis Research Center
21000 Brookpark Road
Cleveland OH 44135

J. Sankar
North Carolina A&T State Univ.
Dept. of Mechanical Engineering
Greensboro NC 27406

Maxine L. Savitz
AlliedSignal, Inc.
Ceramic Components
P.O. Box 2960, MS:T21
Torrance CA 90509-2960

Ashok Saxena
GTRI
Materials Engineering
Atlanta GA 30332-0245

David W. Scanlon
Instron Corporation
100 Royall Street
Canton MA 02021

Robert E. Schafrik
Natl Materials Advisory Board
2101 Constitution Ave., N.W.
Washington DC 20418

James Schienle
AlliedSignal Engines
P.O. Box 52180, MS:1302-2P
Phoenix AZ 85072-2180

Gary Schnittgrund
PyroPacific Processes
16401 Knollwood Drive
Granada Hills CA 91344

Mark Schomp
Lonza, Inc.
17-17 Route 208
Fair Lann NJ 07410

Robert B. Schulz
U.S. Department of Energy
Office of Transportation Technologies
EE-33, Forrestal Building
Washington DC 20585

William T. Schwessinger
Multi-Arc Scientific Coatings
1064 Chicago Road
Troy MI 48083-4297

Nancy Scoville
Thermo Electron Technologies
P.O. Box 9046
Waltham MA 02254-9046

Thomas M. Sebestyen
U.S. Department of Energy
Office of Transportation Technologies
EE-32, Forrestal Building
Washington DC 20585

William J. Shack
Argonne National Laboratory
9700 S. Cass Avenue, Bldg. 212
Argonne IL 60439

Richard K. Shaltens
NASA Lewis Research Center
21000 Brookpark Road, MS:302-2
Cleveland OH 44135

Robert S. Shane
1904 NW 22nd Street
Stuart FL 34994-9270

Ravi Shankar
Chromalloy
Research and Technology
Blaisdell Road
Orangeburg NY 10962

Terence Sheehan
Alpex Wheel Company
727 Berkley Street
New Milford NJ 07646

Thomas Shreves
American Ceramic Society, Inc.
735 Ceramic Place
Westerville OH 43081-8720

Richard Silberglitt
FM Technologies, Inc.
10529-A Braddock Road
Fairfax VA 22032

Mary Silverberg
Norton Company
SGNICC/NRDC
Goddard Road
Northboro MA 01532-1545

John Skildum
3M Company
3M Center
Building 224-2S-25
St. Paul MN 55144

Jay R. Smyth
AlliedSignal Engines
111 S. 34th Street, MS:503-412
Phoenix AZ 85034

Rafal A. Sobotowski
British Petroleum Company
Technical Center, Broadway
3092 Broadway Avenue
Cleveland OH 44115

Boyd W. Sorenson
DuPont Lanxide Composites
1300 Marrows Road
Newark DE 19711

Charles A. Sorrell
U.S. Department of Energy
Office of Industrial Technologies
EE-232, Forrestal Building
Washington DC 20585

Charles Spuckler
NASA Lewis Research Center
21000 Brookpark Road, MS:5-11
Cleveland OH 44135-3191

Gordon L. Starr
Cummins Engine Company, Inc.
P.O. Box 3005, Mail Code:50182
Columbus IN 47202-3005

Tom Stillwagon
AlliedSignal, Inc.
Ceramic Components
P.O. Box 2960, MS:T21
Torrance CA 90509-2960

Paul D. Stone
Dow Chemical USA
1776 "Eye" Street, N.W., #575
Washington DC 20006

Thomas N. Strom
NASA Lewis Research Center
21000 Brookpark Road, MS:86-6
Cleveland OH 44135

Willard H. Sutton
United Technologies Corporation
411Silver Lane, MS:24
East Hartford CT 06108

Robert E. Swanson
Metalworking Technology, Inc.
1450 Scalp Avenue
Johnstown PA 15904

Victor J. Tennery
113 Newell Lane
Oak Ridge TN 37830

David F. Thompson
Corning Glass Works
SP-DV-02-1
Corning NY 14831

D. M. Tracey
Norton Company
SGNICC/NRDC
Goddard Road
Northboro MA 01532-1545

Marc Tricard
Norton Company, WGTC
1 New Bond Street, MS-413-201
Worcester MA 01615-0008

W. T. Tucker
General Electric Company
P.O. Box 8, Bldg. K1-4C35
Schenectady NY 12301

John F. Vander Louw
3M Company
3M Center, Bldg. 60-1N-01
Saint Paul MN 55144

Marcel H. Van De Voorde
Commission of the European Community
P.O. Box 2
1755 ZG Petten
THE NETHERLANDS

Stan Venkatesan
Southern Coke & Coal Corp.
P.O. Box 52383
Knoxville TN 37950

Theodore Vojnovich
U.S. Department of Energy
Laboratory Technology Applications
ER-32, Forrestal Bldg.
Washington DC 20585

Janet Wade
AlliedSignal Engines
P.O. Box 52180, MS:1303-2
Phoenix AZ 85072-2180

Richard L. Wagner
Ceramic Technologies, Inc.
537 Turtle Creek South Dr.
Indianapolis IN 46227

Daniel J. Wahlen
Kohler, Co.
444 Highland Drive
Kohler WI 53044

Ronald H. Walecki
AlliedSignal, Inc.
Ceramic Components
P.O. Box 2960, MS:T21
Torrance CA 90509-2960

Michael S. Walsh
Vapor Technologies Inc.
6300 Gunpark Drive
Boulder CO 80301

Robert M. Washburn
ASMT
11203 Colima Road
Whittier CA 90604

James K. Weddell
Du Pont Lanxide Composites Inc.
1300 Marrows Road
P.O. Box 6077
Newark DE 19714-6077

R. W. Weeks
Argonne National Laboratory
MCT-212
9700 S. Cass Avenue
Argonne IL 60439

Robert D. West
Therm Advanced Ceramics
P.O. Box 220
Ithaca NY 14851

Ian A. White
Hoeganaes Corporation
River Road
Riverton NJ 08077

Sheldon M. Wiederhorn
NIST
Building 223, Room A329
Gaithersburg MD 20899

James C. Williams
General Electric Company
Engineering Materials Tech.
One Neumann Way, Mail Drop:H85
Cincinnati OH 45215-6301

Thomas A. Williams
National Renewable Energy Lab
1617 Cole Boulevard
Golden CO 80401

Craig A. Willkens
Norton Company
SGNICC/NRDC
Goddard Road
Northboro MA 01532-1545

Roger R. Wills
Ohio Aerospace Institute (OAI)
22800 Cedar Point Road
Brook Park OH 44142

J. M. Wimmer
AlliedSignal, Inc.
Ceramic Components
2525 West 190th Street
P. O. Box 2960, MS:T21
Torrance CA 90509-2960

Matthew F. Winkler
Seaworthy Systems, Inc.
P.O. Box 965
Essex CT 06426

Thomas J. Wissing
Eaton Corporation
Engineering and Research Center
P.O. Box 766
Southfield MI 48037

James C. Withers
MER Corporation
7960 S. Kolb Road
Building F
Tucson AZ 85706

Dale E. Wittmer
Southern Illinois University
Mechanical Engineering Dept.
Carbondale IL 62901

Warren W. Wolf
Owens Corning Fiberglass
2790 Columbus Road, Route 16
Granville OH 43023

Egon E. Wolff
Caterpillar Inc.
Technical Center
P.O. Box 1875
Peoria IL 61656-1875

George W. Wolter
Howmet Turbine Components Corp.
Technical Center
699 Benston Road
Whitehall MI 49461

John F. Wosinski
Corning Inc.
ME-2 E-5 H8
Corning NY 14830

Bernard J. Wrona
Advanced Composite Materials
1525 S. Buncombe Road
Greer SC 29651

Carl C. M. Wu
Naval Research Laboratory
Ceramic Branch, Code 6373
Washington DC 20375

David C. Wu
AlliedSignal Engines
P.O. Box 52181, MS:301-227
Phoenix AZ 85072-2181

John C. Wurst
U. of Dayton Research Institute
300 College Park
Dayton OH 45469-0101

Neil Wyant
ARCH Development Corp.
9700 S. Cass Avenue, Bldg. 202
Argonne IL 60439

Roy Yamamoto
Ethyl Corporation
P. O. Box 2158
Richmond VA 23218-2158

John Yamanis
AlliedSignal Aerospace Company
P.O. Box 1021
Morristown NJ 07962-1021

Thomas M. Yonushonis
Cummins Engine Company, Inc.
P.O. Box 3005, Mail Code 50183
Columbus IN 47202-3005

Jong Yung
Sundstrand Aviation Operations
4747 Harrison Avenue
Rockford IL 61125

A. L. Zadoks
Caterpillar Inc.
Technical Center, Building L
P.O. Box 1875
Peoria IL 61656-1875

Charles H. Zenuk
Transtech
6662 E. Paseo San Andres
Tucson AZ 85710-2106

Zhenqi Zhu
University of Connecticut
Precision Manufacturing Center
Storrs CT 06269-5119

Carl Zweben
General Electric Company
P. O Box 8555, VFSC/V4019
Philadelphia PA 19101

Department of Energy
Oak Ridge Operations Office
Assistant Manager for Energy
Research and Development
P. O. Box 2001
Oak Ridge TN 37831-8600

Department of Energy (2)
Office of Scientific and Technical
Information
Office of Information Services
P. O. Box 62
Oak Ridge TN 37831

For distribution by microfiche
as shown in DOE/OSTI-4500,
Distribution Category UC-332
(Ceramics/Advanced Materials).